

Coupling of Subchannel Analysis Tools with Advanced Multiscale Core Simulations

Thesis submitted in accordance with the requirements of the University of Liverpool for the degree of
Doctor in Philosophy

By

Sebastian Davies

June 2024

Contents	
Abstract	5
Acknowledgements	6
List of Publications	7
List of Figures	8
List of Tables	12
Abbreviations	13
Chapter 1: Introduction	16
Chapter 2: Background	22
2.1. Neutronics	22
2.1.1. <i>Neutron Transport Equation</i>	22
2.1.2. <i>Approximations to the Neutron Transport Equation</i>	23
2.2. Thermal Hydraulics	24
2.2.1. <i>Fluid and Solid Dynamics Equations</i>	24
2.2.2. <i>Approximations to the Fluid and Solid Dynamics Equations</i>	25
2.3. Coupled Reactor Physics	26
2.3.1. <i>Power Equation and Cross Sections Feedback</i>	26
2.3.2. <i>Approximations to the Power Equation and Cross Sections Feedback</i>	26
2.4. SCALE-POLARIS Code System	26
2.4.1. <i>General Overview</i>	26
2.4.2. <i>Methods in POLARIS</i>	27
2.4.3. <i>Solution</i>	28
2.5. LOTUS Transport Code	28
2.5.1. <i>General Overview</i>	29
2.5.2. <i>Methods in LOTUS</i>	29
2.5.3. <i>Solution</i>	30
2.6. Open MC Transport Code	30
2.6.1. <i>General Overview</i>	30
2.6.2. <i>Methods in Open MC</i>	31
2.6.3. <i>Solution</i>	32
2.7. DYN3D Nodal Code	32
2.7.1. <i>General Overview</i>	32
2.7.2. <i>Methods in NK</i>	32
2.7.3. <i>Methods in FLOCAL</i>	33
2.7.4. <i>Solution</i>	34
2.8. CTF Subchannel Code	36
2.8.1. <i>General Overview</i>	36
2.8.2. <i>Methods in CTF</i>	36
2.8.3. <i>Solution</i>	38
Chapter 3: Thermal Hydraulics Validations and Verifications within a Subchannel Code and the Associated Module within a Nodal Code	39
3.1. Introduction	40
3.2. Codes Used in the Validations and Verifications	43
3.2.1. <i>CTF Subchannel Code</i>	43
3.2.2. <i>FLOCAL Thermal Hydraulics Module</i>	44
3.3. Specifications Used in the Validations and Verifications	44
3.3.1. <i>PSBT Benchmark</i>	44
3.3.2. <i>FLOCAL Developer Benchmark</i>	47
3.4. Models Used in the Validations and Verifications	48

3.4.1. PSBT Benchmark	48
3.4.2. FLOCAL Developer Benchmark	49
3.5. Results and Analysis	50
3.5.1. PSBT Benchmark	50
3.5.2. FLOCAL Developer Benchmark	54
3.6. Conclusions	56
3.7. Future Work	57
3.8. Nomenclature.....	57
3.9. Appendix A: PSBT Benchmark	59
3.10. Appendix B: FLOCAL Developer Benchmark.....	62
3.11. References.....	64
Chapter 4: One Way Coupling of a Nodal Code and a Subchannel Code	67
4.1. Introduction	68
4.2. Codes Used in the Verification	72
4.2.1. DYN3D Nodal Code.....	72
4.2.2. CTF Subchannel Code	73
4.3. Specifications Used in the Verification.....	74
KAIST Benchmark.....	74
4.4. Models and Scripts Used in the Verification.....	76
4.4.1. KAIST Benchmark.....	76
4.4.2. DYN3D and CTF Coupling Scripts.....	77
4.5. Results and Analysis	78
KAIST Benchmark.....	78
4.6. Conclusions	89
4.7. Future Work	89
4.8. Nomenclature.....	90
4.9. Appendix A: Code Types.....	91
4.10. Appendix B: KAIST Benchmark	92
4.11. References.....	102
Chapter 5: Two Ways Coupling of a Nodal Code and a Subchannel Code	106
5.1. Introduction	107
5.2. Codes within the Verification	111
5.2.1. DYN3D Nodal Code.....	111
5.2.2. CTF Subchannel Code	112
5.3. Modules within the Verification	112
DYN3D and CTF Coupling Modules	113
5.4 Specifications within the Verification.....	115
Modified KAIST Benchmark.....	115
5.5. Models within the Verification.....	118
Modified KAIST Benchmark.....	118
5.6. Results and Analysis	120
5.6.1. Fuel Assemblies.....	120
5.6.2. Mini-Cores	126
5.7. Conclusions	131
5.8. Future Work	132
5.9. Nomenclature.....	133
5.10. Appendix A. Fuel Assemblies	134
5.11. Appendix B. Mini-Cores	137
5.12. References.....	140

Chapter 6: Multi Ways Coupling of a Transport Code a Subchannel Code and a Nodal Code	144
6.1. Coupling Software Environment Used within the Verifications	145
<i>Customized Coupling Software Environment</i>	145
6.2. Specifications Used within the Verifications	148
<i>Customized Benchmark</i>	148
6.3. Models Used within the Verifications	151
6.3.1. <i>Fuel Assembly Level</i>	151
6.3.2. <i>Fuel Pin or Materials Level</i>	152
6.4. Results and Analysis	154
6.4.1. <i>Quarter Core with Reflectors</i>	154
6.4.2. <i>Fuel Assemblies & Quarter Core without Reflectors</i>	157
6.5. Appendix. Fuel Assemblies & Quarter Core without Reflectors	164
Chapter 7: Conclusions	167
Chapter 8: Future Work	168
Appendix	170
References	172

Abstract

Nuclear reactors could allow to answer the energy demands and achieve low CO₂ emissions in the country while nuclear simulation software can improve the efficiency without affecting the safety of nuclear reactors and therefore, the UK government is currently investing resources in the next generation of PWR and new nuclear simulation software. In nuclear reactors, the physical phenomena such as power production, heat and mass transfer, and fuel behaviour are coupled in between, although in nuclear simulation software, these physical phenomena have often been simulated independently. Several state-of-the-art multiscale and multi-physics software developments, including NURESIM and CASL, are being created, which include improved nuclear codes and coupling software environments. These cannot answer the demands of academia, the industry, and the nuclear regulator in the UK. NURESIM does not generally include the most advanced neutron transport methods, only providing improved coupled reactor physics. CASL generally requires thousands of processor/hours to deliver a solution which cannot be covered by the available computational clusters or workstations, providing full coupled reactor physics in all the reactor core.

A multiscale and multi-physics software development is being created for the UK, which currently includes a nodal code, a transport code, a subchannel code, and a customized coupling software environment. It will eventually answer the demands of academia, the industry, and the nuclear regulator in the UK. It includes the most advanced neutron transport methods, providing simplified, improved, and full coupled reactor physics. It requires few processor/hours to deliver a solution which can be covered by the available computational clusters or workstations. It provides improved and full coupled reactor physics only in the hottest fuel assemblies with boundary conditions obtained providing simplified coupled reactor physics in all the reactor core. Validation and verification are fundamental for it to become state-of-the-art software. In this PhD project, the multiscale and multi-physics software development has been created along with its associated acknowledgements, validations, and verifications. These acknowledgements, validations, and verifications have outlined or proven several outcomes.

Initially, an acknowledgement of the neutronics, thermal hydraulics, coupled reactor physics, SCALE-POLARIS code system lattice module, LOTUS, and Open MC transport codes, DYN3D nodal code, and CTF subchannel code were performed through their description. This has allowed an understanding of the theory used in the nuclear codes and of the nuclear codes used in later work. Then, validations and verifications of the accuracy and methodology available in CTF and FLOCAL (module of DYN3D) to provide thermal hydraulics at the fuel rod level were performed through the PSBT benchmark, previously covered by other partners using CTF, and through the FLOCAL developer benchmark not covered before. These have proven that CTF provides high accuracy in 1x1 and 5x5 bundles when compared to experimental data and other thermal hydraulics codes and a wide range of crossflow and turbulent mixing methods in a 2x1 bundle when compared to FLOCAL.

Later, a one-way DYN3D and CTF coupling and the associated verification of the inner coupling iterations within an outer iteration were performed through the KAIST benchmark, previously tested by other partners using other neutronics codes, and through coupling scripts. These have proven that the DYN3D and CTF coupling provides improved feedback in 17x17 fuel assemblies compared to DYN3D using 1 processor within computational times of 20 minutes compared to 2 minutes. Then, a two-ways DYN3D and CTF coupling and the associated verification of the outer coupling iterations and convergence were performed through modified and created modules within DYN3D and a customized coupling software environment, and through the modified KAIST benchmark. These have proven that the DYN3D and CTF coupling provides improved coupled reactor physics in 17x17 fuel assemblies and 51x51 mini cores compared to DYN3D using 1 processor within computational times ranging from 1 to 10 hours compared to 2 to 20 minutes.

Finally, a multi ways coupling between LOTUS, CTF and DYN3D and its associated verification were performed through the customized coupling software environment, and through the customized benchmark. These have proven that the LOTUS and CTF coupling with DYN3D provides full coupled reactor physics in a 3x3 quarter core with reflectors composed of 17x17 fuel assemblies or a 34x34 quarter core without reflectors compared to a DYN3D and CTF coupling with DYN3D applying parallelization across 36 processors within computational times ranging from 3 to 24 hours compared to 1 to 8 hours.

Acknowledgements

Initially, I would like to thank my two academic supervisors Prof. Bruno Merk and Prof. Andrew Levers. Both their guidance and insights have allowed me to better understand the project from a general point of view. Without them, I would not have had the opportunity to do this PhD project. Also, I would like to thank my industrial supervisor Paul Bryce. His engagement has allowed me to tailor the PhD project to the needs of the industry. Without him, I would not have gained the experience of partially working with the industry. Moreover, I would like to thank Dr. Dzianis Litskevich. His dedication and patience have allowed me to get through some of the most complex technical barriers as well as better understand the PhD project from a technical point of view. Without him, I would not have been able to advance in some of the critical steps within this PhD project.

Additionally, I am hugely grateful to my wife Yulia. Her love, encouragement, dedication, patience, and support have inspired me since the day We got married as well as given me peace of mind during the PhD project. Without her, I would not have been able to either start or complete this PhD project. Also, I am hugely grateful to my parents. Their love and support have laid the path since I was a child up to now doing this PhD project. Without them, I would not have been able to get to the current stage of my life. Finally, I am also grateful to my rabbits. Their company has cheered me up since the day they arrived at the family up to now doing this PhD project. Without them, I would not have felt so much joy during the PhD project.

List of Publications

The author has constructed the thesis including four journal articles. Three first authored journal articles were published in the MDPI journal of Energies and one second authored journal article was published in the Elsevier journal of Progress in Nuclear Energy consisting of:

- 1) Litskevich, D.; Atkinson, S.; **Davies, S.** Verification of the current coupling collision probability method with orthogonal flux expansion for the assembly calculations. *Prog. Nucl. Energy* 2020, 130, <https://doi.org/10.1016/j.pnucene.2020.103562>.
- 2) **Davies, S.**; Rohde, U.; Litskevich, D.; Merk, B.; Bryce, P.; Levers, A.; Detkina, A.; Atkinson, S.; Ravindra, V. CTF and FLOCAL Thermal Hydraulics Validations and Verifications within a Multiscale and Multiphysics Software Development. *Energies* 2021, 14, 1220. <https://doi.org/10.3390/en14051220>.
- 3) **Davies, S.**; Litskevich, D.; Rohde, U.; Detkina, A.; Merk, B.; Bryce, P.; Levers, A.; Ravindra, V. DYN3D and CTF Coupling within a Multiscale and Multiphysics Software Development (Part I). *Energies* 2021, 14, 5060. <https://doi.org/10.3390/en14165060>.
- 4) **Davies, S.**; Litskevich, D.; Merk, B.; Levers, A.; Bryce, P.; Detkina, A. DYN3D and CTF Coupling within a Multiscale and Multiphysics Software Development (Part II). *Energies* 2022, 15, 4843. <https://doi.org/10.3390/en15134843>.

The contributions to the journal articles can be found in the following tables.

Verification of the current coupling collision probability method with orthogonal flux expansion for the assembly calculations															
Author/Contribution	Conc.	Dat. Cur.	Form. Ana.	Fun. Acq.	Inv.	Met.	Proj. Adm.	Res.	Soft.	Sup.	Val. & Ver.	Vis.	Writ. Orig. Dra.	Writ. Rev & Edit	
Litskevich, D.	✓		✓	✓	✓	✓	✓	✓	✓		✓	✓	✓	✓	
Atkinson, S.					✓				✓			✓	✓	✓	
Davies, S.		✓											✓	✓	

CTF and FLOCAL Thermal Hydraulics Validations and Verifications within a Multiscale and Multiphysics Software Development															
Author/Contribution	Conc.	Dat. Cur.	Form. Ana.	Fun. Acq.	Inv.	Met.	Proj. Adm.	Res.	Soft.	Sup.	Val. & Ver.	Vis.	Writ. Orig. Dra.	Writ. Rev & Edit	
Davies, S.	✓	✓	✓		✓	✓		✓			✓	✓	✓	✓	
Rohde, U.		✓			✓	✓		✓	✓					✓	
Litskevich, D.	✓			✓			✓		✓					✓	
Merk, B.	✓			✓			✓			✓				✓	
Bryce, P.				✓						✓				✓	
Levers, A.										✓				✓	
Detkina, A.														✓	
Atkinson, S.														✓	
Ravindra v.														✓	

DYN3D and CTF Coupling within a Multiscale and Multiphysics Software Development (Part I)															
Author/Contribution	Conc.	Dat. Cur.	Form. Ana.	Fun. Acq.	Inv.	Met.	Proj. Adm.	Res.	Soft.	Sup.	Val. & Ver.	Vis.	Writ. Orig. Dra.	Writ. Rev & Edit	
Davies, S.	✓	✓	✓		✓	✓		✓	✓		✓	✓	✓	✓	
Litskevich, D.	✓			✓			✓		✓					✓	
Rohde, U.						✓			✓					✓	
Detkina, A.				✓				✓						✓	
Merk, B.	✓			✓			✓			✓				✓	
Bryce, P.										✓				✓	
Levers, A.										✓				✓	
Ravindra v.														✓	

DYN3D and CTF Coupling within a Multiscale and Multiphysics Software Development (Part II)															
Author/Contribution	Conc.	Dat. Cur.	Form. Ana.	Fun. Acq.	Inv.	Met.	Proj. Adm.	Res.	Soft.	Sup.	Val. & Ver.	Vis.	Writ. Orig. Dra.	Writ. Rev & Edit	
Davies, S.	✓	✓	✓		✓	✓		✓	✓		✓	✓	✓	✓	
Litskevich, D.	✓			✓			✓		✓					✓	
Merk, B.	✓			✓			✓			✓				✓	
Levers, A.										✓				✓	
Bryce, P.				✓						✓				✓	
Detkina, A.								✓						✓	

Conc. ≡ Conceptualization; **Dat. Cur.** ≡ Data Curation; **Form. Ana.** ≡ Formal Analysis; **Fun. Acq.** ≡ Funding Acquisition; **Inv.** ≡ Investigation; **Met.** ≡ Methodology; **Proj. Adm.** ≡ Project Administration; **Res.** ≡ Resources; **Soft.** ≡ Software; **Sup.** ≡ Supervision; **Val. & Ver.** ≡ Validation & Verification; **Vis.** ≡ Visualization; **Writ. Orig. Dra.** ≡ Writing Original Draft; **Writ. Rev. & Edit.** ≡ Writing Review & Editing

List of Figures

Figure 1.1. NURESIM.	19
Figure 1.2. CASL.	19
Figure 1.3. Multiscale and multi-physics software development.....	20
Figure 1.4. Reactor core at the fuel assembly level and fuel assembly at the fuel pin or materials levels.	20
Figure 2.1. SCALE-POLARIS steady state scheme.....	28
Figure 2.2. LOTUS steady state scheme	30
Figure 2.3. (a) DYN3D steady state coupling scheme, (b) DYN3D steady state thermal hydraulics scheme, (c) DYN3D steady state neutronics scheme.	35
Figure 2.4. CTF pseudo-steady state scheme	38
Figure 3.GA. Chapter 3 graphical abstract.....	39
Figure 3.1. Multiscale and multi-physics software development.....	42
Figure 3.2. (a) CTF 1 × 1 design; (b) CTF 5 × 5 design.	48
Figure 3.3. CTF and FLOCAL 2 × 1 design.	49
Figure 3.4. CTF vs. experimental void fraction.	50
Figure 3.5. (a) Codes void fraction mean errors; (b) codes void fraction error standard deviation.	51
Figure 3.6. CTF vs. experimental void fraction.	52
Figure 3.7. Codes void fraction mean errors.	52
Figure 3.8. Codes void fraction error standard deviation.	53
Figure 3.9. CTF vs. experimental critical-heat flux.	53
Figure 3.10. Codes departure from nucleate-boiling heights.	54
Figure 3.11. (a) CTF void fraction axial distributions; (b) FLOCAL void fraction axial distributions.	55
Figure 3.12. (a) CTF departure from nucleate boiling (DNB) axial distributions; (b) FLOCAL DNB axial distributions.	56
Figure 3.A1. Gamma-ray transmission method (subchannel).....	59
Figure 3.A2. Gamma-ray transmission method (bundle).	60
Figure 3.A3. CTF vs. experimental equilibrium quality.....	61
Figure 3.A4. CTF vs. experimental density.	61
Figure 3.A5. CTF vs. experimental equilibrium quality.....	61
Figure 3.A6. (a) CTF mass-flux axial distributions; (b) FLOCAL mass-flux axial distributions.	62
Figure 3.A7. (a) CTF mass-flux axial distributions; (b) FLOCAL mass-flux axial distributions.	63
Figure 3.A8. (a) CTF coolant-temperature axial distributions; (b) FLOCAL coolant-temperature axial distributions.	64
Figure 4.GA. Chapter 4 graphical abstract.....	67
Figure 4.1. (a) External coupling. (b) internal coupling. (c) parallel coupling.....	71
Figure 4.2. (a) DYN3D UOX-2 (CR/BA16) 17 × 17 model, (b) CTF UOX-2 (CR/BA16) 17 × 17 model.	76
Figure 4.3. (a) DYN3D internal coupling, (b) DYN3D, and CTF external coupling.....	78
Figure 4.4. (a) UOX-2 (CR) fluid density feedback values, (b) UOX-2 (BA16) fluid density feedback values. .	79
Figure 4.5. DYN3D coupling transversal fluid density feedback distribution.	80
Figure 4.6. DYN3D and CTF coupling transversal fluid density feedback distribution.....	81
Figure 4.7. (a) UOX-2 (CR) fluid temperature feedback values, (b) UOX-2 (BA16) fluid temperature feedback values.....	82
Figure 4.8. Axial fluid temperature feedback distributions.....	83
Figure 4.9. DYN3D coupling transversal fluid temperature feedback distribution.	83
Figure 4.10. DYN3D and CTF coupling transversal fluid temperature feedback distribution.	84
Figure 4.11. (a) UOX-2 (CR) fuel temperature feedback values, (b) UOX-2 (BA16) fuel temperature feedback values.....	85
Figure 4.12. Axial fuel temperature feedback distributions.	86
Figure 4.13. DYN3D coupling transversal fuel temperature feedback distribution.	86
Figure 4.14. DYN3D and CTF coupling transversal fuel temperature feedback distribution.....	87
Figure 4.15. (a) UOX-2 (CR) pressure drop feedback values, (b) UOX-2 (BA16) pressure drop feedback values.	88
Figure 4.A1. UOX-2 (CR) and UOX-2 (BA16) locations within the KAIST 1A LWR reactor core.....	92
Figure 4.A2. (a) UOX-2 (CR) mass flux feedback values, (b) UOX-2 (BA16) mass flux feedback values.	92

Figure 4.A3. Axial mass flux feedback distribution.....	94
Figure 4.A4. DYN3D coupling transversal mass flux feedback distribution.....	94
Figure 4.A5. DYN3D and CTF coupling transversal mass flux feedback distribution.....	95
Figure 4.A6. (a) UOX-2 (CR) void fraction feedback values, (b) UOX-2 (BA16) void fraction feedback values.....	96
Figure 4.A7. Axial void fraction feedback distribution.....	97
Figure 4.A8. DYN3D coupling transversal void fraction feedback distribution.....	98
Figure 4.A9. DYN3D and CTF coupling transversal void fraction feedback distribution.....	98
Figure 4.A10. (a) UOX-2 (CR) DNBR feedback values, (b) UOX-2 (BA16) DNBR feedback values.....	99
Figure 4.A11. Axial DNBR feedback distribution.....	100
Figure 4.A12. DYN3D coupling transversal DNBR feedback distribution.....	101
Figure 4.A13. DYN3D and CTF coupling transversal DNBR feedback distribution.....	101
Figure 5.GA. Chapter 5 graphical abstract.....	106
Figure 5.1. (a) One-way coupling and (b) two-way coupling.....	110
Figure 5.2. DYN3D (NK-FLOCAL) decoupling and external feedback importation.....	113
Figure 5.3. DYN3D and CTF coupling within the customized coupling software environment.....	114
Figure 5.4. (a) DYN3D 17 × 17 fuel assembly mesh, (b) CTF 17 × 17 fuel assembly mesh, (c) DYN3D 3 × 3 mini-core mesh, and (d) CTF 3 × 3 mini-core mesh.....	119
Figure 5.5. (a) DYN3D and CTF coupling UOX-2 (CR) fuel assembly reactivity difference convergence and (b) DYN3D and CTF coupling UOX-2 (BA-16) fuel assembly reactivity difference convergence.....	121
Figure 5.6. (a) UOX-2 (CR) fuel assembly average axial fission power distributions and (b) UOX-2 (BA-16) fuel assembly average axial fission power distributions.....	122
Figure 5.7. (a) UOX-2 (CR) axial fission power distributions and (b) UOX-2 (BA-16) axial fission power distributions.....	124
Figure 5.8. (a) DYN3D UOX-2 (CR) fuel assembly transversal fission power distribution, (b) DYN3D and CTF coupling UOX-2 (CR) fuel assembly transversal fission power distribution, (c) DYN3D UOX-2 (BA-16) fuel assembly transversal fission power distribution and (d) DYN3D and CTF coupling UOX-2 (BA-16) fuel assembly transversal fission power distribution.....	124
Figure 5.9. (a) Relative difference between DYN3D and CTF coupling and DYN3D UOX-2 (CR) fuel assembly transversal fission power distributions and (b) relative difference between DYN3D and CTF coupling and DYN3D UOX-2 (BA-16) fuel assembly transversal fission power distributions.....	125
Figure 5.10. (a) DYN3D and CTF Coupling UOX-2 (CR) fuel assembly maximum fission power convergence and (b) DYN3D and CTF Coupling UOX-2 (BA-16) fuel assembly maximum fission power convergence.....	126
Figure 5.11. (a) DYN3D and CTF Coupling homogeneous mini-core reactivity difference convergence and (b) DYN3D and CTF Coupling heterogeneous mini-core reactivity difference convergence.....	127
Figure 5.12. (a) Homogeneous mini-core average axial fission power distributions and (b) heterogeneous mini-core average axial fission power distributions.....	128
Figure 5.13. (a) Homogeneous mini-core axial fission power distributions and (b) heterogeneous mini-core axial fission power distributions.....	129
Figure 5.14. (a) DYN3D homogeneous mini-core transversal fission power distribution, (b) DYN3D and CTF coupling homogeneous mini-core transversal fission power distribution, (c) DYN3D heterogeneous mini-core transversal fission power distribution and (d) DYN3D and CTF coupling heterogeneous mini-core transversal fission power distribution.....	130
Figure 5.15. (a) Relative difference between DYN3D and CTF coupling and DYN3D homogeneous mini-core transversal fission power distributions and (b) relative difference between DYN3D and CTF coupling and DYN3D heterogeneous mini-core transversal fission power distributions.....	131
Figure 5.16. (a) DYN3D and CTF Coupling homogeneous mini-core maximum fission power convergence and (b) DYN3D and CTF Coupling heterogeneous mini-core maximum fission power convergence.....	131
Figure 5.A1. (a) Relative difference between DYN3D and CTF coupling and DYN3D UOX-2 (CR) fuel assembly transversal moderator density distributions, (b) relative difference between DYN3D and CTF coupling and DYN3D UOX-2 (BA-16) fuel assembly moderator density distributions, (c) relative difference between DYN3D and CTF coupling and DYN3D UOX-2 (CR) fuel assembly transversal moderator temperature distributions, (d) relative difference between DYN3D and CTF coupling and DYN3D UOX-2 (BA-16) fuel assembly moderator temperature distributions, (e) relative difference between DYN3D and CTF coupling and DYN3D UOX-2 (CR)	

<i>fuel assembly transversal fuel temperature distributions and (f) relative difference between DYN3D and CTF coupling and DYN3D UOX-2 (BA-16) fuel assembly fuel temperature distributions.</i>	135
Figure 5.A2. (a) DYN3D and CTF coupling UOX-2 (CR) fuel assembly minimum moderator density convergence, (b) DYN3D and CTF coupling UOX-2 (BA-16) fuel assembly minimum moderator density convergence, (c) DYN3D and CTF coupling UOX-2 (CR) fuel assembly maximum moderator temperature convergence, (d) DYN3D and CTF coupling UOX-2 (BA-16) fuel assembly maximum moderator temperature convergence, (e) DYN3D and CTF coupling UOX-2 (CR) fuel assembly maximum fuel temperature convergence and (f) DYN3D and CTF coupling UOX-2 (BA-16) fuel assembly maximum fuel temperature convergence.	136
Figure 5.A3. (a) Relative difference between DYN3D and CTF coupling and DYN3D homogeneous mini-core transversal moderator density distributions, (b) relative difference between DYN3D and CTF coupling and DYN3D heterogeneous mini-core transversal moderator density distributions, (c) relative difference between DYN3D and CTF coupling and DYN3D homogeneous mini-core transversal moderator temperature distributions, (d) relative difference between DYN3D and CTF coupling and DYN3D heterogeneous mini-core transversal moderator temperature distributions, (e) relative difference between DYN3D and CTF coupling and DYN3D homogeneous mini-core transversal fuel temperature distributions and (f) relative difference between DYN3D and CTF coupling and DYN3D heterogeneous mini-core transversal fuel temperature distributions.	138
Figure 5.A4. (a) DYN3D and CTF coupling homogeneous mini-core minimum moderator density convergence, (b) DYN3D and CTF coupling heterogeneous mini-core minimum moderator density convergence, (c) DYN3D and CTF coupling homogeneous mini-core maximum moderator temperature convergence, (d) DYN3D and CTF coupling heterogeneous mini-core maximum moderator temperature convergence, (e) DYN3D and CTF coupling homogeneous mini-core maximum fuel temperature convergence and (f) DYN3D and CTF coupling heterogeneous mini-core maximum fuel temperature convergence.	139
Figure 6.1. Coupling between LOTUS and CTF at the fuel pin/materials level with DYN3D at the fuel assembly level vs coupling between DYN3D and CTF at the fuel pin level with DYN3D at the fuel assembly level (Simplified).	145
Figure 6.2. Coupling between LOTUS and CTF at the fuel pin level with DYN3D at the fuel assembly level vs coupling between DYN3D and CTF at the fuel pin level with DYN3D at the fuel assembly level (Detailed)..	146
Figure 6.3. DYN3D at the fuel assembly level quarter core with reflectors.	152
Figure 6.4. (a) DYN3D at the fuel pin level or LOTUS at either the fuel pin or materials level fuel assembly; (b) DYN3D at the fuel pin level or LOTUS at either the fuel pin or materials level quarter core without reflectors.	153
Figure 6.5. (a) CTF at the fuel pin level fuel assembly; (b) CTF at the fuel pin level quarter core without reflectors.	154
Figure 6.6. (a) DYN3D at the fuel assembly level quarter core with reflectors total fission power distribution; (b) DYN3D at the fuel assembly level quarter core with reflectors total mass flow distribution.	155
Figure 6.7. Average axial fission power distribution for the individual fuel assemblies and quarter core without reflectors.	156
Figure 6.8. Effective multiplication factor values for the individual fuel assemblies and quarter core without reflectors.	157
Figure 6.9. Absolute reactivity difference convergence for the individual fuel assemblies and quarter core without reflectors.	158
Figure 6.10. Average transversal fission power distribution for the individual fuel assemblies and quarter core without reflectors.	159
Figure 6.11. (a) LOTUS + CTF (Fuel Pin/Materials Level) and DYN3D + CTF (Fuel Pin Level) relative average transversal fission power distribution differences for the central fuel assembly; (b) LOTUS + CTF (Fuel Pin/Materials Level) and DYN3D + CTF (Fuel Pin Level) relative average transversal fission power distribution differences for the side fuel assembly; (c) LOTUS + CTF (Fuel Pin/Materials Level) and DYN3D + CTF (Fuel Pin Level) relative average transversal fission power distribution differences for the corner fuel assembly; (d) LOTUS + CTF (Fuel Pin/Materials Level) and DYN3D + CTF (Fuel Pin Level) relative average transversal fission power distribution differences for the quarter core without reflectors.	160
Figure 6.12. Maximum fission power differences for the individual fuel assemblies and quarter core without reflectors.	161

Figure 6.13. Maximum and average axial fuel temperature distributions for the individual fuel assemblies and quarter core without reflectors..... 162

Figure 6.14. (a) LOTUS + CTF (Fuel Pin/Materials Level) and DYN3D + CTF (Fuel Pin Level) relative maximum transversal fuel temperature distribution differences for the central fuel assembly; **(b)** LOTUS + CTF (Fuel Pin/Materials Level) and DYN3D + CTF (Fuel Pin Level) relative maximum transversal fuel temperature distribution differences for the side fuel assembly; **(c)** LOTUS + CTF (Fuel Pin/Materials Level) and DYN3D + CTF (Fuel Pin Level) relative maximum transversal fuel temperature distribution differences for the corner fuel assembly; **(d)** LOTUS + CTF (Fuel Pin/Materials Level) and DYN3D + CTF (Fuel Pin Level) relative maximum transversal fuel temperature distribution differences for the quarter core without reflectors. 163

Figure 6.15. Maximum fuel temperature difference convergence for the individual fuel assemblies and quarter core without reflectors. 164

Figure 6.A1. Minimum and average axial DNBR distributions for the individual fuel assemblies and quarter core without reflectors..... 165

Figure 6.A2. (a) LOTUS + CTF (Fuel Pin/Materials Level) and DYN3D + CTF (Fuel Pin Level) relative minimum transversal DNBR distribution differences for the central fuel assembly; **(b)** LOTUS + CTF (Fuel Pin/Materials Level) and DYN3D + CTF (Fuel Pin Level) relative minimum transversal DNBR distribution differences for the side fuel assembly; **(c)** LOTUS + CTF (Fuel Pin/Materials Level) and DYN3D + CTF (Fuel Pin Level) relative minimum transversal DNBR distribution differences for the corner fuel assembly; **(d)** LOTUS + CTF (Fuel Pin/Materials Level) and DYN3D + CTF (Fuel Pin Level) minimum transversal DNBR distribution differences for the quarter core without reflectors..... 166

List of Tables

<i>Table 2.1. Methods and updates in POLARIS.</i>	27
<i>Table 2.2. Methods and updates in LOTUS.</i>	29
<i>Table 2.3. Methods and updates in Open MC.</i>	30
<i>Table 2.4. Methods and updates in NK and FLOCAL.</i>	32
<i>Table 2.5. Methods and updates in CTF.</i>	36
<i>Table 3.1. 1 × 1 and 5 × 5 geometry from the PSBT (PWR subchannel and bundle tests) benchmark.</i>	45
<i>Table 3.2. 1 × 1 and 5 × 5 materials from the PSBT benchmark.</i>	45
<i>Table 3.3. 5 × 5 spacer grids from the PSBT benchmark.</i>	46
<i>Table 3.4. 1 × 1 and 5 × 5 power distributions from the PSBT benchmark.</i>	46
<i>Table 3.5. 1 × 1 (S1) and 5 × 5 (B7 and A8) initial and boundary conditions from the PSBT benchmark.</i>	46
<i>Table 3.6. 2 × 1 geometry from the FLOCAL developer benchmark.</i>	47
<i>Table 3.7. 2 × 1 local blockage from the FLOCAL developer benchmark.</i>	47
<i>Table 3.8. 2 × 1 power distributions from the FLOCAL developer benchmark.</i>	47
<i>Table 3.9. 2 × 1 initial and boundary conditions FLOCAL developer benchmark.</i>	48
<i>Table 3.10. Acronyms.</i>	57
<i>Table 3.11. Symbols.</i>	58
<i>Table 4.1. The 17 × 17 geometry from the KAIST benchmark.</i>	74
<i>Table 4.2. The 17 × 17 materials from the KAIST benchmark.</i>	75
<i>Table 4.3. The 17 × 17 spacer grids from the KAIST benchmark.</i>	75
<i>Table 4.4. The 17 × 17 initial and boundary conditions.</i>	75
<i>Table 4.A1. Code descriptions.</i>	91
<i>Table 5.1. The 17 × 17 fuel assembly and 3 × 3 mini-core geometries from the modified KAIST benchmark.</i>	115
<i>Table 5.2. The fuel/burnable absorber in and guide tube geometries from the modified KAIST benchmark.</i>	116
<i>Table 5.3. The fuel/burnable absorber in and guide tube materials from the modified KAIST benchmark.</i>	117
<i>Table 5.4. The 17 × 17 fuel assemblies initial and boundary conditions.</i>	117
<i>Table 5.5. The 3 × 3 mini-cores initial and boundary conditions.</i>	117
<i>Table 5.6. UOX-2 (CR) and UOX-2 (BA-16) fuel assemblies effective multiplication factor values.</i>	120
<i>Table 5.7. Homogeneous and heterogeneous mini-cores effective multiplication factor values.</i>	126
<i>Table 6.1. Quarter core with reflectors geometry.</i>	149
<i>Table 6.2. Quarter core with reflectors boundary conditions.</i>	149
<i>Table 6.3. 17x17 fuel assemblies and 34x34 quarter core without reflectors geometry.</i>	150
<i>Table 6.4. Guide tube and burnable absorber / fuel pin geometry.</i>	151
<i>Table 6.5. Materials.</i>	151
<i>Table 6.6. Boundary conditions for the individual fuel assemblies and quarter core without reflectors.</i>	155

Abbreviations

Acronym	Full Description
1D, 2D, 3D	One, Two, and Three Dimensions
AGR	Advanced Gas Reactor
AMR	Advanced Modular Reactor
BEIS	Department for Business and Industrial Strategy
CASL	Consortium for Advanced Simulation of LWRs
CCCP	Current Coupled Collision Probability
CCCPO	Current Coupled Collision Probability with Orthonormal Polynomials Expansion
CE	Continuous Energy
CEA	Commissariat à l'énergie atomique et aux énergies alternatives
CFD	Computational Fluid Dynamics
CP	Collision Probability
CTF/COBRA-TF	Coolant Boiling in Rod Arrays Two Fluid
DNB	Departure from Nucleate Boiling
DNBR	Relative Departure from Nucleate Boiling
DNS	Direct Numerical Simulation
DYN3D/NK/FLOCAL	Dynamical 3 Dimensional
EDF	Electricite De France
EPR	Evolutionary Pressurised Reactor
ESSM	Embedded Self Shielded Method
EURATOM	European Atomic Energy Community
FDR/HZDR	Forschung Zentrum Dresden/Helmholtz Zentrum Dresden Rossendorf
FEM	Finite Element Method
FORTRAN	Formula Translator
GUI	Graphical User Interface
GWe	Gigawatts Electric
HPC	High Performance Computer
INL	Idaho National Laboratory
JFNK	Jacobi Free Newton Krylov
KAIST	Korean Advanced Institute of Science & Technology
LES	Large Eddies Simulation
LHS	Left Hand Side
LOTUS/PYLOTUS	Liverpool Transport Solver
LWR	Light Water Reactor
MC	Monte Carlo
MG	Multigroup
MIT	Massachusetts Institute of Technology
MOC	Method of Characteristics
MOOSE	Multiphysics Object Oriented Simulation Environment
NCSU	North Carolina State University
NEM	Nodal Expansion Method
NURESIM	Nuclear Reactor Simulator
OC	Open Cascade
OECD	Organisation for Economic Cooperation and Development
ORNL	Oak Ridge National Laboratory
OS	Operator Splitting
PK	Point Kinetics
PN	Spherical Harmonics
PNL	Pacific Northwest Laboratories
PSU	Pennsylvania State University
PWR	Pressurised Water Reactor

RANS	Reynolds Average Navier Stokes
RHS	Right Hand Side
RWTH Aachen	Rheinisch-Westfälische Technische Hochschule Aachen
SALOME	Simulation Numerique par Architecture Logicielle en Open Source et a Methodologie d'Evolution
SN	Discrete Ordinates
UK	United Kingdom
UOL	University of Liverpool
USA	United States of America
USDE	United States Department of Energy
VERA	Virtual Environment for Reactor Applications
VVER	Water Energetic Reactor

Symbol	Full Description
h_k	Field enthalpy
Γ_k	Phase change rate
$\chi_{di}(E)$	Probability density that delayed neutrons emitted have the current energy
$\chi_p(E)$	Probability density that prompt neutrons emitted have the current energy
Q_k	Field energy conduction
$A_{\rho_{m,rel}}, A_{T_{m,rel}}, A_{T_{f,rel}}, A_{q_{fis,rel}}, A_{k_{eff}}$	Absolute convergence tolerances for each magnitude
$C_i(r, t)$	Concentration of the delayed neutron precursor
Q_s	Solid to liquid heat transfer
Q_k	Heat flux
$R_{\rho_{m,rel}}, R_{T_{m,rel}}, R_{T_{f,rel}}, R_{q_{fis,rel}}, R_{k_{eff}}$	Relative convergence tolerances for each magnitude
$c_{p_{clad}}, c_{p_{fuel}}$	Specific heat for the clad and fuel
c_p	Solid specific heat
k_{clad}, k_{fuel}	Thermal conductivity for the clad and fuel
k_{eff}^i and k_{eff}^{i-1}	Current and previous iteration effective multiplication factor
$q_{fis, LOTUS/DYN3D}^i$	Current iteration LOTUS at either the fuel pin or materials levels or DYN3D at the fuel pin level fission power distribution
$q_{fis,rel}^i$ and $q_{fis,rel}^{i-1}$	Current and previous iteration underrelaxed fission power distribution
q_{wk}'''	Wall to field heat transfer
u_k, v_k, w_k	Field velocity components
L_k	Source/sink of mass due to condensation/ evaporation and entrainment and de-entrainment
M_e^T	Source/sink of mass due to void drift and turbulent mixing
M_k^L	Source/sink of momentum due to condensation/ evaporation and entrainment and de-entrainment
M_k^T	Source/sink of momentum due to void drift and turbulent mixing
M_k^d	Source/sink of momentum due to interfacial drag forces
T_k^{ij}	Turbulent shear stress
V_k	Field velocity
q_k^T	Turbulence heat flux
τ_k^{ij}	Viscous shear stress
$\Sigma_f(r, E', t)$	Macroscopic fission cross section
$\Sigma_i(r, E, \Omega, t, T_F, T_M, \rho_M, C_B)$	Cross section feedback
$\Sigma_s(r, E' \rightarrow E, \Omega' \rightarrow \Omega, t)$	Macroscopic scattering cross section
$\Sigma_t(r, E, t)$	Total macroscopic cross section
α_k	Field volume fraction
$\theta_{feed}, \theta_{fis}$	Feedback and fission power under-relaxation factor

λ_i	Delayed neutron precursor decay constant
$\nu_p(E')$	Average number of prompt neutrons
ρ_k	Field density
$\rho_{m,CTF}^i, T_{m,CTF}^i, T_{f,CTF}^i$	Current iteration CTF at the fuel pin level moderator density and temperature, and fuel temperature distributions
$\rho_{m,rel}^i, T_{m,rel}^i, T_{f,rel}^i$ and $\rho_{m,rel}^{i-1}, T_{m,rel}^{i-1}, T_{f,rel}^{i-1}$	Current and previous iteration underrelaxed moderator density and temperature, and fuel temperature distributions
$^{235}\text{U}, ^{238}\text{U}, \text{UO}_2$	Uranium isotopes and dioxide
CO_2	Carbon Dioxide
E	Energy
Fe	Iron
g	Gravity
Gd_2O_3	Digadolinium Trioxide
H_2O	Water
He	Helium
P	Pressure
Sn	Tin
t	Time
T	Solid temperature
V	Solid volume
Zr	Zirconium
Ω	Direction of motion
Q'''	Volumetric heat density
$S(r, E, \Omega, t)$	Other sources
r	Position
ρ	Solid density
$\phi(r, E, \Omega, t)$	Angular neutron flux
$\phi(r, E, t)$	Scalar neutron flux

Chapter 1: Introduction

Nuclear reactors have become an indispensable source of energy for the UK (United Kingdom) to answer its energy demands and achieve its low CO₂ (Carbon Dioxide) emissions policy. In general, the energy supply is being affected by higher energy demands [1,2] due to the further electrification, expansion or construction of infrastructure such as railways, airports, ports, motorways, cities, and other infrastructure and assets. Nuclear reactors allow the energy supply to become more readily available by providing large amounts of power. Traditionally, the energy supply has mostly depended on fossil fuels [3,4] due to the low operating costs despite the large CO₂ emissions of infrastructure such as coal power plants. Nuclear reactors avoid the dependence of the energy supply on fossil fuels by applying nuclear reactions that do not lead to CO₂ emissions. Traditionally, the energy supply has been impacted by power shortages [5,6] due to adverse weather conditions over infrastructure such as wind farms and solar plants. Nuclear reactors avoid any impacts on the energy supply from adverse weather conditions [7] by not depending on them and remaining operational every day.

Initially, the UK government invested resources according to the requirements for the design, construction or improvement, operation, deployment, maintenance, and decommissioning of the current generations of nuclear reactors [8] that contribute to the energy supply. In total, eight AGR (Advanced Gas Reactor) and one PWR (Pressurised Water Reactor) are being operated across different sites, which contribute to the energy supply with 5.9 GWe of installed capacity between them. These will be maintained until the next generation of nuclear reactors becomes available [9], after which they will be decommissioned. Currently, the UK government is investing resources according to the requirements for the design, construction or improvement, operation, and maintenance of the next generation of PWR [10–13] that will contribute to the energy supply. As of now, two EPR (Evolutionary Pressurised Reactor) [14] are being constructed at Hinkley Point C, which will be followed by another two EPR that will be constructed at Sizewell C, and possibly followed by another two EPR that could be constructed at Bradwell B, which will contribute to the energy supply with 1.6 GWe of installed capacity per nuclear reactor. These will be operated with improved efficiency and passive safety systems and maintained during their lifespans. Additionally, the AMR (Advanced Modular Reactor) [15] is being designed and could be constructed at different sites, which will contribute to the energy supply with 400 MWe of installed capacity per nuclear reactor. These can be constructed with modularity, improved flexibility, and operated and maintained more easily than EPR during their lifespans. Finally, a nuclear research and development programme has been designed by BEIS (Department of Business, Energy, and Industrial Strategy), which will improve the efficiency and safety of the next generation of nuclear reactors [16,17]. It is comprised by several parts such as advanced fuels, digital reactor design, safety and security, recycling and waste management, manufacturing and materials, and a national toolkit.

Nuclear simulation software has become an indispensable tool for the UK to improve efficiency without affecting the safety of the current and next generation of nuclear reactors. In general, the design and operation of nuclear reactors are affected by physical phenomena such as power production, heat and mass transfer, and fuel behaviour. Nuclear simulation software allows the design and operation of nuclear reactors to be improved by providing simulations of each physical phenomena with varying levels of fidelity. Traditionally, the design and operation of nuclear reactors have mainly depended on extra conservative safety margins [18] due to the simplicity of methods and computational limitations. Nuclear simulation software could not avoid the dependence of the design and operation of nuclear reactors on high conservative safety margins by providing simulations of the coupled physical phenomena with limited fidelity. Currently, the design and operation of nuclear reactors could depend on less conservative safety margins due to the improved methods and available computational resources. Nuclear simulation software can avoid the dependence of the design and operation of nuclear reactors on high conservative safety margins by providing simulations of the coupled physical phenomena with high fidelity.

Currently, the UK government is investing resources according to the requirements for the design, implementation, deployment, and maintenance of new nuclear simulation software [19–21] that will contribute to the improved design and operation of nuclear reactors. Nuclear simulation software design can be classified according to their requirements [22] into various states. State of the science software includes the latest methods not necessarily applied in all academia. State of the art of science

and technology software includes new methods applied in all academia but not in the industry. State of the art software includes new methods applied in all academia and partially in the industry. Acknowledged rules of technology software includes the standard methods typically applied in all academia and the industry. Nuclear simulation software design should include requirements that simultaneously answer the demands of academia, the industry, and the nuclear regulator, some of which include. Overcoming conservatism with new methods and computer resources. Creating a system architecture for data transfer between nuclear codes. Extending the coupling to include high fidelity for improved simulation of coupled physical phenomena. Integrating the coupling into a user-friendly software framework to reduce human induced errors.

In a nuclear reactor, the present physical phenomena such as power production, heat and mass transfer, and fuel behaviour depend on each other [23,24] and hence are said to be coupled in several ways. The power production is coupled to the heat and mass transfer through the fission reaction rates, which result in heat deposition. The heat and mass transfer are coupled to the power production through the moderator density and temperature and the fuel temperature, which results in feedback. The power production is coupled to the fuel behaviour through irradiation, which results in fuel integrity changes. The fuel behaviour is coupled to the power production through the fuel burnup, which results in a power decrease. The heat and mass transfer are coupled to the fuel behaviour through the fuel temperature, which results in fuel integrity changes. The fuel behaviour is coupled to the heat and mass transfer through the fuel burnup, which results in a heat transfer decrease.

In nuclear simulation software, the power production has been commonly simulated separately through neutronics and less commonly simulated coupled with several degrees of fidelity. Nodal codes [25–27] allow the simulation of the power production through simplified neutron diffusion. This limits the neutron flux to not depend on the direction inside the medium, the medium to not contain neutron sources and sinks within a minimum distance, and the neutron flux to vary slowly in space and time. Hence, simplified neutron diffusion is useful at the scale of the fuel assembly level. Lattice and transport codes [28–30] allow the simulation of the power production through full neutron transport. This allows the neutron flux to depend on the direction inside the medium, the medium to contain neutron sources and sinks within any distance, and the neutron flux to vary as necessary in space and time. Hence, full neutron transport is useful at the scales of the fuel pin and materials levels.

Also, in nuclear simulation software, the heat and mass transfer have been commonly simulated separately through thermal hydraulics and less commonly simulated coupled with several degrees of fidelity. Nodal and system codes [31,32] allow the simulation of the heat and mass transfer through simplified non-mixing fluid dynamics and solid dynamics. This limits the fluid mass, momentum, and energy as well as the solid energy to not depend on the direction inside the medium, the medium to not contain heat and mass sources and sinks within a minimum distance and the fluid mass, momentum, and energy, as well as the solid energy to vary slowly in space and time. Hence, simplified non-mixing fluid dynamics and solid dynamics are useful at the scales of the fuel assembly and power plant levels. CFD (Computational Fluid Dynamics) [33,34] and subchannel codes [35,36] allow the simulation of the heat and mass transfer through full mixing fluid dynamics and solid dynamics. This allows the fluid mass, momentum, and energy, as well as the solid energy, to depend on the direction inside the medium, the medium to contain heat and mass sources and sinks within any distance and the fluid mass, momentum, and energy as well as the solid energy to vary as necessary in space and time. Hence, full mixing fluid dynamics and solid dynamics are useful at the scales of the fuel pin and materials levels.

Finally, in nuclear simulation software, the fuel behaviour has been commonly simulated separately through thermo-mechanics and less commonly simulated coupled with several degrees of fidelity. Fuel performance codes [37] allow the simulation of the fuel behaviour through improved solid dynamics. This allows the solid energy, stresses and strains, and different materials to depend on the direction of the medium and the medium to contain heterogeneities. Hence, improved solid dynamics are useful at the scale of the fuel pin and materials levels.

Coupling may occur, as mentioned, in nuclear simulation software. It describes the dependence, coordination, or information flow within a nuclear code. Coupling between nuclear codes can be subdivided into loose and tight coupling. In loose coupling, the coupled physical phenomena

are simulated separately in the nuclear codes, being subdivided into internal and external coupling. Internal coupling involves extensive modification of the nuclear codes to become a single nuclear code. External coupling involves mild or no modification of the nuclear codes, remaining separate nuclear codes. In tight coupling, the coupled physical phenomena are simulated simultaneously in a nuclear code. Coupling between nuclear codes can also be subdivided into one-way or two-ways coupling. In one-way coupling, the transfer of data between nuclear codes occurs only from one nuclear code to the other. In two-ways coupling, the transfer of data between nuclear codes occurs from one nuclear code to the other and vice versa.

Traditionally, only nodal codes have allowed the simulation of simplified coupled reactor physics with limited fidelity using simplified neutron diffusion, non-mixing fluid dynamics and solid dynamics either limited to the fuel assembly level after performing [38,39] fuel assembly homogenisation or extended to the fuel pin level after performing [40,41] fuel pin power reconstruction. Fuel assembly homogenisation and fuel pin power reconstruction result in the loss of coupled physical phenomena. Traditionally, computational limitations have been present that did not allow the simulation of either improved or full coupled reactor physics with high fidelity. The computational limitations emerged from the complex geometries, materials, coupled physical phenomena, large system sizes, and long computational times. The fuel assembly homogenisation, fuel pin power reconstruction, and computational limitations have contributed to the dependence of the design and operation of nuclear reactors on high conservative safety margins, which are based at the fuel assembly level.

More recently, improved nuclear codes have been developed that are allowing the simulation of either improved or full coupled reactor physics with either improved or high fidelity using either simplified neutron diffusion or full neutron transport, mixing fluid dynamics and solid dynamics extended to the fuel pin and materials [42–46] levels after performing fuel pin power homogenisation or no homogenisation. Fuel pin power homogenisation or no homogenisation results in the capture of additional coupled physical phenomena. More recently, improved computational resources have become available, including computational clusters that are allowing the simulation of either improved or full coupled reactor physics with either improved or high fidelity. The computational resources enable complex geometries, materials, coupled physical phenomena, large system sizes, and lower computational times. The improved nuclear codes and computational resources could reduce the dependence of the design and operation of nuclear reactors on high conservative safety margins, which could be based at the fuel pin and materials levels.

Currently, coupling software environments are being developed such as SALOME (Simulation Numerique par Architecture Logicielle en Open Source et a Methodologie d'Evolution) [47,48], VERA (Virtual Environment for Reactor Applications) [49,50] and MOOSE (Multi-physics Object Oriented Simulation Environment) [51,52] that are allowing to couple nuclear codes or reactor physics through either a simplified coupling interface or a fully coupled software framework. Currently, multiscale and multi-physics software developments are being created such as NURESIM (Nuclear Reactor Simulator) [53,54] and CASL (Consortium for Advanced Simulation of LWRs) [55,56] that are allowing to simulate either improved or full coupled reactor physics with either improved or high fidelity through the coupling software environments and the nuclear codes. The coupling software environments, and multiscale and multi-physics software developments, overcome conservatism with new methods and computer resources, include the system architecture for data transfer between nuclear codes, extend the coupling to include high fidelity for improved simulation of coupled physical phenomena and integrate the coupling into a user-friendly software framework to reduce human induced errors.

The NURESIM multiscale and Multiphysics software development offers either improved or limited fidelity, was developed and is updated by EURATOM (European Atomic Energy Community) and has a structure that can be observed in Figure 1.1.

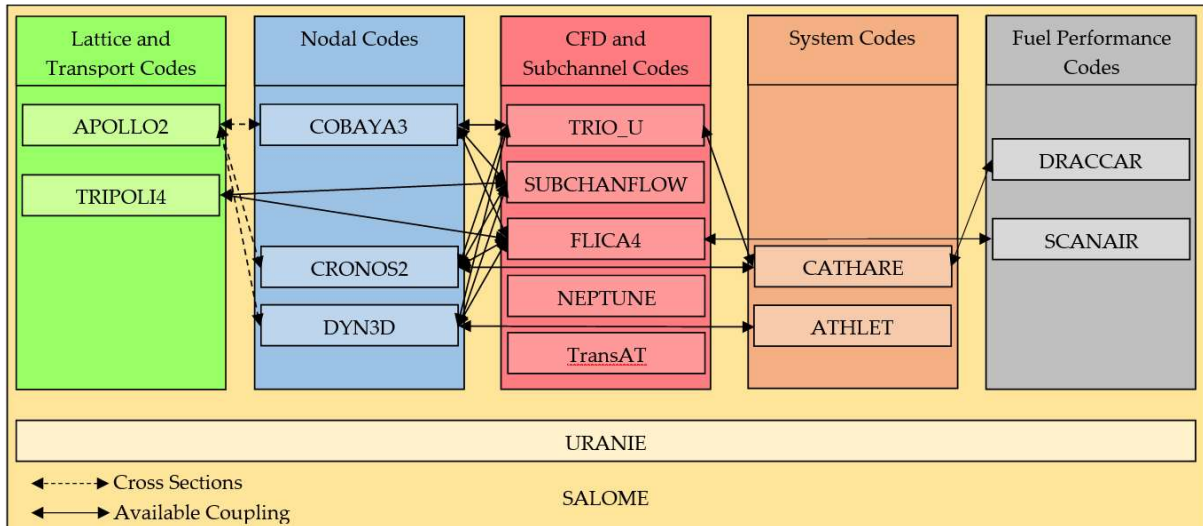


Figure 1.1. NURESIM.

NURESIM uses SALOME to couple the nuclear codes. It uses nodal [57–59], CFD [60], subchannel [61–63], system [64,65] and fuel performance [66,67] codes to provide either simplified or improved coupled reactor physics [68–71] at several levels. Also, it only uses lattice [72] and transport codes [73] to provide cross sections and verification. Finally, it uses other software environments such as for uncertainty quantification. NURESIM, although it is a state-of-the-art software according to its design, does not answer the demands of academia, the industry, or the nuclear regulator in the UK as it does not in general, include the most advanced neutron transport methods or provide full coupled reactor physics at the mentioned levels.

The CASL multiscale and Multiphysics software development offers either high, improved, or limited fidelity through its baseline and advanced components, was developed and is updated by the USDE (United States Department of Energy) and has a structure that can be observed in Figure 1.2.

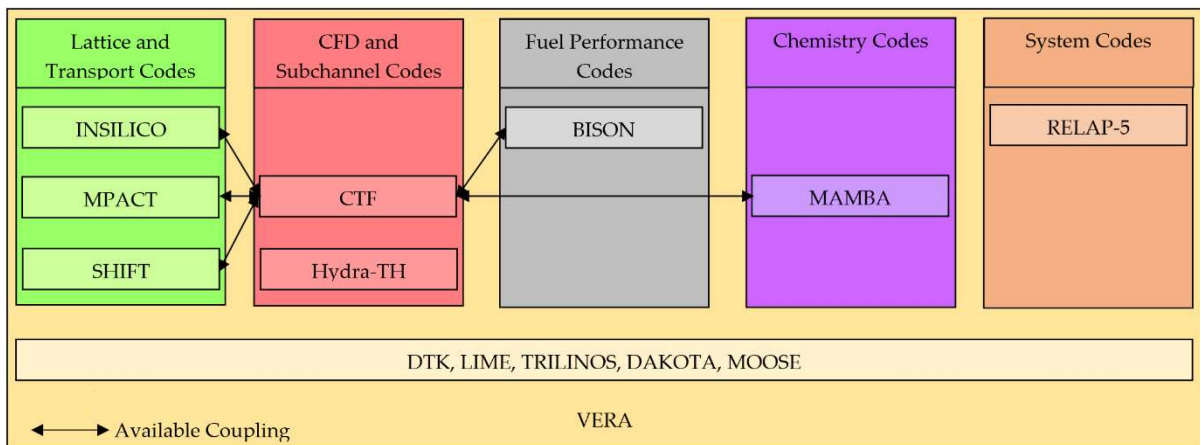


Figure 1.2. CASL.

CASL uses VERA to couple the nuclear codes. It uses transport [74], CFD [75], subchannel [76], fuel performance [77], chemistry [78] and system codes [79] to provide improved or full coupled reactor physics [80–83] at several levels. Also, it uses transport [84,85] codes to provide verification. Finally, it uses other software environments for common input meshing, solving, uncertainty quantification and to couple the fuel performance code. CASL, although it is a state-of-the-art software according to its design, does not answer the demands of academia, the industry or the nuclear regulator in the UK as in general, it requires thousands of processors to deliver a solution within a time of less than a day,

only available in specific computational clusters, applying the most advanced neutron transport methods in all the reactor core to provide full coupled reactor physics at the mentioned levels.

The answer is a multiscale and multi-physics software development between NURESIM and CASL [22] that offers high, improved, or limited fidelity that is being developed by the UOL (University of Liverpool) and has a structure that can be observed in Figure 1.3.

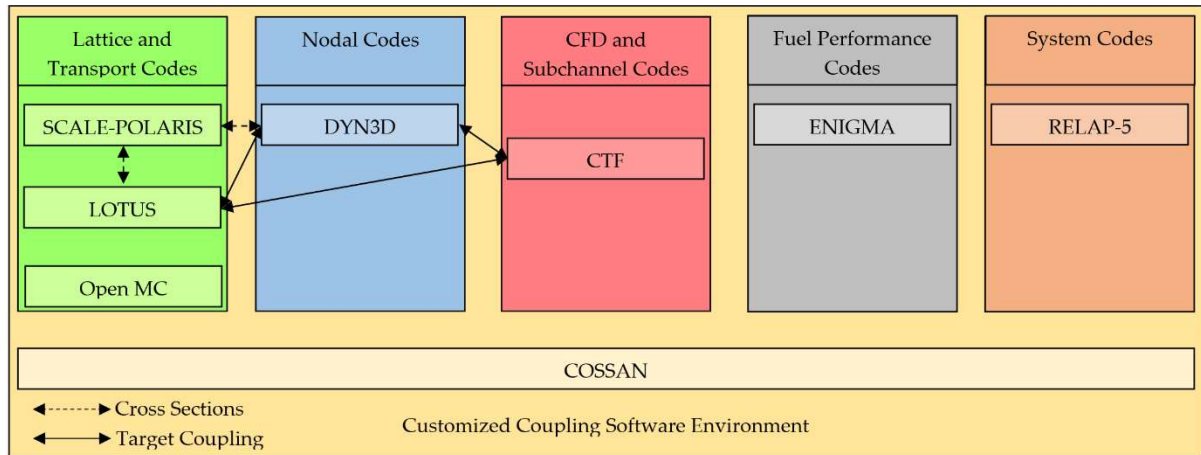


Figure 1.3. Multiscale and multi-physics software development

It will use a customized coupling software environment to couple the nuclear codes. It will use transport [86], nodal [87] and subchannel [88] codes to provide improved or full coupled reactor physics at several levels. Also, it will use a code system lattice module [89] to provide cross sections. Finally, It could include transport [90], fuel performance [91] and system [92] codes to provide verification or further improved or full coupled reactor physics at several levels, and other software environments, such as for uncertainty quantification. This multiscale and multi-physics software development could eventually become state of the art software and answer the demands of academia, industry, and nuclear regulators. It will include the most advanced neutron transport methods and require only few processors to deliver a solution within a time of less than a day, becoming available in any computational cluster and most workstations. This can be achieved by applying the most advanced neutron transport methods only in certain parts of a reactor core, such as the hottest fuel assemblies, with boundary conditions obtained applying the most advanced neutron diffusion methods in all the reactor core to provide full coupled reactor physics at the mentioned levels. A reactor core containing fuel assemblies where these methods are applied can be observed in Figure 1.4.

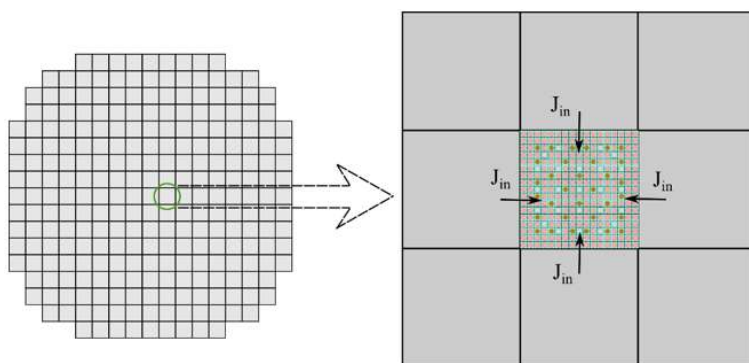


Figure 1.4. Reactor core at the fuel assembly level and fuel assembly at the fuel pin or materials levels.

Validation and verification of this multiscale and multi-physics software development is fundamental for it to become state of the art software. Validation requires comparing the nuclear codes and couplings to real-life experiments. Verification requires comparing the nuclear codes and couplings to other nuclear codes and couplings. Validation and verification of the nuclear codes and their

couplings have been performed from the perspective of academia through the different steps of this PhD project. Further validation and verification of the nuclear codes and their couplings could be performed from an industrial perspective in the future .

The aim is the development of this multiscale and multi-physics software development between NURESIM and CASL, along with its associated validations and verifications. Such aim is divided into several sub-aims and objectives.

- Initially, the first sub-aim within the aim has consisted of the acknowledgement of the neutronics, thermal hydraulics, and coupled reactor physics as well as SCALE-POLARIS, LOTUS, Open MC, DYN3D and CTF.
- Then, the second sub-aim within the aim has consisted of the DYN3D and CTF coupling characterised by several objectives.
 - Initially, an objective within the second sub-aim has consisted of thermal hydraulics validations and verifications of CTF and FLOCAL (module of DYN3D)
 - Another objective within the second sub-aim has consisted of a one-way DYN3D and CTF coupling and its verification.
 - The last objective within the second sub-aim has consisted of a two ways DYN3D and CTF coupling and its verification.
- Finally, the third sub-aim within the aim has consisted of the coupling between LOTUS and CTF as well as DYN3D characterised by several objectives.
 - Initially, an objective within the third sub-aim has consisted of neutronics verifications of LOTUS.
 - The last objective within the third sub-aim has consisted of a multi ways coupling between LOTUS, CTF, and DYN3D and its verification.

The structure of this PhD Thesis is split into several chapters. Chapter 1 includes the introduction. Chapter 2 includes the background. Chapter 3 includes the thermal hydraulics validations and verifications. Chapter 4 includes the one-way coupling. Chapter 5 includes the two ways coupling. Chapter 6 includes the multi-ways coupling. Chapter 7 includes the overall conclusions. Chapter 8 includes future work. The appendix includes the neutronics verifications.

Chapter 2: Background

Accurate simulation of the physical phenomena present in a nuclear reactor depends on the interplay between neutronics, thermal hydraulics, and hence, coupled reactor physics. Moreover, accurate simulation of the physical phenomena present in a nuclear reactor is available in nuclear codes such as SCALE-POLARIS, LOTUS (Liverpool Transport Solver) Open MC, DYN3D (Dynamical 3 Dimensional), and CTF (Coolant Boiling in Rod Arrays Two Fluid). In neutronics, the Boltzmann neutron transport equation describes the neutrons balance in a nuclear reactor, which can be analysed in the code system lattice module, transport, and nodal codes SCALE-POLARIS, LOTUS, Open MC, and DYN3D. In thermal hydraulics, the Navier Stokes fluid dynamics and the solid dynamics equations describe the fluids mass, momentum and energy and the solids energy conservation in a nuclear reactor, which can be analysed in the nodal and subchannel codes DYN3D and CTF. In coupled reactor physics, the power equation and the cross sections feedback describe the heat density and fission reaction rate relation and the cross sections and feedback relation in a nuclear reactor, which can be analysed in the nodal code DYN3D. Approximations are applied in any case to the mentioned equations in the mentioned nuclear codes through several methods to obtain numerical solutions.

The current aim consists of the acknowledgement of the neutronics, thermal hydraulics, and coupled reactor physics and of SCALE-POLARIS, DYN3D, LOTUS, Open MC, and CTF, which are used in this multiscale and multi-physics software development. This acknowledgement of the neutronics, thermal hydraulics and coupled reactor physics performed through their description will allow to comprehend these through their associated equations and approximations, some of which are used in the mentioned nuclear codes. Furthermore, this acknowledgement of SCALE-POLARIS, DYN3D, LOTUS, Open MC and CTF will allow to comprehend these through their associated general features, methods, and solution scheme some of which are applied in later work. This second chapter, hence, comprehends the mentioned theory and nuclear codes description while the couplings, validations and verifications are covered in other chapters.

Several parts comprise the chapter structure. At the beginning, the neutronics in a nuclear reactor are briefly stated, including the neutron transport equation and common approximations used to obtain a numerical solution. Afterwards, the thermal hydraulics in a nuclear reactor are briefly stated, including the fluid and solid dynamics equations and common approximations used to obtain a numerical solution. Then, the coupled reactor physics in a nuclear reactor are briefly stated, including the power equation, the cross sections feedback, and common approximations used to obtain a numerical solution. Later, SCALE-POLARIS code system lattice module is explained in detail, including a general overview, methods, and solution available. Then, LOTUS transport code is explained in detail, including a general overview, methods, and solution available. Also, Open-MC transport code is explained in detail, including a general overview, methods, and solution available. Then, DYN3D nodal code is explained in detail, including a general overview, methods, and solution available. Finally, CTF subchannel code is explained in detail, including a general overview, methods, and solution available.

2.1. Neutronics

As previously discussed, the neutronics in a nuclear reactor are briefly described including the neutron transport equation and common approximations used to obtain a numerical solution.

2.1.1. Neutron Transport Equation

The Boltzmann neutron transport equation is an integrodifferential equation [93] that describes the neutrons balance or conservation by including the different interactions undergone in a nuclear reactor. The neutron transport equation for the neutron flux is given by:

$$\begin{aligned}
& \frac{\partial \phi(r, E, \Omega, t)}{v(E) \partial t} + \Omega \nabla \phi(r, E, \Omega, t) + \Sigma_t(r, E, t) \phi(r, E, \Omega, t) \\
& = \int_{4\pi} \int_0^\infty d\Omega' dE' \Sigma_s(r, E' \rightarrow E, \Omega' \rightarrow \Omega, t) \phi(r, E', \Omega', t) \\
& + \frac{\chi_p(E)}{4\pi} \int_{4\pi} \int_0^\infty d\Omega' dE' \nu_p(E') \Sigma_f(r, E', t) \phi(r, E', \Omega', t) + \sum_{i=1}^N \frac{\chi_{d_i}(E)}{4\pi} \lambda_i C_i(r, t) \\
& + S(r, E, \Omega, t)
\end{aligned} \tag{1}$$

In all these terms, r describes the position, E describes the energy, Ω describes the direction of motion, t describes the time, and $\phi(r, E, \Omega, t)$ describes the angular neutron flux. The first term on the LHS (Left Hand Side) of the mentioned equation describes the time variation of neutrons. The second term on the LHS of the mentioned equation describes the streaming or leakage of neutrons in or out of a given volume. Finally, the third term on the LHS of the mentioned equation describes the removal of neutrons due to scattering and absorption due to the fuel composition, moderation, and control rods. In this term, $\Sigma_t(r, E, t)$ describes the total macroscopic cross section. The first term on the RHS (Right Hand Side) of the mentioned equation describes the source of neutrons due to scattering due to fuel composition or moderation from different energies and directions of motion into the current energy and direction of motion. In this term, $\Sigma_s(r, E' \rightarrow E, \Omega' \rightarrow \Omega, t)$ describes the macroscopic in-scattering cross section. The second term on the RHS of the mentioned equation describes the source of neutrons due to fission that occurs in the fuel at different energies. In this term, $\chi_p(E)$ describes the probability density that prompts neutrons emitted have the current energy, $\nu_p(E')$ describes the average number of prompt neutrons emitted with different energies, and $\Sigma_f(r, E', t)$ describes the macroscopic fission cross-section. The third term on the RHS of the equation describes the source of neutrons due to decay from N-delayed neutron precursors. In this term, $\chi_{d_i}(E)$ describes the probability density that delayed neutrons emitted have the current energy, λ_i describes the delayed neutron precursor decay constant, and $C_i(r, t)$ describes the concentration of the delayed neutron precursor. Finally, the fourth term on the RHS of the equation describes the source of neutrons due to other sources, such as in a start-up. In this term, $S(r, E, \Omega, t)$ describes these sources.

2.1.2. Approximations to the Neutron Transport Equation

Considering the large complexity associated with the neutron transport equation due to the time variation, streaming or leakage, removal, in-scattering, fission, decay, and other terms. No analytical solution to the neutron transport equation is available. Therefore, approximations must be taken to provide a numerical solution through a computer. Numerical solutions can be achieved using either deterministic or probabilistic approximations.

Deterministic approximations apply mathematical methods such as the separate treatment of variables and terms, discretisation through mapping and polynomial expansions, and simplification through direct integration. The accuracy depends on the corresponding approximations. Deterministic approximations are widely used in lattice, transport, and nodal codes to analyse nuclear reactors as they can provide a numerical solution within a reasonable computational time.

Approximations for the discretization or simplification of terms from an energy perspective consist of the MG (Multi Group) and CE (Continuous Energy) methods, with either the mapping and/or integration of the energy. Also, approximations for the discretization or simplification of terms from a direction of motion perspective consist of the diffusion, SN (Discrete Ordinates) [94], and PN (Spherical Harmonics) [95] methods, with either the neglect or mapping and/or expansion of the direction of motion. Moreover, approximations for the discretization or simplification of terms from both a direction of motion and space perspectives consist of the CP (Collision Probability) [96], CCCP (Current Coupled Collision Probability) [97], and MOC (Method of Characteristics) [98] methods, with mapping, integration, and ray tracing of both the direction of motion and space. Furthermore, approximations for the discretization or simplification of terms from a space perspective consist of the NEM (Nodal Expansion Method) [99], FEM (Finite Element Method) [95], finite differences, and PK [100] methods, with either the meshing and expansion or variational principle application or differentials substitution or neglect of space. Additionally, an approximation for the simplification of terms from a space perspective is the albedo method for neutron leakage in space. Finally, approximations for the

discretization or simplification of terms from a time perspective consist of the steady-state and transient-state methods, with the neglect or mapping of time. Some of the mentioned approximations are used in SCALE-POLARIS, DYN3D, and LOTUS and are later described in detail.

Probabilistic approximations apply statistical methods such as the simultaneous treatment of variables and terms, use of random number generators and probability distributions, sampling, and tallying. The accuracy is larger than in other approximations. Probabilistic approximations are also used in transport codes to analyse nuclear reactors although they provide a numerical solution within large computational times.

An approximation for the treatment of the phenomena associated to the terms from a full perspective is the MC (Monte Carlo) [101] method with the generation of histories of the neutrons. Such approximation is used in Open MC and later described in detail.

2.2. Thermal Hydraulics

As previously discussed, the thermal hydraulics in a nuclear reactor are briefly described including the fluid and solid dynamics equations and common approximations used to obtain a numerical solution.

2.2.1. Fluid and Solid Dynamics Equations

The Navier Stokes fluid dynamics equations are a set of differential equations [102] that describe the fluids mass, momentum and energy balance or conservation by including the different interactions undergone in a fluid flow. The fluid dynamics equation for the fluid mass is given by:

$$\frac{\partial(\alpha_k \rho_k)}{\partial t} + \nabla(\alpha_k \rho_k \mathbf{V}_k) = \mathbf{L}_k + \mathbf{M}_e^T \quad (2)$$

In these terms, α_k describes the field fraction, ρ_k describes the field density, and \mathbf{V}_k describes the field velocity. The first term on the LHS of the mentioned equation describes the time variation of the field mass. The second term on the LHS of the mentioned equation describes the advection of the field mass in or out of a volume. The first term on the RHS of the mentioned equation describes the source/sink of field mass due to condensation/ evaporation and entrainment/ de-entrainment. In this term, \mathbf{L}_k describes the field mass transfer. The second term on the RHS of the mentioned equation describes the source/sink of mass due to void drift and turbulent mixing. In this term, \mathbf{M}_e^T describes such mass transfer. The fluid dynamics equation for the fluid momentum is given by:

$$\begin{aligned} \frac{\partial(\alpha_k \rho_k \mathbf{V}_k)}{\partial t} + \frac{\partial(\alpha_k \rho_k u_k \mathbf{V}_k)}{\partial x} + \frac{\partial(\alpha_k \rho_k v_k \mathbf{V}_k)}{\partial y} + \frac{\partial(\alpha_k \rho_k w_k \mathbf{V}_k)}{\partial z} \\ = \alpha_k \rho_k \mathbf{V}_k g - \alpha_k \nabla P + \nabla(\alpha_k (\boldsymbol{\tau}_k^{ij} + \mathbf{T}_k^{ij})) + \mathbf{M}_k^L + \mathbf{M}_k^d + \mathbf{M}_k^T \end{aligned} \quad (3)$$

In these terms, u_k , v_k , w_k describe the field velocity components. The first term on the LHS of the mentioned equation describes the time variation of the field momentum. The second, third and fourth terms on the LHS of the mentioned equation describe the advection of the field momentum in or out of a volume. The first term on the RHS of the mentioned equation describes the gravitational force. In this term, g describes gravity. The second term on the RHS of the mentioned equation describes the pressure force. In this term, P describes the pressure. The third term on the RHS of the mentioned equation describes the viscous shear stress due to wall shear and fluid-fluid shear, and the turbulent shear stress on the field momentum. In this term, $\boldsymbol{\tau}_k^{ij}$ and \mathbf{T}_k^{ij} describe the field momentum stress matrices. The fourth term on the RHS of the mentioned equation describes the source/sink of field momentum due to condensation/ evaporation, and entrainment/ de-entrainment. In this term, \mathbf{M}_k^L describes the field momentum transfer. The fifth term on the RHS of the mentioned equation describes the source/sink of field momentum due to interfacial drag forces. In this term, \mathbf{M}_k^d describes the field momentum transfer. The sixth term on the RHS of the mentioned equation describes the source/sink of field momentum due to void drift and turbulent mixing. In this term, \mathbf{M}_k^T describes the field momentum transfer. The fluid dynamics equation for the fluid energy is given by:

$$\frac{\partial(\alpha_k \rho_k h_k)}{\partial t} + \nabla(\alpha_k \rho_k h_k \mathbf{V}_k) = -\nabla(\alpha_k (\mathbf{Q}_k + \mathbf{q}_k^T)) + \Gamma_k h'_k + q''_{wk} + \alpha_k \frac{\partial P}{\partial t} \quad (4)$$

In these terms, h_k describes the field enthalpy. The first term on the LHS of the mentioned equation describes the time variation of the field enthalpy. The second term on the LHS of the mentioned equation describes the advection of the field energy in or out of a volume. The first term on the RHS of the mentioned equation describes the field energy conduction and turbulence heat flux. In this term, \mathbf{Q}_k , \mathbf{q}_k^T describe the field heat transfers. The second term on the RHS of the mentioned equation describes the field heat transfer due to condensation/ evaporation. In this term, Γ_k describes the phase change rate. The third term on the RHS of the mentioned equation describes the volumetric wall heat transfer to the field. In this term, q''_{wk} describes the wall-to-field heat transfer. The fourth term on the RHS of the mentioned equation describes the pressure work. The solid dynamics equation for the solid energy is given by:

$$\frac{d}{dt} \int_V \rho c_p VT = \oint_A n_k Q_k dA + \int_V Q''' dV - \oint_A Q_s dA \quad (5)$$

The term on the LHS of the mentioned equation describes the time variation of the solid energy. In this term, ρ describes the solid density, c_p describes the solid specific heat, V describes the solid volume, and T describes the solid temperature. The first term on the RHS of the mentioned equation describes the solid energy conduction in all directions. In this term, n_k describes the unit vector orthogonal to surface k , and Q_k describes the heat flux. The second term on the RHS of the mentioned equation describes the solid heat generation. In this term, Q''' describes the volumetric heat density. The third term on the RHS of the mentioned equation describes the solid-to-liquid heat transfer. In this term, Q_s describes the heat flux at the boundary.

2.2.2. Approximations to the Fluid and Solid Dynamics Equations

Considering the large complexity associated with the fluid and solid dynamics equations due to the time variation, advection, viscous and turbulence shear stresses, condensation/evaporation, drag, void drift and turbulent mixing and the different heat transfer terms. No analytical solution to the fluid and solid dynamics equations is available. Therefore, approximations must be taken to provide a numerical solution through a computer. Numerical solutions are mainly achieved using deterministic approximations.

Deterministic approximations apply mathematical methods such as the separate treatment of the variables and terms, discretisation through meshing, and simplification through semi-empirical correlations and direct integration. The accuracy depends on the corresponding approximations. Deterministic approximations are widely used in CFD, subchannel and system codes to analyse nuclear reactors as they can provide a numerical solution within a reasonable computational time.

Approximations for the discretization of terms from a space perspective consist of the channel, subchannel [103], and finite differences methods, with the meshing and partial or full substitution of differentials in space. Also, an approximation for the simplification of terms from a multiphase perspective consists of the flow regime [104] method with the inclusion of semi-empirical models for interphase contact in two-phase flow. Moreover, approximations for the simplification of terms from space and multiphase perspective consist of pressure losses [105], drag [106], and mixing methods [107] with the inclusion of semi-empirical models for either friction and form pressure losses, drag between phases, or the partial neglect of turbulence shear stress over space in one and two-phase flow. Furthermore, approximations for the simplification of terms from a multiphase perspective consist of the boiling [108], entrainment, and heat transfer regime methods with the inclusion of semi-empirical models for fluid-fluid or solid-liquid heat transfer [106] in one and two-phase flow. Other approximations for the simplification of terms from space and multiphase perspective consist of the RANS (Reynolds Average Navier Stokes) [109], LES (Large Eddies Simulation) [110], and DNS (Direct Numerical Simulation) [111] methods with the decomposition, or filtration, and/or integration of the total shear stress over space in one and two-phase flow. Additionally, an approximation for the simplification of terms from a space perspective consists of fuel rod methods with the inclusion of semi-empirical models for solid-solid heat transfer in space. Finally, approximations for the discretization or

simplification of terms from a time perspective consist of steady-state and transient-state methods with the neglect or mapping of time. Some of the mentioned approximations are used in DYN3D and CTF and are later described in detail.

2.3. Coupled Reactor Physics

As previously discussed, the coupled reactor physics in a nuclear reactor are briefly described including the power equation and the cross sections feedback and common approximations used to obtain a numerical solution.

2.3.1. Power Equation and Cross Sections Feedback

The power equation is an equation that describes the power density and fission reaction rate relation in a nuclear reactor. Such equation is given by:

$$q'''(r, t) = \sum_i^N w_f^i \int_0^\infty dE \Sigma_f^i(r, E, t) \phi(r, E, t) \quad (6)$$

The term on the LHS of the mentioned equation describes solid heat generation. In this term, q describes the volumetric heat density. The term on the RHS of the mentioned equation describes the heat deposition due to fission. In this term, w_f^i describes the heat released per fission of isotope i .

The cross sections feedback describes the cross sections and fuel temperature, moderator temperature and density and boron concentration relation in a nuclear reactor. Such relation can be represented by:

$$\Sigma_i(r, E, \Omega, t) \equiv \Sigma_i(r, E, \Omega, t, T_F, T_M, \rho_M, C_B) \quad (7)$$

In all these terms, $\Sigma_i(r, E, \Omega, t)$ and $\Sigma_i(r, E, \Omega, t, T_F, T_M, \rho_M, C_B)$ describe any of the cross sections, T_F describes the fuel temperature, T_M describes the moderator temperature, ρ_M describes the moderator density and C_B describes the boric acid concentration.

2.3.2. Approximations to the Power Equation and Cross Sections Feedback

Considering the large complexity associated with the power equation and the cross sections feedback due to terms discussed previously. No analytical solution to the power equation and cross sections feedback is available. Therefore, approximations must be taken to provide a numerical solution through a computer.

Approximations for the simplification of the terms from energy, space and time perspectives consist of those associated with the neutron transport, fluid and solid dynamics equations with the mapping or meshing, partial or full substitution of differentials, expansion or integration of the energy, space, or time. Also, an approximation for the simplification of the terms from fuel temperature, moderator temperature density and boron concentration perspectives consists of the interpolation [112] method with the inclusion of a model for the estimation of cross sections with feedback. Finally, approximations for the simplification of the terms from a time perspective consist of the OS (Operator Splitting), Picard, and JFNK (Jacobi Free Newton Krylov) [113–115] methods with the full or partial separation or full interaction of the neutron transport, fluid, and solid dynamics equations. Some of the mentioned approximations are used in DYN3D and are later described in detail.

2.4. SCALE-POLARIS Code System Lattice Module

As previously discussed, the SCALE-POLARIS code system lattice module is described in detail including a general overview, methods, and solution available.

2.4.1. General Overview

SCALE [116] is used to analyse neutronics in 1D, 2D, and 3D. It is a code system developed and updated by ORNL (Oak Ridge National Laboratory). It partially reduces the large complexity associated with the cross sections and neutron transport equation in many types of nuclear reactors. It uses deterministic and probabilistic approximations to provide a numerical solution to the former. It

includes several methods and has been improved with updates from a neutronics perspective through the:

- POLARIS and TRITON (lattice) modules.
- ORIGEN (depletion) module.
- NEWT and DENOVO (deterministic transport), and KENO (probabilistic transport) modules.
- TSUNAMI (sensitivity and uncertainty) module.
- Other modules

Only the methods and updates available in the POLARIS module are listed in Table 2.1.

Table 2.1. Methods and updates in POLARIS.

Methods	Updates
-MG	-BWR geometry
-ESSM	-Detectors geometry
-MOC	-Assured quality
-Homogenization	
-Neutronic properties	
-Steady and transient states	

SCALE offers variable accuracy and computational performance due to the different nature of the available modules. It is a code system that has been extensively validated and verified through comparisons of the POLARIS and other modules with experiments and other neutronics codes [117–121]. It is state of the art software used mainly in academia and occasionally in the industry. The source code is locally available through a license. All these factors justify its selection to provide cross-sections for other neutronics codes through the POLARIS module at either the fuel assembly, fuel pin or materials levels.

2.4.2. Methods in POLARIS

Initially, in the MG method, the mapping of the energy into energy groups is performed over the energy spectrum. For each energy group, an equation for the neutron flux is obtained through integration that depends on energy group coefficients. A large number of energy groups are used in general.

Then, in the ESSM method, the inclusion of a model for cross sections generation is performed within the MG method. For each energy group, an equation for the neutron flux according to the intermediate resonance and equivalence theory models is obtained, which depends on self-shielded narrow and wide resonance and absorption cross-sections related through the equivalence cross-sections. The mentioned self-shielded cross sections include the variation due to resonances resulting at different temperatures. Such self-shielded cross sections are obtained by interpolation according to the Bondarenko model.

In the MOC method, the meshing of the space into cells and mapping of the direction of motion into sectors is performed for an unstructured geometry. In the unstructured geometry for each energy group, an equation for the scalar flux in the cells is obtained by linearisation through characteristic curves and integration over the distance from the characteristic curves, which depends on exponentials and sources according to the model. Such characteristic curves describe collision-free paths of neutrons along a direction of motion at any position. A flat flux is assumed in the cells, and exponential evaluation is performed through table look-up. Such distance from the characteristic curves describes the neutron track length. Uniformly spaced neutron track lengths are assumed in the cells. The characteristic curves are obtained by ray tracing in 2D with region volume calculations. In the unstructured geometry for each energy group, the relation for the partial fluxes is obtained by integration over the neutron track length, which depends on exponentials and sources and is used to connect the cells through all the surfaces. In the eigenvalue case, the application of the previous method is performed in any geometry. In the critical spectrum case, the addition of leakage can be performed for cross sections homogenisation and burnup reaction rates.

Additionally, in the homogenization method, the inclusion of a model for cross sections condensation is performed within the MG method. For few energy groups, an output is produced and includes the total, scattering, fission, ν and χ cross sections and diffusion coefficients obtained according to the out-scatter model with corrections for hydrogen in addition to other parameters such as ADF and fuel pin power peak factors.

Meanwhile, in the neutronic properties methods, the assignment of cross-sections is performed in the cells. The cross sections, intermediate resonance parameters and Bondarenko factors are generated from 252 or 56 energy groups ENDF libraries. The cross sections depend on variables such as the burnup, the moderator density and temperature, the fuel temperature, and the boron concentration. The cross sections are treated as uniform within each cell.

2.4.3. Solution

Ultimately, in the steady and transient state methods, either the neglect of time or the mapping of time is performed with iterations between the neutronics occurring until either achieving a convergence criterion defined by a small variation of the effective multiplication factor and fission reaction rates or achieving a defined time. Only the solution in the steady state is presented and can be observed in Figure 2.1.

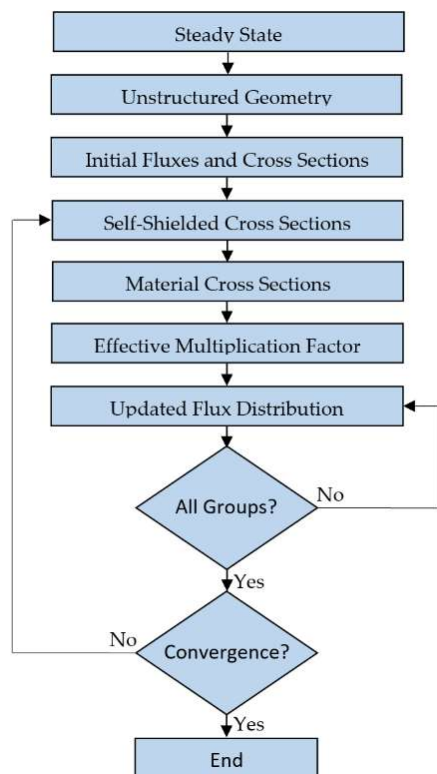


Figure 2.1. SCALE-POLARIS steady state scheme

In the steady state neutronics, an initial guess for the neutron flux distribution and unshielded cross sections allows the calculation of both nuclide self-shielded cross sections which are then mixed to obtain the material cross sections and the effective multiplication factor. These are then used to provide a solution to the neutron transport equation to obtain the updated neutron flux distribution. Such steps conform inner iterations, which are checked for all energy groups. All these steps conform an outer iteration, which is compared to the previous outer iteration through a convergence criterion; if this is not achieved, the next outer iteration is carried out.

2.5. LOTUS Transport Code

As previously discussed, LOTUS transport code is described in detail including a general overview, methods, and solution available.

2.5.1. General Overview

LOTUS [122] is used to analyse neutronics in 1D and 2D. It is a transport code developed at RWTH Aachen (Rheinisch-Westfälische Technische Hochschule Aachen) and updated by UOL (University of Liverpool). It partially reduces the large complexity associated with the neutron transport equation in any type of nuclear reactor. It uses deterministic approximations to provide a numerical solution to the former. It includes several methods and has been improved with updates from a neutronics perspective through its modules. Such methods and updates are listed in Table 2.2.

Table 2.2. Methods and updates in LOTUS.

Methods	Updates
-MG	-User friendliness
-CCCPO	-Computational efficiency
-Albedo	-Assured quality
-Neutronic properties	
-Steady state	

LOTUS offers high accuracy and average computational performance. It is a transport code that has only been partially verified through comparisons to other neutronics codes [123,124]. It is state of the science software used only at the UOL (University of Liverpool). The source code is locally available through the developer. All these factors justify its selection to provide full neutron transport at either the fuel pin or materials levels.

2.5.2. Methods in LOTUS

Essentially, in the MG method, the mapping of the energy into energy groups is performed over the energy spectrum. For each energy group, an equation for the neutron flux is obtained through integration that depends on energy group coefficients. Up to eight energy groups have been tested in other work as seen in the Appendix.

In the CCCPO method, the meshing of the space into cells surrounded by surfaces, meshing of the surfaces into segments, and mapping the direction of motion into sectors is performed for an unstructured geometry. In the unstructured geometry for each energy group, an equation for the scalar neutron flux in the cells is obtained by integration over the cells, which depends on collision probabilities, sources, and partial currents according to the model. An expansion of the scalar neutron flux is performed for each cell through zero, first, and second order orthonormal polynomials without flat flux in them. Such collision probabilities describe the likelihood of born and entering neutrons from another cell and mode to collide in a particular cell and mode. In the unstructured geometry for each energy group, the relation for the partial currents is obtained by integration over the surfaces, segments, and sectors, which depend on collision probabilities and sources and are used to connect the cells through all the surfaces. Such collision probabilities describe the likelihood of born and entering neutrons into a cell to leave without collision through a side, segment, and sector of the cell. The collision probabilities are obtained by ray tracing in 2D or integration over the different neutron paths. In the eigenvalue case, the application of the previous method is performed for an unstructured geometry. In the external source case, the addition of external neutron sources can be performed, assuming only fast neutrons are emitted by these.

Additionally, in the albedo method, the inclusion of models for neutron leakage at the outer boundary cells is performed for an unstructured geometry. For each energy group, a relation between partial currents in the outer boundary cells is given for each surface side by albedo coefficients. The albedo coefficients may have any value between 0 and 1 when neutrons are lost and any value larger than 1 when neutrons are gained through the surface side.

Meanwhile, in the neutronic properties methods, the assignment of cross-sections is performed in the cells. The cross sections are previously generated in lattice codes and may be later, although not usually averaged through fuel pin homogenization within the mentioned codes. The cross sections depend on variables such as the burnup, moderator density and temperature, fuel temperature and boron concentration. The cross sections are treated as uniform within each region of a cell.

2.5.3. Solution

Finally, in the steady state method, the neglect of time is performed with iterations between the neutronics occurring until achieving a convergence criterion defined by a small variation of the effective multiplication factor and fission reaction rates. The solution in the steady state is presented and can be observed in Figure 2.2.

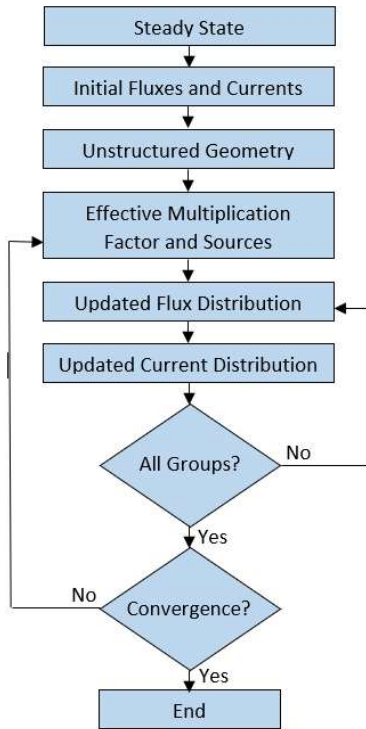


Figure 2.2. LOTUS steady state scheme

In the steady state, an initial guess for the neutron flux and current distributions allows the calculation of the effective multiplication factor and sources. These are then used to provide a solution to the neutron transport equation to obtain the neutron flux and neutron current distributions. Such steps conform inner iterations, which are checked for all energy groups. All these steps conform an outer iteration, which is compared to the previous outer iteration through a convergence criterion; if this is not achieved, the next outer iteration is carried out.

2.6. Open MC Transport Code

As previously discussed, Open MC transport code is described in detail including a general overview, methods, and solution available.

2.6.1. General Overview

Open MC [125] is used to analyse neutronics in 1D, 2D, and 3D. It is a transport code developed at MIT (Massachusetts Institute of Technology) and updated by UChicago Argonne. It partially reduces the large complexity of the phenomena associated with the cross sections and neutron transport equation in any type of nuclear reactor. It uses probabilistic approximations to provide a numerical solution to the former. It includes several methods and has been improved with updates from a neutronics perspective through its modules. Such methods and updates are listed in Table 2.3.

Table 2.3. Methods and updates in Open MC.

Methods	Updates
-CE and MG	-User friendliness
-ACE and Standard Format	-Computational efficiency

-MC
-Boundary Conditions
-Tallies
-Neutronic properties
-Steady state

-Assured quality

Open MC offers very high accuracy, although low computational performance due to the high demand associated with the previous methods. It is a transport code that has been extensively validated and verified through comparisons with experiments and other neutronics codes [126–130]. It is state of the art software used mainly in academia and occasionally in the industry. The source code is generally available to the public. All these factors justify its selection to provide additional verification of the full neutron transport and improved or full coupled reactor physics at either the fuel pin or materials levels.

2.6.2. Methods in Open MC

Firstly, in the CE or MG methods, either the full consideration or the mapping of the energy into energy groups is performed over the energy spectrum. The accuracy of the CE method is higher, although the performance is worse than in the MG method.

Then, in the ACE format method, the inclusion of a model for cross sections generation is performed within the CE method. Conversion of ENDF data into tabulated energy functions is obtained by linear interpolation between energy values. The associated total cross sections of each material require a binary search of the energy grid of each nuclide. Such binary search for the corresponding energy and cross section can be performed according to either unionized energy grid or indexing technique models, with the latter relying on a set of pointers and being faster than the former. The associated total cross sections of each material are self-shielded and include their variation resulting at different temperatures. Such self-shielded cross-sections are obtained by interpolation according to the probability tables model. In the standard format method, input cross sections are represented within the MG method for comparison with other neutronics codes.

In the MC method, the meshing of the space into cells encompassed by any surfaces to conform universes is performed for any geometry. In any geometry, for each particle, properties are initialized through the sampling of a source site. The current location cell and associated cross sections are determined through the particle coordinates and previously mentioned methods. The distances to the nearest cell surface and the next collision are obtained which depend either on the encompassing surfaces or on a pseudo-random number and total macroscopic cross-section. If the distance to the nearest cell surface is smaller than the distance to the next collision, the particle is displaced towards the cell surface and continues from that location cell. If the distance to the next collision is smaller than the distance to the nearest cell surface, the particle undergoes a collision. The probability of a collision with a nuclide within a material and of a reaction with a nuclide within all reactions is obtained through sampling, which depends either on the total nuclide and material macroscopic cross sections or on specific reaction and total nuclide cross sections. If there is a scattering reaction, the particle continues with an outgoing energy and solid angle obtained through the sampling of probability distributions according to the free gas, Maxwell, and $S(\alpha,\beta)$ scattering law models from that location cell. If there is an absorption reaction including fission, the particle dies with source sites possibly being created through the sampling of probability distributions according to the survival biasing technique. In the eigenvalue case, the application of the successive generations method is performed in any geometry. For each generation, tracking of the particles occurs from birth to death. Multiple generations can be grouped into batches to reduce the correlation between pseudo-random numbers. In the external source case, the addition of other source sites can be performed according to a modification of the previously mentioned method.

Additionally, in the boundary conditions method, the inclusion of a model for neutron leakage at the outer boundary cells is performed for an unstructured geometry. The boundary conditions are either vacuum or reflective.

Moreover, in the tallies method, the inclusion of a system to obtain physical quantities of interest is performed for any geometry. The tallies are defined by combinations of filters and scoring functions where the former limit the events that can score to the latter. Such filters and scoring functions

include the cells, universes, and materials for the former and the neutron flux and reaction rates for the latter. The tallies are scored through track length and collision estimators and are scaled according to the bins associated with the scoring functions according to a mapping technique. Pre- and post-collision filters and scattering and fission scoring functions can be used to generate MG cross-sections.

Meanwhile, in the neutronic properties methods, the assignment of cross sections is performed in the cells. The cross sections depend on variables such as the burnup, moderator density and temperature, fuel temperature and boron concentration.

2.6.3. Solution

Lastly, in the steady state method, the neglect of time is performed with cycles between the neutronics occurring until achieving a convergence criterion defined by a small variation of the Shannon entropy.

2.7. DYN3D Nodal Code

As previously discussed, DYN3D nodal code is described in detail including a general overview, methods, and solution available.

2.7.1. General Overview

DYN3D [131,132] is used to analyse both neutronics and thermal hydraulics in 1D, 2D and 3D. It is a nodal code developed at FDR (Forschung Zentrum Dresden) and updated by HZDR (Helmholtz Zentrum Dresden Rossendorf). It greatly reduces the large complexity associated with the neutron transport and the fluid and solid dynamics equations in LWR and VVER. It uses deterministic approximations to provide a numerical solution to them. It includes several methods and has been improved with updates from neutronics and thermal hydraulics perspectives through the:

- NK (Neutron Kinetics) module.
- FLOCAL (Thermal Hydraulics) module.

The methods and updates available in the NK and FLOCAL modules are listed in Table 2.4.

Table 2.4. Methods and updates in NK and FLOCAL.

Methods		Updates	
-MG	-Fluid mixture	-Inverse point kinetics	-Pernica DNB
-Diffusion	-Channel		-Particle in Cell
-NEM	-Pressure losses		
-Albedo	-Boiling		
-Fuel pin power reconstruction	-Heat transfer regime		
-Neutronic properties	-Fuel rods		
-Control rods	-Thermal properties		
-Steady and transient states			

DYN3D offers low accuracy, although high computational performance due to the low demand associated with the previous methods. It is a nodal code that has been extensively validated and verified through comparisons of the NK and FLOCAL modules with experiments and other neutronics and thermal hydraulics codes [133–137]. It is part of the acknowledged rules of technology used in academia and the industry. The source code is available through a license. All these factors justify its selection to provide simplified coupled reactor physics through both the NK and FLOCAL modules at the fuel assembly level.

2.7.2. Methods in NK

Initially, in the MG method, the mapping of the energy into energy groups is performed over the energy spectrum. For each energy group, an equation for the neutron flux is obtained through integration that depends on energy group coefficients. Typically, two energy groups are used, which correspond to fast and thermal.

Then, in the diffusion method, the neglect of the direction of motion is performed over the solid angle. An equation for the neutron flux is obtained through Fick's law, which depends on the diffusion coefficient.

In the NEM method, the meshing of the space into nodes surrounded by surfaces is performed for square or hexagonal geometries. Either in square or hexagonal geometries, an equation for the neutron flux either for each of the 3D space components or for the hexagonal plane and axial space components is obtained by transverse integration over the other space components and depends on sources and either on a regular or an unregular transversal leakage according to the models. Transversal leakage describes the neutron leakage in a space component due to the other space components. An expansion of the neutron flux, source, and either the regular or unregular transversal leakage is performed either for each of the 3D space components or for the hexagonal plane and axial space components through either 1D or 2D second-order polynomials and exponentials. Either in square or hexagonal geometries, a relation for the partial currents is obtained through the previously mentioned law and is used to connect the nodes through either the side or the side and corner surfaces. Finally, the nodes can or cannot be further discretized into additional nodes. In the eigenvalue case, the application of the previous method is performed in any geometry. In the external source case, the addition of external neutron sources can be performed, assuming only fast neutrons are emitted by these. In the poisoned case, the addition of Xe and Sm can also be performed with their concentrations being in equilibrium. In the transient state case, the addition of delayed neutron precursors can also be performed with an expansion of the delayed neutron precursor group concentrations through polynomials.

Additionally, in the albedo method, the inclusion of models for neutron leakage at the outer boundary nodes is performed either for square or hexagonal geometries. Either in square or hexagonal geometries for each energy group, a relation between partial currents in the outer boundary nodes is given for either each side surface by albedo coefficients or for each side and corner surface by the former and the extrapolation length according to the models. The albedo coefficients are 0 when there are vacuum conditions and 1 when there are reflective conditions and can also be previously determined through reflectors.

Moreover, in the fuel pin power reconstruction method, the inclusion of models for fuel pin power distributions in the nodes can be performed either for square or hexagonal geometries. Either in square or hexagonal geometries for each energy group, an equation for the scalar flux in 2D obtained by superposition of form functions from lattice codes can be used for the fuel pins according to the models. The successive smoothing of the scalar flux is performed assuming an exponential behaviour and proportionality between prompt and delayed neutron distributions and axial leakage described by transversal buckling. The fuel pin power reconstruction is used to analyse a nuclear reactor at the fuel pin level.

Meanwhile, in the neutronic properties methods, the assignment of cross-sections is performed in the nodes. The cross sections are previously generated in lattice codes and later averaged through fuel assembly homogenization within the mentioned codes. Currently, interpolation of the cross sections is performed assuming individual changes to the variables. The cross sections depend on variables such as the burnup, moderator density and temperature, fuel temperature and boron concentration. The cross sections are treated as uniform within each node.

Additionally, in the control rod methods, the modification of cross sections is performed in the nodes. The cross sections without control rods are replaced by those with control rods in the fuel assemblies. Currently, the motion of the control rods can be included through the axial velocity. The control rods may be homogeneous or heterogeneous in composition.

2.7.3. *Methods in FLOCAL*

Initially, in the fluid mixture method, the characterisation of the fluids into a fluid mixture is performed for the multiphase. Equations for the fluid mixture mass, momentum, and energy as well as the vapor mass are obtained by summing up the individual phases which depend on each other.

In the channel method, the meshing of the space into nodes that can be further subdivided into additional nodes to conform channels is performed for any geometry. Equations for the fluid mixture mass, momentum, energy, vapor mass, and solid energy are obtained by integration over the axial

component, which depends on closure terms according to several models. Such closure terms describe the heat and mass transfer within a node. Several relations for the closure terms are obtained by semi-empirical models, which depend on the corresponding factors and are used within the nodes.

Then, in the pressure losses method, the inclusion of empirical models for fluid friction and form pressure losses is performed either for one- or two-phase flow. In any flow, a relation for the friction pressure losses is given by the friction coefficient and the two-phase multiplier, according to the Filonenko and Oshmachkin models. In any flow, a relation for the form pressure losses is given by inlet and total flow blockage coefficients according to a model. The total flow blockage coefficient is 0 when there are no spacer grids.

Moreover, in the boiling methods, the inclusion of semi-empirical models for fluid mixture and vapor heat transfer is performed for two-phase flow. Several relations for the evaporation and condensation rates are used which depend on the heat transfer coefficient and slip ratio or relation between vapor and fluid mixture velocities. A relation for the slip ratio is given according to a model.

Furthermore, in the heat transfer regime method, the inclusion of semi-empirical models for solid and fluid mixture heat transfer is performed either for general nuclear reactor behaviour or accident scenarios by comparison of the heat flux to the critical heat flux. Correlations for the critical heat flux for variable pressure ranges are given for the wall according to the Biasi, Osmachkin, Bezrukov and Astakhov models. Under general nuclear reactor behaviour, further comparisons are performed for single-phase convection where there is only liquid or boiling and saturated boiling, where there is liquid and some or many bubbles according to the model. A heat transfer coefficient is used according to either the Rayleigh or the Rassokhin and Borishanskji models. In accident scenarios, other comparisons are performed only for single-phase vapor where there is only vapor, according to the model. A heat transfer coefficient is used according to another model.

In the fuel rod methods, the inclusion of semi-empirical models for solid-solid heat transfer within the fuel rods is performed for the fuel, clad, and gap. Only one fuel rod is contained in each node. In the fuel and clad, where there is heat conduction, heat transfer coefficients are used according to the MATPRO-11 models. In the gap where there is gas conduction, pellet-clad contact conduction and radiative heat transfer, a heat transfer coefficient is used according to the GAPCON and Stefan Boltzmann models. In the clad where there are redox chemical reactions, corrections for the heat transfer coefficient are used according to a model.

Meanwhile, in the thermal properties methods, the assignment of thermal properties, such as the thermal conductivity or the specific heat, is performed in the nodes. The thermal properties of the fluid mixture are previously included through the IFC-67 and IAWPS tables. The thermal properties of the solids are previously included through MATPRO-11 tables. The thermal properties are treated as uniform within each node.

2.7.4. Solution

Ultimately, in the steady and transient state methods, either the neglect or the mapping of time is performed with iterations between the neutronics and thermal hydraulics occurring until either achieving a convergence criterion defined by a small variation of the effective multiplication factor, fission power and feedback distributions or achieving a defined time. Only the solution in the steady state is presented, including the neutronics, thermal hydraulics and coupling and can be observed in Figure 2.3

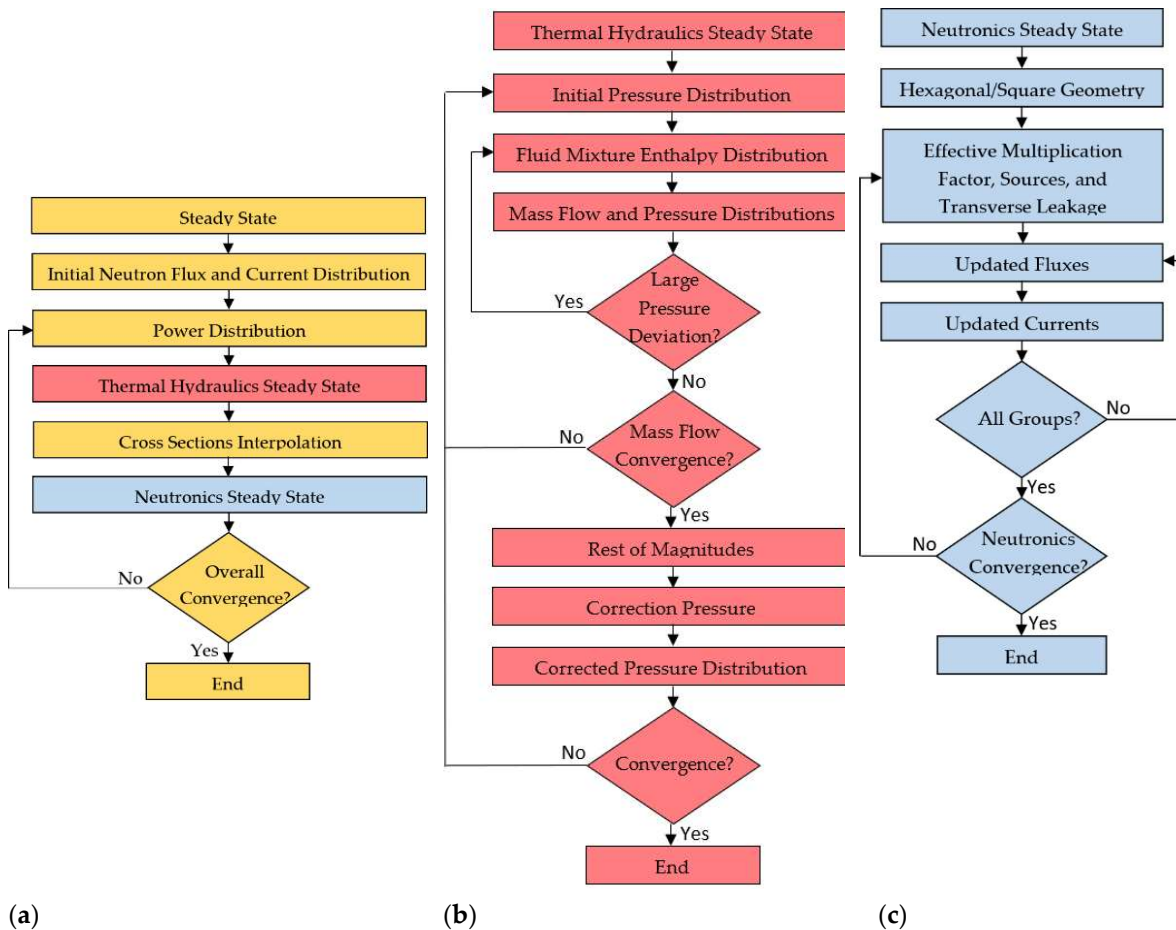


Figure 2.3. (a) DYN3D steady state coupling scheme, (b) DYN3D steady state thermal hydraulics scheme, (c) DYN3D steady state neutronics scheme.

In the steady state coupling, an initial guess for the neutron flux and current distributions allows the calculation of the power distribution. This is then followed by under-relaxation of the power distribution. In the steady-state thermal hydraulics, this is used in the calculation of the fluid mixture density, velocity and temperature, and the fuel temperature distributions. This is then followed by interpolation of the cross sections for each energy group. In the steady state neutronics, these are used in the calculation of the neutron flux and current distributions and then used again. All these steps conform an outer iteration, which is compared to the previous outer iteration through a convergence criterion; which if not achieved, leads to the next outer iteration.

In the steady state thermal hydraulics, an initial guess for the power distribution and the pressure allows the calculation of the pressure distribution. These are then used to provide a solution to the fluid mixture energy, mass, and momentum equations to obtain the fluid mixture enthalpy and, hence, fluid mixture density, temperature, void fraction, mass flow and pressure distributions. Such steps conform inner iterations, which are checked for deviations. All these are used to provide a solution to the fuel rod equation to obtain the fuel temperature, pressure correction and corrected pressure distribution. All these steps conform an outer iteration, which is compared to the previous outer iteration through a convergence criterion; which if not achieved, leads to the next outer iteration.

In the steady state neutronics, an initial guess for the neutron flux and current distributions, allows the calculation of the effective multiplication factor, sources, and transversal leakage. These are then used to provide a solution to the neutron diffusion equations to obtain the neutron flux and neutron current distributions. Such steps conform inner iterations, which are checked for all energy groups. All these steps conform an outer iteration, which is compared to the previous outer iteration through a convergence criterion; which if not achieved, leads to the next outer iteration.

2.8. CTF Subchannel Code

As previously discussed, CTF subchannel code is described in detail including a general overview, methods, and solution available.

2.8.1. General Overview

CTF [138,139] is used to analyse thermal hydraulics in 3D. It is a subchannel code developed at PNWL and updated by PSU (Pennsylvania State University) and NCSU (North Carolina State University). It partially reduces the large complexity associated with the fluid and solid dynamics equations in LWR. It uses deterministic approximations to provide a numerical solution to the former. It includes several methods and has been improved with updates from a thermal hydraulics perspective through its modules. Such methods and updates are listed in Table 2.5.

Table 2.5. Methods and updates in CTF.

Methods	Updates
-Two fluids three fields	-Turbulent mixing
-Subchannel	-User friendliness
-Flow regime	-Computational efficiency
-Pressure losses	-Assured quality
-Inter cell drag	
-Turbulent mixing	
-Interphase drag	
-Interphase heat transfer	
-Entrainment/de-entrainment	
-Heat transfer regime	
-Fuel rods	
-Thermal properties	
-Pseudo steady and transient states	

CTF offers high accuracy, although average computational performance. It is a subchannel code that has been extensively validated and verified through comparisons with experiments and other thermal hydraulics codes [140–144]. It is state of the art software used mainly in academia and occasionally in the industry. The source code is available through a license. All these factors justify its selection to provide full mixing fluid dynamics at the fuel pin level.

2.8.2. Methods in CTF

Essentially, in the two fluids and three fields method, the characterisation of the fluids into liquid and vapor phases and liquid, vapor and droplet fields is performed for the multiphase. Equations for the liquid and vapor mass, momentum and energy and the droplet mass and momentum are obtained, which depend on each other.

In the subchannel method, the meshing of the space into mesh cells, subdivided into staggered scalar mesh cells for scalar quantities and axial and transversal mesh cells for vectorial quantities to conform subchannels, is performed for square geometry. Equations for the liquid and vapor mass, momentum, energy and the droplet mass and momentum as well as the solid energy are obtained either by integration over the axial and transversal space components or integration over the three space components which depend on the flow regime and closure terms according to several models. Such closure terms describe the heat and mass transfer between mesh cells, within a mesh cell or within fuel rod mesh cells. Several relations for the closure terms are obtained by semi-empirical models, which depend on the corresponding factors and are used either to connect the mesh cells through gaps, or within the mesh cells, or between fuel rod mesh cells.

Also, in the flow regime method, the inclusion of semi-empirical models for the interphase contact area between the liquid, vapor and droplets is performed either for standard wall where the wall remains fully wet or for hot wall where the wall becomes partially or fully dry with possible quench front by comparison of the wall temperature to the critical heat flux temperature. Under

standard wall regimes, further comparisons are performed according to the model for small bubble flow where there are small bubbles or small-large bubble flow where there are small and large bubbles or turbulent/churn flow where there are large bubbles or mist/annular flow where there is still a liquid film but mostly vapor. An interphase contact area is used according to several models. Under hot wall regimes, further comparisons are performed according to the model for inverted annular flow where there is a vapor film but mostly liquid or falling film flow where there is a liquid film with a top quench front but mostly vapor or top deluge flow where there are liquid slugs with a top quench front but more liquid. An interphase contact area is used according to other models.

Then, in the pressure losses method, the inclusion of semi-empirical models for fluid friction and form pressure losses is performed either for one- or two-phase flow. In any flow, a relation for the friction pressure losses is given by the friction coefficient and the two-phase multiplier according to the McAdams, Zigrang-Sylvester, Churchill and other models and the previous flow regime method. In any flow, a relation for the form pressure losses is given by flow blockage coefficients according to a model. The flow blockage coefficients can vary according to the spacer grid type.

Also, in the inter-mesh cell drag method, the inclusion of a semi-empirical model for large void fraction gradients is performed for two-phase flow. An equation for the drag force is used, which depends on the drag coefficient and inter-mesh cell interface contact area. A constant drag coefficient is used in the model. A relation for the inter mesh cell interface contact area is given by another model. The large void fraction gradients may occur with liquid pooling and vapor jets.

Additionally, in the turbulent mixing and void drift method, the inclusion of a semi-empirical model for liquid and vapor mixing is performed for two-phase flow. An equation for the mixing rate is used, which depends on the eddy viscosity, eddy diffusivity and mixing length according to the Todreas and Kazimi model. The separation of the mixing rate into non-equilibrium and equilibrium is performed with liquid moving to higher vapor mesh cells and vapor moving to higher liquid mesh cells in the former, and vapor moving to large area mesh cells in the latter. A relation between the mixing rate and the average mass flow rate is given by the mixing coefficient and two-phase multiplier according to the Rogers and Rosehart and Beus models. The mixing coefficient can vary according to the mesh cell.

Then, in the interface drag method, the inclusion of a semi-empirical model for void fraction differences is performed for two-phase flow. An equation for the drag force is used, which depends on the drag coefficient and interface contact area. A relation for the drag coefficients is given by several models and the previous flow regime method. A relation for the interface contact area is given by the previous flow regime method.

Moreover, in the interface heat transfer method, the inclusion of semi-empirical models for liquid, vapor and droplet heat transfer is performed for two-phase flow. Several equations for the evaporation and condensation rates are used, which depend on the heat transfer coefficient and interface contact area. A relation for the heat transfer coefficients for different scenarios is given by other models. A relation for the interface contact area is given by the previous flow regime method.

Additionally, in the entrainment/de-entrainment method, the inclusion of semi-empirical models for liquid and droplet interaction is performed for two-phase flow. Several equations for the entrainment rate are used, which depend on mass transfer coefficients and interface contact area. A relation for the mass transfer coefficients for different scenarios is given by several models. A relation for the interface contact area is given by the previous flow regime method.

Furthermore, in the heat transfer regime method, the inclusion of semi-empirical models for solid-liquid heat transfer between the liquid and fuel rods is performed either for general nuclear reactor behaviour or accident scenarios by comparison of the wall temperature to the critical heat flux temperature. Correlations for the critical heat flux for variable pressure ranges are given for the wall according to the Biasi, W-3, Bowring, and Groeneveld look-up table models. Under general nuclear reactor behaviour, further comparisons are performed for single-phase liquid where there is only liquid or subcooled and saturated boiling where there is liquid and some or many bubbles according to the model. A heat transfer coefficient is used according to either the Dittus-Boelter and Sparrow or the Chen or the Thorn models. In accident scenarios, other comparisons are performed for single-phase vapor where there is only vapor or transition boiling where there is liquid and vapor or dispersed flow

film boiling where there is mostly vapor with a stable vapor film. A heat transfer coefficient is used according to other models.

In the fuel rod methods, the inclusion of semi-empirical models for solid-solid heat transfer within the fuel rods is performed for the fuel, clad, and gap. In the fuel and clad, where there is heat conduction, a heat transfer coefficient is used according to the model. In the fuel where there is deformation, corrections for the heat transfer coefficient are used according to the FRACAS-I model. In the gap where there is gas conduction, pellet-clad contact conduction and radiative heat, a heat transfer coefficient is used according to the GAPCON and Stefan Boltzmann models. In the clad where there are redox chemical reactions, corrections for the heat transfer coefficient are used according to the model.

Meanwhile, in the thermal properties methods, the assignment of thermal properties such as the thermal conductivity or the specific heat is performed in the mesh cells. The thermal properties of the liquid, vapor and droplets are previously included through the EPRI, CTF original, and IAWPS tables. The thermal properties of the solids are previously included through MATPRO-11 tables. The thermal properties are treated as uniform within each mesh cell.

2.8.3. Solution

Finally, in the pseudo steady and transient state methods, the mapping of time is performed with iterations between the thermal hydraulics, occurring until either achieving a convergence criterion defined by a small variation of the feedback distributions or achieving a defined time. Only the solution in the pseudo-steady state is presented and can be observed in Figure 2.4.

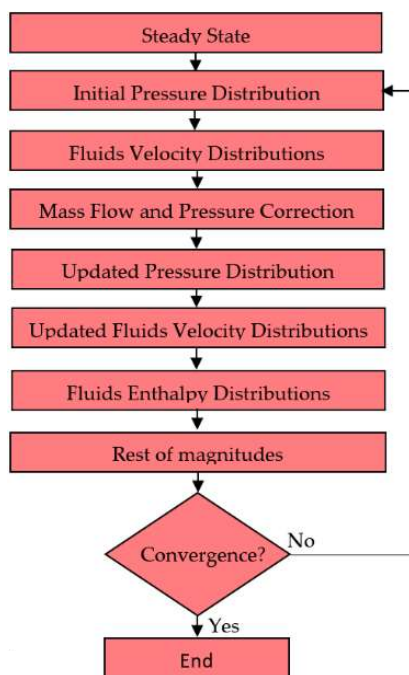


Figure 2.4. CTF pseudo-steady state scheme

In the pseudo-steady state, an initial guess for the power distribution and the pressure allows the calculation of the pressure matrix. These are then used to provide a solution to the fluids momentum and mass equations to obtain the fluids velocity and mass flow distributions, pressure matrix correction and updated pressure matrix. These are then used to provide a solution to the fluids momentum and energy equations to obtain the updated fluids velocity and enthalpy distributions. All these are used to provide a solution to the fuel rod equation to obtain the fuel temperature distribution. Such steps conform inner iterations and all of them an outer iteration, which is compared to the previous outer iteration through a convergence criterion; which if not achieved, leads to the next outer iteration.

Chapter 3: Thermal Hydraulics Validations and Verifications within a Subchannel Code and the Associated Module within a Nodal Code

The accuracy and methodology available in FLOCAL and CTF to provide thermal hydraulics at the heater rod level is not so well known in research. This can be achieved in the former through discretization of the nodes; in the latter, it is available by default. Therefore, a validation and verification of the accuracy available in CTF, and a verification of the methodology available in CTF and FLOCAL have been performed separately through the PSBT and FLOCAL developer benchmarks.

The PSBT benchmark [145–147] is a validated and verified benchmark by the OECD (Organisation for Economic Cooperation & Development) for LWR thermal hydraulics with previous work carried out using CTF [148,149]. It includes void fraction and DNB benchmarks that contain 1x1 and 5x5 bundles with heater rods, uniform, or non-uniform power distributions, without or with spacer grids and a wide range of boundary conditions. The FLOCAL developer benchmark is a proposed benchmark by HZDR for LWR thermal hydraulics with no previous work carried out using any thermal hydraulics codes. It includes power variation and flow blockage exercises that contain a 2x1 bundle with heater rods, uniform, or non-uniform power distributions, without or with a flow blockage and a single set of boundary conditions. In CTF and FLOCAL, the PSBT and FLOCAL developer benchmarks have been simulated including methods for the 1x1, 5x5 and 2x1 bundles such as the meshes, subchannel or channel, nucleate boiling, DNB, friction and form pressure losses and variable crossflow and turbulent mixing, including no crossflow, partial crossflow, crossflow, Rogers and Rosehart turbulent mixing and constant mixing. A graphical abstract for this chapter can be seen in Figure 3.GA.

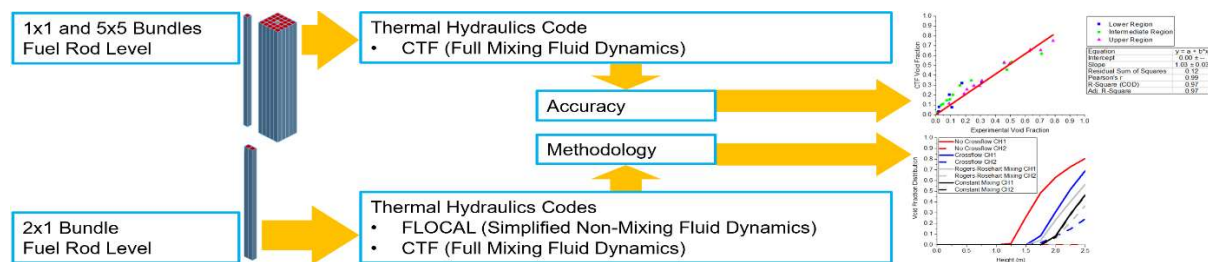


Figure 3.GA. Chapter 3 graphical abstract.

The validation of the accuracy available in CTF when compared to experimental data has shown small void fraction differences in the 1x1 and 5x5 bundles and small DNB differences in the 5x5 bundle. Also, the verification of the accuracy available in CTF when compared to other thermal hydraulics codes results has shown small void fraction mean errors and standard deviations at the requested heights in the 1x1 and 5x5 bundles and similar DNB first occurrence heights in the 5x5 bundle. Finally, the verification of the methodology available in CTF when compared to FLOCAL has shown a variation of the void fraction and DNB distributions in the 2x1 bundle. Void fraction and DNB differences between CTF and experimental data occurred due to the γ -ray transmission measurement and nucleate boiling methods used in the 1x1 and 5x5 bundles and the thermo-couples measurement, crossflow and turbulent mixing and DNB methods used in the 5x5 bundle. Also, void fraction and DNB differences between CTF and other thermal hydraulics codes occurred due to their different nature in general. Finally, void fraction and DNB differences in CTF and FLOCAL occurred due to the boundary conditions variation, different mass, momentum, and heat transfer in the constant mixing, Rogers and Rosehart mixing, crossflow, partial crossflow, and no crossflow methods, either the subchannel or channel and the previously mentioned methods used in the 2x1 bundle.

Hence, such validations and verifications have proven that CTF offers high accuracy and a wide range of crossflow and turbulent mixing methods, which further justifies its selection to provide thermal hydraulics at the fuel rod level in the most heterogeneous cases. Also, such verification has proven that FLOCAL offers only the no crossflow method, which still justifies its selection to provide thermal hydraulics at the fuel rod level in the most homogeneous cases. This chapter comprises the journal article CTF and FLOCAL Thermal Hydraulics Validations and Verifications within a Multiscale and Multiphysics Software Development [150], published in the MDPI Journal of Energies. All author contributions can be found in the list of publications section.

CTF and FLOCAL Thermal Hydraulics Validations and Verifications within a Multiscale and Multiphysics Software Development

Sebastian Davies ^{1,*}, Ulrich Rohde ², Dzianis Litskevich ¹, Bruno Merk ¹, Paul Bryce ³, Andrew Levers ¹, Anna Detkina ¹, Seddon Atkinson ¹, and Venkata Ravindra ¹

¹ School of Engineering, University of Liverpool, Liverpool L69 3GH, UK; d.litskevich@liverpool.ac.uk (D.L.); b.merk@liverpool.ac.uk (B.M.); alevers@liverpool.ac.uk (A.L.); a.detkina@liverpool.ac.uk (A.D.); seddon.atkinson@liverpool.ac.uk (S.A.); venkat@liverpool.ac.uk (V.R.)

² Institute of Fluid Dynamics, Helmholtz Zentrum Dresden Rossendorf, Dresden 01328, Germany; u.rohde@hzdr.de

³ EDF Energy, Gloucester GL4 3RS, UK; paul.bryce@edf-energy.com

* Correspondence: s.r.davies@liverpool.ac.uk; Tel.: +44-7502270482

Received: 22 January 2021; Accepted: 13 February 2021; Published: 18 February 2021

Abstract: Simulation codes allow one to reduce the high conservatism in nuclear reactor design improving the reliability and sustainability associated with nuclear power. Full core coupled reactor physics at the rod level are not provided by most simulation codes. This has led in the UK to the development of a multiscale and multi-physics software development focused on LWRS. In terms of the thermal hydraulics, simulation codes suitable for this multiscale and multi-physics software development include the subchannel code CTF and the thermal hydraulics module FLOCAL of the nodal code DYN3D. In this journal article, CTF and FLOCAL thermal hydraulics validations and verifications within the multiscale and multi-physics software development have been performed to evaluate the accuracy and methodology available to obtain thermal hydraulics at the rod level in both simulation codes. These validations and verifications have proved that CTF is a highly accurate subchannel code for thermal hydraulics. In addition, these verifications have proved that CTF provides a wide range of crossflow and turbulent mixing methods, while FLOCAL in general provides the simplified no-crossflow method as the rest of the methods were only tested during its implementation into DYN3D.

Keywords: nuclear reactor; thermal hydraulics; simulation; subchannel code; CTF; FLOCAL; PSBT

3.1. Introduction

A nuclear renaissance in the UK (United Kingdom) is on the verge of occurring due the reliability and sustainability associated with nuclear power which makes it ideal as an energy source to conform part of the future energy plan of the country. Its reliability depends on its capability to answer the local or national electricity demands by providing the intended output. In addition, its reliability depends on its capability to operate under safety limits by using either active or passive safety systems. Finally, its reliability depends on its capability to avoid nuclear proliferation by minimising the possibilities of theft and terrorism activities. Its sustainability depends on its capability to behave cost effectively by becoming economically competitive when compared to renewable energy sources. In addition, its sustainability depends on its capability to operate under environment friendly standards by using different types of fuel cycles. Finally, its sustainability depends on its capability to evolve by providing alternative technologies.

All these capabilities have been improved in the UK through the different generations of nuclear reactors. Generation I nuclear reactors were developed through the 1950s and 1960s to prove the applicability of nuclear power to provide electricity consisting of the previously used MAGNOX (magnesium oxide gas reactor). Generation II nuclear reactors were developed through the 1970s to improve the reliability and sustainability associated with nuclear power by increasing the production of electricity, including active safety systems, encompassing a closed fuel cycle, and extending the lifespan to 60 years consisting of the currently used AGR (advanced gas reactor) and PWR (pressurised

water reactor). Generation III and III+ nuclear reactors were developed in the 1990s to improve the reliability and sustainability associated to nuclear power by enhancing fuel technology and thermal efficiency, adding modular components, including passive safety systems, and extending the lifespan to further than 60 years consisting of the currently-under-construction EPR (European pressurised reactor) and the currently planned SMR (small modular reactor). Generation IV nuclear reactors are being currently developed to improve the reliability and sustainability associated with nuclear power by including full actinide recycling consisting of the envisioned SFR (sodium fast reactor), MSR (molten salt reactor) and HTR (high-temperature reactor).

Nuclear reactor analysis [1] provides the necessary methodology to describe the wide phenomena that occur in nuclear reactors. It is mainly subdivided into neutronics, which analyses power production by solving the neutron transport equation, and into thermal hydraulics, which analyses heat transfer by solving the fluid and solid dynamics equations. No heat transfer in a nuclear reactor occurs unless there is power production, and hence, the neutronics are said to be coupled to the thermal hydraulics. The neutronics can be analysed through different methods ranging from simplified neutron diffusion to full neutron transport. The thermal hydraulics can be analysed through different methods ranging from simplified fluid dynamics to full fluid dynamics.

Simulation codes provide the necessary accuracy to describe the correct phenomena that occur in nuclear reactors. The neutronics of nuclear reactors can be modelled through lattice and transport codes [2,3] with high accuracy at the rod level, with some of them offering homogenisation procedures to provide the necessary neutronics data for use in other simulation codes. The thermal hydraulics of nuclear reactors can be modelled through fluid dynamics codes such as system codes [4,5] with low accuracy at several levels and through subchannel codes [6,7] with high accuracy at the rod level, as well as through CFD (computational fluid dynamics) codes [8,9] with high accuracy at less than the rod level. Coupled reactor physics in nuclear reactors can be modelled through nodal codes [10,11] with variable accuracy at the assembly level, with some of them offering rod power reconstruction to provide improved accuracy at the rod level.

Existing computational constraints during the times when most simulation codes were originally developed led to the inability to provide full core direct (no reconstruction) coupled reactor physics at the rod level. Rod power reconstruction has always been limited in terms of accuracy and methodology through its inability to encapsulate all the coupled reactor physics phenomena, because it is applied after calculations at the assembly level. The fuel behaviour and nuclear reactor risks analysis is also limited in terms of accuracy and methodology either through their simplification or neglect. The mentioned issues have had an impact on the credibility of simulation codes as safety parameters are based at the assembly level rather than at the rod level, which has resulted in high conservatism in nuclear reactor design.

Full core direct (no reconstruction) coupled reactor physics at the rod level can be achieved if high accuracy and innovative methodology are considered, which would allow one to redefine safety parameters at the rod level and hence reduce the high conservatism in nuclear reactor design improving the reliability and sustainability associated with nuclear power. The next generation of simulation codes are aimed at providing the mentioned with special emphasis on the world spread LWR (light water reactor). Some of these simulation codes include CASL (consortium for advanced simulation of LWRs) [12,13] and NURESIM (nuclear reactor simulator) [14,15] both of which include high accuracy and innovative methodology to provide full core coupled reactor physics with several accuracy levels. CASL is too computationally expensive for the UK, while NURESIM does not offer coupled reactor physics at the rod level.

Hence, a multiscale and multi-physics software development between CASL and NURESIM (multiscale multi-physics software development) [16] for LWR has been presented which will include high accuracy and innovative methodology to deliver full core coupled reactor physics from the assembly level to the rod level. This multiscale and multi-physics software development will acknowledge the requests of the UK by reducing the high conservatism in nuclear reactor design to improve the reliability and sustainability associated with nuclear power; creating a code-coupling environment for data exchange between the simulation codes to provide coupled reactor physics; expanding the simulation codes coupling to the rod level to improve the description of the phenomena that occur in nuclear reactors; and finally, improving the user friendliness of the code coupling

environment to reduce user induced mistakes. This multiscale and multi-physics software development will be made computationally inexpensive for the UK by providing coupled reactor physics at the rod level only in certain assemblies and providing coupled reactor physics at the assembly level in all the reactor core.

Several codes will be incorporated into this multiscale and multi-physics software development to include high accuracy and innovative methodology through the following: full neutron-transport codes such as the LTS (Liverpool transport solver) [17] used at the UOL (University of Liverpool) to provide neutronics at the rod level; full fluid-dynamics codes, specially subchannel codes such as CTF (coolant boiling in rod arrays) [18], extensively used for research and commercial purposes to provide thermal hydraulics at the rod level; simplified neutron diffusion and simplified fluid-dynamics nodal codes such as DYN3D (dynamical 3 dimensional) [19], extensively used as well for research and commercial purposes to provide coupled neutronics and thermal hydraulics in general at the assembly level; and finally, fuel-performance codes such as ENIGMA [20], extensively used for commercial purposes to provide thermo-mechanics as well as risk assessment codes, such as COSSAN [21], used at the UOL (University of Liverpool) to provide an estimation of nuclear reactor risks. Finally, the mentioned codes will be coupled to provide coupled reactor physics both at the assembly level and the rod level. The mentioned multiscale and multi-physics software development can be observed in Figure 3.1.

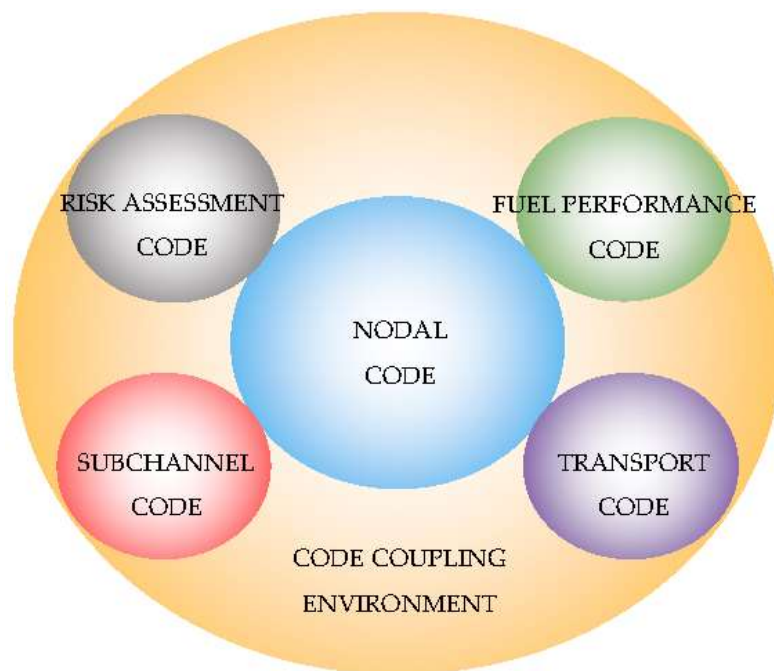


Figure 3.1. Multiscale and multi-physics software development.

The aim is to create the coupling between the nodal code DYN3D and the subchannel code CTF within the mentioned multiscale and multi-physics software development to provide improved neutronics and thermal hydraulics at the rod level. The first objective into achieving this aim consists of evaluating the accuracy and methodology available to obtain thermal hydraulics at the rod level in both the subchannel code CTF and the thermal-hydraulics module FLOCAL of the nodal code DYN3D, as the accuracy and methodology available to obtain thermal hydraulics at the assembly level in the thermal-hydraulics module FLOCAL of the nodal code DYN3D are known in research. This evaluation will allow one to justify why the subchannel code CTF has been selected to provide high-accuracy thermal hydraulics at the rod level, as well as to justify when FLOCAL rather than CTF should be used to provide improved thermal hydraulics at the rod level. This initial journal article therefore covers the CTF and FLOCAL accuracy and methodology validations and verifications of the thermal hydraulics at the rod level, while the coupling between DYN3D and CTF at the rod level will be covered in future journal articles.

Thermal hydraulics at the rod level are available by default in the subchannel code CTF [22] but not in the thermal hydraulics module FLOCAL of the nodal code DYN3D [23] where thermal hydraulics at the assembly level are in general available. A possibility in the thermal hydraulics module FLOCAL consists of modelling heater-cell-scaled nodes containing one rod instead of assembly-scaled nodes containing many rods to obtain improved thermal hydraulics at the rod level. However, the improved thermal hydraulics at the rod level in the thermal hydraulics module FLOCAL are in general limited in terms of crossflow and mixing methods as opposed to in the high-accuracy thermal hydraulics at the rod level in the subchannel code CTF.

The layout of this journal article is divided into several steps. First, a CTF description has been presented [24,25], and hence general aspects and approach are mentioned to describe the first code used in the accuracy and methodology validations and verifications. Second, a FLOCAL description has been presented [26,27], and hence general aspects and approach are mentioned to describe the second code used in the methodology verification. Third, the tabulation of the specifications used in the CTF accuracy validation and verification has been presented consisting of the PSBT (PWR subchannel and bundle tests) benchmark [28–31]. Fourth, the tabulation of the specifications used in the FLOCAL and CTF methodology verification has been presented consisting of the FLOCAL developer benchmark. Fifth, the description of the models used in the CTF accuracy validation and verification has been presented according to the specifications. Sixth, the description of the models used in the CTF and FLOCAL methodology verification has been presented according to the specifications.

The results and analysis obtained for the CTF accuracy validation and verification through the PSBT benchmark is comprised by CTF to experimental data comparisons as well as CTF to other codes comparisons. It is divided into the void distribution and the DNB (departure from nucleate boiling) benchmarks. Tests presented include results for the void fraction in a 1×1 bundle and results for the void fraction and departure from nucleate boiling in a 5×5 bundle with guide tube, although the full benchmark was originally covered in the simulations. The mentioned magnitudes have been chosen as these allow to analyse accuracy in nuclear reactors from a thermal-hydraulics perspective. It can be seen how the mentioned comparisons allow one to show the high accuracy available in CTF compared to other codes.

The results and analysis obtained for the CTF and FLOCAL methodology verification through the FLOCAL developer benchmark are comprised by CTF to FLOCAL comparisons. It is divided into power variation and mass-flux-blockage exercises. Tests presented include results for the void fraction and departure from nucleate boiling in 2×1 fuel cells. The mentioned magnitudes have been chosen as these allow one to analyse methodology in nuclear reactors from a thermal-hydraulics perspective. It can be seen how the mentioned comparisons show the innovative methodology available in CTF and in FLOCAL.

Conclusions related to the CTF and FLOCAL accuracy and methodology validations and verifications have been presented to confirm that the first objective in the aim of creating a coupling between CTF and DYN3D within the multiscale and multi-physics software development has been fulfilled by validating and verifying the accuracy of CTF, as well verifying the methodology available in both CTF and FLOCAL. Finally, future work that remains is presented to provide an insight of the next objectives in the aim to create a coupling between CTF and DYN3D within the multiscale and multi-physics software development.

3.2. Codes Used in the Validations and Verifications

As previously mentioned CTF and FLOCAL are the codes selected as they are extensively used for research and commercial purposes, and hence their main aspects and approach are described in the following subsections.

3.2.1. CTF Subchannel Code

COBRA-TF [24,25] is a subchannel code created to study both general LWR (square geometry) behaviour and accident-related scenarios. It was coded in FORTRAN in the 80s and 90s by PNL (Pacific Northwest Laboratories), funded by the NRC (Nuclear Regulation Commission) and has since been upgraded by NCU (North Carolina University) and PSU (Pennsylvania State University) to conform CTF. It is widely employed both for steady and transient state analysis due to its capabilities, such as

3D simulation. Most systems, except pressurizers, can be simulated in CTF with these being described through vertical stacks of nodes which represent subchannels. Either rectangular or subchannel coordinates can be used to describe the mentioned system.

A two-fluids (liquid, vapor) and three-flow-fields (liquid film, liquid droplets, and vapor) simulation scheme is employed aided by flow regime/heat-transfer phenomena including two-phase heat, mass and momentum transfer between phases and nodes, entrainment, and quench front tracking. The simulation scheme is set on the nodes where each field is simulated through its own set of mass, momentum, and energy equations. Exceptionally, the liquid and droplet fields remain in thermal equilibrium and therefore share the same energy equation. Finally, the solution to the equations is obtained by employing finite differences and numerical techniques. The SIMPLE (semi-implicit method for pressure-linked equations) algorithm is used to solve the conservation equations which conform a type of homogeneous equilibrium method.

Several settings are necessary to provide results such as the following: stating the time dependence of the simulation in addition to preconditions to carry these out; guessing the flow regime to determine the contact area between phases required to obtain the heat and mass transfer between phases as well as the correct macro and micro nodes closure terms necessary to include the appropriate aggregate physical effects; obtaining the micro node closure terms that link the conservation equations for distinct phases in an equivalent node yielding physical effects between phases, including phase change and entrainment; obtaining the macro node closure terms that link the conservation equations for a same phase in distinct nodes yielding physical effects such as void drift and turbulent mixing; determining the solution to the transport equation associated to the area between phases to acknowledge the mentioned for the droplet field; determining the solution to the conservation equations for the rod to obtain the heat transfer and departure from nucleate boiling necessary to acknowledge the heat conductance; and guessing several solid thermal and mechanical aspects through lists and included models.

3.2.2. FLOCAL Thermal Hydraulics Module

FLOCAL [26,27] is the thermal hydraulics module of the nodal code DYN3D created to study general LWR-VVER (square and hexagonal geometries) behaviour. It was coded in FORTRAN in the 90s by HZDR (Helmholtz Zentrum Dresden Rossendorf) and has since been upgraded to conform part of DYN3D. It is widely employed both for steady and transient state analysis due to its capabilities, such as 3D simulation. Either a reactor core or a smaller system can be simulated in FLOCAL, with these being described through vertical stacks of nodes which generally represent full channels. Either rectangular or hexagonal coordinates can be used to describe the mentioned system. A two-fluids (liquid, vapor) simulation scheme is utilized aided by heat-transfer phenomena including: two-phase heat, mass, and momentum transfer between phases. The simulation scheme is set on the nodes where the fluid mixture is simulated through its set of mass, momentum, and energy equations. Exceptionally, the fluid-vapor mass equation is solved apart from the other equations. Finally, the solution to the equations is obtained by employing finite differences and numerical techniques. An implicit-method algorithm is implemented to solve the conservation equations

Several settings are necessary to provide results such as the following: stating the time dependence of the simulation in addition to preconditions to these out; obtaining the constitutive relations that link the conservation equations for distinct phases in the nodes yielding physical effects including phase change; determining the solution to the conservation equations for the rod to obtain the heat transfer and departure from nucleate boiling necessary to acknowledge the heat conductance; and guessing several solid thermal and mechanical aspects through lists and included models.

3.3. Specifications Used in the Validations and Verifications

As previously mentioned, the CTF accuracy validation and verification have been performed through the replication of the PSBT benchmark. The FLOCAL and CTF methodology verification has been performed through the replication of the FLOCAL developer benchmark. Hence, the specifications used in the mentioned are described in the following subsections.

3.3.1. PSBT Benchmark

The PSBT benchmark [28–31] is a validated benchmark for LWR thermal-hydraulics simulation. Experimental data has been obtained by NUPEC at their facilities in Japan using a test rig and several test sections using gamma-ray transmission methods. Code results have been provided by many academic and industrial partners using CFD codes as well as subchannel and system codes. It is divided into the void distribution and the DNB benchmarks. Series of tests carried out include the following: steady-state fractional and full 1×1 bundles with uniform axial and radial power distributions, and steady-state 5×5 and 6×6 bundles with either uniform or cosine axial power distributions and variable radial power distributions, as well as different spacer-grids arrangements and possibility of a central guide tube. The PSBT benchmark includes a wide range of accuracy tests with different outlet pressures, powers, mass fluxes, and inlet temperatures. Only the data for certain test series has been presented, such as test series S1, which corresponds to the full 1×1 bundle of the void distribution benchmark, and test series B7 and A8, which correspond to the 5×5 with guide-tube bundles of the void distribution and DNB benchmarks.

Specifications include the geometry, materials, spacer grids, power distributions, and initial and boundary conditions. The geometry is described for the 1×1 and 5×5 bundles as observed in Table 3.1:

Table 3.1. 1×1 and 5×5 geometry from the PSBT (PWR subchannel and bundle tests) benchmark.

Type	1×1 Bundle	5×5 Bundle
Number of Heater Rods	1	24
Number of Guide Tubes	0	1
Channel Width (m)	0.0126	0.0649
Cell Width (m)	0.0126	0.0126
Axial Length (Active) (m)	1.555	3.658
Heater-Rod Diameter (m)	0.0095	0.0095
Thimble-Rod Diameter (m)	-	0.01224
Heater-/Thimble-Rod Thickness (m)	-	0.0065

The materials are described for all the bundles as observed in Table 3.2:

Table 3.2. 1×1 and 5×5 materials from the PSBT benchmark.

Clad Composition	Inconel 600
Density (kg/m ³)	$\rho_{clad} = 16.01846(5.261008 \cdot 10^{-2} - 1.345453 \cdot 10^{-2}T_c - 1.194357 \cdot 10^{-7}T_c^2)$ (8)
Specific Heat (J/kg K)	$c_{P\ clad} = 4186(0.1014 + 4.378952 \cdot 10^{-5}T_c - 2.046138 \cdot 10^{-8}T_c^2 + 3.418111 \cdot 10^{-11}T_c^3 - 2.060318 \cdot 10^{-13}T_c^4 + 3.682836 \cdot 10^{-16}T_c^5 - 2.458648 \cdot 10^{-19}T_c^6 + 5.597571 \cdot 10^{-23}T_c^7)$ (9)
Thermal Conductivity (W/m K)	$k_{clad} = 1.729577(8.011332 + 4.643719 \cdot 10^{-3}T_c + 1.872857 \cdot 10^{-6}T_c^2 - 3.914512 \cdot 10^{-9}T_c^3 + 3.475513 \cdot 10^{-12}T_c^4 - 9.936696 \cdot 10^{-16}T_c^5)$ (10)

Spacer grids can be any of 3 types including nonmixing vane, mixing vane, and simple, which are represented using pressure-loss coefficients stated for the 5×5 bundle in Table 3.3:

Table 3.3. 5×5 spacer grids from the PSBT benchmark.

NMV Pressure-Loss Coefficient	0.7
MV Pressure-Loss Coefficient	1.0
SP Pressure-Loss Coefficient	0.4
	NMV: 0.0025, 3.501
Spacer Grid Locations (m)	MV: 0.471, 0.925, 1.378, 1.832, 2.285, 2.739, 3.247 SP: 0.237, 0.698, 1.151, 1.605, 2.059, 2.512, 2.993

The power distributions are described for the 1×1 and 5×5 bundles as observed in Table 3.4:

Table 3.4. 1×1 and 5×5 power distributions from the PSBT benchmark.

		0.85	0.85	0.85	0.85	0.85
		0.85	1.00	1.00	1.00	0.85
Radial Power Distributions	1.00	0.85	1.00	0.00	1.00	0.85
		0.85	1.00	1.00	1.00	0.85
		0.85	0.85	0.85	0.85	0.85
Axial Power Distributions	Uniform					Cosine

The initial and boundary conditions for each test are described first for Test Series S1 of the void distribution benchmark, then for Test Series B7 of the void distribution benchmark, and finally for Test Series A8 of the DNB benchmark, as observed in Table 3.5:

Table 3.5. 1×1 (S1) and 5×5 (B7 and A8) initial and boundary conditions from the PSBT benchmark.

Case	Outlet Pressure (bar)	Power (kW)	Inlet Mass Flux (kg/m ² s)	Inlet Temperature (C)
1.1222	165.72	50	3050	334.7
1.1223	165.72	49.90	3055.55	339.7
1.2211	147.10	90	3030.55	295.4
1.2221	147.10	69.8	3022.22	299.4
1.2223	147.10	69.8	3030.55	319.6
1.2237	147.29	60	3036.11	329.6
1.2422	147.10	60	1388.88	284.1
1.2423	147.29	59.90	1369.44	299.3
1.4311	98.39	79.90	1391.66	214.2
1.4312	98.20	79.80	1397.22	248.9
1.4325	98.29	59.80	1397.22	253.8
1.4326	98.10	60.10	1394.44	268.8
1.5221	73.99	49.90	1394.44	219.2
1.5222	73.50	50	1394.44	243.9
1.6221	49.49	50	1391.66	189.2
1.6222	49	49.90	1388.88	204.2
7.1221	164.24	3385	4186.11	301.8
7.1122	164.17	3384	4186.11	306.8
7.1341	165.47	2391	2200	289.4
7.1342	165.48	2391	2205.55	295.3
7.2221	146.40	3503	3058.33	272.1
7.3121	121.28	3502	4222.22	276.1
7.3451	122.65	2023	1388.88	242.8
7.3452	122.67	2021	1397.22	260.1
7.4561	98.34	1023	600	196.8

7.4562	98.35	1023	600	214.9
7.6321	48.87	3541	2250	153.5
7.6322	48.69	3536	2238.88	168.6
08-1330	49.19	(Protected)	1411.11	150.8
08-2150	73.99		3111.11	264
08-2750	73.79		3111.11	239.3
08-3770	98.49		4816.66	262.2
08-4230	122.79		1397.22	262.1
08-4240	122.69		2244.44	261.9
08-5130	147.10		1375	321.6
08-5140	147.39		2225	321.3
08-5220	147.29		575	279.5
08-5252	147.19		3091.66	281.5
08-6230	165.71		1386.11	295.6

3.3.2. FLOCAL Developer Benchmark

The FLOCAL developer benchmark is a proposed benchmark for LWR thermal-hydraulics simulation. Code results have been provided by the FLOCAL developer. It is divided into power variation and mass-flux-blockage exercises. Tests carried out include steady-state 2×1 heater cells with uniform axial power distribution and variable radial power distribution as well as possibility of local blockage. The FLOCAL developer benchmark includes two methodology tests with different power but same outlet pressures, mass fluxes, and inlet temperatures. All the data for the tests has been presented.

Specifications include the geometry, power distributions and initial and boundary conditions. The geometry is described the two heater cells as observed in Table 3.6:

Table 3.6. 2×1 geometry from the FLOCAL developer benchmark.

Type	
Number of Heater Rods	2
Cell Width (m)	0.0122
Axial Length (Active) (m)	2.500
Heater Rod Diameter (m)	 0.0090

The local blockage is represented using a pressure-loss coefficient stated for the mass-flux-blockage exercise in Table 3.7:

Table 3.7. 2×1 local blockage from the FLOCAL developer benchmark.

Local Pressure Loss Coefficient	20.0
Local Blockage Location (m)	1.50

The power distributions are described first for the power variation and then the mass-flux-blockage exercises as observed in Table 3.8:

Table 3.8. 2×1 power distributions from the FLOCAL developer benchmark.

Radial Power Distribution	1.13	0.86	1.00	1.00
Axial Power Distribution	Uniform		Uniform	

The initial and boundary conditions first for the power variation and then the mass-flux-blockage exercises are described as observed in Table 3.9:

Table 3.9. 2×1 initial and boundary conditions FLOCAL developer benchmark.

Test	Outlet Pressure (bar)	Power (kW)	Inlet Mass Flux (kg/m ² s)	Inlet Temperature (C)
1	100	197.1	4999.77	210
2	100	195	4999.77	210

3.4. Models Used in the Validations and Verifications

As previously mentioned, the CTF accuracy validation and verification have been performed through the replication of the PSBT benchmark. The FLOCAL and CTF methodology verification has been performed through the replication of the FLOCAL developer benchmark. Hence, the models used in the mentioned are described in the following subsections.

3.4.1. PSBT Benchmark

In CTF, the models comprise in the 1×1 bundle one subchannel containing one heater rod while in the 5×5 bundle 36 subchannels (subchannel-centered system) linked by 60 gaps between them containing 24 heater rods and one guide tube. These have been incorporated into one axial section conformed in the 1×1 bundle by 30 uniform axial node layers while conformed in the 5×5 bundle by 36 non-uniform axial node layers in the case of the void distribution benchmark or 70 non-uniform axial node layers in the case of the DNB benchmark conditioned in any case by the spacer-grid locations. No time dependence has been included to reach thermodynamical equilibrium (steady state). The CTF heater rod and subchannel-centred system designs can be observed in Figure 3.2.

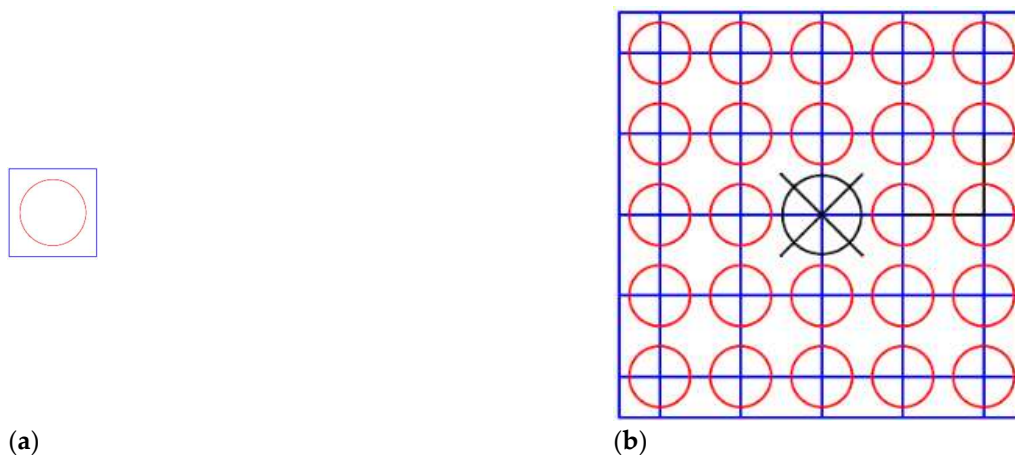


Figure 3.2. (a) CTF 1×1 design; (b) CTF 5×5 design.

In all the bundles, Thom's correlation [32] has been employed to simulate nucleate boiling as it remains valid at higher pressures than Chen's correlation. In the 5×5 bundle, in the case of the DNB benchmark, the W-3 correlation [33,34] has been employed to simulate departure from nucleate boiling it being typically used to study LWR. In the 5×5 bundle, a constant single-phase mixing coefficient with a value of 0.05 and a two-phase multiplier according to Beus with a value of 5.0 as well as an equilibrium weighting void drift factor with a value of 1.4 [35] have been employed to simulate turbulent mixing and void drift being typically used to study LWR. In all the bundles the original CTF model has been employed to simulate entrainment and deposition to include liquid droplets fluid phenomena. In all the bundles, McAdams two-phase multiplier correlation [36] has been employed to simulate heater-rod friction pressure losses typically being used to study LWR. In the 5×5 bundle several coefficients with a value of 0.5 have been employed to simulate velocity head losses friction pressure losses between heater rods as well as wall friction pressure losses between heater rods and walls. In addition, in the 5×5 bundle coefficients with values according to the spacer-grids specifications have been employed to simulate form pressure losses in the corresponding axial node

layers. In all the bundles, the Krylov solver has been used to obtain a solution to the pressure equation with it being more effective than Gaussian elimination.

3.4.2. FLOCAL Developer Benchmark

In CTF and FLOCAL, the models comprise two heater cells linked by one gap between them in the case of the former containing two heater rods. These have been incorporated into one axial section conformed by 10 uniform axial node layers. No time dependence has been included to reach thermodynamical equilibrium (steady state). The heater-rod-centred system design in both CTF and FLOCAL can be observed in Figure 3.3.

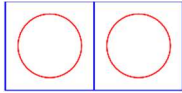


Figure 3.3. CTF and FLOCAL 2×1 design.

Thom's correlation [32] has been employed to simulate nucleate boiling in CTF as it remains valid at higher pressures than Chen's correlation, while Rassokhin and Borishaskji [37] correlation has been employed to simulate nucleate boiling in FLOCAL, with it being the existing one. The W-3 correlation [33,34] has been employed to simulate departure from nucleate boiling in CTF, with it being typically used to study LWR, while the Bezrukov and Astakhov correlation [38] has been employed to simulate departure from nucleate boiling in FLOCAL, with it being one of the several available. Different methods later mentioned have been implemented to simulate both crossflow and turbulent mixing in both CTF and FLOCAL. The original CTF model has been employed to simulate entrainment and deposition to include liquid-droplets fluid phenomena, while no model has been employed in FLOCAL, as it does not allow liquid droplets. McAdams two-phase multiplier correlation [36] has been employed to simulate heater-rod friction pressure losses in CTF it being typically used to study LWR while Filonenko's and Osmachkin's one- and two-phase multiplier correlation [39] has been employed to simulate heater-rod friction pressure losses in FLOCAL, with it being the existing one. A single coefficient with a value of 0.5 has been employed to simulate velocity head friction pressure losses between heater rods in CTF, while no coefficient has been employed to simulate velocity head friction pressure losses between heater rods in FLOCAL. A coefficient with a value according to the specifications has been employed to simulate the local blockage in the mass-flux-blockage exercise as a pseudospacer-grid-form pressure loss in the corresponding axial node layer in both CTF and FLOCAL. The Krylov solver has been used to obtain a solution to the pressure equation in CTF, with it being more effective than Gaussian elimination, while Gaussian elimination has been used to obtain a solution to the pressure equation in FLOCAL, with it being the existing one.

Crossflow and turbulent mixing methods simulated in CTF include the following: The no-crossflow method, where mass, momentum, and energy equations for each channel are solved without allowing mass, momentum, and energy transfer between the heater cells. The crossflow method where mass, momentum, and energy equations for each channel are solved allowing mass, momentum, and energy transfer between the heater cells. The Rogers and Rosehart mixing method where mass, momentum, and energy equations for each channel are solved allowing mass, momentum, and energy transfer as well as void drift and turbulent mixing through an empirical-correlation-calculated single-phase mixing coefficient and a two-phase multiplier with a value of 5.0 as well as an equilibrium weighting void drift factor with a value of 1.4 [40]. The constant-mixing method where mass, momentum, and energy equations for each channel are solved allowing mass, momentum, and energy transfer as well as void drift and turbulent mixing through a constant single-phase mixing coefficient with a value of 0.05 and a two-phase multiplier with a value of 5.0 as well as an equilibrium weighting void drift factor with a value of 1.4.

Crossflow methods simulated in FLOCAL include the following: The no-crossflow method, where mass, momentum and energy equations for each channel are solved without allowing mass, momentum, and energy transfer between the heater cells. The partial-crossflow method where mass, momentum, and energy equations for each channel are solved allowing only mass and momentum

transfer between the heater cells. The crossflow method where mass, momentum, and energy equations for each channel are solved allowing mass, momentum, and energy transfer between the heater cells.

3.5. Results and Analysis

Considering the thermal-hydraulics results obtained with CTF through the replication of the PSBT benchmark [28–31], CTF to experimental data as well as CTF to other codes results comparisons within the accuracy validation and verification in the steady state are presented for the void fraction as well as the departure from nucleate boiling. Considering the thermal hydraulics results obtained with FLOCAL and CTF through the replication of the FLOCAL developer benchmark. CTF to FLOCAL comparisons within the methodology verification in the steady state are presented for the void fraction as well as for the departure from nucleate boiling.

3.5.1. PSBT Benchmark

Code to experimental accuracy comparisons within the steady-state void distribution benchmark for the single subchannel (Test Series S1) are presented for the void fraction, while the density and equilibrium quality are presented in appendix A. Experimental data available consists of a gamma-ray transmission method composed both by CT (narrow gamma beam) as well as chordal (wide gamma beam) measurements with the setup being contained in appendix A. In both cases, density values were measured and later converted to void fraction values. A relationship between both measurements was then derived to determine the corrected average void fraction value in the subchannel. Void fraction values are presented for the single subchannel at a single location (1.4 m). Linear fitting with interception at the origin has been performed to show similarities and differences between CTF and the experimental values as observed in Figure 3.4.

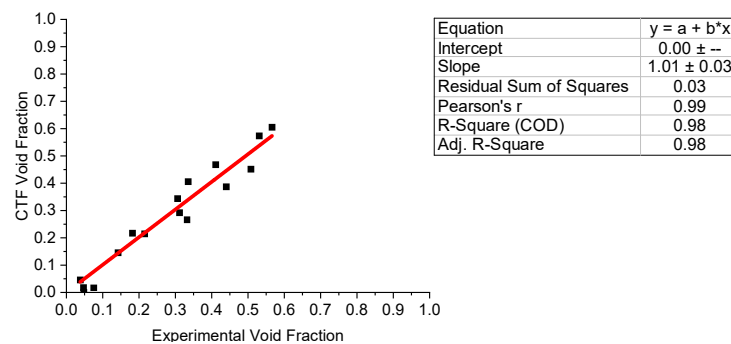


Figure 3.4. CTF vs. experimental void fraction.

Differences between the experimental and CTF void fraction values at the mentioned axial locations are small with no tendency in the estimation of the values. Several reasons were found to cause the observed differences between the CTF and the experimental data: The gamma-ray transmission method used underestimates the void fraction as these experimental measurements were taken at the centres of subchannels instead of near the heated surfaces where most of the void fraction occurs under general LWR behaviour. The nucleate boiling model used affects the void fraction as it may respond differently to the different initial and boundary conditions.

Code to code accuracy comparisons within the steady-state void distribution benchmark for the single subchannel (Test Series S1) are presented only for the void fraction. Code results have been provided by 20 academic and industrial partners including porous media codes (THYC), CFD codes (ANSYS, NEPTUNE...), subchannel codes (VIPRE, SUBCHANFLOW...), and system codes (TRACE, CATHARE...) results with a full list of codes being contained in appendix A. Void fraction values for each code are presented for the single subchannel at a single axial location (1.4 m). Errors and standard deviations values are calculated to show similarities and differences between CTF, and the other codes as observed in Figure 3.5 and given by the next equation.

$$\Delta\bar{x} = \sum_{t=1}^M \frac{\Delta x_t}{N} \quad \sigma = \pm \sqrt{\sum_{t=1}^M \frac{(\Delta x_t - \Delta\bar{x})^2}{M-1}} \quad \text{where } \Delta x_t = x_{t \text{ code}} - x_{t \text{ exp}} \quad (11)$$

Where $x_{t \text{ code}}$, $x_{t \text{ exp}}$ describe either an experimental or code value per test and per datum of any magnitude. Δx_t describes the difference between the code and experimental values for a certain parameter in a test within a series. $\Delta\bar{x}$ describes the average difference between tests within a series.

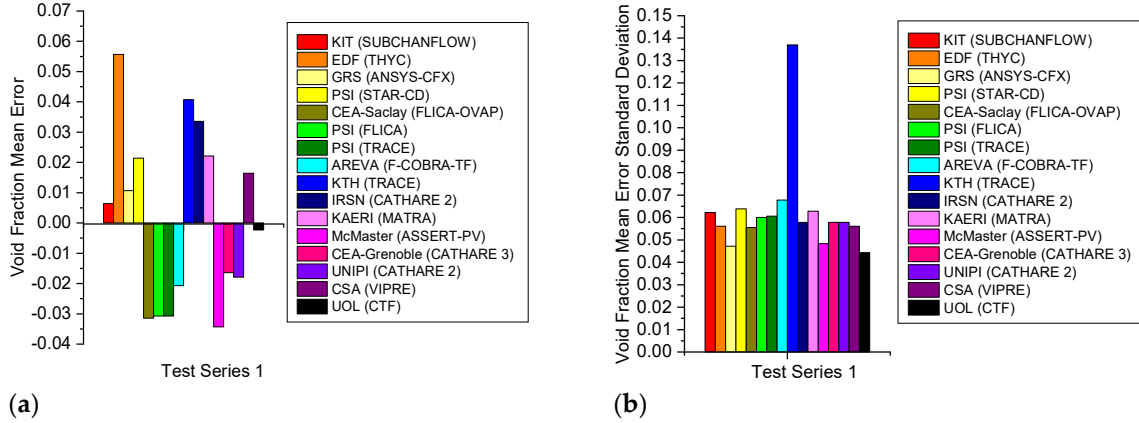


Figure 3.5. (a) Codes void fraction mean errors; (b) codes void fraction error standard deviation.

Differences between most system codes and CTF void fraction values at the single location are large with most system codes showing larger mean errors and standard deviations compared to CTF. Differences between most subchannel codes and CTF at the single location are variable with some subchannel codes showing larger mean errors and standard deviations than CTF, and others similar mean errors and standard deviations compared to CTF. Differences between CFD/porous media codes and CTF at the single axial location are large with most CFD/porous media codes showing larger mean errors and standard deviations compared to CTF. Most of the CFD/porous media codes as well as system codes show overestimation of the values, while most of the subchannel codes show underestimation of the values. Several reasons were found to cause the observed differences between the CTF and other codes results: System codes tend to offer lower accuracy compared to subchannel codes and hence consume less time to achieve results. CFD/porous media codes however tend to offer in general higher accuracy compared to subchannel codes and hence consume more time to achieve results.

Codes for experimental accuracy comparisons within the steady-state void distribution benchmark for the 5×5 bundle with guide tube (Test Series B7) are presented for the void fraction with the equilibrium quality being presented in appendix A. Experimental data available consists of a gamma-ray transmission method composed both by CT (narrow gamma multibeam) as well as chordal (wide gamma multibeam) measurements with the setup being contained in appendix A. In both cases, density values were measured and later converted to void fraction values. A relationship between both measurements was then derived to determine the corrected average void fraction value only in the central subchannels of the 5×5 bundle. Void fraction values are presented for the central subchannels at three different axial locations including a lower region (2.216 m) and an intermediate region (2.669 m), as well as an upper region (3.177 m). Linear fitting with interception at the origin has been performed to show similarities and differences between CTF and the experimental values as observed in Figure 3.6.

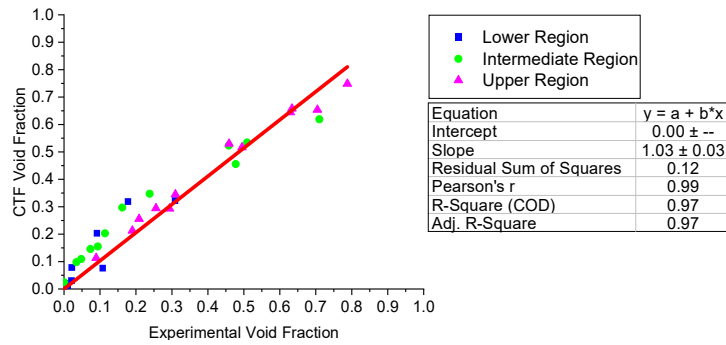


Figure 3.6. CTF vs. experimental void fraction.

Differences between the experimental and CTF void fraction values at the three axial locations are small with slight overestimation of the lower region and intermediate region values and slight underestimation of the upper region values. Several reasons were found to cause the observed differences between the CTF and the experimental data: The gamma-ray transmission method used underestimates the void fraction as these experimental measurements were taken at the centres of subchannels instead of near the heated surfaces where most of the void fraction occurs under general LWR behaviour. The nucleate boiling model used affects the void fraction as it may respond differently to the different initial and boundary conditions. The crossflow and mixing models used affect the void fraction codes which include crossflow as well as turbulent mixing models achieve the best correlation between experimental measurements and code results.

Code-to-code accuracy comparisons within the steady-state void distribution benchmark for the 5×5 bundle with guide tube (Test Series B7) are presented for the void fraction. Code results have been provided by 16 academic and industrial partners including porous-media codes (THYC), subchannel codes (MATRA, SUBCHANFLOW...), and system codes (TRACE, CATHARE...) results with a full list of the participants and code types being contained in appendix A. Void fraction values for each code are presented for the central subchannels at three different axial locations including a lower region (2.216 m), an intermediate region (2.669 m), and an upper region (3.177 m). Errors and standard deviations values are calculated to show similarities and differences between CTF, and the other codes as observed in Figures 3.7 and 3.8 and given by Equation (4).

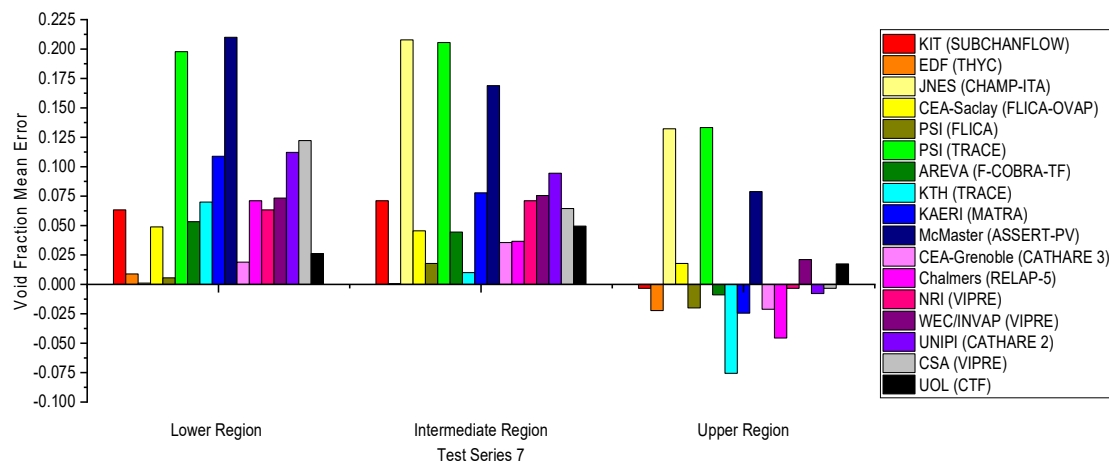


Figure 3.7. Codes void fraction mean errors.

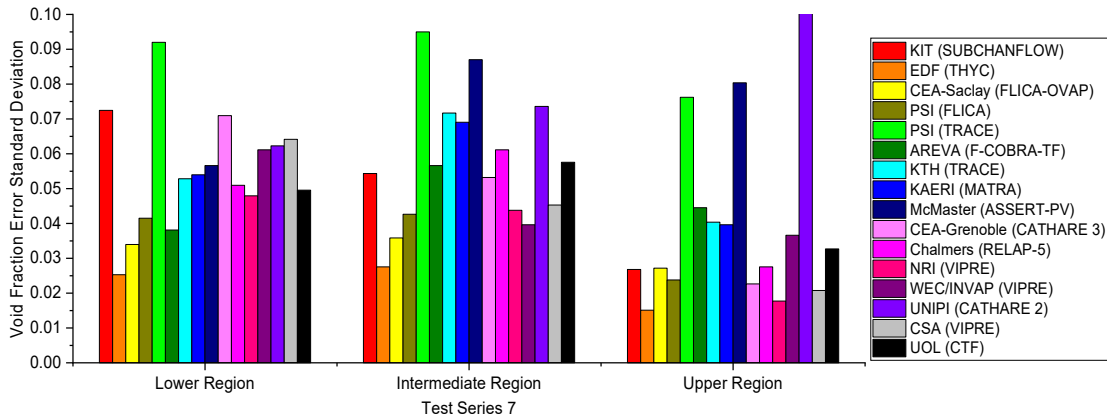


Figure 3.8. Codes void fraction error standard deviation.

Differences between most system codes and CTF void fraction values at the 3 axial locations are large, with most system codes showing larger mean errors and standard deviations compared to CTF. Differences between most subchannel codes and CTF at the three axial locations are variable, with some subchannel codes showing larger mean errors and standard deviations compared to CTF, and others, similar mean errors and standard deviations compared to CTF. Differences between the porous-media code and CTF at the three axial locations are similar, with the mentioned one showing smaller mean errors and standard deviations compared to CTF. Most of the codes show overestimation of the lower region and intermediate region values as well as underestimation of the higher region values. Several reasons were found to cause the observed differences between the CTF and other codes results: System codes tend to offer lower accuracy compared to subchannel codes and hence consume less time to achieve results. CFD/porous-media codes however tend to offer in general higher accuracy compared to subchannel codes and hence consume more time to achieve results.

Code-to-experimental accuracy comparisons within the steady state DNB benchmark for the 5 × 5 bundle with guide tube (Test Series A8) are presented for the departure from nucleate boiling. Experimental data available consists of a thermocouples method composed of measurements at several locations with the setup being contained in appendix A. The wall temperature was measured where a rise of more than 11 C confirmed departure from nucleate boiling with the critical heat flux being defined by the power at the step prior to this wall temperature rise measurement. Critical powers values are presented for the rods at the first occurrence height. Linear fitting with interception at the origin has been performed to show the similarities and differences between CTF and the experimental values, as observed in Figure 3.9.

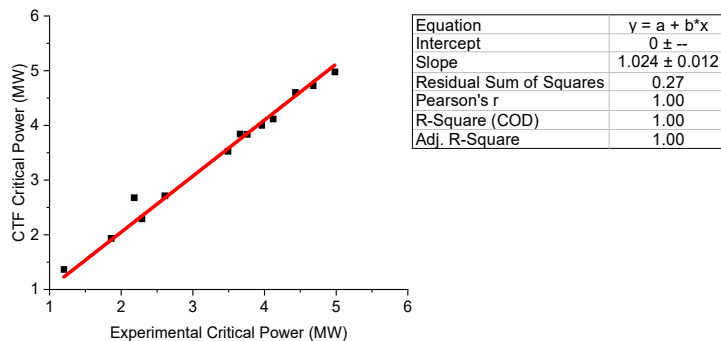


Figure 3.9. CTF vs. experimental critical-heat flux.

Differences between the experimental and CTF critical power values at the first occurrence height are low with slight overestimation of the values. Several reasons were found to cause the observed differences between the CTF and the experimental data: The thermocouples method used overestimates the departure from nucleate boiling as detection can be delayed due to the discrete

number of measurement points, and the critical heat-flux correlation used affects the departure from nucleate boiling as many different correlations are available which offer different code results.

Code-to-code accuracy comparisons within the steady state DNB benchmark for the 5×5 bundle with guide tube (Test Series A8) are presented for the departure from nucleate boiling. Code results have been provided by 10 academic and industrial partners including porous-media codes (THYC), subchannel codes (MATRA, SUBCHANFLOW...), and system codes (TRACE, CATHARE...) results with a full list of the participants and code types being contained in appendix A. The first occurrence height for each code is presented for the corresponding heater rod as observed in Figure 3.10.

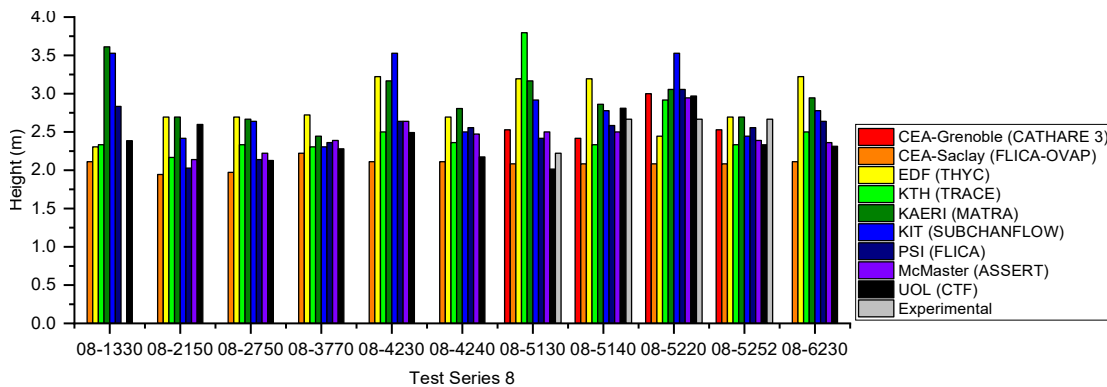


Figure 3.10. Codes departure from nucleate-boiling heights.

Differences between the system codes and CTF departure from nucleate-boiling first-occurrence height values are small with the mentioned two showing similar values compared to CTF. Differences between most subchannel codes and CTF departure from nucleate-boiling first-occurrence height values are variable with some subchannel codes showing larger values compared to CTF and others similar values compared to CTF. Differences between the porous-media code and CTF departure from nucleate-boiling first-occurrence height values are large with the mentioned one showing larger values compared to CTF. Several reasons were found to cause the observed differences between the CTF and other codes results: System codes tend to offer lower accuracy compared to subchannel codes and hence consume less time to achieve results. CFD/porous-media codes however tend to offer in general higher accuracy compared to subchannel codes and hence consume more time to achieve results.

3.5.2. FLOCAL Developer Benchmark

CTF to FLOCAL method comparisons within the power variation exercise for the 2×1 heater cells are presented for the void fraction and departure from nucleate boiling with the mass flux and coolant temperature being presented for the power variation and the local mass-flux blockage exercises in appendix B. Code results have been provided by the FLOCAL developer. Void fraction distributions are presented for the two heater cells to show similarities and differences in the methods available in both CTF and FLOCAL as observed in Figure 3.11.

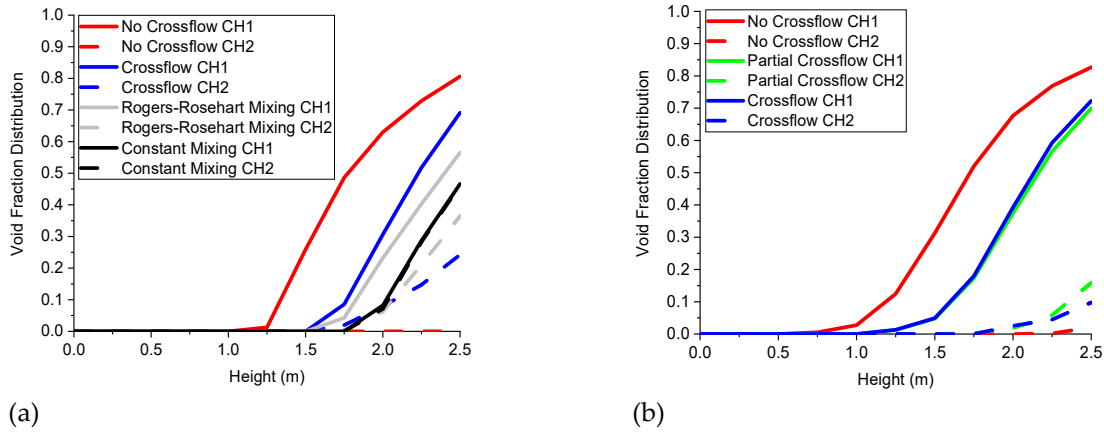


Figure 3.11. (a) CTF void fraction axial distributions; (b) FLOCAL void fraction axial distributions.

The void fraction distribution in CTF and FLOCAL is determined through the fluid density, fluid velocity, and fluid enthalpy distributions which are obtained through the solution to the mass, momentum, and energy equations. No value occurs in any method in both CTF and FLOCAL until the shift from single-phase heat transfer to nucleate-boiling heat transfer which occurs once the wall temperature surpasses the fluid saturation temperature.

In both CTF and FLOCAL, a void fraction distribution rise under nucleate-boiling heat transfer is observed in all the methods. The void fraction distribution in heater cell 1 increases more due its high power resulting on lower fluid densities, higher vapor, and lower liquid velocities, as well as higher fluid enthalpies when compared to heater cell 2. The void fraction distribution in heater cell 2 increases less due its low power resulting on higher fluid densities, lower vapor, and higher liquid velocities as well as lower fluid enthalpies when compared to heater cell 1.

In both CTF and FLOCAL, a higher void fraction distribution increase under nucleate-boiling heat transfer is observed in the no-crossflow method compared to the crossflow method. This occurs due to the exclusion in the conservation equations of mass, momentum, and energy transfer between heater cells. This results in lower fluid densities, higher vapor, and lower liquid velocities as well as higher fluid enthalpies.

In CTF, a higher void fraction distribution increase under nucleate-boiling heat transfer is observed in the crossflow method as opposed to in the Rogers and Rosehart and the constant mixing methods. This occurs due to the exclusion in the conservation equations of turbulent mixing and void drift between heater cells. This results in lower fluid densities, higher vapor, and lower liquid velocities as well as higher fluid enthalpies. In CTF, equal void fraction distribution increase under nucleate-boiling heat transfer is observed in the constant mixing method as opposed to in the Rogers and Rosehart mixing method. This occurs due to the high user specified single mixing coefficient in the case of the former compared to the empirical-correlation-calculated single-mixing coefficient in the case of the latter. This results in equal fluid densities, fluid velocities, and fluid enthalpies between heater cells.

In FLOCAL, an almost equal void fraction distribution increase under nucleate-boiling heat transfer is observed in both the partial crossflow and crossflow methods. This occurs due to the minor contribution of energy transfer in the conservation equations between heater cells. This results in almost equal fluid densities, fluid velocities, and fluid enthalpies.

Between CTF and FLOCAL, only the void fraction distributions in the crossflow and the no-crossflow methods can be compared as the rest are not present in both codes. The crossflow method differs between both codes due to different nucleate-boiling correlations as observed through the delayed onsets of the void fraction distribution in CTF as opposed to in FLOCAL. The no-crossflow method remains identical between codes due to the exclusion of all fluid phenomena occurring between heater cells.

Departure from nucleate boiling ratio distributions is presented for the two subchannels to show similarities and differences in the methods available in both CTF and FLOCAL as observed in Figure 3.12.

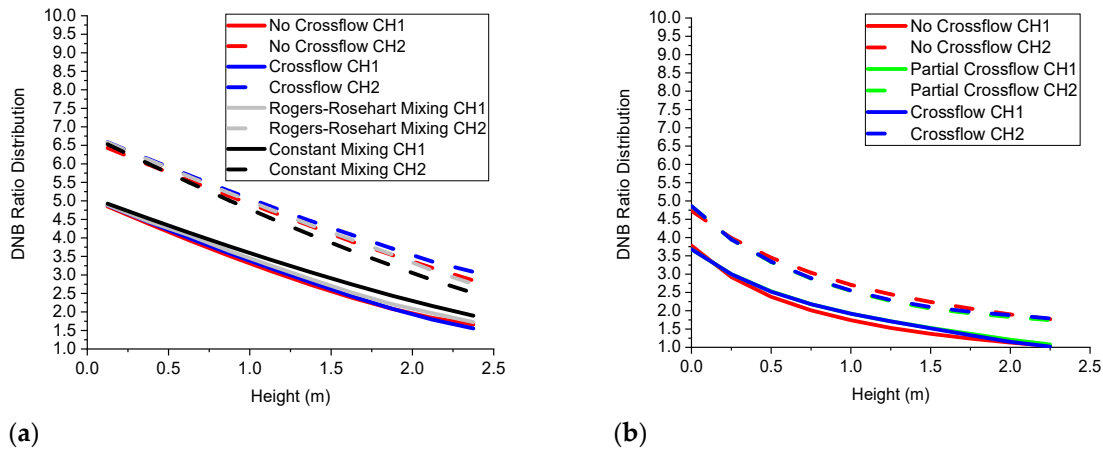


Figure 3.12. (a) CTF departure from nucleate boiling (DNB) axial distributions; (b) FLOCAL DNB axial distributions.

The departure from nucleate-boiling ratio distribution in CTF and FLOCAL is determined through the power distribution and the critical-heat-flux correlation, where the former is initially provided while the latter is obtained through an empirical correlation. No critical value occurs in any method both CTF and FLOCAL as the heat flux does not surpass the critical heat flux.

In both CTF and FLOCAL, a departure from nucleate-boiling ratio distribution decrease under all heat transfer regimes is observed in all the methods. The departure from nucleate-boiling ratio distribution in heater cell 1 decreases more due to its high power, low mass flux, and high pressure drop resulting in lower critical heat fluxes when compared to heater cell 2. The departure from nucleate-boiling ratio distribution in heater cell 2 decreases less due to its low power, high mass flux, and low pressure drop resulting on higher critical heat fluxes when compared to heater cell 1.

In both CTF and FLOCAL, a larger departure from nucleate-boiling ratio distribution decrease under all heat-transfer regimes is observed in the no-crossflow method compared to the crossflow method. This occurs due to the influence on the critical-heat-flux correlation of the absence in the conservation equations of mass, momentum, and energy transfer between heater cells via the mass-flux distributions and pressure drops. This results in lower critical-heat fluxes.

In CTF, a milder departure from nucleate-boiling ratio distribution decrease under all heat-transfer regimes is observed in the crossflow method as opposed to in the Rogers and Rosehart and the constant mixing methods. This occurs due to the influence on the critical-heat-flux correlation of the exclusion in the conservation equations of turbulent mixing and void drift between heater cells via the mass-flux distributions and pressure drops. This results in mildly lower critical-heat fluxes. In CTF, a more equal departure from nucleate-boiling ratio distribution decrease is observed in the constant mixing method as opposed to in the Rogers and Rosehart mixing method. This occurs due to the influence on the critical heat-flux correlation of the high user-specified single mixing coefficient in the case of the former compared to the empirical-correlation-calculated single mixing coefficient in the case of the latter via the mass-flux distributions and pressure drops. This results in more equal critical heat fluxes in both heater cells.

In FLOCAL, an almost equal departure from nucleate-boiling ratio distribution decrease rise under all heat-transfer regimes is observed in both the partial crossflow and crossflow methods. This occurs due to the minor influence on the critical heat-flux correlation of energy transfer in the conservation equations between heater cells. This results in less different critical heat fluxes between heater cells.

Between CTF and FLOCAL, only the departure from nucleate-boiling ratio distributions in the crossflow and the no-crossflow methods can be compared as the rest are not present in both codes. The crossflow method and no-crossflow method differ between both codes due to different critical heat-flux correlations as observed through the larger separation between the departure from nucleate-boiling distributions in CTF as opposed to in FLOCAL.

3.6. Conclusions

In terms of thermal hydraulics, the first objective in the aim of creating a coupling between CTF and DYN3D within the multiscale and multi-physics software development has been fulfilled by validating and verifying the accuracy in CTF and the methodology available in both CTF and FLOCAL.

Considering the CTF accuracy validation and verification performed through the replication of the PSBT benchmark. CTF provides accurate void fraction and critical power values with no significant tendency overall in the estimation when compared to the experimental data. The observed differences between the CTF results and the experimental data are due to reasons such as the gamma-ray transmission method as well as the nucleate-boiling model. The observed differences between the CTF results and the experimental data in the 5×5 bundle are also due to reasons such as the crossflow and mixing models as well as the thermocouples method and the critical heat-flux correlation. CTF provides small void fraction mean error and standard deviation values as well as accurate departure from nucleate boiling first occurrence height values when compared to other codes results. The observed differences between the CTF results and the other codes results are due to reasons such as the nature of the codes.

Considering the CTF and FLOCAL methodology verification performed through the replication of the FLOCAL developer benchmark. CTF and FLOCAL provide a wide range of methods for the void fraction and departure from nucleate-boiling ratio distributions. The observed differences in the CTF and FLOCAL results are due to reasons such as the exclusion in the conservation equations of mass, momentum, and energy transfer between heater cells, as well as the exclusion of different turbulent mixing and void drift between heater cells. The observed differences between the comparable CTF and FLOCAL results are due to reasons such as the different nucleate boiling and critical heat-flux correlations.

In general, CTF is a highly accurate code when compared to other codes which are less accurate or consume more time to achieve results. Therefore, CTF will be used to provide thermal hydraulics at the rod level within the multiscale and multi-physics software development. In general, CTF provides a wide range of crossflow and turbulent mixing methods when compared to FLOCAL where only the no-crossflow method is available. Therefore, CTF will be used to provide thermal hydraulics at the rod level in cases with more heterogeneous power distributions, while FLOCAL will be used to provide thermal hydraulics at both the assembly and rod levels in cases with more homogeneous power distributions.

3.7. Future Work

As mentioned before, the next objective in the aim of creating a coupling between the subchannel code CTF and the nodal code DYN3D within the multiscale and multi-physics software development consists of creating the initial stage in the coupling by allowing the exchange of power distributions from DYN3D to CTF to partially fulfil the connection between the CTF subchannel code block and the DYN3D nodal code block within the mentioned multiscale and multi-physics software development. Finally, the last objective in the aim of creating a coupling between the subchannel code CTF and the nodal code DYN3D coupling within multiscale and multi-physics software development will consist of creating the last stage in the coupling by not only allowing the exchange of power distributions from DYN3D to CTF, as well as the exchange of all the thermal-hydraulics distributions from CTF into the code coupling environment.

3.8. Nomenclature

The acronyms and symbols in the overall text have an associated meaning given in Table 3.10 and Table 3.11.

Table 3.10. Acronyms.

Acronym	Full Description
AGR	Advanced Gas Reactor
CASL	Consortium for Advanced Simulation of Light Water Reactors
CFD	Computational Fluid Dynamics
CTF/COBRA-TF	Coolant Boiling in Rod Arrays

DNB/DNBR	Departure from Nucleate Boiling Ratio
DYN3D (FLOCAL)/DYN3D	Dynamical 3-Dimensional Multigroup Thermal Hydraulics Module
FORTTRAN	Formula Translator
HTR	High Temperature Reactor
HZDR/FDR	Helmholtz Zentrum Dresden Rossendorf
LTS	Liverpool Transport Solver
LWR	Light Water Reactor
MAGNOX	Magnesium Oxide Gas Reactor
MV/NMV/SP	Mixing vane, non-mixing vane and simple spacers
MSR	Molten Salt Reactor
NCSU	North Carolina State University
NRC	Nuclear Regulation Commission
NUPEC	Nuclear Power Engineering Centre
NURESIM	Nuclear Reactor Simulator
PNL	Pacific Northwest Laboratories
PSBT	PWR Subchannel and Bundle Tests
PSU	Pennsylvania State University
PWR	Pressurised Water Reactor
SFR	Sodium Fast Reactor
UK	United Kingdom
UOL	University of Liverpool

Table 3.11. Symbols.

Symbol	Full Description
ρ_{clad}	Clad Density
$c_{p\ clad}$	Clad Specific Heat
k_{clad}	Clad Thermal Conductivity
T_c	Clad Temperature
$x_{t\ code}, x_{t\ exp}$	Code or Experimental Value
Δx_t	Difference between Code and Experimental Values per Test
$\Delta \bar{x}$	Average Difference between Code and Experimental Values for all Tests

Author Contributions: I: S.D. as the main author have written this article including the introduction, codes used in the validations and verifications, specifications and models used in the validations and verifications, results an analysis, conclusions, and future work. U.R. as the next author has provided FLOCAL as a result of him being the developer and has suggested the data used in the FLOCAL developer benchmark. D.L. as the next author has introduced the multiscale and multi-physics software development. B.M. and A.L. as the next authors and academic supervisors have provided help from theoretical and practical perspectives. P.B. as the next author and industrial supervisor has suggested the data used in the PSBT benchmark. A.D., S.A., and V.R. as the last authors and advisors have provided help from theoretical and practical perspectives. All authors have read and agreed to the published version of the journal article.

Funding: This research was funded by the EPSRC, EDF, and the UOL through the funding of the EPSRC grant “Innovative LWR Simulation Tool for the Nuclear Renaissance in the UK”, EPSRC grant number EP/R005850/1.

Institutional Review Board Statement: Not applicable.

Data Availability Statement: see the References.

Conflicts of Interest: The authors declare no conflict of interest. The funders had no role in the design of the study; in the collection, analyses, or interpretation of data; in the writing of the manuscript, or in the decision to publish the results.

3.9. Appendix A: PSBT Benchmark

The gamma-ray transmission method used to obtain experimental data composed both by CT (narrow gamma beam) as well as chordal (wide gamma beam) measurements of the fluid density can be observed in Figures 3.A1 and 3.A2.

Sub-channel Test

CT Measurement

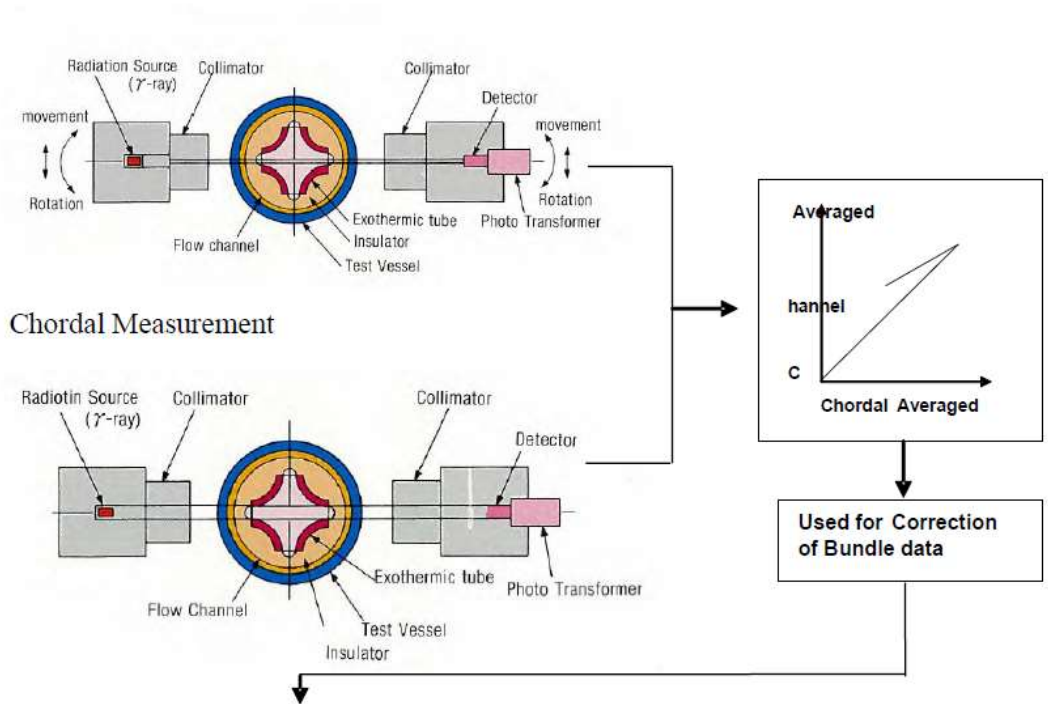
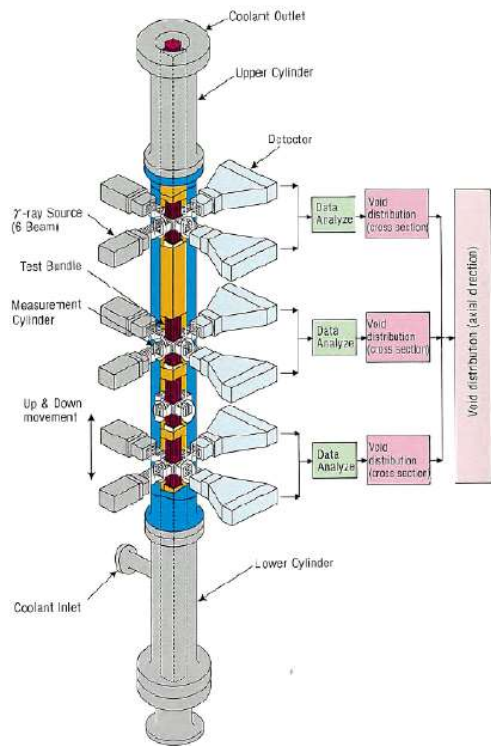


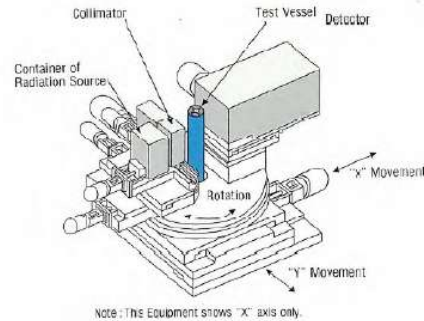
Figure 3.A1. Gamma-ray transmission method (subchannel).

Bundle Test



Void Measurement Equipment

Sub-channel Test



Bundle Test

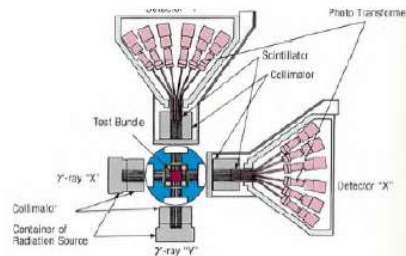


Figure 3.A2. Gamma-ray transmission method (bundle).

The system, subchannel, and CFD codes used to obtain other code results classified according to their associated participant and type in Table 3.12.

Table 3.12. Academic and industrial partners codes.

Participant	Code	Type
ANSYS	ANSYS	CFD
GRS	ANSYS-CFX	CFD
HZDR	ANSYS-CFX	CFD
EDF	NEPTUNE	CFD
ANL	STAR-CD	CFD
PSI	STAR-CD	CFD
EDF	THYC	Porous Media
JNES	CHAMP-ITA	Subchannel
PSI	FLICA	Subchannel
CEA-Saclay	FLICA-OVAP	Subchannel
McMaster	ASSERT-PV	Subchannel
KAERI	MATRA	Subchannel
NRI	VIPRE	Subchannel
WEC/INVAP	VIPRE	Subchannel
CSA	VIPRE	Subchannel
KIT	SUBCHANFLOW	Subchannel
Areva	F-COBRA-TF	Subchannel
UOL	CTF	Subchannel
PSI	TRACE	System
KTH	TRACE	System
UNIPI	CATHARE-2	System
IRSN	CATHARE-2	System

Equilibrium quality and density values are presented for the single subchannel at a single location (1.4 m). Linear fitting with interception at the origin has been performed to show the similarities and differences between CTF and the experimental values as observed in Figures 3.A3 and 3.A4.

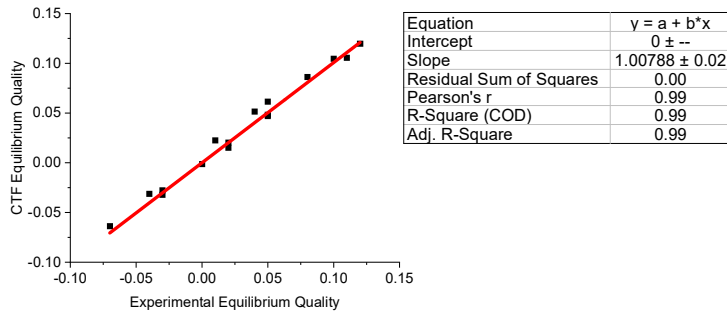


Figure 3.A3. CTF vs. experimental equilibrium quality.

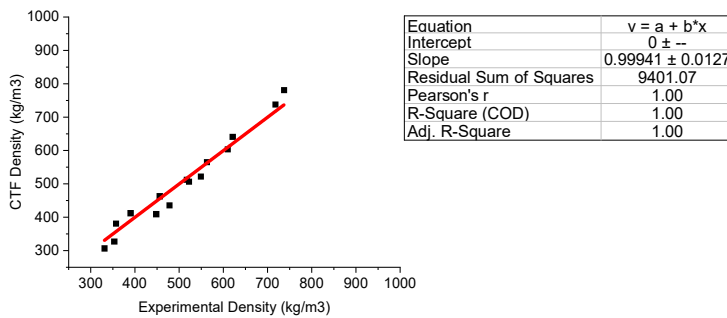


Figure 3.A4. CTF vs. experimental density.

Differences between the experimental and CTF equilibrium quality and density values at the mentioned axial location are small with no tendency in the estimation of the values. Several reasons were found to cause the observed differences between the CTF and the experimental data: The gamma-ray transmission method used underestimates density, as these experimental measurements were taken at the centres of subchannels instead of near the heated surfaces where lower densities occur under general LWR behaviour. The nucleate-boiling model used affects the equilibrium quality and density, as they may respond differently to the different initial and boundary conditions.

Equilibrium quality values are presented for the central subchannels at three different axial locations including a lower region (2.216 m) and an intermediate region (2.669 m), as well as an upper region (3.177 m). Linear fitting with interception at the origin has been performed to show the similarities and differences between CTF and the experimental values as observed in Figure 3.A5.

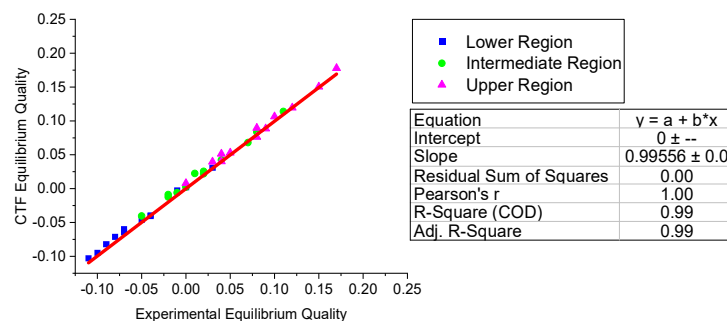


Figure 3.A5. CTF vs. experimental equilibrium quality.

Differences between the experimental and CTF equilibrium quality values at the three axial locations are small with slight overestimation of the lower region and intermediate region values and slight underestimation of the upper region values. Several reasons were found to cause the observed differences between the CTF and the experimental data: The gamma-ray transmission method used underestimates density, as these experimental measurements were taken at the centres of subchannels instead of near the heated surfaces where lower densities occur under general LWR behaviour. The nucleate-boiling model used affects the equilibrium quality as it may respond differently to the different initial and boundary conditions. The crossflow and mixing models used affect the equilibrium quality, codes which include crossflow as well as turbulent mixing models that achieve the best correlation between experimental measurements and code results.

3.10. Appendix B: FLOCAL Developer Benchmark

Mass-flux distributions are presented for the two subchannels to show similarities and differences in the methods available in both CTF and FLOCAL first for the power variation exercise and then for the mass-flux-blockage exercise as observed in Figures 3.A6 and 3.A7.

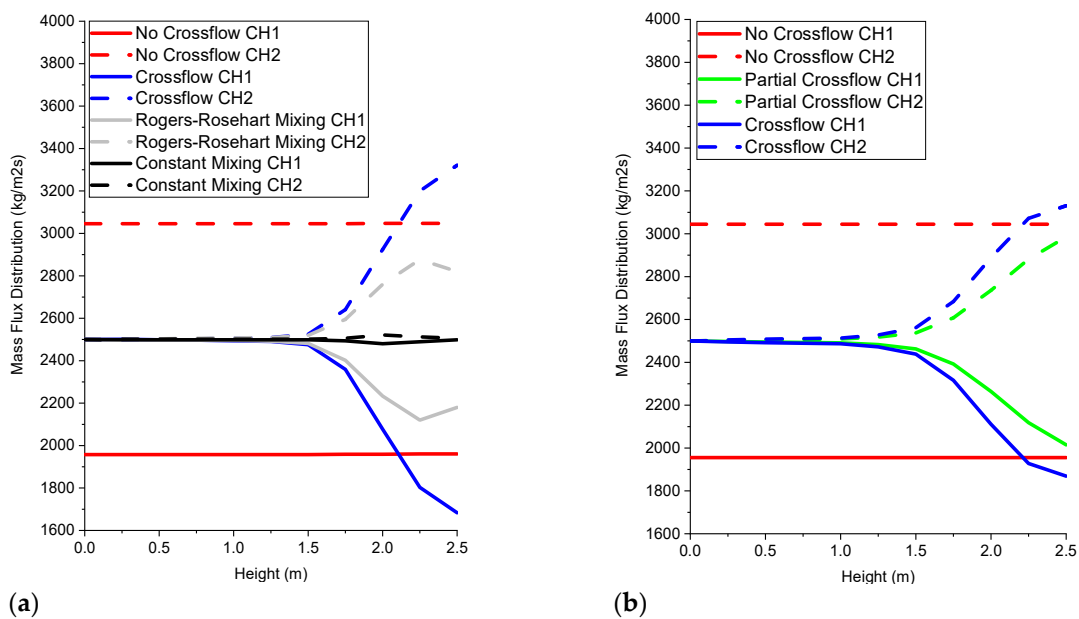


Figure 3.A6. (a) CTF mass-flux axial distributions; (b) FLOCAL mass-flux axial distributions.

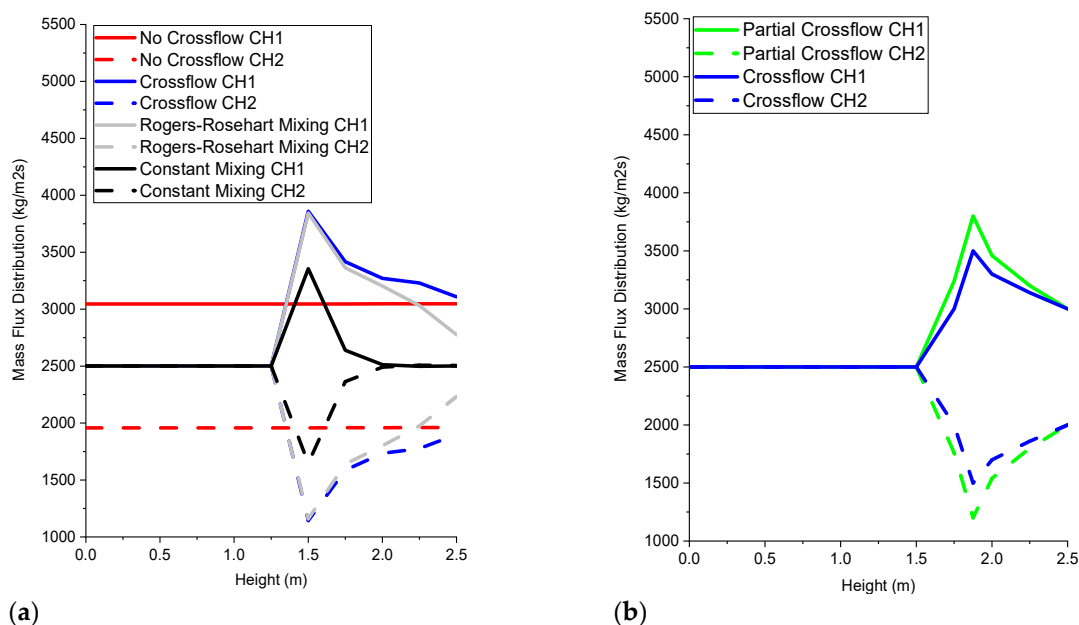


Figure 3.A7. (a) CTF mass-flux axial distributions; (b) FLOCAL mass-flux axial distributions.

The mass-flux distribution in CTF and FLOCAL is determined through both the fluid velocity and density distributions which are obtained mainly through the solution to both the mass and momentum equations. In the power variation exercise no redistribution occurs in all the different methods in CTF and FLOCAL apart from the no-crossflow method until the shift from single-phase heat transfer to nucleate-boiling heat transfer which occurs once the wall temperature surpasses the fluid saturation temperature. In the mass-flux-blockage exercise no redistribution occurs in all the different methods in CTF and FLOCAL apart from the no-crossflow method until the shift from single-phase heat transfer to nucleate-boiling heat transfer which occurs once the wall temperature surpasses the fluid saturation temperature.

In both CTF and FLOCAL, mass-flux redistribution under nucleate-boiling heat transfer is observed in most methods. In the power variation exercise, the mass-flux distribution in heater cell 1 decreases due its high power resulting on higher vapor and lower liquid velocities as well as lower fluid densities when compared to heater cell 2. In the power variation exercise, the mass flux distribution in heater cell 2 increases due to its low power losses resulting on lower vapor and higher liquid velocities as well as higher fluid densities when compared to heater cell 1. In the mass-flux-blockage exercise, the mass-flux distribution in heater cell 1 increases due to the absence of a pseudospacer resulting on lower vapor and higher liquid velocities as well as higher fluid densities when compared to heater cell 2. In the mass-flux-blockage exercise the mass-flux distribution in heater cell 2 decreases due to the presence of the pseudo spacer resulting on higher vapor and lower liquid velocities, as well as lower fluid densities when compared to heater cell 1.

In both CTF and FLOCAL, mass-flux redistribution under nucleate-boiling heat transfer is observed in the crossflow method as opposed to in the no-crossflow method. This occurs in both exercises due to the allowance in the conservation equations of mass, momentum, and energy transfer between heater cells. This results in nonconstant vapor and liquid velocities as well as fluid densities in both heater cells.

In CTF, a more homogeneous mass-flux redistribution under nucleate boiling is observed in the Rogers and Rosehart and the constant mixing methods as opposed to in the crossflow method. This occurs in both exercises due to the allowance in the conservation equations of turbulent mixing and void drift between heater cells. This results in more homogeneous vapor and liquid velocities as well as fluid densities in both heater cells. In CTF, an almost equal mass-flux redistribution under nucleate-boiling heat transfer is observed in the constant mixing method as opposed to in the Rogers and Rosehart mixing method. This occurs in both exercises due to the high user-specified single mixing coefficient in the case of the former compared to the empirical correlation calculated single mixing coefficient in the case of the latter. This results in almost equal vapor and liquid velocities as well as fluid densities in both heater cells.

In FLOCAL, a lower mass-flux redistribution under nucleate boiling is observed in the partial-crossflow method as opposed to in the crossflow method. This occurs in both exercises due to the exclusion of energy transfer in the conservation equations between heater cells. This results in less different vapor and liquid velocities as well as fluid densities between heater cells.

Between CTF and FLOCAL, only the mass-flux distributions in the no-crossflow and the crossflow methods can be compared as the rest are not present in both codes. The no-crossflow method remains identical between both codes resulting from the exclusion of all fluid phenomena occurring between heater cells. The crossflow method differs between codes due to the different mass and momentum transfer models between heater cells as observed through the further divergence of the mass-flow distribution in CTF compared to FLOCAL.

Coolant-temperature distributions are presented for the two subchannels to show similarities and differences in the methods available in both CTF and FLOCAL as observed in Figure 3.A8.

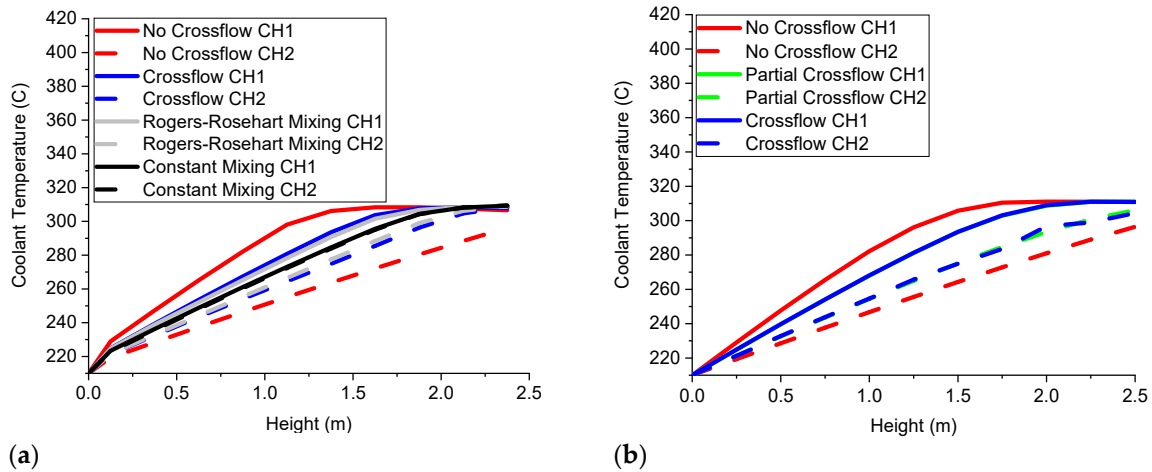


Figure 3.A8. (a) CTF coolant-temperature axial distributions; (b) FLOCAL coolant-temperature axial distributions.

The coolant-temperature distribution in CTF and FLOCAL is determined through the fluid enthalpy distribution which is obtained through the solution to the energy equation. The values increase in all methods in both CTF and FLOCAL under both single-phase heat transfer and subcooled boiling and begins to stabilize as it approaches saturated boiling with both types of boiling conforming nucleate boiling where the latter would occur if the fluid temperature equals its saturation temperature.

In both CTF and FLOCAL, a coolant-temperature distribution increase under nucleate-boiling heat transfer is observed in all the methods. The coolant-temperature distribution in heater cell 1 increases more due its high power resulting on higher fluid enthalpies when compared to heater cell 2. The coolant temperature distribution in heater cell 2 increases less due its low power resulting on lower fluid enthalpies when compared to heater cell 1.

In both CTF and FLOCAL, a faster coolant-temperature distribution increase under nucleate-boiling heat transfer is observed in the no-crossflow method compared to the crossflow method. This occurs due to the exclusion in the conservation equations of mass, momentum, and energy transfer between heater cells. This results in higher fluid enthalpies.

In CTF, a slightly faster coolant-temperature distribution increase under nucleate-boiling heat transfer is observed in the crossflow method as opposed to in the Rogers and Rosehart and the constant mixing methods. This occurs due to the exclusion in the conservation equations of turbulent mixing and void drift between heater cells. This results in higher fluid enthalpies. In CTF, unequally fast coolant-temperature distribution increase under nucleate-boiling heat transfer is observed in the Rogers and Rosehart mixing method as opposed to in the constant mixing method. This occurs due to the empirical-correlation-calculated single mixing coefficient in the case of the former compared to the high user-specified single mixing coefficient in the case of the latter. This results in unequal fluid enthalpies in both heater cells.

In FLOCAL, almost equally fast coolant-temperature distribution increase under nucleate-boiling heat transfer is observed in both the partial-crossflow and crossflow methods. This occurs due to the minor contribution of energy transfer in the conservation equations between heater cells. This results in almost identical fluid enthalpies between heater cells.

Between CTF and FLOCAL, only the coolant-temperature distributions in the crossflow and the no-crossflow methods can be compared as the rest are not present in both codes. The crossflow method differs between both codes due to the energy-transfer models between heater cells as observed through the different top values of the coolant temperature distribution in CTF as opposed to in FLOCAL. The no-crossflow method remains identical between codes due to the exclusion of all fluid phenomena occurring between heater cells.

3.11. References

1. Duderstadt, J.J.; Hamilton, L.J. Nuclear Reactor Analysis; John Wiley & Sons, Ed.; Department of Nuclear Engineering, The University of Michigan: Ann Arbor, MI, USA, 1975.

2. Ahlin, A.; Edenius, M. CASMO: A Fast Transport Theory Assembly Depletion Code for LWR Analysis. *Trans. Am. Nucl. Soc. IAEA* 1977, 26, RN:8347766.
3. Ahlin, A.; Edenius, M. CASMO-2 for Generation of Effective pdq Cross Sections. *Trans. Am. Nucl. Soc. IAEA* 1982, 14, RN:14776775.
4. Bestion, D. System Code Models and Capabilities. THICKET 2008, Session II, 26.
5. Bajorek, S.M.; Bernard, M.; Gingrich, C.; Hoxie, C.L.; Ireland, A.; Kelly, J.; Mahaffy, J.; Murray, C.; Spore, J.; Staudenmeier, J.; et al. Development, Validation and Assessment of the Trace Thermal Hydraulics System Code. In *Proceedings of the 16th International Topical Meeting on Nuclear Reactor Thermal Hydraulics*, Chicago, IL, USA, 30 August–4 September 2015; Volume 14.
6. Moorthi, A.; Kumar, A.; Velusamy, K. A review of sub-channel thermal hydraulic codes for nuclear reactor core and future directions. *Nucl. Eng. Des.* 2018, 332, 329–344, doi:10.1016/j.nucengdes.2018.03.012.
7. Srikantiah, G.S. VIPRE—A Reactor Core Thermal-Hydraulics Analysis Code for Utility Applications. *Nucl. Tehnol.* 2017, 5450, 216–227, doi:10.13182/NT92-A34744.
8. Höhne, T.; Krepper, E.; Rohde, U. Application of CFD Codes in Nuclear Reactor Safety Analysis. *Hindawi* 2010, 2010, doi:10.1155/2010/198758.
9. Podila, K.; Rao, Y.F. A Comparative Study of the Commercial CFD Codes to Simulate Nuclear Fuel Bundles; Ontario, Canada, IAEA 2015, RN:49103678.
10. Hall, S.K. The Development of a Nodal Method for the Analysis of PWR Cores with Advanced Fuels; Imperial College of London: London, UK, 2013.
11. EDF UK PANTHER: PWR AGR Neutronics Thermal Hydraulics Evaluation Route. Available online: <https://www.answerssoftwareservice.com/panther/> (23/02/2021).
12. Szilard, R.; Zhang, H.; Brian Kothe, D.; Turinsky, P. CASL The Consortium for Advanced Simulation of Light Water Reactors; INL 2011, INL/CON-11-22917.
13. US Department of Energy CASL Consortium for Advanced Simulation of Light Water Reactors. Available online: <https://casl.gov/> (23/02/2021).
14. Chauliac, C.; Aragones, J.; Bestion, D.; Weiss, F. NURESIM—A European simulation platform for nuclear reactor safety: Multi-scale and multi-physics calculations, sensitivity and uncertainty analysis. *Elsevier* 2011, 241, 3416–3426.
15. Euratom NURESIM Nuclear Reactor Safety Simulation Platform. Available online: <https://cordis.europa.eu/project/id/323263> (23/02/2021).
16. Merk, B.; Bankhead, M.; Litskevich, D.; Gregg, R.; Peakman, A.; Shearer, C. On a Roadmap for Future Industrial Nuclear Reactor Core Simulation in the U.K. to Support the Nuclear Renaissance. *Energies* 2018, 11, 3509, doi:10.3390/en11123509.
17. Litskevich, D.; Atkinson, S.; Davies, S. Verification of the current coupling collision probability method with orthogonal flux expansion for the assembly calculations. *Prog. Nucl. Energy* 2020, 130, doi:10.1016/j.pnucene.2020.103562.
18. Kucukboyaci, V.; Salko, R. COBRA-TF Parallelization and Application to PWR Reactor Core. In *Proceedings of the Joint International Conference on Mathematics and Computation*, Nashville, TN, USA, 19–23 April 2015, doi:10.13140/RG.2.1.1247.6962.
19. Rohde, U.; Kliem, S.; Grundmann, U.; Baier, S.; Bilodid, Y.; Duerigen, S.; Fridman, E.; Gommlich, A.; Grahn, A.; Holt, L.; et al. Progress in Nuclear Energy The reactor dynamics code DYN3D e models, validation and applications. *Prog. Nucl. Energy* 2016, 89, 170–190, doi:10.1016/j.pnucene.2016.02.013.
20. Jackson, P.; Turnbull, J.. Enigma Fuel Performance Code. *Nucl. Energy* 1990, 21, 107–114.
21. Patelli, E. COSSAN: A Multidisciplinary Software Suite for Uncertainty Quantification and Risk Management; Springer 2017, ISBN 9783319123851, doi:10.1007/978-3-319-12385-1.
22. Zhao, X.; Wysocki, A.J.; Shirvan, K.; Salko, R.K. Assessment of the Subchannel Code CTF for Single- and Two-Phase Flows. 2019, 205, 338–351, doi:10.1080/00295450.2018.1507221.
23. Duerigen, S.; Rohde, U.; Bilodid, Y.; Mittag, S. The reactor dynamics code DYN3D and its trigonal-geometry nodal diffusion model. *Kerntechnik* 2013, 78, 310–318, doi:10.3139/124.110382.

24. Salko Jr, R.; Avramova, M.; Wysocki, A.; Hu, J.; Toptan, A.; Porter, N.; Blyth, T.S. CTF User Manual; OSTI, Oak Ridge, TN, USA, 2020; 1550748.
25. Salko Jr, R.; Avramova, M.; Wysocki, A.; Hu, J.; Toptan, A.; Porter, N.; Blyth, T.S. CTF Theory Manual; 2019; OSTI, Oak Ridge, TN, USA, 2020, doi:10.2172/1550750.
26. Grundmann, U.; Rohde, U.; Mittag, S.; Kliem, S. The reactor dynamics code DYN3D—Models, validation and applications. *Prog. Nucl. Energy* 2016, 89, 140, doi:10.1016/j.pnucene.2016.02.013.
27. Grundmann, U.; Rohde, U. The Code DYN3D/M2 for the Calculation of Reactivity Initiated Transients in Light Water Reactors with Hexagonal Fuel Elements—Code Manual and Input Data Description; Helmholtz-Zentrum Dresden-Rossendorf: Dresden, Germany, 2012.
28. Japan Energy Safety Organisation. Benchmark Based on NUPEC PWR Subchannel and Bundle Tests (PSBT): Assembly Specifications and Benchmark Database; 2009; JNES, Volume JNES/SAE-T.
29. Rubin, A.; Schoedel, A.; Avramova, M. Benchmark Based on NUPEC PWR Sub-Channel and Bundle Test (PSBT) Volume I Experimental Database and Final Problem Specifications; OECD 2012; Volume I.
30. Rubin, A.; Avramova, M.; Velazquez-Lozada, A. International Benchmark on Pressurised Water Reactor Sub-channel and Bundle Tests Volume II: Benchmark Results of Phase I—Void Distribution; OECD 2015; Volume II.
31. Rubin, A.; Avramova, M.; Velazquez-Lozada, A. Pressurised Water Reactor Sub-Channel and Bundle Tests Volume III: Departure from International Benchmark on; OECD 2015; Volume III.
32. Thorn, B.J.R.S.; Walkert, W.M.; Fallon, T.A.; Reising, G.F.S. Boiling in Subcooled Water During Flow up Heated Tubes or Annuli. 1965, 180, 226–246, doi:10.1243/PIME_CONF_1965_180_117_02.
33. Tong, L.S. Prediction of Departure from Nucleate Boiling for an Axially Non-Uniform Heat Flux Distribution. *J. Nucl. Energy* 1967, 21, 221–248, doi:10.1016/S0022-3107(67)90054-8.
34. Tong, L. Boiling Crisis and Critical Heat Flux; IAEA, Pittsburgh, PA, USA, 1972, RN:4051410
35. Beus, S. Two Phase Turbulent Mixing Model for Flow in Rod Bundles; OSTI, Pittsburgh, PA, USA, 1972; 4656469.
36. McAdams, W. Heat Transmission, 1st ed.; Pub, K., Ed.; McGraw-Hill: New York, NY, USA, 1985; ISBN 0898748763.
37. Poljanin, L.; Ibragimov, M. Teploobmen v jadernikh reaktorakh. Ehnergoizdat 1982, Moscow, USSR, 296.
38. Bezrukov, Yu; Astakhov, V. Experimental investigation and static analysis of data on crisis of heat exchange in beams of rods for WWER reactors. *Teploehnergetika* 1976, Moscow, USSR, 8, 80–82.
39. Osmachkin, V.; Borisov, V. The hydraulic resistance of fuel rod bundles in a boiling water flow. IAEA 1970, 2, 24.
40. Rogers, J.T.; Rosehart, R.G. Mixing by Turbulent Interchange in Fuel Bundles. *Correlations and Interfaces*. ASME 1972, 72-HT-53.

Chapter 4: One Way Coupling of a Nodal Code and a Subchannel Code

Simplified coupled reactor physics are generally available in DYN3D at the fuel pin level after performing fuel pin power reconstruction. Alternatively, simplified coupled reactor physics can also become available in DYN3D at the fuel pin level after performing fuel pin homogenization. Partially improved coupled reactor physics have become available in the DYN3D and CTF coupling after transferring the power distributions from the former to the latter. Hence, a verification of the inner coupling iterations within an outer coupling iteration in the DYN3D and CTF coupling has been performed through the KAIST benchmark.

The KAIST-1A benchmark [151] is a less verified benchmark than the PSBT benchmark by KAIST (Korean Advanced Institute of Science & Technology) for PWR neutronics and thermal hydraulics previously tested using other neutronics codes but not using other neutronics and thermal hydraulics codes [152,153]. It includes a multi-parameter variation exercise that contains two 17x17 fuel assemblies with fuel pins, guide tubes, without or with burnable absorber pins, spacer grids and several boundary conditions. Cross sections have been generated in SCALE-POLARIS through methods such as ESSM and MOC for two energy groups. The 17x17 fuel assemblies in DYN3D and CTF have been simulated through methods such as the meshes, two energy groups, NEM, reflection, either channel or subchannel, friction and form pressure losses, nucleate boiling, DNB and only in CTF crossflow and turbulent mixing. The mentioned benchmark has been applied together with coupling scripts.

Coupling scripts for the DYN3D and CTF coupling have been created for the transfer of the power distributions from the former to the latter and transfer of feedback distributions from the latter to the former. Such transfer includes the extraction, normalisation, and importation of the power distributions from DYN3D to CTF and the extraction, and conversion from subchannel to fuel cell of the feedback distributions from CTF to DYN3D. However, only the transfer of power distributions has been performed in the inner coupling iterations, with convergence occurring only in each individual nuclear code. A graphical abstract for this chapter can be seen in Figure 4.GA.

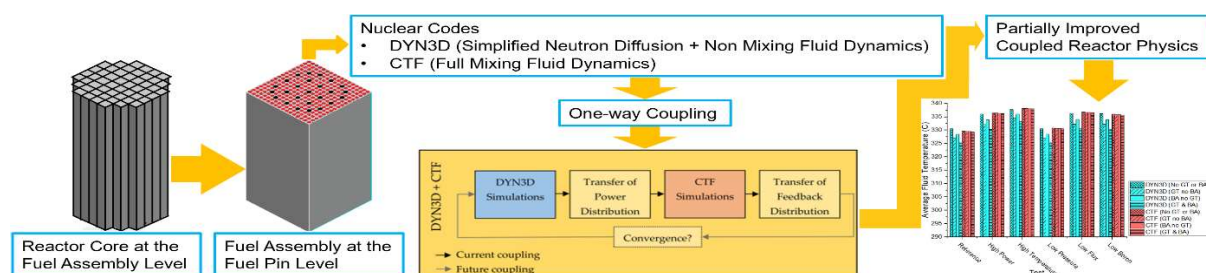


Figure 4.GA. Chapter 4 graphical abstract.

The verification of the inner coupling iterations within an outer coupling iteration in the DYN3D and CTF coupling, when compared to DYN3D, has shown differences in the fluid density and temperature, fuel temperature and pressure drop values and distributions in the 17x17 fuel assemblies. Fluid density and temperature, fuel temperature and pressure drop differences between fuel assemblies occurred due to the presence of burnable absorbers in one of them. Also, fluid density and temperature, fuel temperature and pressure drop differences between the reference and other tests occurred due to the variation of the boundary conditions. Finally, fluid density and temperature, fuel temperature and pressure drop differences between fuel cells occurred due to methods such as the channel or subchannel, evaporation, nucleate boiling, fuel rod, friction and form pressure losses, and the absence or presence of crossflow and turbulent mixing.

Therefore, this verification has proven that the DYN3D and CTF coupling provides improved feedback distributions using 1 processor within computational times of 20 minutes, which justifies its use to provide improved coupled reactor physics at the fuel pin level. Also, this verification has proven that DYN3D provides simplified feedback distributions using 1 processor within computational times of 2 minutes, which justifies its use to provide simplified coupled reactor physics at the fuel assembly or fuel pin level. This chapter includes the journal article DYN3D and CTF Coupling within a Multiscale and Multiphysics Software Development (Part I) [154], published in the MDPI Journal of Energies. All author contributions can be found in the list of publications section.

DYN3D and CTF Coupling within a Multiscale and Multiphysics Software Development (Part I)

Sebastian Davies ^{1,*}, Dzianis Litskevich ¹, Ulrich Rohde ², Anna Detkina ¹, Bruno Merk ¹, Paul Bryce ³, Andrew Levers ¹ and Venkata Ravindra ¹

1 School of Engineering, University of Liverpool, Liverpool L69 3GH, UK; dzianis@liverpool.ac.uk (D.L.); a.detkina@liverpool.ac.uk (A.D.); merk@liverpool.ac.uk (B.M.); alevs@liverpool.ac.uk (A.L.); venkat@liverpool.ac.uk (V.R.)

2 Institute of Innovation, Helmholtz Zentrum Dresden Rossendorf, 01328 Dresden, Germany; u.rohde@hzdr.de

3 EDF Energy, Gloucester GL4 3R, UK; paul.bryce@edf-energy.com

* Correspondence: s.r.davies@liverpool.ac.uk; Tel.: +44-750-2270-482

Received: 16 May 2021; Accepted: 10 August 2021; Published: 13 August 2021

Abstract: Understanding and optimizing the relation between nuclear reactor components or physical phenomena allows us to improve the economics and safety of nuclear reactors, deliver new nuclear reactor designs, and educate nuclear staff. Such relation in the case of the reactor core is described by coupled reactor physics as heat transfer depends on energy production while energy production depends on heat transfer with almost none of the available codes providing full coupled reactor physics at the fuel pin level. A Multiscale and Multiphysics nuclear software development between NURESIM and CASL for LWRs has been proposed for the UK. Improved coupled reactor physics at the fuel pin level can be simulated through coupling nodal codes such as DYN3D as well as subchannel codes such as CTF. In this journal article, the first part of the DYN3D and CTF coupling within the Multiscale and Multiphysics software development is presented to evaluate all inner iterations within one outer iteration to provide partially verified improved coupled reactor physics at the fuel pin level. Such verification has proven that the DYN3D and CTF coupling provides improved feedback distributions over the DYN3D coupling as crossflow and turbulent mixing are present in the former.

Keywords: nuclear reactor; coupled reactor physics; nodal code; subchannel code; DYN3D; CTF; KAIST

4.1. Introduction

Globally, the use of nuclear power has expanded to 31 countries with 443 nuclear reactors operating and 52 nuclear reactors under construction, which have made nuclear power become the second largest source of carbon free power [1]. Around 80% of the nuclear reactors are LWR (Light Water Reactor) which provide improved economics and safety when compared to previous nuclear reactors [2] by: Simplifying the nuclear reactor design as there is no distinction between the coolant and moderator. Decreasing the nuclear reactor size as the high moderation allows yielding a certain power density while using less fuel and the high cooling allows to keep a certain power density, while using a compact design. Increasing the nuclear reactor stability as the high moderation decreases with high power leading to a reduction in the criticality and the high cooling increases with the high fluid density, which leads to a reduction in the temperatures. Increasing the nuclear reactor efficiency as the high moderation allows achieving a high fuel burn up or utilisation and the high cooling allows to achieve a high heat conductance.

In the UK, there is currently great interest in LWR as can be observed through the different projects that are being funded across the country including both the construction of new nuclear reactors to provide power to the future generations [3] as well as the development of a nuclear innovation programme [4] to improve the economics and safety of nuclear reactors, deliver new nuclear reactor designs, and educate nuclear staff. Large nuclear reactors currently considered include the EPR

(European Pressurised Reactor) by Areva for HPC (Hinkley Point C) and Sizewell C [5], with each nuclear reactor providing 1650 MW of power for a period of 60 years. Small nuclear reactors currently considered include the AMR (Advanced Modular Reactor) by Rolls Royce for remote sites [6] with each nuclear reactor providing 440 MW of power for a large period. The nuclear innovation programme was approved by BEIS (Department of Business, Energy, and Industrial Strategy) in 2016 with support from different academic and industrial partners across the UK, which will invest over 460 million pounds over the following years. It is structured into advanced fuels, advanced manufacturing and materials, advanced reactor design, and recycle and reprocess, providing innovation across the whole nuclear fuel cycle. A project within the advanced reactor design known as DRD (Digital Reactor Design) [7] is being developed by different academic and industrial partners across the UK to deliver virtual replicas of nuclear reactors, providing innovation from a computational perspective.

It is important to understand the relation between components or physical phenomena in a LWR to improve the economics and safety of nuclear reactors, deliver new nuclear reactor designs, and educate nuclear staff by acknowledging the physical phenomena that take place [8,9] including the energy production analysed using neutronics, the heat and mass transfer analysed using thermal hydraulics, the fuel behaviour analysed using thermo-mechanics, and risks analysed using probability analysis. The neutronics, thermal hydraulics, thermo-mechanics, and probability analysis are said to be coupled to each other in the following ways: The power production in the nuclear reactor depends both on the heat and mass transfer through the fuel, moderator temperatures, and the moderator density, leading to reactivity feedback as well as on the fuel behaviour through the fuel burnup, which leads to cross section changes. The heat and mass transfer in the nuclear reactor depends both on the power production through the fission chain reaction, leading to heat deposition as well as on the fuel behaviour through the fuel burnup, which leads to thermal conductivity and specific heat changes. The fuel behaviour in the nuclear reactor depends both on the power production through irradiation, leading to fuel integrity changes, and on the heat and mass transfer through the fuel temperature, which also leads to fuel integrity changes. The risks in the nuclear reactor depend both on the power production through the heat deposition, which may lead to melting in the fuel as well as on the heat and mass transfer through the clad temperature, which may lead to DNB (Departure from Nucleate Boiling).

It is important to optimize the relation between components or physical phenomena in a LWR to improve the economics and safety of nuclear reactors, deliver new nuclear reactor designs, and educate nuclear staff by simulating the physical phenomena that take place [10–12] including the neutronics simulated using lattice, neutron transport, and nodal codes [13–19], the thermal hydraulics simulated using system, nodal, subchannel and CFD codes [17–22], the thermo-mechanics simulated using fuel performance codes [23–25], and the probability analysis simulated using risk assessment codes [26]. None of the mentioned codes provide full coupled reactor physics at the fuel pin level due to computational limitations that existed during the times when these codes were originally developed, which resulted from the geometry complexity, the large number of fuel pins, the coupled physical phenomena, and the large simulation times. Only nodal codes provide simplified coupled reactor physics at the fuel assembly level after performing fuel assembly homogenisation, where average fuel assembly cross sections are derived from fuel pin cross sections. Some nodal codes provide simplified coupled reactor physics at the fuel pin level after performing fuel pin reconstruction, where fuel pin power distributions are derived from additional shaping functions. Both fuel assembly homogenisation and fuel pin power reconstruction are limited in terms of coupling due to the loss of coupled physical phenomena, which has led to safety parameters being based on simplified coupled reactor physics at the fuel assembly level, rather than being based on full coupled reactor physics at the fuel pin level, resulting in the imposition of extra safety margins both in nuclear reactor operation and design.

Current state-of-the-art simulation codes that aim to provide full or improved coupled reactor physics at the fuel pin level for LWR include NURESIM (Nuclear Reactor Simulator) [27,28] and CASL (Consortium for Advanced Simulation of LWR) [29,30]. NURESIM is a development by Euratom, that aimed to provide full coupled reactor physics at the fuel pin level, although computational limitations led to the development of a simplification known as SALOME [31], which has the aim of providing improved coupled reactor physics at the fuel pin level by using lattice codes such as APOLLO2 [32] to provide the fuel assembly homogenisation required in nodal codes. Nodal codes such as COBAYA3,

CRONOS2 [33], and DYN3D (Dynamical 3 Dimensional) [34] provide simplified coupled reactor physics at the fuel assembly level and the fuel pin power reconstruction required for simplified coupled reactor physics at the fuel pin level as well as the boundary conditions used in other codes. CFD and subchannel codes such as TRIO_U [35], SUBCHANFLOW [36], FLICA4 [37], NEPTUNE [38], and TransAT [39] provide full thermal hydraulics at the fuel pin level and the boundary conditions used in other codes. System codes such as CATHARE (Code for Analysis of Thermal Hydraulics during an Accident of Reactor and Safety Evaluation) [40] and ATHLET (Analysis of Thermal Hydraulics of Leaks and Transients) [41] provide simplified thermal hydraulics at the nuclear power plant level and the boundary conditions used in other codes. Finally, fuel performance codes such as DRACCAR [42] and SCANAIR (Systems of Codes for Analysing Reactivity Initiated Accidents) [43] provide full thermo-mechanics at the fuel pin level and the boundary conditions used in other codes. CASL is a development by the USDE (United States Department of Energy), that aimed to provide improved coupled reactor physics at the fuel pin level, although solution requirements led to a new development known as CASL-Advanced [44], which has the aim of providing full coupled reactor physics at the fuel pin level by using spectral codes such as ORIGEN [45] and SCALE [46] to provide the fuel pin cross sections required in neutron transport codes. Neutron transport codes such as MPACT [47], INSILICO [48], and SHIFT [49] provide full neutronics at the fuel pin level and the boundary conditions used in other codes. CFD and subchannel codes such as CTF (Coolant Boiling in Rod Arrays Three Flow Fields) [50] and HYDRA-TH [51] provide full thermal hydraulics at the fuel pin level and the boundary conditions used in other codes. System codes such as RELAP5 (Reactor Excursion and Leak Analysis Program) [52] provide simplified thermal hydraulics at the nuclear power plant level and the boundary conditions used in other codes. Finally, fuel performance codes such as BISON provide full thermo-mechanics at the fuel pin level and the boundary conditions used in other codes. SALOME is not adequate for the UK as it neglects full coupled reactor physics at the fuel pin level with lattice codes only being used to provide the fuel assembly homogenisation required in nodal codes, while CASL-Advanced is not affordable by the UK as it extends introduces computational limitations through the extension of full coupled reactor physics at the fuel pin level to all the reactor core. All the codes can be found classified in the Appendix A.

Another project within the nuclear innovation programme between NURESIM and CASL known as Multiscale and Multiphysics Software Development is a development by the UOL (University of Liverpool) [53] which has the aim of providing both improved and full coupled reactor physics at the fuel pin level for LWR while remaining both adequate for the UK as well as affordable by the UK by using spectral codes such as SCALE [15,54] to provide both the fuel pin cross sections required in neutron transport codes and the fuel assembly homogenisation required in nodal codes. Nodal codes such as DYN3D [17,34] provide simplified coupled reactor physics at the fuel assembly level and the fuel pin power reconstruction required for simplified coupled reactor physics at the fuel pin level as well as the boundary conditions used in other codes. Neutron transport codes such as LOTUS [14,55] (Liverpool Transport Solver) provide full neutronics at the fuel pin level and the boundary conditions used in other codes. Subchannel codes such as CTF [20,50] provide full thermal hydraulics at the fuel pin level and the boundary conditions used in other codes. System codes such as RELAP5 [52] provide simplified thermal hydraulics at the nuclear power plant level and the boundary conditions used in other codes. Finally, fuel performance codes such as ENIGMA [56] provide full thermo-mechanics at the fuel pin level and the boundary conditions used in other codes. This Multiscale and Multiphysics Software Development will be adequate for the UK as it provides full coupled reactor physics at the fuel pin level with neutron transport codes being used to provide full neutronics at the fuel pin level and will be affordable by the UK as it reduces computational limitations through the restriction of full coupled reactor physics at the fuel pin level only to the fuel assemblies of interest in the reactor core.

The coupling between any two of the mentioned codes [57,58] within the Multiscale and Multiphysics Software Development involves several steps such as simulations using the first code, the transfer of data from the first code to the second code, simulations using the second code, and finally the transfer of data from the second code to the first code. Each of these coupling steps conform to an inner iteration while all coupling steps conform to an outer iteration with outer iterations being run on a cyclic basis until some convergence criterion is verified, which usually consists of a comparison

between the current and the previous outer iterations. The coupling between any two of the mentioned codes can be external, internal, and in parallel, which implies different levels of coupling integration [59]. In external coupling, both codes are run separately, and the transfer of data is done using additional scripts, apart from both codes. In internal coupling, both codes are run separately, and the transfer of data is done using additional internal libraries within the codes themselves. In parallel coupling, both codes are run simultaneously, and the transfer of data is done using additional internal libraries within the codes themselves. The mentioned types of coupling between any two of the mentioned codes within the Multiscale and Multiphysics Software Development can be observed in Figure 4.1.

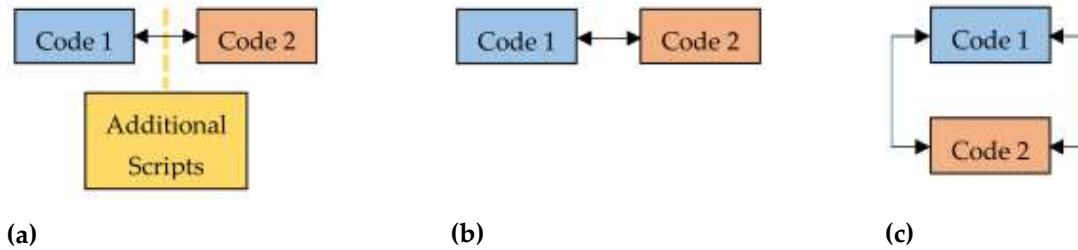


Figure 4.1. (a) External coupling. (b) internal coupling. (c) parallel coupling.

The aim consists of coupling the nodal code DYN3D and the subchannel code CTF within the Multiscale and Multiphysics Software Development to provide improved coupled reactor physics at the fuel pin level [53]. The previous objective to achieve this aim consisted of CTF and FLOCAL (thermal hydraulics module of DYN3D) thermal hydraulics validations and verifications [20] that were performed to evaluate the accuracy and methodology available to provide thermal hydraulics at the fuel pin level. CTF was observed to provide high accuracy when compared to other fluid dynamics codes, allowing the justification as to why CTF was chosen to provide full thermal hydraulics at the fuel pin level in this Multiscale and Multiphysics Software Development. CTF was observed to provide a wide range of crossflow and turbulent mixing methods while FLOCAL was observed to provide only the no crossflow method, allowing us to justify why CTF should be used to provide full thermal hydraulics at the fuel pin level in cases with more heterogeneous power distributions and why FLOCAL should be used to provide simplified thermal hydraulics at the fuel pin level in cases with more homogeneous power distributions in this Multiscale and Multiphysics Software Development.

The current objective in achieving this aim consists of the first part of the DYN3D and CTF coupling, which was performed to evaluate all inner iterations within an outer iteration to provide partially verified improved coupled reactor physics at the fuel pin level, where the NK (neutronics module of DYN3D) and FLOCAL coupling within DYN3D provide simplified coupled reactor physics at the fuel pin level that can be used as a reference. This evaluation allows one to show through external coupling how the transfer of power distributions from DYN3D to CTF and how the transfer of feedback distribution from CTF to DYN3D takes place as well as justify through the thermal hydraulics when the DYN3D and CTF coupling rather than just DYN3D should be used to provide improved coupled reactor physics at the fuel pin level. This second journal article therefore covers the DYN3D and CTF coupling inner iterations within one outer iteration verification to provide partially verified improved coupled reactor physics at the fuel pin level, while the DYN3D and CTF coupling outer iterations within the convergence criteria verification to provide fully verified improved coupled reactor physics at the fuel pin level will be covered in the next journal article.

Simplified coupled reactor physics at the fuel assembly level in DYN3D are available after performing fuel assembly homogenisation; additionally, simplified coupled reactor physics at the fuel pin level in DYN3D are available after performing fuel pin reconstruction. Another alternative for simplified coupled reactor physics at the fuel pin level in DYN3D is available by directly simulating fuel pin scaled nodes using fuel pin cross sections instead of simulating fuel assembly scaled nodes using fuel assembly cross sections. Full thermal hydraulics at the fuel pin level in CTF are available by default. Nevertheless, the simplified coupled reactor physics at the fuel pin level in DYN3D are limited

in terms of neutronics by neutron diffusion and limited in terms of thermal hydraulics by the lack of crossflow and turbulent mixing. However, the improved coupled reactor physics at the fuel pin level in the DYN3D and CTF coupling are only limited in terms of neutronics by neutron diffusion but complemented in terms of thermal hydraulics by the wide range of crossflow and turbulent mixing.

The structure of this journal article consists of several parts. First, a DYN3D description comprehending general features, updates, etc. [60,61] was performed to present the first code used in the coupling inner iterations within one outer iteration verification. Second, a CTF description comprehending general features, updates, etc. [62,63] was undertaken to present the second code used in the coupling inner iterations within one outer iteration verification. Third, the specifications description covering the KAIST (Korean Advanced Institute of Science and Technology) benchmark [64] was performed to present the data used in the coupling inner iterations within one outer iteration verification. Fourth, the models description for the simulation of the benchmark was performed to present its implementation into the coupling inner iterations within one outer iteration verification. Fifth, the scripts description comprehending the transfer of power distributions from DYN3D to CTF as well as the transfer of feedback distributions from CTF to DYN3D was performed to present the coupling inner iterations within one outer iteration verification.

The results and analysis obtained for the DYN3D and CTF coupling inner iterations within one outer iteration verification through the KAIST benchmark were comprehended by DYN3D coupling to DYN3D and CTF coupling comparisons. Tests presented include results for the fluid density feedback, fluid temperature feedback, fuel temperature feedback, and the pressure drop feedback in 17×17 fuel assemblies with guide tubes and with or without burnable absorber fuel pins. All these magnitudes were chosen to analyse the DYN3D and CTF coupling in nuclear reactors from a thermal hydraulics perspective. It can be observed how this comparison allows one to show the DYN3D and CTF coupling compared to the DYN3D coupling.

Conclusions regarding the DYN3D and CTF coupling inner iterations within one outer iteration verification were made to corroborate the second objective with the aim of providing the DYN3D and CTF coupling within the Multiscale and Multiphysics Software Development, which was fulfilled by verifying the DYN3D and CTF coupling inner iterations within one outer iteration. Finally, future work that remains is presented to address the last objective with the aim of providing the DYN3D and CTF coupling within the Multiscale and Multiphysics Software Development.

4.2. Codes Used in the Verification

As previously mentioned, DYN3D and CTF were the codes that were selected as they are widely used in both academia and the industry, and hence their main features, version updates, equations, and solution approach are described in the next two subsections.

4.2.1. DYN3D Nodal Code

DYN3D [60,61,65] was developed using FORTRAN 90 in the early 1990s by FZD (Forschung Zentrum Dresden) and has been continuously updated. It is an LWR-VVER (square and hexagonal geometries) coupled reactor physics nodal code developed for the purpose of studying general nuclear reactor behaviour. Capabilities such as 3D modelling have resulted in the code being widely used for LWR-VVER steady and transient state analysis. In terms of neutronics, it uses the neutron diffusion approach with two energy groups complemented by nodal expansion methods such as nodal expansion, SP3 (only square geometry) HEXNEM1-2 (only hexagonal geometry), ADF (Assembly Discontinuity Factors), and pin power reconstruction. In terms of thermal hydraulics, it uses a none crossflow, or turbulent mixing 2-fluid approach complemented by heat transfer models such as two-phase heat transfer and interphase heat transfer.

DYN3D-MG is an updated version of DYN3D developed by HZDR (Helmholtz Zentrum Dresden Rossendorf). Updates include implementing the neutron diffusion approach with multi energy groups, improving the calculation of reactivity by inverse point kinetics as performing the calculation of dynamical reactivities, implementing the Pernica departure from nucleate boiling correlation, and improving the calculation of boric acid transport by using the particle in cell method.

A reactor core or smaller system can be modelled in DYN3D and is represented through a set of nodes that generally conform to channels. The neutron diffusion N energy groups and M delayed

neutron precursor modelling approach is applied to the set of nodes with each energy group being modelled through its own neutron diffusion equation and each delayed neutron precursor group being modelled through its own concentration equation. The none crossflow or turbulent mixing two fluid (liquid, vapor) modelling approach is applied to the set of nodes with the fluid mixture being modelled through a set of fluid mass, fluid momentum, and fluid energy conservation equations with the vapor mass equation being treated separately. All the equations were formulated using either a cartesian or hexagonal coordinate system. These were then finally expressed in a finite difference form and solved using numerical methods. An implicit method was applied to all the equations.

Certain conditions are required to obtain a solution to the neutron diffusion and concentration equations such as including the steady or transient nature of the system to perform the calculations, acknowledging other possible external neutron sources that account for additional fast neutrons that affect the nodes neutron fluxes, determining the poisoning state of the reactor to obtain the correct contributions to the absorption cross section, and performing pin reconstruction to produce solutions at the fuel pin level in addition to the fuel assembly level.

Certain conditions are required to obtain a solution to the fluid mass, fluid momentum, and fluid energy equations such as including the steady or transient nature of the system to perform the calculations, determining the constitutive relations that relate the fluid mass, fluid momentum, and fluid energy equations for the two phases in the nodes leading to effects such as phase change, determining fluid and solid thermal and mechanical properties using tables and implemented correlations.

4.2.2. CTF Subchannel Code

COBRA-TF [62,63,66] was developed using FORTRAN 77 in 1980 by PNL (Pacific Northwest Laboratories, Washington, WA, USA), sponsored by the NRC (Nuclear Regulation Commission) and has been continuously updated. It is a LWR (square geometry) thermal hydraulics subchannel code developed for the purpose of studying general nuclear reactor behaviour and accident scenarios. Capabilities such as full 3D modelling have resulted in the code being widely used for LWR steady and transient state analysis. In terms of thermal hydraulics, it uses a wide crossflow and turbulent mixing two fluid, three flow field approach complemented by flow regime/heat transfer dependent models such as two-phase heat transfer, interphase heat transfer and drag, entrainment, and quench front tracking.

CTF is an updated version of COBRA-TF developed and maintained by the PSU (Pennsylvania State University, Pennsylvania, PA, USA) and NCSU (North Carolina State University, Raleigh, NC, USA). Updates include changing the source code to FORTRAN 90, improving user friendliness by providing error check and free format input, assuring quality by using wide validation and verification, improving void drift, turbulent mixing, and heating models, enhancing computational efficiency by introducing new numerical methods, finally, improving the physical model and user modelling information.

Any system, apart from pressurisers, can be modelled in CTF and is represented through a matrix of mesh cells that conform to subchannels. The wide crossflow and turbulent mixing two fluid (liquid, vapor), three flow field (liquid film, liquid droplets, and vapor) modelling approach is applied to the mesh cells with each field being modelled through its own set of fluid mass, fluid momentum, and fluid energy conservation equations with the liquid and droplet fields being in thermal equilibrium between them, and hence sharing the same energy equation. The equations were formulated using either a cartesian or a simplified subchannel coordinate system. These were then finally expressed in a finite difference form and solved using numerical methods. A homogeneous equilibrium method was applied to the conservation equations known as SIMPLE (Semi Implicit Method for Pressure Linked Equations).

Certain conditions are required to obtain a solution to the fluid mass, fluid momentum, and fluid energy equations such as including the steady or transient nature of the system to perform the calculations, determining the flow regime to obtain the correct macro and micro mesh cell closure terms necessary to account for the correct collective phenomena, determining the macro mesh cell closure terms that relate the conservation equations for the same phase in different mesh cells leading to phenomena such as void drift and turbulent mixing, determining the micro mesh cell closure terms

that relate the conservation equations for different phases in the same mesh cell leading to inter-phase effects such as phase change and entrainment, and determining fluid and solid thermal and mechanical properties using tables and implemented correlations.

4.3. Specifications Used in the Verification

As previously mentioned, the DYN3D and CTF coupling inner iterations within one outer iteration verification was performed by covering the KAIST benchmark. Hence, the specifications used in the above-mentioned are described in the following subsection.

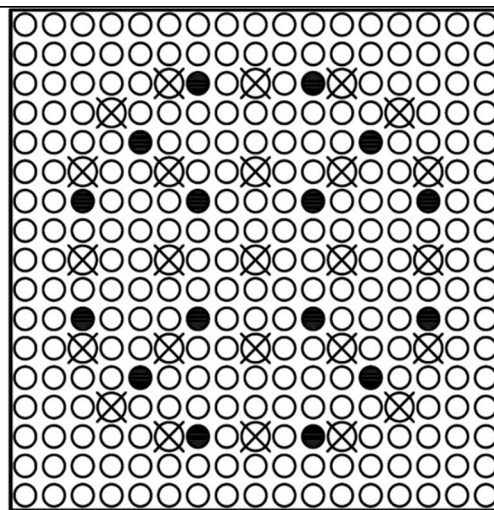
KAIST Benchmark

The KAIST benchmark [64] is a benchmark for PWR reactor core neutronics and thermal hydraulics simulation. No experimental data or other code results are available. Tests performed include steady state 17×17 assemblies containing fuel pins and guide tubes as well as burnable absorber pins with variation dependant axial and radial power distributions and uniform pressure losses. The KAIST benchmark has been expanded through a multi parameter variation exercise consisting of six coupling tests based on a reference PWR under general nuclear reactor behaviour, where variation of a single parameter is applied to either the total power, the inlet temperature, the outlet pressure, the inlet mass flux, or the inlet boric acid. All the data for the tests has been presented.

Specifications include the geometry, materials, spacer grids, and initial and boundary conditions [64]. The geometry is described for the 17×17 assemblies with or without burnable absorber pins as observed in Table 4.1.

Table 4.1. The 17×17 geometry from the KAIST benchmark.

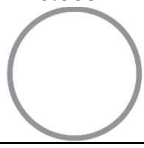
Type	UOX-2 (CR) 17×17 Assembly	UOX-2 (BA16) 17×17 Assembly
Number of Fuel Pins	264	248
Number of Burnable Absorber Pins	0	16
Number of Guide Tubes	25	25
Channel Width (m)	0.2142	0.2142
Cell Width (m)	0.0126	0.0126
Axial Length (Active) (m)	3.658	3.658



- Fuel Pin
- Burnable Absorber/ Fuel Pin
- ⊗ Guide Tube



Type	Fuel/Burnable Absorber Pin
Clad Diameter (m)	0.0095
Clad Thickness (m)	0.00057
Gap Thickness (m)	0.000085
Fuel Pin Diameter (m)	0.0082



Type	Guide Tube
Guide Tube Diameter (m)	0.01224
Clad Thickness (m)	0.000405

The materials are described as observed in Table 4.2.

Table 4.2. The 17×17 materials from the KAIST benchmark.

Fuel Pin Composition	UO ₂ (3.3% ²³⁵ U, 96.7% ²³⁸ U)	
Burnable Absorber Pin Composition	UO ₂ (0.711% ²³⁵ U, 90.289% ²³⁸ U) + Gd ₂ O ₃ (9.0%)	
Clad Composition	Zircalloy (97.91% Zr, 1.59% Sn, 0.5% Fe)	
Energy Groups (eV)	Group 0≡ (0.62506, 2231300) Group 1≡ (0.000014, 0.62506)	
Fuel Density (kg/m ³)	10040	
Fuel Specific Heat (J/kg K)	$c_{p_{fuel}} = \frac{8.5013 \cdot 10^8 e^{\frac{535.285}{T}}}{T^2 \left(e^{\frac{535.285}{T}} - 1 \right)^2} + 0.0243T + \frac{1.6587 \cdot 10^{12}}{T^2} e^{-\frac{18968}{T}}$	(12)
Fuel Thermal Conductivity (W/m K)	$k_{fuel} = \max\left(\frac{2335}{464 + T}, 1.1038\right) + 7.027 \cdot 10^{-3} \cdot 10^{-3} e^{1.867 \cdot 10^{-3} T}$	(13)
Clad Density (kg/m ³)	6400	
Clad Specific Heat (J/kg K)	$c_{p_{clad}} = 252.54 + 0.11474T$	(14)
Clad Thermal Conductivity (W/m K)	$k_{clad} = 7.51 + 2.09 \cdot 10^{-2} T - 1.45 \cdot 10^{-5} T^2 + 7.67 \cdot 10^{-9} T^3$	(15)
Gap Gas	He	
Gap Heat Conductance (kJ/m ² K)	5678	

Spacer grids are uniform and are described as observed in Table 4.3.

Table 4.3. The 17×17 spacer grids from the KAIST benchmark.

Pressure Loss Coefficient	0.30
Spacer Grids Location (m)	Uniform

The initial and boundary conditions are described as observed in Table 4.4.

Table 4.4. The 17×17 initial and boundary conditions.

Case	Outlet Pressure (Bar)	Power (MW)	Mass Flux (kg/m ² s)	Inlet Temperature (C)	Boric Acid Concentration (ppm)
Reference	155	25.960	2889.33	293.33	2250
High Power	155	30.287	2889.33	293.33	2250
High Temperature	155	25.960	2889.33	303.33	2250

Low Pressure	145	25.960	2889.33	293.33	2250
Low Flux	155	25.960	2476.58	293.33	2250
Low Boron	155	25.960	2889.33	293.33	1125

4.4. Models and Scripts Used in the Verification

As previously mentioned, the DYN3D and CTF coupling inner iterations within one outer iteration verification were performed by simulating the KAIST benchmark in addition to using additional coupling scripts. Hence, the models and scripts used in the above-mentioned are described in the following subsections.

4.4.1. KAIST Benchmark

Models used in DYN3D include 289 fuel cells (fuel pin centred system) conformed by 36 uniform axial node layers along with in the case of the UOX-2 (CR) fuel assembly, 264 fuel pins, and 25 guide tubes or in the case of the UOX-2 (BA16) fuel assembly, 248 fuel pins as well as 16 burnable absorber pins, and 25 guide tubes that have been modelled in the steady state. Models used in CTF include 324 subchannels (subchannel centred system) connected in between by 612 gaps contained in one section conformed by 36 uniform axial node layers along with in the case of the UOX-2 (CR) fuel assembly, 264 fuel pins, and 25 guide tubes or in the case of the UOX-2 (BA16) fuel assembly, 248 fuel pins as well as 16 burnable absorber pins and 25 guide tubes that have been modelled in the steady state. The fuel pin centred system model in DYN3D and the subchannel centred system model in CTF for both the UOX-2 (CR) and UOX-2 (BA16) fuel assemblies can be observed in Figure 4.2.

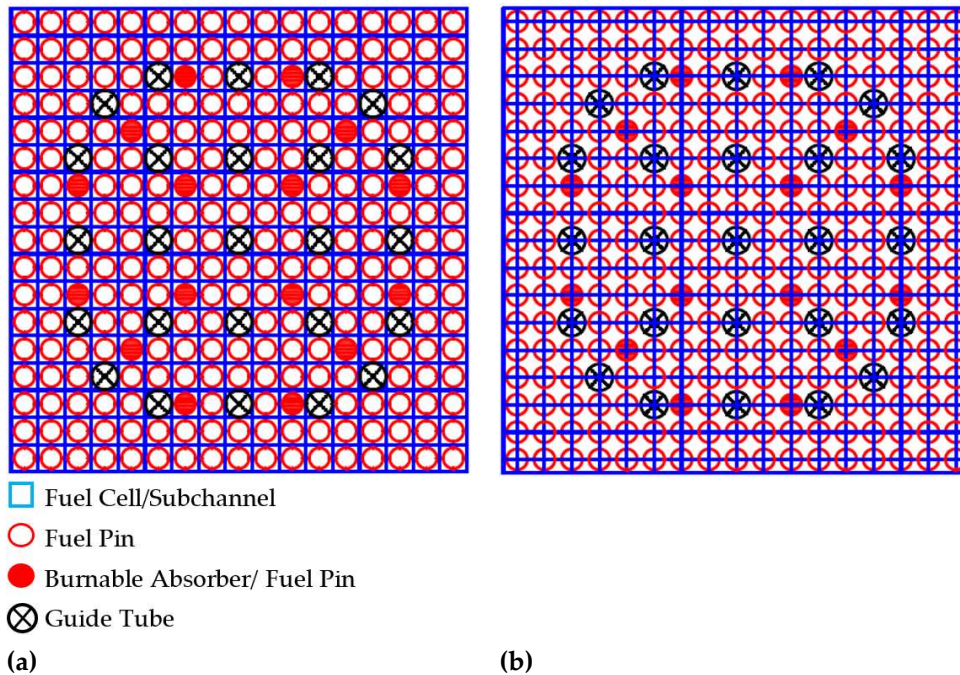


Figure 4.2. (a) DYN3D UOX-2 (CR/BA16) 17×17 model, (b) CTF UOX-2 (CR/BA16) 17×17 model.

Regarding the neutronics in DYN3D, two energy groups were modelled including fast and thermal energy groups according to the KAIST benchmark specifications. Steady state was achieved by division of the multiplication cross sections by the effective criticality factor as it is useful for experimental repetitions, allowing the power and the boric acid concentration to be predefined. Reflective boundary conditions have been used for any re-entering current into any of the energy groups as otherwise due to the node sizes, neutrons would escape the system. The homogenised cross sections for the fuel and burnable absorber pins and guide tubes were previously obtained using SCALE-POLARIS simulating multiple feedback parameter combinations to construct multidimensional cross section tables through which DYN3D performs interpolation, as is generally

done in nodal codes. The effective criticalities for certain tests with constant thermal hydraulics feedback have been compared between DYN3D and SCALE-POLARIS, leading to similar values.

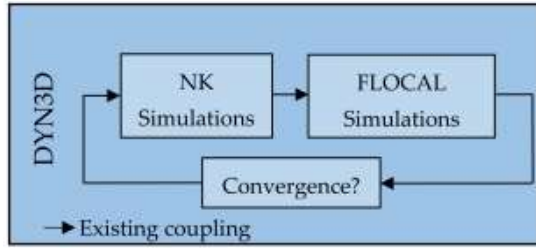
Regarding the thermal hydraulics in both DYN3D and CTF, friction pressure losses have been modelled in the case of DYN3D using Filonenko's and Osmachkin's [67] one phase and two-phase multipliers correlation due to it being the only one available, while these have been modelled in the case of CTF using McAdam's [68] correlation due to it being widely used in LWR analysis. Spacer grid pressure losses have been modelled in both DYN3D and CTF using a uniform pressure loss coefficient of 0.30, as estimated through previous simulations. The pressure equation has been solved in the case of DYN3D using Gaussian elimination due to it being the method available, while this has been solved in the case of CTF using the Krylov solver due to it being a method more effective than Gaussian elimination. Nucleate boiling has been modelled in the case of DYN3D using the Rassokhin and Borishaskji [69] correlation due to it being the one available, while this has been modelled in the case of CTF using the Thom [70] correlation due to it being validated for a wider pressure range than the Chen correlation. Departure from nucleate boiling has been modelled in the case of DYN3D using the Bezrukov and Astakhov (OKB-2) [71] correlation due to this one being the best available, while this has been modelled in the case of CTF using the W-3 [72,73] correlation due to it being widely used in LWR analysis. Crossflow is not available in the case of DYN3D, while this has been modelled in the case of CTF using the available CTF model. Turbulent mixing is not available in the case of DYN3D, while this has been modelled in the case of CTF using the Rogers and Rosehart correlation, which depends on an empirical correlation determined single-phase mixing coefficient and a two-phase multiplier with a value of 5.0 as well as an equilibrium weighting void drift factor with a value of 1.4 [74] due to it being the best available. Entrainment and deposition for the droplets are not available in the case of DYN3D, while these have been modelled in the case of CTF using the original CTF model due to the necessary accuracy.

4.4.2. DYN3D and CTF Coupling Scripts

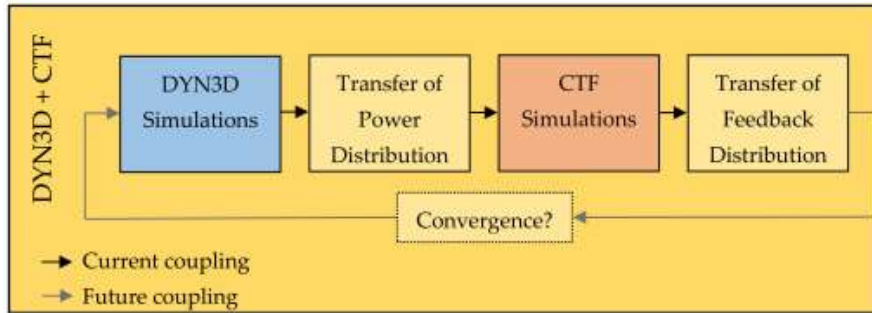
Additional scripts have been developed using PYTHON quite recently at the UOL. These are LWR-VVER (square and hexagonal geometries) coupled reactor physics coupling scripts that were developed for the purpose of performing the DYN3D and CTF coupling within the Multiscale and Multiphysics Software Development. Capabilities such as the transfer of power distributions from DYN3D to CTF, and the transfer of feedback distribution from CTF to DYN3D as well as the output of any distribution from both codes have resulted in the additional scripts being necessary to provide the DYN3D and CTF coupling inner iterations within one outer iteration verification. In terms of structure, these use a set of python modules including numpy, pandas, and matplotlib along with functions, control flow statements, and data structures.

Any system modelled in both DYN3D and CTF can be interpreted by the additional scripts. The transfer of power distributions from DYN3D to CTF script reads the power distribution for each fuel pin cell from the output (`_lst`) of DYN3D. Then, it normalises the power distribution for each fuel pin cell by its corresponding average value and reformats these as required in CTF. Finally, it writes the mentioned power distributions for each fuel pin cell to the input (`.inp`) of CTF. The transfer of feedback distributions from CTF to DYN3D script reads the feedback distributions for each fuel pin cell or subchannel from the outputs (`.vtk`) of CTF. Then, it converts any subchannel feedback distribution to a fuel pin cell feedback distribution. Next, it averages the feedback distribution to feedback values (fuel temperature, moderator temperature, moderator density, and boric acid concentration) and reformats these as required in DYN3D. Finally, it writes the mentioned feedback values to the input (`_kin`) of DYN3D. Both coupling scripts can in general, read any distribution for each fuel pin cell or subchannel from the mentioned outputs of DYN3D and CTF. Then, both coupling scripts can, in general, manipulate any distribution as desired by the user. Finally, both coupling scripts can, in general, write any value or distribution to an external file or provide graphical representation as desired by the user.

Currently, the coupling scripts are being used in external coupling, although in the future their functionality will be implemented through internal libraries in other couplings. Both the DYN3D internal coupling scheme as well as the DYN3D and CTF external coupling scheme can be observed in Figure 4.3.



(a)



(b)

Figure 4.3. (a) DYN3D internal coupling, (b) DYN3D, and CTF external coupling.

Currently, DYN3D and CTF coupling inner iterations within one outer iteration verification have been performed, although in the future, DYN3D and CTF coupling outer iterations within the convergence criteria verification will be performed. Hence, the DYN3D internal coupling criteria are being used in external coupling, although in the future, a DYN3D and CTF internal coupling criteria will be implemented in a similar way as for the former.

The results and analysis obtained for the DYN3D and CTF coupling inner iterations within one outer iteration verification through the KAIST benchmark require both average feedback values as well as average feedback distributions and their evaluation either including (or not) the burnable absorber pin cell feedback distributions and either including (or not) the guide tube cell feedback distributions. This is performed by ignoring the corresponding burnable absorber pin or guide tube cell when performing any average over the fuel assembly.

4.5. Results and Analysis

Results for the feedback in the DYN3D internal coupling as well as for the DYN3D and CTF external coupling were obtained through the simulation of the KAIST benchmark [64]. DYN3D to DYN3D and CTF coupling comparisons within the DYN3D and CTF coupling inner iterations within one outer iteration verification in the steady state are presented for the fluid density feedback, fluid temperature feedback, fuel temperature feedback, and the pressure drop feedback.

KAIST Benchmark

DYN3D to DYN3D and CTF coupling comparisons within the multi parameter variation exercise for the UOX-2 (CR) as well as the UOX-2 (BA16) 17×17 fuel assemblies are shown for the fluid density feedback, fluid temperature feedback, fuel temperature feedback, and the pressure drop feedback, while the mass flux feedback, void fraction feedback, and departure from nucleate boiling feedback are shown in the Appendix B. The location of the UOX-2 (CR) and the UOX-2 (BA16) fuel assemblies within the PWR reactor core can also be found in the Appendix B. The fluid density feedback value between fuel cells at the average axial node layer in both the UOX-2 (CR) and the UOX-2 (BA16) fuel assemblies is provided to show the similarities and differences between coupling values. All these values can be observed in Figure 4.4.

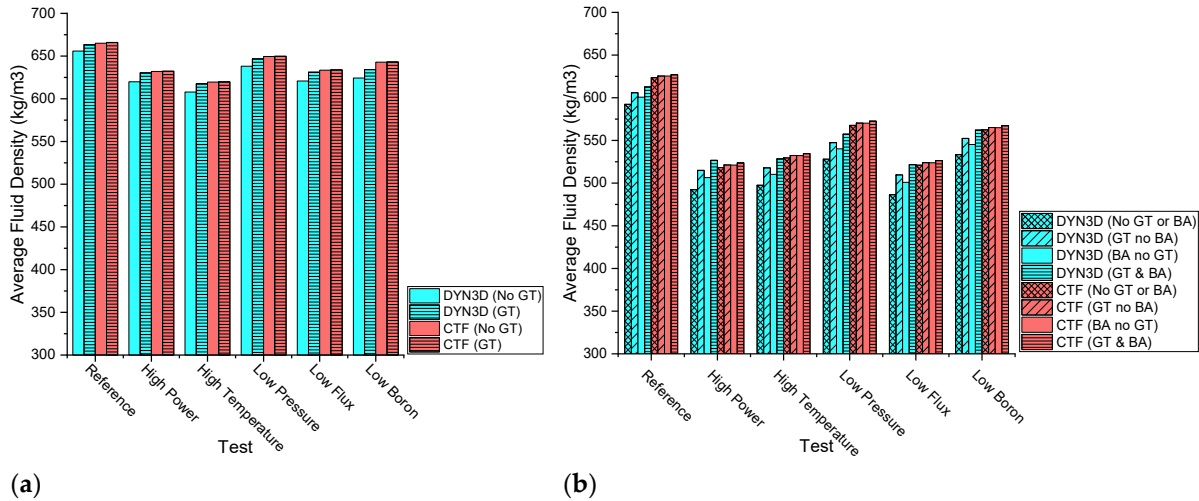


Figure 4.4. (a) UOX-2 (CR) fluid density feedback values, (b) UOX-2 (BA16) fluid density feedback values.

Both FLOCAL and CTF derive the fluid density by solving the fluid mass equation.

In both the DYN3D and the DYN3D and CTF couplings with or without burnable absorber pin and/or guide tube cells, the fluid density feedback value between fuel cells at the average axial node layer was observed to decrease in all the tests in the UOX-2 (BA16) fuel assembly when compared to in the UOX-2 (CR) fuel assembly. This fluid density feedback value decrease occurs due to lower power in the burnable absorber pin cells, which result in higher powers in the fuel pin cells, leading to an equivalent total power such as when there are equal powers in all the fuel pin cells, which results in lower fluid densities according to the fluid mass equation.

In both the DYN3D and the DYN3D and CTF couplings with or without burnable absorber pin and/or guide tube cells, the fluid density feedback value between fuel cells at the average axial node layer was observed to decrease with high power, high temperature, low pressure, low flux, and low boron when compared to the reference in both the UOX-2 (CR) and in the UOX-2 (BA16) fuel assemblies. This fluid density feedback value decrease occurs due to different reasons: In the high-power variation, this occurs due to the higher volumetric wall heat transfer term, which results in lower fluid densities according to the fluid mass equation. In the high temperature variation, this occurs due to higher inlet fluid enthalpy, which results in lower fluid densities according to the fluid mass equation. In the low-pressure variation, this occurs due to the lower pressure force term, which results in lower fluid densities according to the fluid mass equation. In the low mass flux variation, this occurs due to the lower inlet mass flow, which results in lower fluid densities according to the fluid mass equation. In the low boron variation, this occurs due to the lower boric acid concentration, which results in lower fluid densities according to the boron transport models.

In the DYN3D coupling without burnable absorber pin and/or guide tube cells compared to with burnable absorber pin and/or guide tube cells, the fluid density feedback value between all fuel cells at the average axial node layer was observed to decrease in all the tests in both the UOX-2 (CR) and in the UOX-2 (BA16) fuel assemblies. This fluid density feedback value decrease occurs particularly due to either the absence of power in the guide tube cells or lower power in the burnable absorber pin cells as well as in general due to the lack of mass transfer between fuel cells, leading to lower fluid densities according to the fluid mass equation.

In the DYN3D and CTF coupling without burnable absorber pin and/or guide tube cells compared to those with burnable absorber pin and/or guide tube cells, the fluid density feedback value between all fuel cells at the average axial node layer was observed to remain almost unchanged in all the tests in both the UOX-2 (CR) and in the UOX-2 (BA16) fuel assemblies. This fluid density feedback value near equivalence occurs, in general, due to the presence of mass transfer between fuel cells, leading to homogeneous fluid densities in both the guide tube cells and burnable absorber pin cells, which results, in general, in unchanged fluid densities, according to the fluid mass equation.

Between the DYN3D and the DYN3D and CTF couplings with or without burnable absorber pin and/or guide tube cells, the fluid density feedback values between fuel cells at the average axial node layer in both the UOX-2 (CR) and in the UOX-2 (BA16) fuel assemblies were observed to be different. These fluid density feedback value differences occurred due to different terms in the fluid mass equation including the evaporation as well as the crossflow and turbulent mixing models between fuel cells. According to the obtained fluid density feedback values between fuel cells at the average axial node layer in the UOX-2 (CR) fuel assembly, most variations can be regarded as compatible between both couplings while in the UOX-2 (BA16) fuel assembly, also most of the variations can be regarded as compatible between both couplings. Such variations can be regarded as compatible between couplings due to the similarity of the fluid density feedback values.

Transversal fluid density feedback distributions for all the fuel cells at the average axial node layer are provided for the UOX-2 (CR) fuel assembly compatible reference case to show the similarities and differences between both coupling distributions as observed in Figures 4.5 and 4.6.

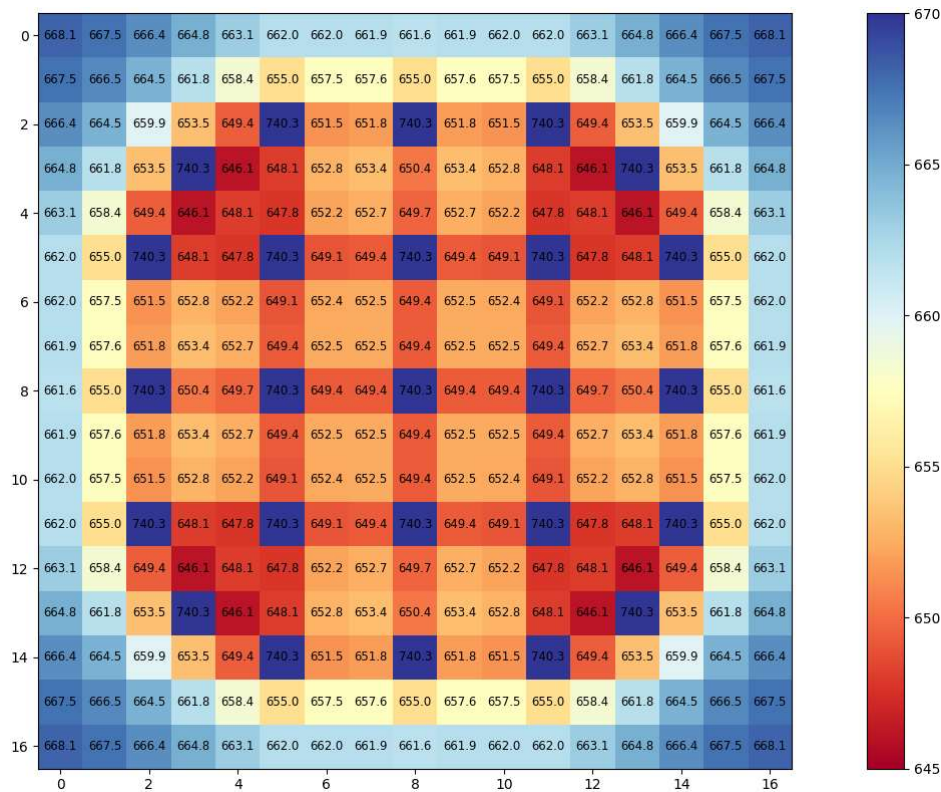


Figure 4.5. DYN3D coupling transversal fluid density feedback distribution.

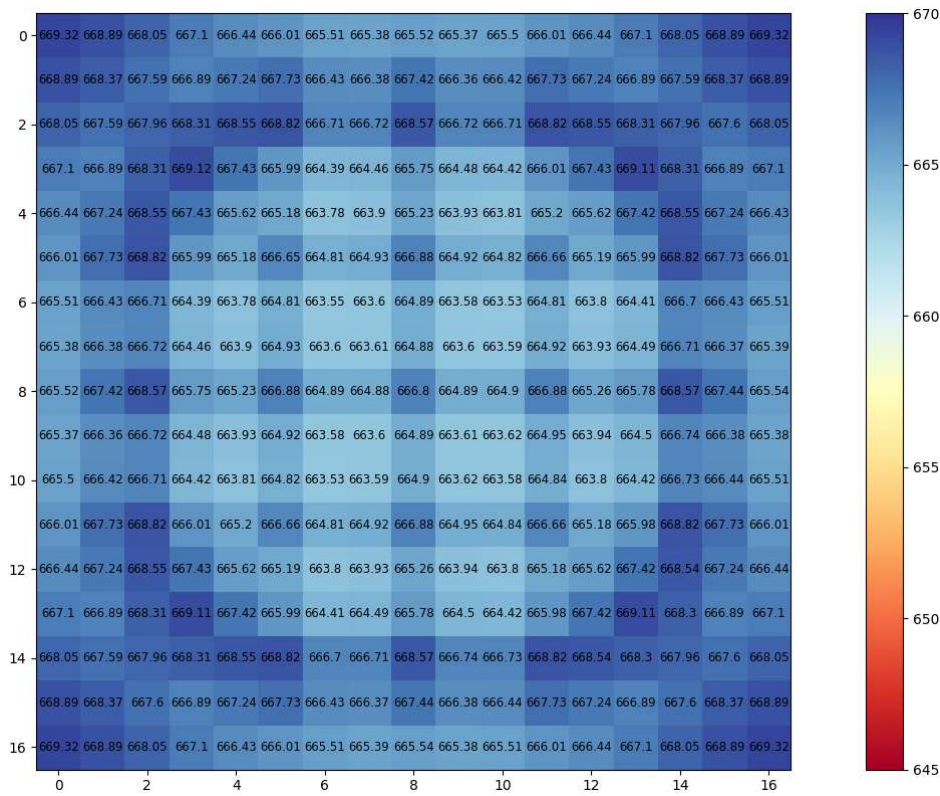
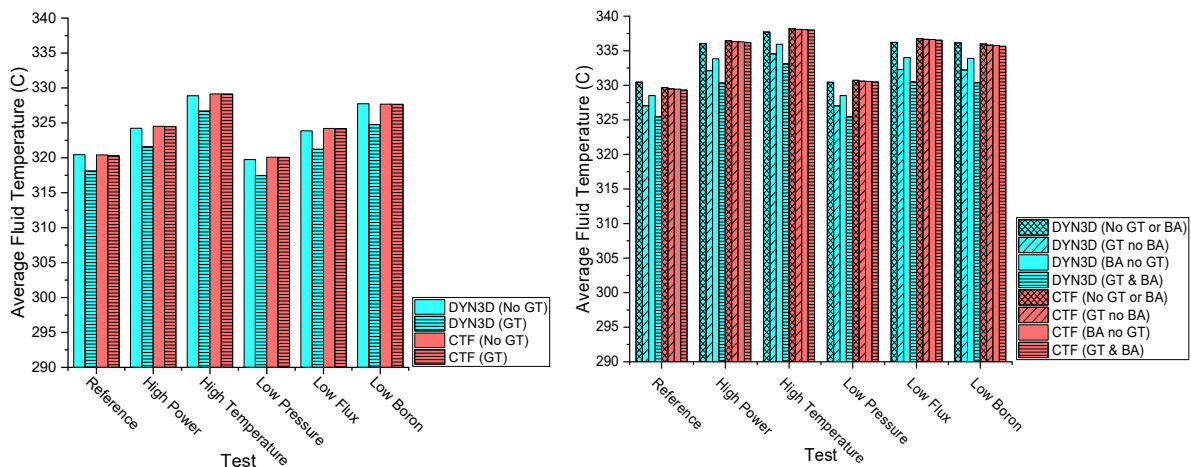


Figure 4.6. DYN3D and CTF coupling transversal fluid density feedback distribution.

In both the DYN3D and the DYN3D and CTF couplings, the transversal fluid density feedback distribution for all fuel cells at the average axial node layer in the UOX-2 (CR) fuel assembly compatible reference case was observed to decrease more in the central than in the side or corner fuel cells. This transversal fluid density feedback distribution decrease occurred in both couplings due to the fuel cell neighbours, leading to higher heat fluxes in the central fuel cells, which resulted in lower fluid densities according to the fluid mass equation.

Between the DYN3D and the DYN3D and CTF couplings, the transversal fluid density feedback distribution for all the fuel cells at the average axial node layer in the UOX-2 (CR) fuel assembly compatible reference case were observed to be different. These transversal fluid density feedback distribution differences occurred due to different terms in the fluid mass equation including the evaporation as well as the crossflow and turbulent mixing models between fuel cells.

The fluid temperature feedback value between fuel cells at the average axial node layer in both the UOX-2 (CR) and the UOX-2 (BA16) fuel assemblies is provided to show the similarities and differences between the coupling values. All these values can be observed in Figure 4.7.



(a)

(b)

Figure 4.7. (a) UOX-2 (CR) fluid temperature feedback values, (b) UOX-2 (BA16) fluid temperature feedback values.

Both FLOCAL and CTF derive the fluid temperature from the fluid enthalpy, which is mainly obtained by solving the fluid energy equation.

In both the DYN3D and the DYN3D and CTF couplings with or without burnable absorber pin and/or guide tube cells, the fluid temperature feedback value between fuel cells at the average axial node layer was observed to increase in all the tests in the UOX-2 (BA16) fuel assembly when compared to in the UOX-2 (CR) fuel assembly. This fluid temperature feedback value increase occurred due to lower powers in the burnable absorber pin cells, which resulted in higher powers in the fuel pin cells, leading to an equivalent total power as when there are equal powers in all the fuel pin cells, which results in higher fluid enthalpies according to the fluid energy equation.

In both the DYN3D and the DYN3D and CTF couplings with or without burnable absorber pin and/or guide tube cells, the fluid temperature feedback value between fuel cells at the average axial node layer was observed to increase with high power, high temperature, low flux, and low boron when compared to the reference in both the UOX-2 (CR) and in the UOX-2 (BA16) fuel assemblies. This fluid temperature feedback value increase occurred due to different reasons: in the high-power variation, this occurred due to the higher volumetric wall heat transfer term, which resulted in higher fluid enthalpies according to the fluid energy equation. In the high temperature variation, this occurred due to higher inlet fluid enthalpy, which resulted in higher fluid enthalpies according to the fluid energy equation. In the low mass flux variation, this occurred due to the lower inlet mass flow, which resulted in higher fluid enthalpies according to the fluid energy equation. In the low boron variation, this occurred due to the lower boric acid concentration term, which resulted in higher fluid enthalpies according to the fluid energy equation. In both the DYN3D and the DYN3D and CTF couplings with or without burnable absorber pin and/or guide tube cells, the fluid temperature feedback value between all fuel cells at the average axial node layer was observed to remain constant with low pressure when compared to the reference in both the UOX-2 (CR) and in the UOX-2 (BA16) fuel assemblies.

In the DYN3D coupling without burnable absorber pin and/or guide tube cells compared to with burnable absorber pin and/or guide tube cells, the fluid temperature feedback value between fuel cells at the average axial node layer was observed to increase in all the tests in both the UOX-2 (CR) and in the UOX-2 (BA16) fuel assemblies. This fluid temperature feedback value increase occurred, in particular, due to either the absence of power in the guide tube cells or lower power in the burnable absorber pin cells as well as in general, due to the lack of energy transfer between fuel cells, leading to higher fluid enthalpies according to the fluid energy equation.

In the DYN3D and CTF coupling without burnable absorber pin and/or guide tube cells compared to with burnable absorber pin and/or guide tube cells, the fluid temperature feedback value between all fuel cells at the average axial node layer was observed to remain almost unchanged in all the tests in both the UOX-2 (CR) and in the UOX-2 (BA16) fuel assemblies. This fluid temperature feedback value near equivalence occurred, in general, due to the presence of energy transfer between fuel cells, leading to homogeneous fluid temperatures in both the guide tube cells and burnable absorber pin cells, which resulted, in general, in unchanged enthalpies according to the fluid energy equation.

Between the DYN3D and the DYN3D and CTF couplings with or without burnable absorber pin and/or guide tube cells, the fluid temperature feedback values between all fuel cells at the average axial node layer in both the UOX-2 (CR) and in the UOX-2 (BA16) fuel assemblies were observed to be different. These fluid temperature feedback value differences occurred due to different terms in the fluid energy equation including the nucleate boiling correlations as well as the crossflow and turbulent mixing models between fuel cells. According to the obtained fluid temperature feedback values between fuel cells at the average axial node layer in the UOX-2 (CR) fuel assembly, most variations can be regarded as compatible between both couplings while in the UOX-2 (BA16) fuel assembly, also most of the variations can be regarded as compatible between both couplings. Such variations can be regarded as compatible between couplings due to the similarity of the fluid temperature feedback values.

Axial fluid temperature feedback distributions for central, side, and corner fuel cells and average between fuel cells as well as transversal fluid temperature feedback distributions for all the fuel cells at the average axial node layer are provided for the UOX-2 (CR) fuel assembly compatible reference case to show the similarities and differences between both coupling distributions, as observed in Figures 4.8., 4.9., 4.10.

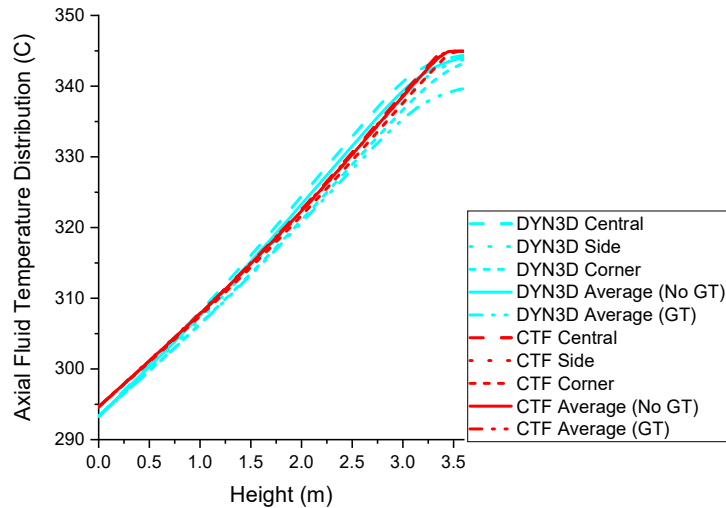


Figure 4.8. Axial fluid temperature feedback distributions.

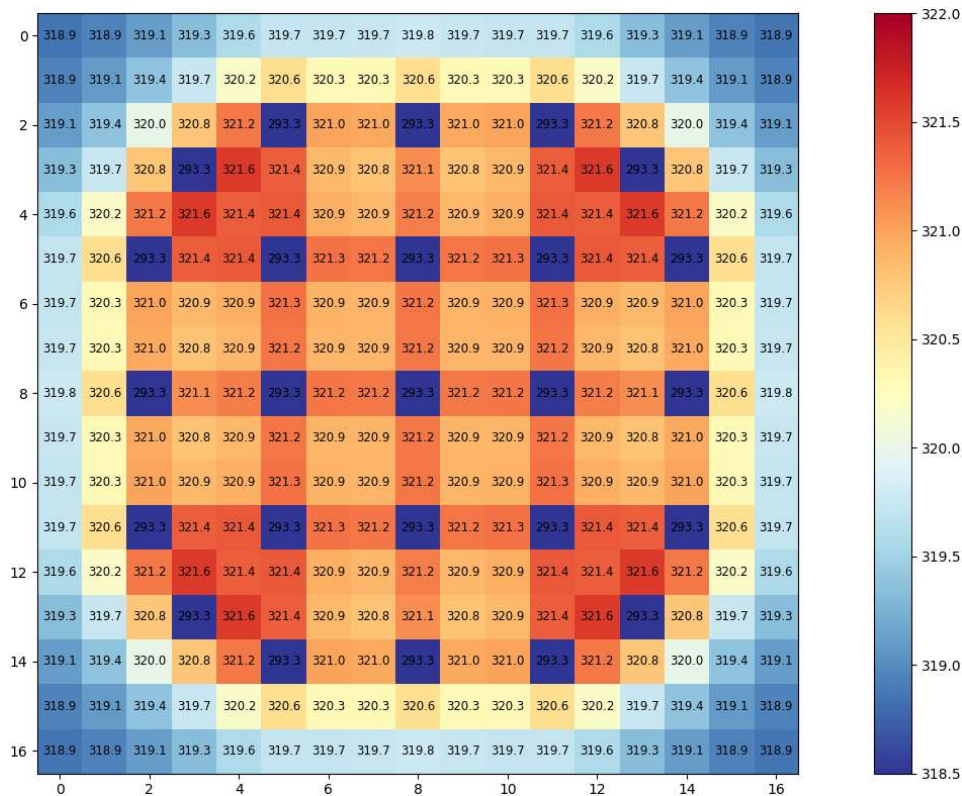


Figure 4.9. DYN3D coupling transversal fluid temperature feedback distribution.

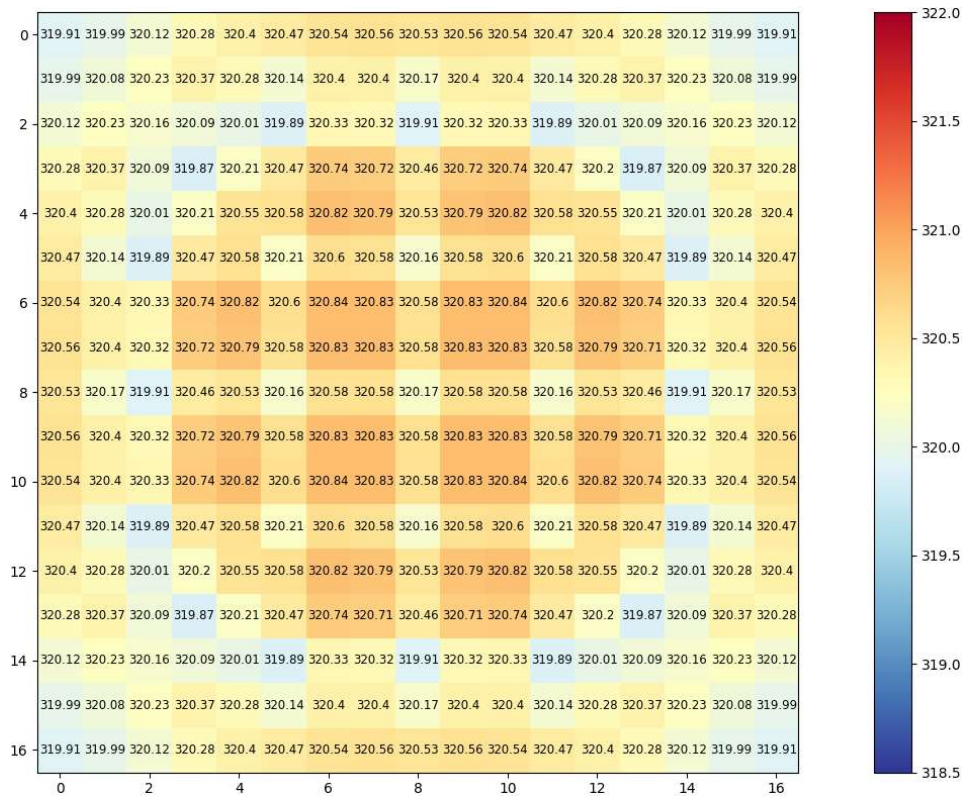


Figure 4.10. DYN3D and CTF coupling transversal fluid temperature feedback distribution.

In both the DYN3D and the DYN3D and CTF couplings, the axial fluid temperature feedback distribution for the central, corner, and side fuel cells as well as the transversal fluid temperature feedback distribution for all fuel cells at the average axial node layer in the UOX-2 (CR) fuel assembly compatible reference case was observed to increase more in the central than in the side or corner fuel cells. This axial and transversal fluid temperature feedback distribution increase occurred in both couplings due to the fuel cell neighbours, leading to higher heat fluxes in the central fuel cells, which resulted in lower fluid densities according to the fluid mass equation in the central fuel cells, which resulted in higher fluid enthalpies according to the fluid energy equation.

Between the DYN3D and the DYN3D and CTF couplings, the axial fluid temperature feedback distribution for the central, corner, and side fuel cells as well as the transversal fluid temperature feedback distribution for all the fuel cells at the average axial node layer for the UOX-2 (CR) fuel assembly compatible reference case were observed to be different. These axial and transversal fluid temperature feedback distribution differences occurred due to different terms in the fluid energy equation including the nucleate boiling correlations as well as the crossflow and turbulent mixing models between fuel cells.

The fuel temperature feedback value between fuel pins at the average axial node layer in both the UOX-2 (CR) and the UOX-2 (BA16) fuel assemblies is provided to show the similarities and differences between coupling values. All these values can be observed in Figure 4.11.

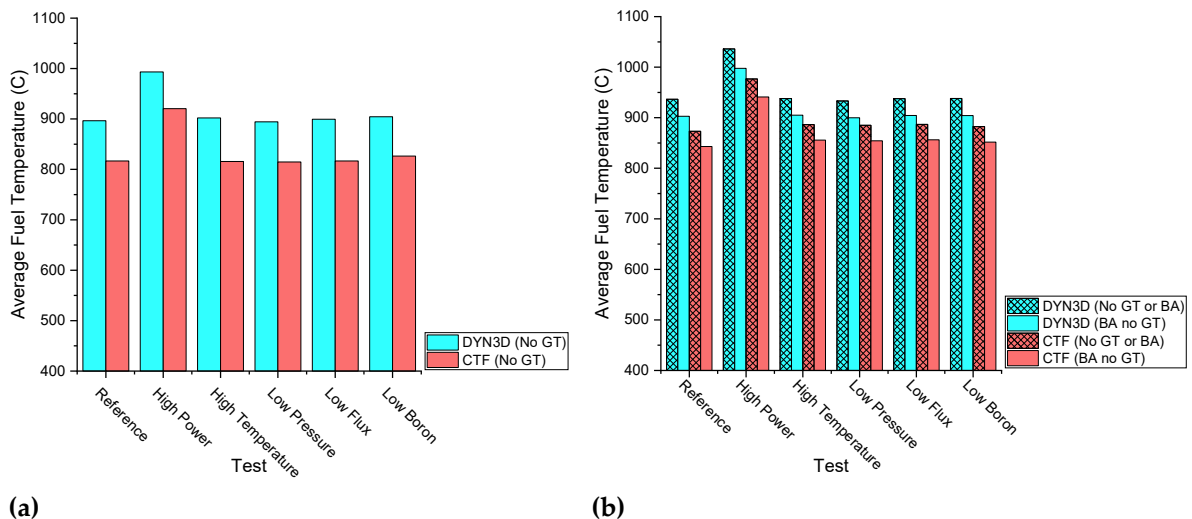


Figure 4.11. (a) UOX-2 (CR) fuel temperature feedback values, (b) UOX-2 (BA16) fuel temperature feedback values.

Both FLOCAL and CTF derive the fuel temperature from the solid enthalpy, which is mainly obtained by solving the solid energy equation. In any case, the fuel temperature results from the volumetric heat density in the solid energy equation.

In both the DYN3D and the DYN3D and CTF couplings with or without burnable absorber pin cells and without guide tube cells, the fuel temperature feedback value between fuel pins at the average axial node layer was observed to increase in all the tests in the UOX-2 (BA16) fuel assembly when compared to the UOX-2 (CR) fuel assembly. This fuel temperature feedback value increase occurred due to lower powers in the burnable absorber pin cells, which resulted in higher powers in the fuel pin cells, leading to an equivalent total power as in the UOX-2 (CR) fuel assembly where there were equal powers in all the fuel pin cells, which resulted in higher solid enthalpies according to the solid energy equation.

In both the DYN3D and the DYN3D and CTF couplings with or without burnable absorber pin cells and without guide tube cells, the fuel temperature feedback value between fuel pins at the average axial node layer was observed to increase only with high power when compared to the reference in both the UOX-2 (CR) and in the UOX-2 (BA16) fuel assemblies. This fuel temperature feedback value increase occurred due to the higher volumetric heat density term, which resulted in higher solid enthalpies according to the solid energy equation. In both the DYN3D and the DYN3D and CTF couplings with or without burnable absorber pin cells and without guide tube cells, the fuel temperature feedback value between fuel pins at the average axial node layer was observed to remain constant with high temperature, low pressure, low flux, and low boron in both the UOX-2 (CR) and UOX-2 (BA16) fuel assemblies.

In both the DYN3D and the DYN3D and CTF couplings with or without burnable absorber pin cells and without guide tube cells, the fuel temperature feedback value between all fuel pins at the top axial node layer was observed in all the tests in both the UOX-2 (CR) and in the UOX-2 (BA16) fuel assemblies due to the absence of power in the guide tube cells.

In both the DYN3D and the DYN3D and CTF couplings with burnable absorber pin and without guide tube cells compared to without burnable absorber and guide tube cells, the fuel temperature feedback value between all fuel pins at the average axial node layer was observed to decrease in all the tests in the UOX-2 (BA16) fuel assembly. This fuel temperature feedback value decrease occurred due to lower power in the burnable absorber pin cells, leading to low temperatures in the burnable absorber pin cells, which resulted, in general, in lower solid enthalpies according to the solid energy equation.

Between the DYN3D and the DYN3D and CTF couplings with or without burnable absorber pin cells and without guide tube cells, the fuel temperature feedback value between fuel pins at the average axial node layer in both the UOX-2 (CR) and in the UOX-2 (BA16) fuel assemblies were

observed to be different. These fuel temperature feedback value differences occurred due to different terms in the solid energy equation. According to the obtained fuel temperature feedback values between fuel pins at the average axial node layer in the UOX-2 (CR) fuel assembly, the variations can be regarded as less compatible between both couplings than in the UOX-2 (BA16) fuel assembly, where all variations can be regarded as compatible between both couplings. Such variations can be regarded as compatible between couplings due to the similarity of the fuel temperature feedback values.

Axial fuel temperature feedback distributions for central, side, and corner fuel pins and average between fuel pins as well as transversal fuel temperature feedback distributions for all the fuel pins at the average axial node layer are provided for the UOX-2 (CR) fuel assembly compatible reference case to show the similarities and differences between both coupling distributions, as observed in Figures 4.12., 4.13., 4.14.

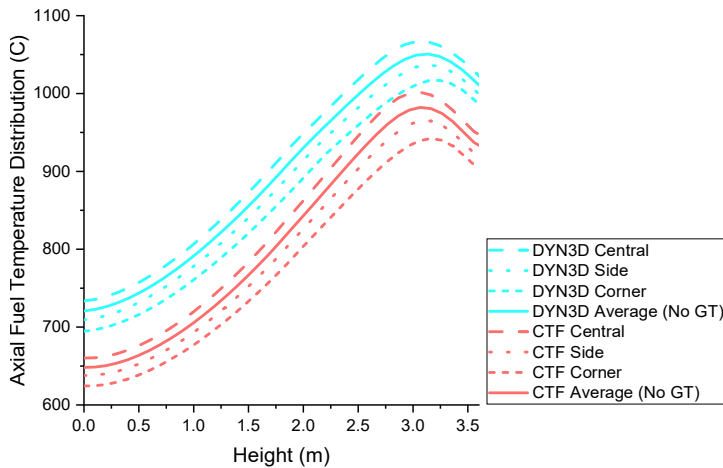


Figure 4.12. Axial fuel temperature feedback distributions.

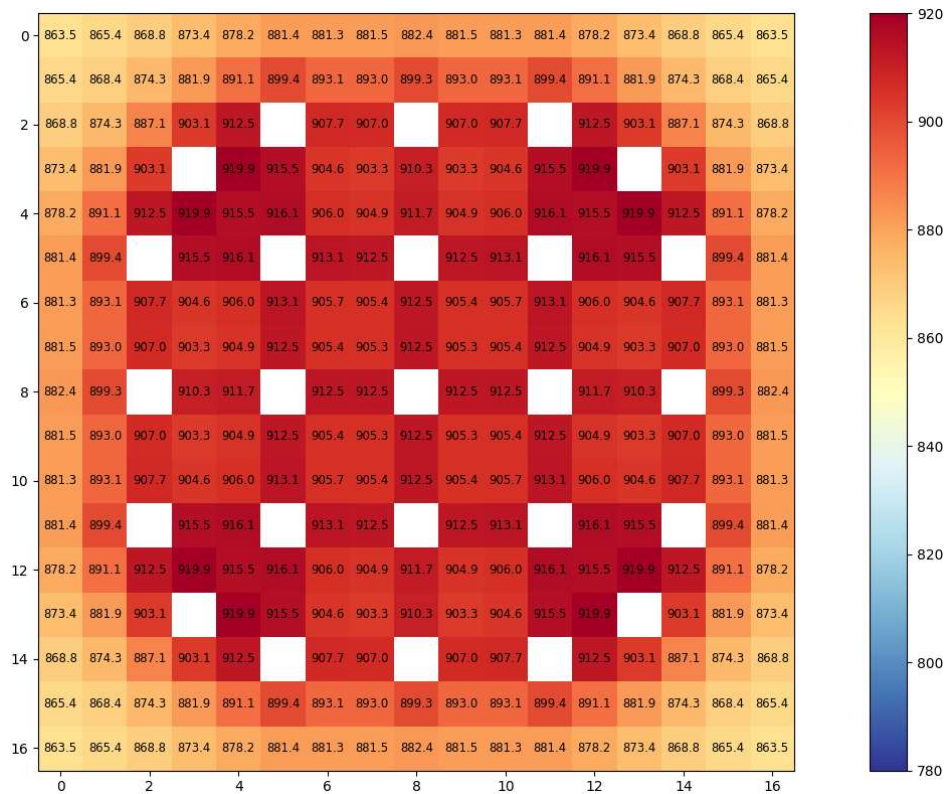


Figure 4.13. DYN3D coupling transversal fuel temperature feedback distribution.

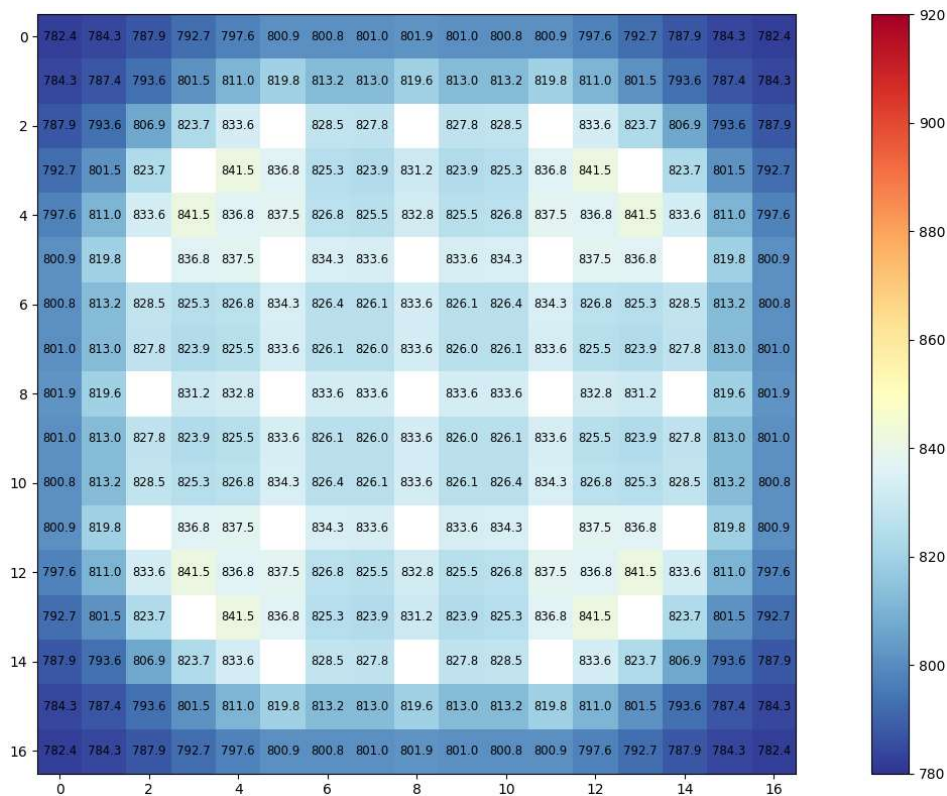


Figure 4.14. DYN3D and CTF coupling transversal fuel temperature feedback distribution.

In both the DYN3D and the DYN3D and CTF couplings, the axial fuel temperature feedback distribution for the central, corner, and side fuel pins as well as the transversal fuel temperature feedback distribution for all fuel pins at the average axial node layer in the UOX-2 (CR) fuel assembly compatible reference case were observed to increase more in the central fuel pins than in the side or corner fuel pins. This axial and transversal fuel temperature feedback distribution increase occurred in both couplings due to the fuel cell neighbours, leading to higher heat fluxes in the central fuel cells, which resulted in higher solid enthalpies according to the solid energy equation.

Between the DYN3D and the DYN3D and CTF couplings, the axial fuel temperature feedback distribution for the central, corner, and side fuel pins as well as the transversal fuel temperature feedback distribution for all the fuel pins at the average axial node layer in the UOX-2 (CR) fuel assembly compatible reference case were observed to be different. These axial and transversal fuel temperature feedback distribution differences occurred due to different terms in the solid energy equation.

The pressure drop feedback value in both the UOX-2 (CR) and the UOX-2 (BA16) fuel assemblies is provided to show the similarities and differences between coupling values. All these values can be observed in Figure 4.15.

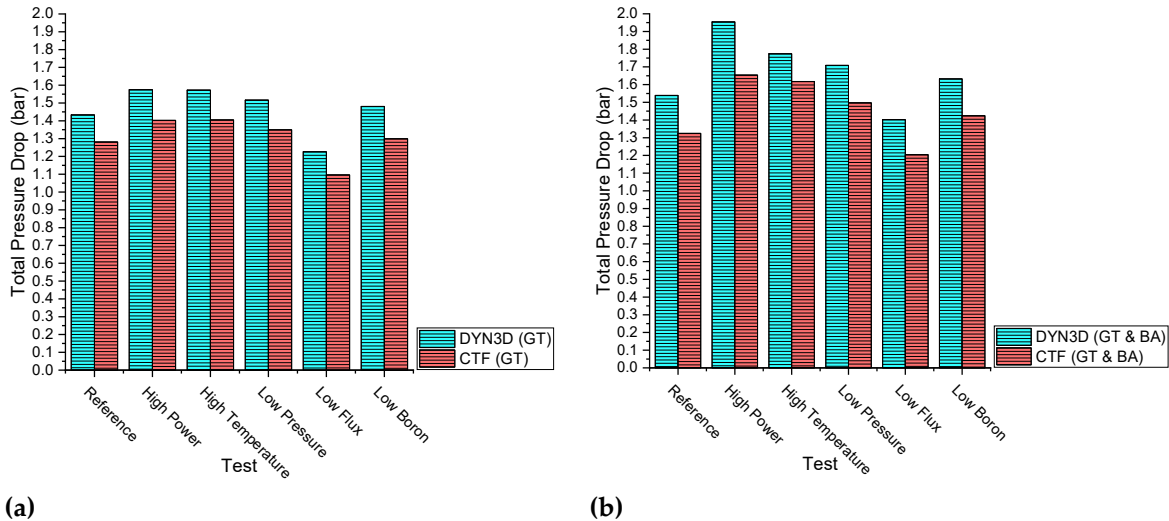


Figure 4.15. (a) UOX-2 (CR) pressure drop feedback values, (b) UOX-2 (BA16) pressure drop feedback values.

Both FLOCAL and CTF derive the pressure drop from the friction, form, gravity, and acceleration pressure losses, which are obtained through different pressure loss correlations. In any case, the pressure drop resulted from the pressure force term in the fluid momentum equation.

In both the DYN3D and the DYN3D and CTF couplings with burnable absorber pin and/or guide tube cells, the pressure drop feedback value observed to increase in all the tests in the UOX-2 (BA16) fuel assembly when compared to in the UOX-2 (CR) fuel assembly. This pressure drop feedback value increase occurred due to lower powers in the burnable absorber pin cells, which resulted in higher powers in the fuel pin cells, leading to a higher pressure drop as when there were equal powers in all the fuel pin cells, which resulted in higher friction and acceleration pressure losses according to the pressure loss correlations.

In both the DYN3D and the DYN3D and CTF couplings with burnable absorber pin and/or guide tube cells, the pressure drop feedback value was observed to increase with high power, high temperature, and low pressure when compared to the reference in both the UOX-2 (CR) and in the UOX-2 (BA16) fuel assemblies. This pressure drop feedback value increase occurred due to different reasons: In the high-power variation, this occurred due to the higher volumetric wall heat transfer term, which resulted in higher friction and acceleration pressure losses according to the pressure loss correlations. In the high temperature variation, this occurred due to the higher inlet fluid enthalpy, which resulted in higher friction and acceleration pressure losses according to the pressure loss correlations. In the low-pressure variation, this occurred due to the lower pressure force term which results on higher friction and acceleration pressure losses according to the pressure loss correlations. In both the DYN3D and the DYN3D and CTF couplings with burnable absorber pin and/or guide tube cells, the pressure drop feedback value was observed to decrease with low flux when compared to the reference in both the UOX-2 (CR) and in the UOX-2 (BA16) fuel assemblies. This pressure drop feedback value decrease occurred due to the lower inlet mass flow, which resulted in lower friction and acceleration pressure losses according to the pressure loss correlations. In both the DYN3D and the DYN3D-CTF couplings with burnable absorber pin and/or guide tube cells, the pressure drop feedback value was observed to remain constant in the UOX-2 (CR) and UOX-2 (BA16) fuel assemblies with low boron when compared to the reference.

In both the DYN3D and the DYN3D and CTF couplings with burnable absorber pin and/or guide tube cells, the pressure drop feedback value was observed in all the tests in both the UOX-2 (CR) and in the UOX-2 (BA16) fuel assemblies as in the DYN3D coupling where only the pressure drop feedback value for the whole fuel assembly was available, while in the DYN3D and CTF coupling, full pressure distributions for each fuel cell were available.

Between the DYN3D and the DYN3D and CTF couplings with burnable absorber pin and/or guide tube cells, the pressure drop feedback values in the UOX-2 (CR) and in the UOX-2 (BA16) fuel

assemblies were observed to be different. These pressure drop feedback value differences occurred due to different friction and form pressure loss correlations. According to the obtained pressure drop feedback values in the UOX-2 (CR) fuel assembly, all variations can be regarded as compatible between both couplings while in the UOX-2 (BA16) fuel assembly, also all the variations can be regarded as compatible between both couplings. Such variations can be regarded as compatible between couplings due to the similarity of the pressure drop feedback values.

4.6. Conclusions

As has been observed, the current objective in the aim of coupling the nodal code DYN3D and the subchannel code CTF within the Multiscale and Multiphysics Software Development has been fulfilled as the coupling inner iterations within one outer iteration have been partially verified, providing improved coupled reactor physics at the fuel pin level, allowing to show through external coupling, the transfer of power distributions from DYN3D to CTF as well as the transfer of feedback distributions from CTF to DYN3D and as justify through thermal hydraulics when to use the DYN3D coupling and when to use the DYN3D and CTF coupling. The improved coupled reactor physics at the fuel pin level in the DYN3D and CTF coupling were only limited in terms of neutronics by neutron diffusion but complemented in terms of thermal hydraulics by the wide range of cross flow and turbulent mixing.

Considering the coupled reactor physics at the fuel pin level obtained using both the DYN3D and the DYN3D and CTF couplings through the replication of the KAIST benchmark, the DYN3D and CTF coupling provides improved feedback at the fuel pin level compared to the DYN3D coupling in the cases of the fluid density feedback, fluid temperature feedback, fuel temperature feedback, and pressure drop feedback. This may be in the case of the fluid density feedback due to different terms in the fluid mass equation including the evaporation as well as the crossflow and turbulent mixing models between fuel cells as the DYN3D and CTF coupling contains the latter models, as opposed to the DYN3D coupling. This may be the case of the fluid temperature feedback due to different terms in the fluid energy equation including the nucleate boiling correlation as well as the crossflow and turbulent mixing models between fuel cells as the DYN3D and CTF coupling contains the latter models, as opposed to the DYN3D coupling. This may be the case of the fuel temperature feedback due to different terms in the solid energy equation as the DYN3D and CTF coupling contains different models to the DYN3D coupling. This may be, in the case of the pressure drop feedback, due to different friction and form loss correlations as the DYN3D and CTF coupling contains different models to the DYN3D coupling.

In general, the DYN3D coupling provides similar feedback values as the DYN3D and CTF coupling, however, the DYN3D and CTF coupling provides improved feedback distributions over the DYN3D coupling as crossflow and other terms are modelled in the latter. Nevertheless, the DYN3D coupling requires lower simulation times than the DYN3D and CTF coupling to achieve results, as simulation times in the DYN3D coupling were around 1 to 2 min compared to 20 or more minutes in the DYN3D and CTF coupling, using in both cases a single core as conducted in serial simulations as opposed to multiple cores used in parallel simulations.

4.7. Future Work

Finally, the last objective in the aim of coupling the nodal code DYN3D and the subchannel code CTF within the Multiscale and Multiphysics software consists of the second part of the DYN3D and CTF coupling that will be performed to evaluate all outer iterations within the convergence criteria to provide fully verified improved coupled reactor physics at the fuel pin level. This evaluation will allow one to show through other couplings how the outer iterations within the convergence criteria takes place as well as justify through the neutronics when the DYN3D and CTF coupling, rather than just DYN3D, should be used to provide improved coupled reactor physics at the fuel pin level, or when LOTUS and any other fluid dynamics coupling should be used to provide full coupled reactor physics at the fuel pin level. The most pragmatic approach will always be taken to improve the economics and safety of nuclear reactors.

4.8. Nomenclature

The acronyms and symbols in the overall text have an associated meaning given below.

Acronyms:

Acronym	Full Description
ADF	Assembly Discontinuity Factor
AMR	Advanced Modular Reactor
ATHLET	Analysis of Thermal Hydraulics of Leaks and Transients
BA16	16 Burnable Absorber Pins
BEIS	Department of Business, Energy, and Industrial Strategy
CASL	Consortium for Advanced Simulation of LWRS
CATHARE	Code for Analysis of Thermal Hydraulics during an Accident of Reactor and Safety Evaluation
CFD	Computational Fluid Dynamics
CTF/COBRA-TF	Coolant Boiling in Rod Arrays Two Fluid
CR	Control Rods
DNB/DNBR	Departure from Nucleate Boiling
DRD	Digital Reactor Design
DYN3D/FLOCAL	Dynamical 3 Dimensional
EPR	European Pressurised Reactor
FORTTRAN	Formula Translator
HPC	Hinkley Point C
HZDR	Helmholtz Zentrum Dresden Rossendorf
KAIST	Korean Advanced Institute of Science and Technology
LOTUS	Liverpool Transport Solver
LWR	Light Water Reactor
NCSU	North Carolina State University
NRC	Nuclear Regulation Commission
NURESIM	Nuclear Reactor Simulator
PNL	Pacific Northwest Laboratories
PSU	Pennsylvania State University
PWR	Pressurised Water Reactor
RELAP5	Reactor Excursion and Leak Analysis Program
SCANAIR	Systems of Codes for Analysing Reactivity Initiated Accidents
UK	United Kingdom
UOL	University of Liverpool

Symbols:

Symbol	Full Description
BA16	16 Burnable Absorber Pins
$c_{p_{clad}}$	Clad Specific Heat
$c_{p_{fuel}}$	Fuel Specific Heat
k_{clad}	Clad Thermal Conductivity
k_{fuel}	Fuel Thermal Conductivity
Fe	Iron
Gd ₂ O ₃	Digadolinium Trioxide
He	Helium
²³⁵ U, ²³⁸ U	Uranium Isotopes
UO ₂	Uranium Dioxide
Sn	Tin
Zr	Zirconium

Author Contributions: S.D., as the main author, wrote this article including the introduction, codes used in the verification, specifications used in the verification, models and scripts used in the verification, results and analysis, conclusions, and future work. D.L., as the next author, provided LOTUS as a result of being the developer and introduced the Multiscale and Multiphysics Software Development. U.R., as the next author, provided FLOCAL as a result of being the developer. A.D., as the next author, provided the fuel pin cross sections using SCALE-POLARIS. B.M. and A.L., as the next authors and academic supervisors, provided help from a theoretical perspective. P.B., as the next author and industrial supervisor, provided help from a theoretical perspective. V.R., as the last author and advisor, provided help from a practical perspective. All authors have read and agreed to the published version of the manuscript.

Funding: This research was funded by the EPSRC, EDF, and the UOL through the funding of the EPSRC grant “Innovative LWR Simulation Tool for the Nuclear Renaissance in the UK”, EPSRC grant number EP/R005850/1.

Institutional Review Board Statement: Not applicable.

Data Availability Statement: See the references.

Conflicts of Interest: The authors declare no conflicts of interest. The funders had no role in the design of the study; in the collection, analyses, or interpretation of data; in the writing of the manuscript, or in the decision to publish the results.

4.9. Appendix A: Code Types

The spectral, lattice, neutron transport, nodal, system, subchannel, CFD, and fuel performance codes and risk assessment codes mentioned in the introduction are classified according to their type and developer in Table 4.A1.

Table 4.A1. Code descriptions.

Code	Type	Developer
ORIGEN	Spectral	ORNL
SCALE	Spectral	ORNL
APOLLO2	Lattice	Areva
INSILICO	Neutron Transport	UT-Batelle
LOTUS	Neutron Transport	UOL
MPACT	Neutron Transport	ORNL
SHIFT	Neutron Transport	ORNL
COBAYA3	Nodal	UPM
CRONOS2	Nodal	CEA-Saclay
DYN3D	Nodal	HZDR
ATHLET	System	GRS
CATHARE	System	CEA-Grenoble
RELAP5	System	INL
CTF	Subchannel	PNL
FLICA4	Subchannel	Cea-Saclay
SUBCHANFLOW	Subchannel	KIT
HYDRA-TH	CFD	INL
NEPTUNE	CFD	EDF
TRANS-AT	CFD	TRANS-AT
TRIO_U	CFD	IRSN
BISON	Fuel Performance	INL
DRACCAR	Fuel Performance	IRSN

4.10. Appendix B: KAIST Benchmark

The location of the UOX-2 (CR) and the UOX-2 (BA16) fuel assemblies within the LWR reactor core are presented in Figure 4.A1.

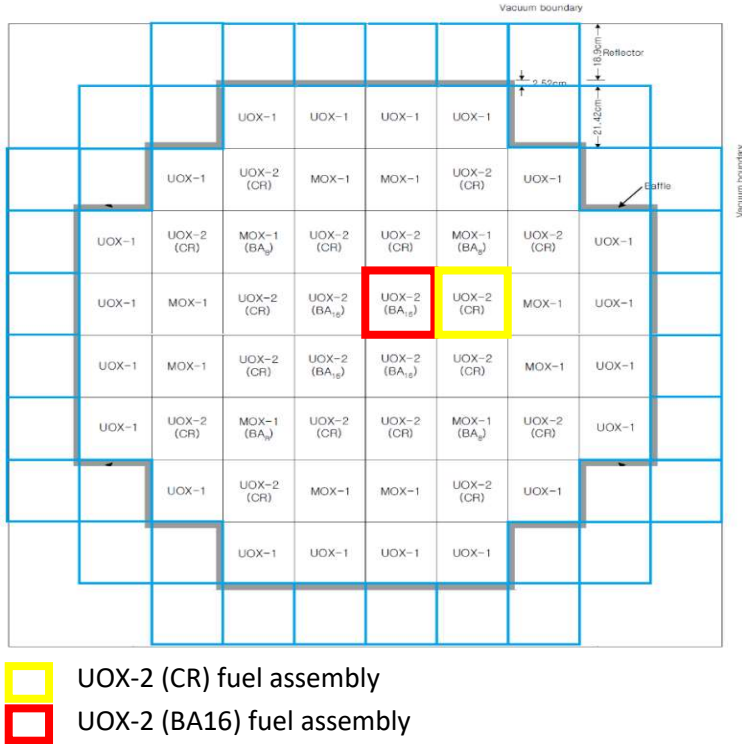


Figure 4.A1. UOX-2 (CR) and UOX-2 (BA16) locations within the KAIST 1A LWR reactor core.

The mass flux feedback value between fuel cells at the average axial node layer in both the UOX-2 (CR) and the UOX-2 (BA16) fuel assemblies is provided to show the similarities and differences between coupling values. All these values can be observed in Figure 4.A2.

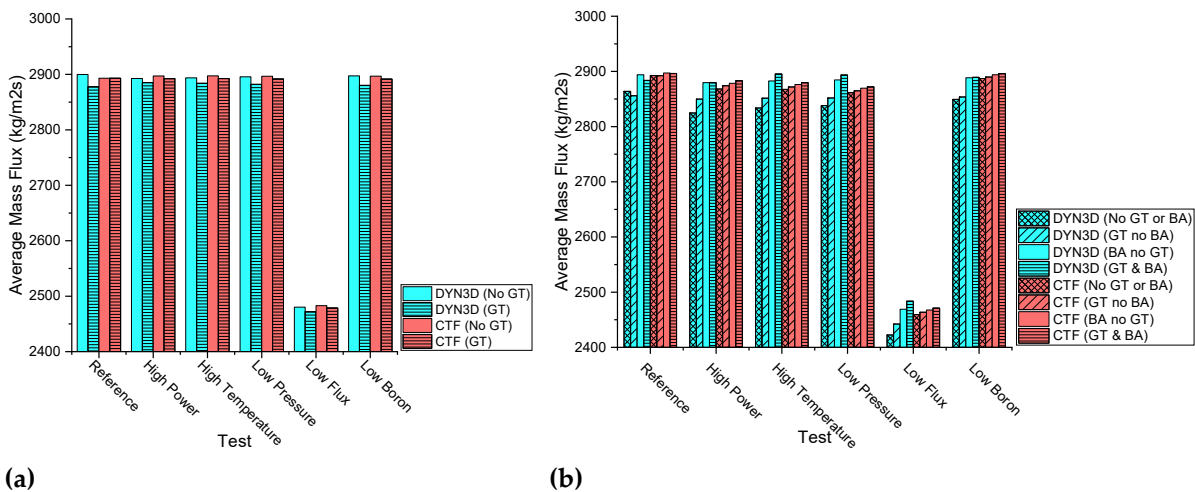


Figure 4.A2. (a) UOX-2 (CR) mass flux feedback values, (b) UOX-2 (BA16) mass flux feedback values.

Both FLOCAL and CTF derive the mass flux from the fluid density and fluid velocity, which are mainly obtained by solving the fluid mass and fluid momentum equations.

In both the DYN3D and the DYN3D and CTF couplings with or without burnable absorber pin and/or guide tube cells, the mass flux feedback value between fuel cells at the average axial node layer was observed to remain similar in all the tests in the UOX-2 (BA16) fuel assembly when compared to the UOX-2 (CR) fuel assembly. This mass flux feedback value near equivalence occurred due to mass conservation in the corresponding test.

In both the DYN3D and the DYN3D and CTF couplings with or without burnable absorber pin and/or guide tube cells, the mass flux feedback value between fuel cells at the average axial node layer was observed to decrease only with low flux when compared to the reference in both the UOX-2 (CR) and UOX-2 (BA16) fuel assemblies. This mass flux feedback value decrease occurred due to the lower inlet mass flow, which resulted in lower fluid densities as well as higher vapor and lower liquid velocities according to the fluid mass and fluid momentum equations. In both the DYN3D and the DYN3D and CTF couplings, the mass flux feedback value between fuel cells at the average axial node layer was observed to remain constant with high power, high temperature, low pressure, and low boron when compared to the reference in both the UOX-2 (CR) and in the UOX-2 (BA16) fuel assemblies.

In the DYN3D coupling with burnable absorber pin and/or guide tube cells compared to without burnable absorber pin and/or guide tube cells, the mass flux feedback value between all fuel cells at the average axial node layer was observed to decrease in all the tests in the UOX-2 (CR) fuel assembly and increase in all the tests in the UOX-2 (BA16) fuel assembly. This mass flux feedback value decrease and increase occurred, in particular, due to either the absence of power in the guide tube cells or lower power in the burnable absorber pin cells as well as in general due to the lack of mass and momentum transfer between fuel cells, leading to higher mass flux in either the guide tube or burnable absorber pin cells, which resulted, in general, in higher fluid densities, lower vapor, and higher liquid velocities according to the fluid mass and fluid momentum equations.

In the DYN3D and CTF coupling with burnable absorber pin and/or guide tube cells compared to without burnable absorber pin and/or guide tube cells, the mass flux feedback value between fuel cells at the average axial node layer was observed to decrease in all the tests in the UOX-2 (CR) fuel assembly and increase in all the tests in the UOX-2 (BA16) fuel assembly. This mass flux feedback value decrease and increase occurred, in general, due to the presence of mass and momentum transfer between fuel cells, leading to homogeneous mass flux in both the guide tube and burnable absorber pin cells, which resulted, in general, in almost unchanged fluid densities, vapor, and liquid velocities according to the fluid mass and fluid momentum equations.

Between the DYN3D and the DYN3D and CTF couplings with or without burnable absorber pin and/or guide tube cells, the mass flux feedback values between fuel cells at the average axial node layer in both the UOX-2 (CR) and in the UOX-2 (BA16) fuel assemblies were observed to be different. These mass flux feedback value differences occurred due to different terms in the fluid mass and fluid momentum equations including the evaporation, viscous stress as well as the crossflow and turbulent mixing models between fuel cells. According to the obtained mass flux feedback values between fuel cells at the average axial node layer in the UOX-2 (CR) fuel assembly, most variations can be regarded as compatible between both couplings while in the UOX-2 (BA16) fuel assembly, also most of the variations can be regarded as compatible between both couplings. Such variations can be regarded as compatible between couplings due to the similarity of the mass flux feedback values.

Axial mass flux feedback distributions for central, side, and corner fuel cells and average between fuel cells as well as transversal mass flux feedback distributions for all the fuel cells at the average axial node layer are provided for the UOX-2 (CR) fuel assembly compatible reference case to show the similarities and differences between both coupling distributions, as observed in Figures 4.A3, 4.A4, 4.A5.

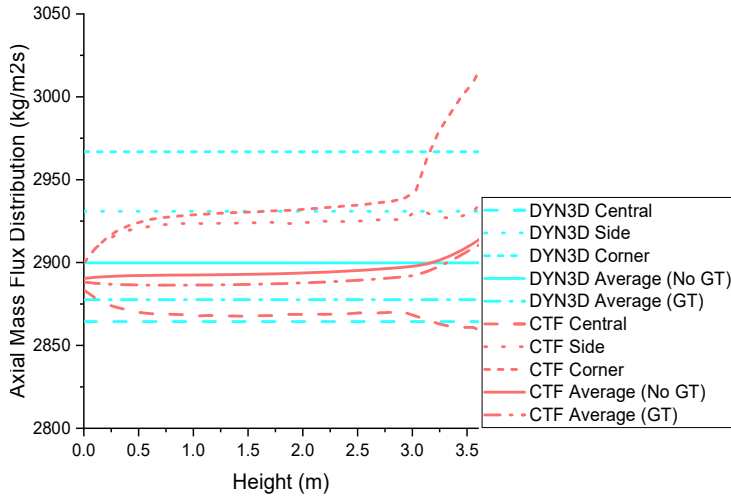


Figure 4.A3. Axial mass flux feedback distribution.

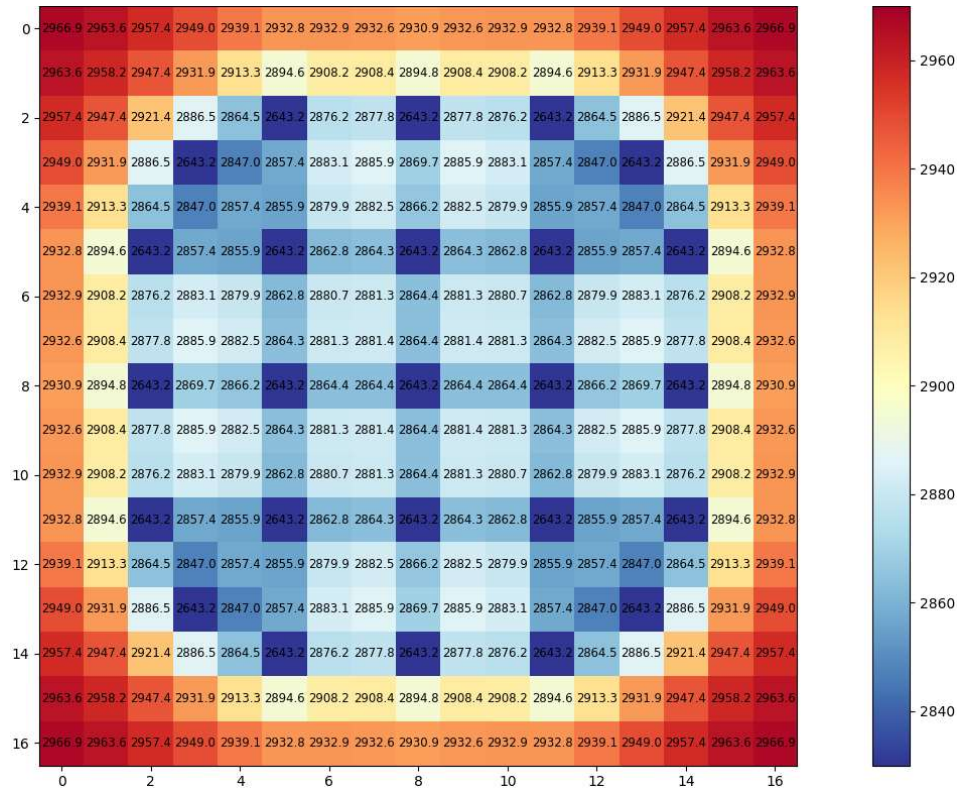


Figure 4.A4. DYN3D coupling transversal mass flux feedback distribution.

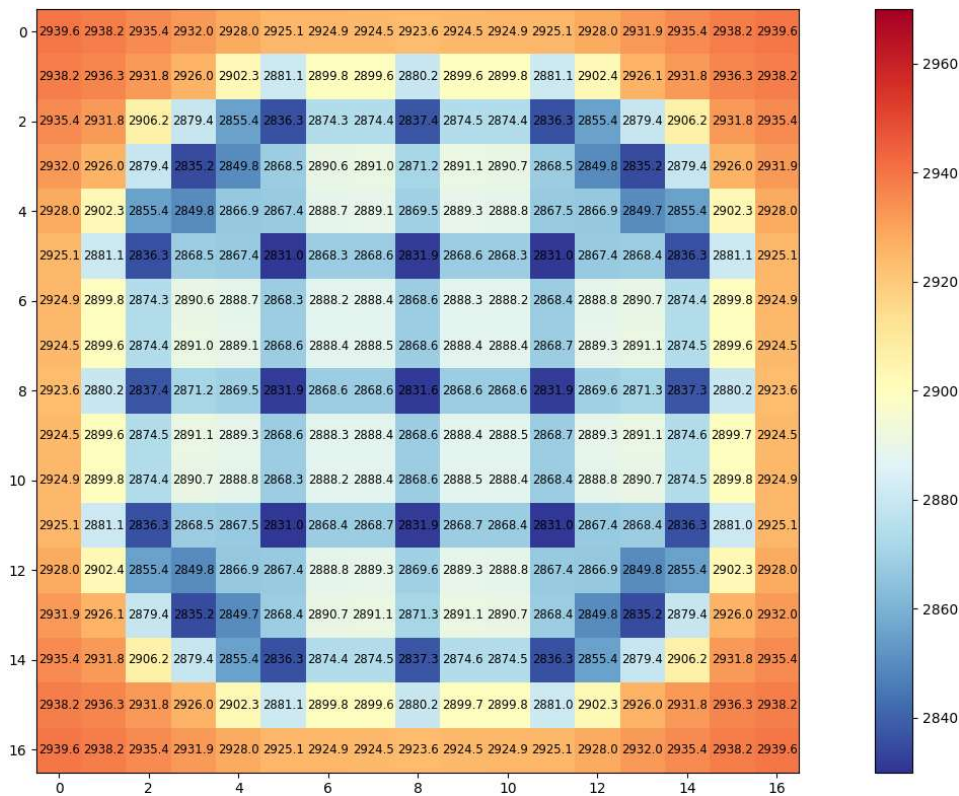


Figure 4.A5. DYN3D and CTF coupling transversal mass flux feedback distribution.

In both the DYN3D and the DYN3D and CTF couplings, the axial mass flux feedback distribution in the central, side, and corner fuel cells as well as the transversal mass flux feedback distribution for all fuel cells at the average axial node layer in the UOX-2 (CR) fuel assembly compatible reference case was observed to decrease more in the central than in the side or corner fuel cells. This axial and transversal mass flux feedback distribution decrease occurred in both couplings due to the fuel cell neighbours, leading to higher heat fluxes in the central fuel cells, which resulted in lower fluid densities, higher vapor, and lower liquid velocities according to the fluid mass and fluid momentum equations.

Between the DYN3D and the DYN3D and CTF couplings, the axial mass flux feedback distribution for the central, corner, and side fuel cells as well as the transversal mass flux feedback distribution for all the fuel cells at the average axial node layer in the UOX-2 (CR) fuel assembly compatible reference case were observed to be different. These axial and transversal mass flux feedback distribution differences occurred due to different terms in the fluid mass and fluid momentum equations including the evaporation, viscous stress as well as the crossflow and turbulent mixing models between fuel cells.

The void fraction feedback value between fuel cells at the top axial node layer in both the UOX-2 (CR) and the UOX-2 (BA16) fuel assemblies is provided to show the similarities and differences between coupling values. All these values can be observed in Figure 4.A6.

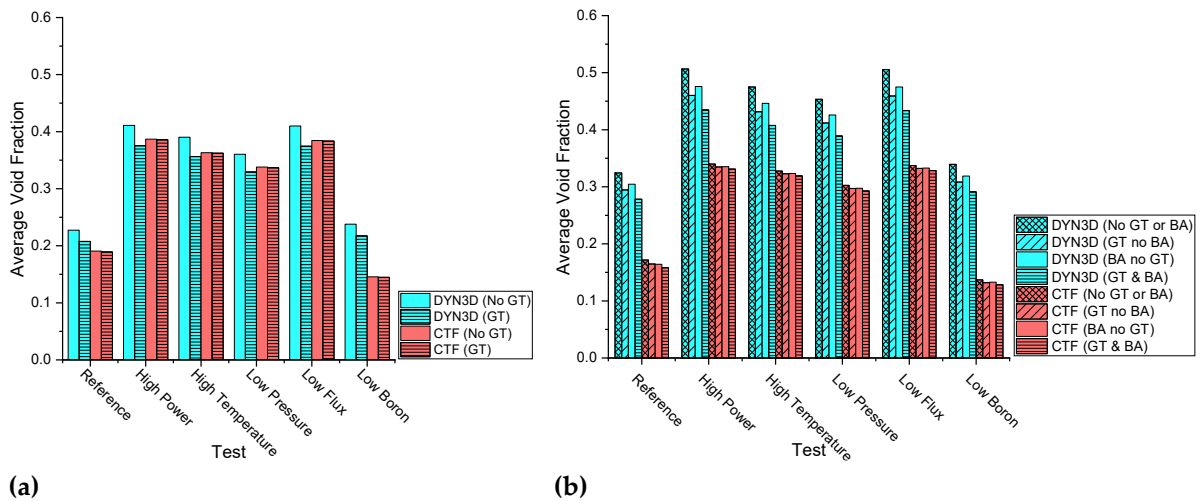


Figure 4.A6. (a) UOX-2 (CR) void fraction feedback values, (b) UOX-2 (BA16) void fraction feedback values.

Both FLOCAL and CTF derive the void fraction from the fluid density, fluid velocity, and fluid enthalpy, which are mainly obtained by solving the fluid mass, fluid momentum, and fluid energy equations.

Only in the DYN3D coupling with or without burnable absorber pin and/or guide tube cells, the void fraction feedback value between fuel cells at the top axial node layer was observed to increase in all the tests in the UOX-2 (BA16) fuel assembly when compared to in the UOX-2 (CR) fuel assembly. This void fraction feedback value increase occurred due to lower powers in the burnable absorber pin cells, which resulted in higher powers in the fuel pin cells, leading to an equivalent total power as when there were equal powers in all the fuel pin cells, which resulted in lower fluid densities, higher vapor, and lower liquid velocities as well as higher fluid enthalpies according to the fluid mass, fluid momentum, and fluid energy equations.

In both the DYN3D and the DYN3D and CTF couplings with or without burnable absorber pin and/or guide tube cells, the void fraction feedback value between fuel cells at the top axial node layer was observed to increase with high power, high temperature, low-pressure, and low flux when compared to the reference in both the UOX-2 (CR) and in the UOX-2 (BA16) fuel assemblies. This void fraction feedback value increase occurred due to different reasons: in the high-power variation, this occurred due to the higher volumetric wall heat transfer term, which resulted in lower fluid densities, higher vapor, and lower liquid velocities as well as higher fluid enthalpies according to the fluid energy equation. In the high temperature variation, this occurred due to higher inlet fluid enthalpy, which resulted in higher fluid enthalpies according to the fluid energy equation. In the low-pressure variation, this occurred due to the lower pressure force term, which resulted in lower fluid densities, higher vapor, and lower liquid velocities according to the fluid mass and fluid momentum equations. In the low mass flux variation, this occurred due to the lower inlet mass flow, which resulted in lower fluid densities, higher vapor, and lower liquid velocities as well as higher fluid enthalpies according to the fluid mass, fluid momentum, and fluid energy equations. Only in the DYN3D and CTF coupling with or without burnable absorber pin and/or guide tube cells was the void fraction feedback value between the fuel cells at the top axial node layer observed to decrease with low boron when compared to the reference in both the UOX-2 (CR) and in the UOX-2 (BA16) fuel assemblies. This void fraction feedback value decrease occurred due to the full boron transport model in the DYN3D and CTF coupling, which resulted in higher liquid velocities according to the boron tracking and precipitation equations when compared to the simplified boron transport model in the DYN3D coupling, which resulted in almost constant liquid velocities according to the simplified boron transport equation.

In the DYN3D coupling with burnable absorber pin and guide tube cells compared to without burnable absorber pin and/or guide tube cells, the void fraction feedback value between fuel cells at the top axial node layer was observed to decrease in all the tests in both the UOX-2 (CR) and in the UOX-2 (BA16) fuel assemblies. This void fraction feedback value decrease occurred, in particular, due

to either the absence of power in the guide tube cells or lower power in the burnable absorber pin cells as well as in general due to the lack of mass, momentum, and energy transfer between fuel cells, leading to no vapor in the guide tube cells and low vapor in the burnable absorber pin cells, which resulted, in general, in higher fluid densities, lower vapor, and higher liquid velocities as well as higher fluid enthalpies according to the fluid mass, fluid momentum, and fluid energy equations.

In the DYN3D and CTF coupling with burnable absorber pin and guide tube cells compared to without burnable absorber pin and/or guide tube cells, the void fraction feedback value between fuel cells at the top axial node layer was observed to remain almost unchanged in all the tests in both the UOX-2 (CR) and in the UOX-2 (BA16) fuel assemblies. This void fraction feedback value near equivalence occurred, in general, due to the presence of mass, momentum, and energy transfer between fuel cells, leading to homogeneous vapor in both the guide tube cells and burnable absorber pin cells, which resulted, in general, in unchanged fluid densities, vapor, and liquid velocities as well as higher fluid enthalpies according to the fluid mass, fluid momentum, and fluid energy equations.

Between the DYN3D and the DYN3D and CTF couplings with or without burnable absorber pin and/or guide tube cells, the void fraction feedback values between all fuel cells at the top axial node layer in both the UOX-2 (CR) and in the UOX-2 (BA16) fuel assemblies were observed to be different. These void fraction feedback value differences occurred due to different terms in the fluid mass, fluid momentum, and fluid energy equations including the evaporation, viscous stress, nucleate boiling correlations as well as the crossflow and turbulent mixing models between fuel cells. According to the obtained void fraction feedback values between fuel cells at the top axial node layer in the UOX-2 (CR) fuel assembly, most variations can be regarded as compatible between both couplings, while in the UOX-2 (BA16) fuel assembly, almost none of the variations can be regarded as compatible between both couplings. Such variations can be regarded as compatible between couplings due to the similarity in the void fraction feedback values.

Axial void fraction feedback distributions for central, side, and corner fuel cells and average between fuel cells as well as transversal void fraction feedback distribution for all the fuel cells at the top axial node layer are provided for the UOX-2 (CR) fuel assembly compatible reference case to show the similarities and differences between both coupling distributions, as observed in Figures 4.A7, 4.A8, 4.A9.

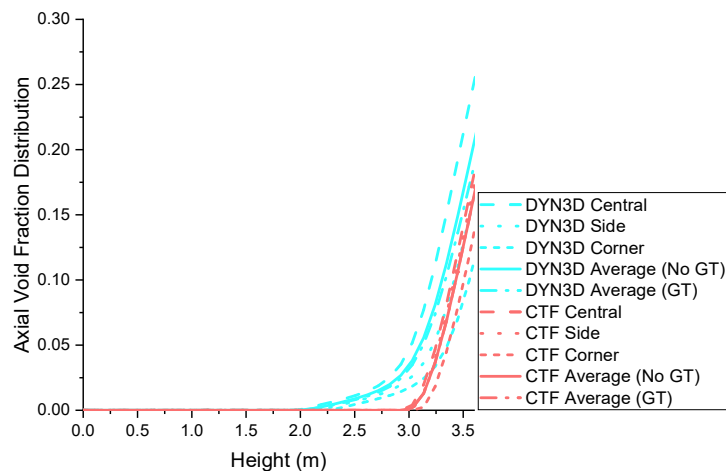


Figure 4.A7. Axial void fraction feedback distribution.

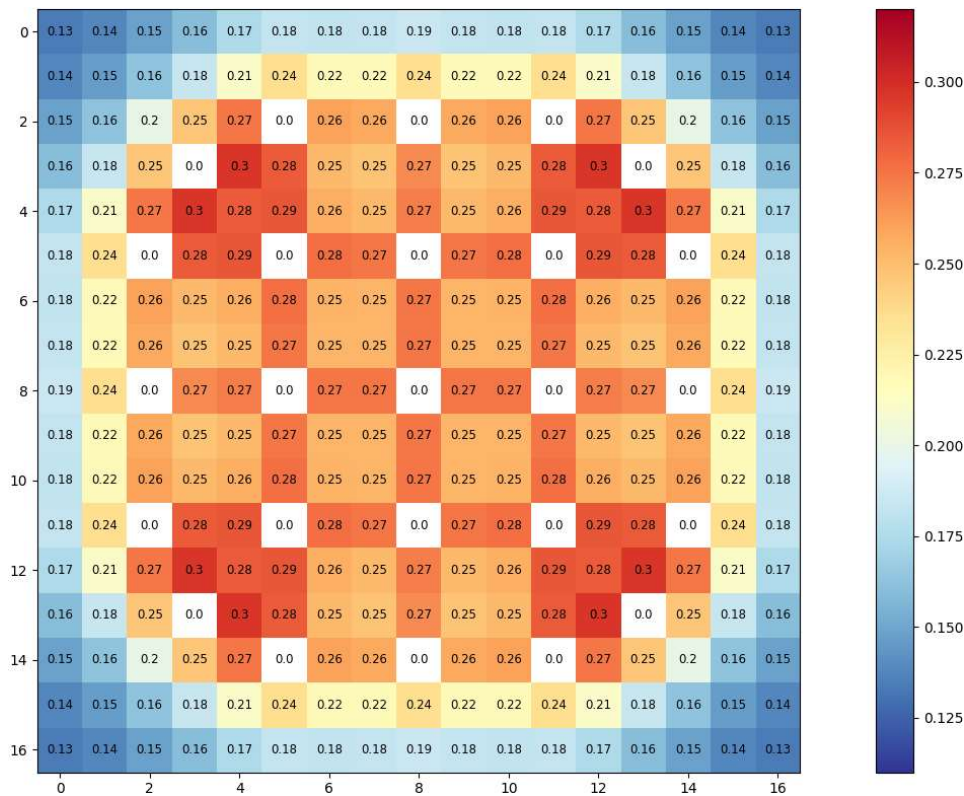


Figure 4.A8. DYN3D coupling transversal void fraction feedback distribution.

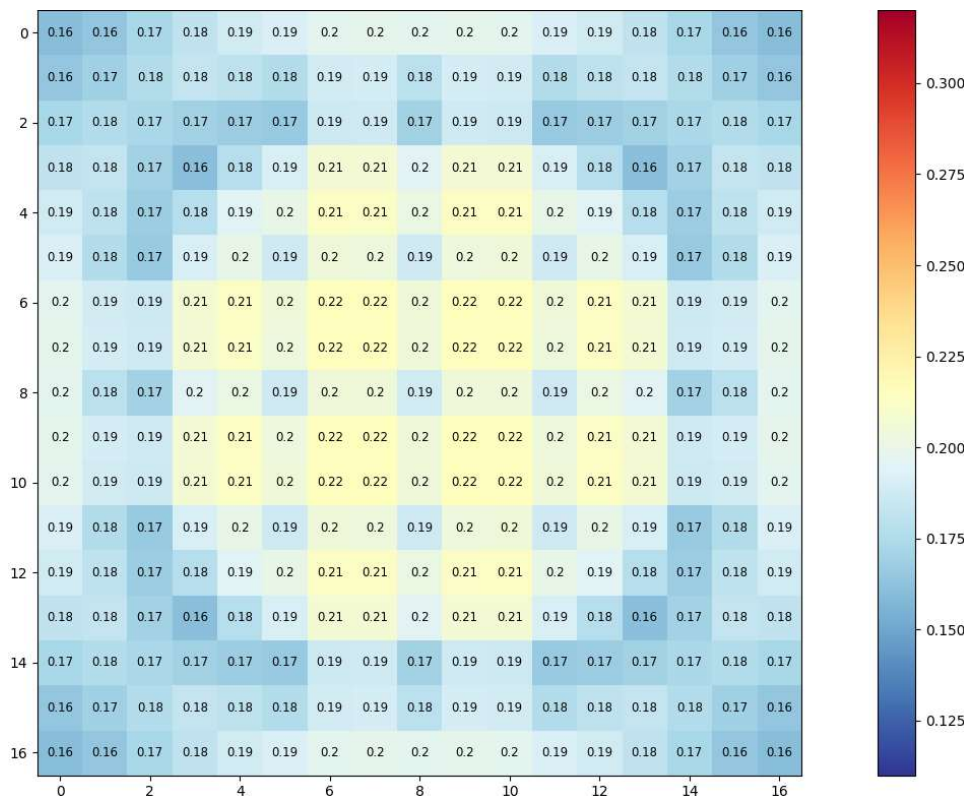


Figure 4.A9. DYN3D and CTF coupling transversal void fraction feedback distribution.

In both the DYN3D and the DYN3D and CTF couplings, the axial void fraction feedback distribution for the central, side, and corner fuel cells as well as the transversal void fraction feedback distribution for all fuel cells at the top axial node layer in the UOX-2 (CR) fuel assembly compatible

reference case was observed to increase more in the central than in the side or corner fuel cells. This axial and transversal void fraction feedback distribution increase occurred in both couplings due to the fuel cell neighbours, leading to higher heat fluxes in the central fuel cells, which resulted, in general, in higher fluid densities, lower vapor, and higher liquid velocities as well as higher fluid enthalpies according to the fluid mass, fluid momentum, and fluid energy equations.

Between the DYN3D and the DYN3D and CTF couplings, the axial void fraction feedback distribution for the central, corner, and side fuel cells as well as the transversal void fraction feedback distribution for all the fuel cells at the top axial node layer for the UOX-2 (CR) fuel assembly compatible reference case was observed to be higher in the DYN3D coupling and lower in the DYN3D and CTF coupling. These axial and transversal void fraction feedback distribution differences occurred due to different terms in the fluid mass, fluid momentum, and fluid energy equations including the evaporation, viscous stress, nucleate boiling correlations as well as the crossflow and turbulent mixing models between fuel cells.

The relative departure from nucleate boiling feedback value between fuel pins at the top axial node layer in both the UOX-2 (CR) and the UOX-2 (BA16) fuel assemblies is provided to show the similarities and differences between coupling values. All these values can be observed in Figure 4.A10.

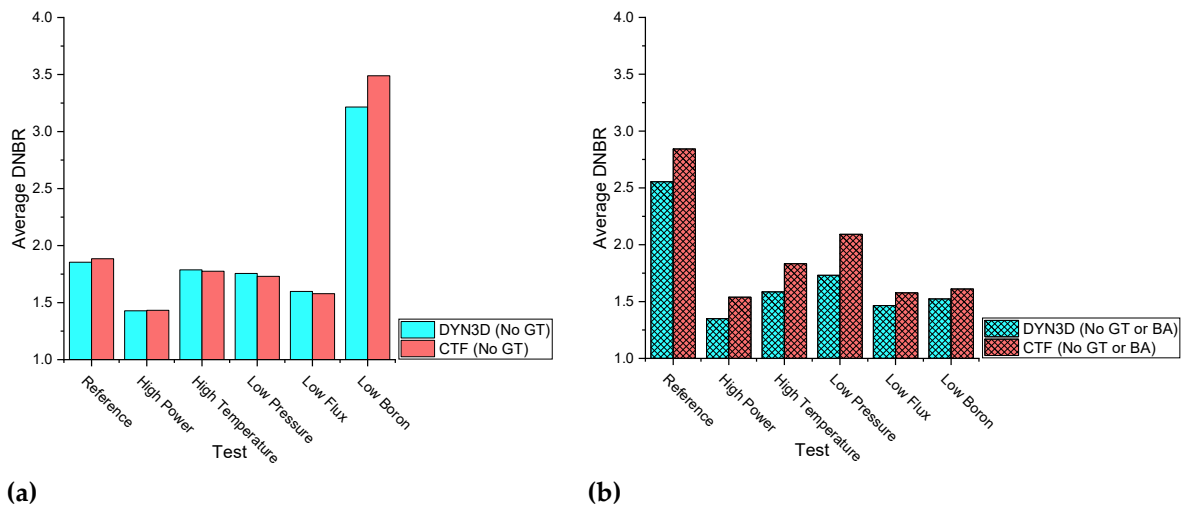


Figure 4.A10. (a) UOX-2 (CR) DNBR feedback values, (b) UOX-2 (BA16) DNBR feedback values.

Both FLOCAL and CTF derive the relative departure from nucleate boiling from the heat flux, which is mainly obtained by solving the solid energy equation as well as the critical heat flux, which is obtained using different empirical departure from nucleate boiling correlations.

In both the DYN3D and the DYN3D and CTF couplings without burnable absorber pin and/or guide tube cells, the relative departure from nucleate boiling feedback value between fuel pins at the top axial node layer was observed to decrease in some tests in the UOX-2 (BA16) fuel assembly when compared to the UOX-2 (CR) fuel assembly. This relative departure from nucleate boiling feedback value decrease occurred due to lower powers in the burnable absorber pin cells, which resulted in higher powers in the fuel pin cells, leading to an equivalent total power as when there were equal powers in all the fuel pin cells, which resulted in higher heat fluxes according to the solid energy equation.

In both the DYN3D and the DYN3D and CTF couplings without burnable absorber pin and/or guide tube cells, the relative departure from nucleate boiling feedback value between fuel pins at the top axial node layer was observed to decrease with high power, high temperature, low-pressure, and low flux when compared to the reference in both the UOX-2 (CR) and in the UOX-2 (BA16) fuel assemblies. This relative departure from the nucleate boiling feedback value decrease occurred due to different reasons: in the high-power variation, this occurred due to the higher volumetric wall heat transfer term, which resulted in higher heat fluxes according to the solid energy equation. In the high temperature variation, this occurred due to higher inlet fluid enthalpy, which resulted in higher critical heat fluxes according to the departure from nucleate boiling correlation. In the low-pressure variation,

this occurred due to the lower pressure force term, which resulted in lower critical heat fluxes according to the critical heat flux correlation. In the low mass flux variation, this occurred due to the lower inlet mass flow, which resulted in lower critical heat fluxes according to the critical heat flux correlation. In both the DYN3D and the DYN3D and CTF couplings without burnable absorber pin and/or guide tube cells, the relative departure from nucleate boiling feedback value between fuel pins at the top axial node layer was observed to decrease with low boron when compared to the reference in the UOX-2 (BA16) fuel assembly. This relative departure from nucleate boiling feedback value increase in the low boron variation occurred due to the lower boric acid concentration term, which resulted in more heterogeneous heat fluxes according to the solid energy equation.

In both the DYN3D and the DYN3D and CTF couplings without burnable absorber pin and/or guide tube cells, the relative departure from nucleate boiling feedback value between all fuel pins at the top axial node layer was observed in all the tests in both the UOX-2 (CR) and in the UOX-2 (BA16) fuel assemblies due to either the absence of power in the guide tube cells or lower power in the burnable absorber pin cells, which resulted in higher relative departure from nucleate boiling feedback value in both the guide tube cells and burnable absorber pin cells.

Between the DYN3D and the DYN3D and CTF couplings without burnable absorber pin and guide tube cells, the relative departure from nucleate boiling feedback values between fuel pins at the top axial node layer in both the UOX-2 (CR) and in the UOX-2 (BA16) fuel assemblies were observed to be different. These relative departure from nucleate boiling feedback value differences occurred due to different critical heat flux correlations. According to the obtained relative departure from nucleate boiling feedback values between fuel pins at the top axial node layer in the UOX-2 (CR) fuel assembly, most variations can be regarded as compatible between both couplings while in the UOX-2 (BA16) fuel assembly, also most of the variations can be regarded as compatible between both couplings. Such variations can be regarded as compatible between couplings due to the similarity of the relative departure from nucleate boiling feedback values.

Axial relative departure from nucleate boiling feedback distributions for central, side, and corner fuel pins and average between fuel pins as well as transversal relative departure from nucleate boiling feedback distributions for all the fuel pins at the top axial node layer is provided for the UOX-2 (CR) fuel assembly compatible reference case to show the similarities and differences between both coupling distributions, as observed in Figures 4.A11, 4.A12, 4.A13.

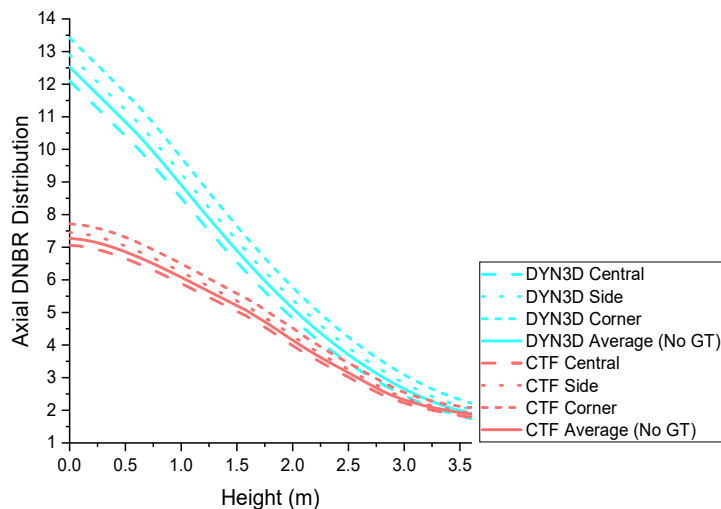


Figure 4.A11. Axial DNBR feedback distribution.

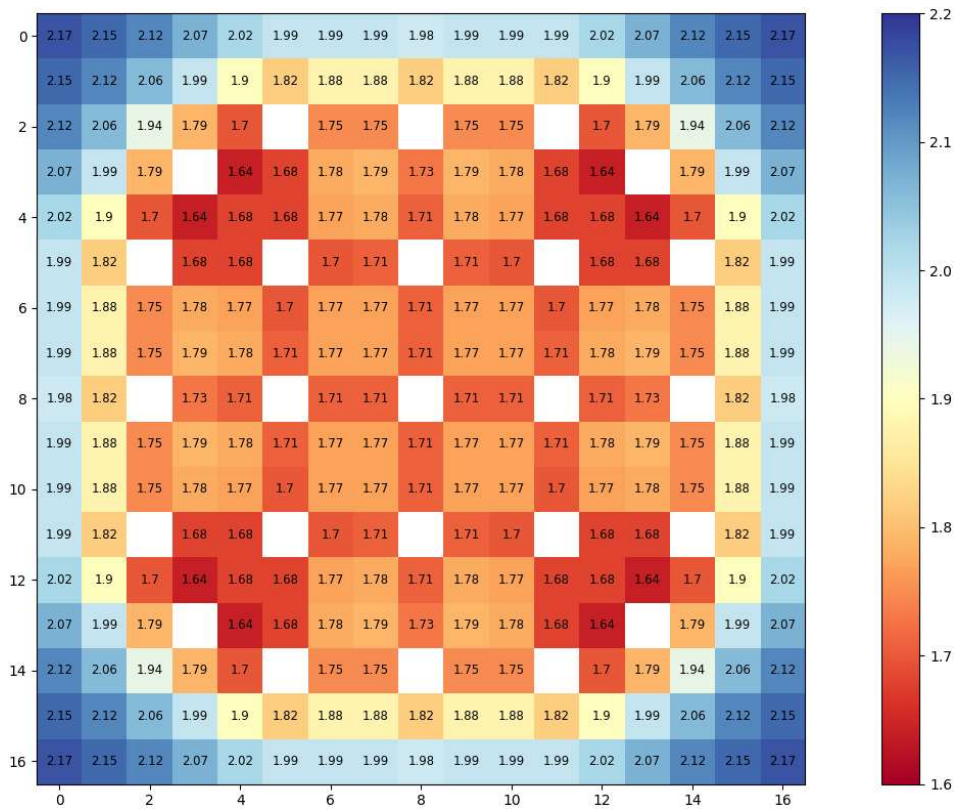


Figure 4.A12. DYN3D coupling transversal DNBR feedback distribution.

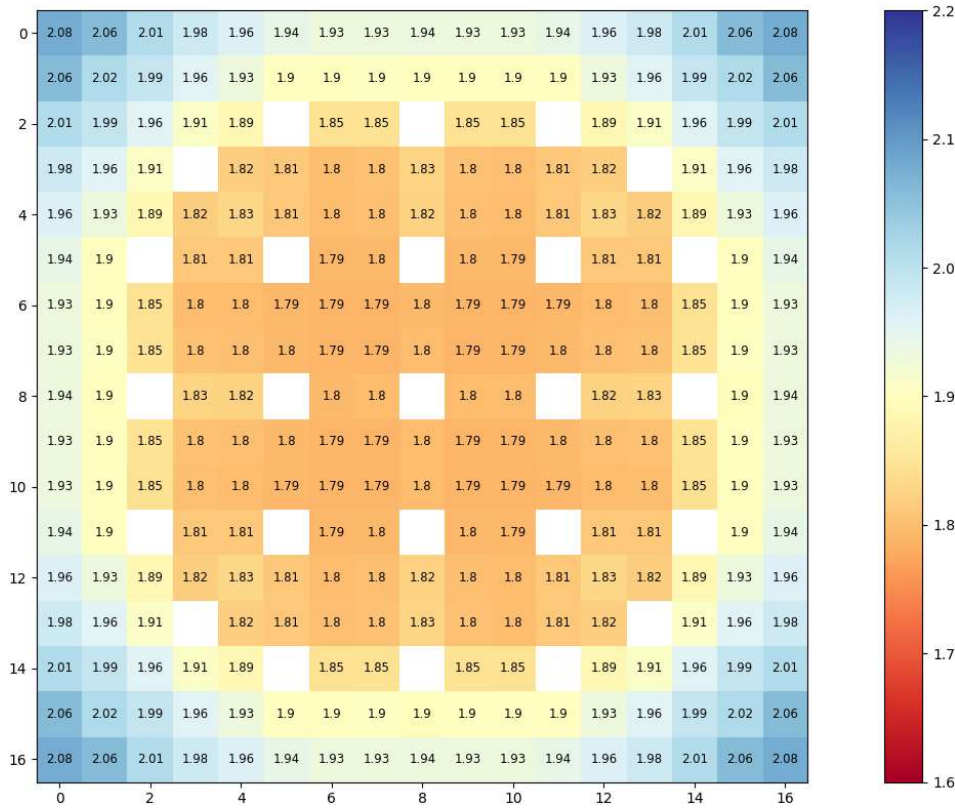


Figure 4.A13. DYN3D and CTF coupling transversal DNBR feedback distribution.

In both the DYN3D and the DYN3D and CTF couplings, the axial relative departure from nucleate boiling feedback distribution for the central, corner, and side fuel pins as well as the

transversal relative departure from nucleate boiling feedback distribution for all fuel pins at the top axial node layer in the UOX-2 (CR) fuel assembly compatible reference case was observed to decrease more for the central fuel pins than for the side or corner fuel pins. This axial and transversal relative departure from nucleate boiling feedback distribution decrease occurred in both couplings due to the fuel cell neighbours, leading to higher heat fluxes in the central fuel cells according to the solid energy equation.

Between the DYN3D and the DYN3D and CTF couplings, the axial relative departure from nucleate boiling feedback distribution for the central, corner, and side fuel pins as well as the transversal departure from nucleate boiling distribution for all the fuel pins at the top axial node layer in the UOX-2 (CR) fuel assembly compatible reference case were observed to be different. These axial and transversal relative departures from nucleate boiling feedback distribution differences occurred due to different critical heat flux correlations.

4.11. References

1. World Nuclear Association. World Nuclear Power Performance Report; World Nuclear Association: London, UK, 2020; pp. 1–68.
2. Institution of Electric Engineers. Nuclear Reactor Types; Institution of Electric Engineers: London, UK, 2005; pp. 1–15, ISBN 085-296-581-8.
3. Health and Safety Executive. Public Report on the Generic Design Assessment of New Nuclear Reactor Designs; Health and Safety Executive: Merseyside, UK, 2007; pp. 1–38.
4. UK Government Funding for Nuclear Innovation. Available online: <https://www.gov.uk/guidance/funding-for-nuclear-innovation> (accessed on 13 August 2021).
5. EDF Nuclear New Build Projects. Available online: <https://www.edfenergy.com/energy/nuclear-new-build-projects> (accessed on 13 August 2021).
6. Rolls Royce UK Small Modular Reactor: Pioneering Intelligent Power. Available online: <https://www.rolls-royce.com/products-and-services/nuclear/small-modular-reactors.aspx#/> (accessed on 13 August 2021).
7. Kyrieleis, A. Digital Reactor Design. Presented at Nuclear Virtual Engineering Capability. Warrington, UK, October 2019; pp. 1–30.
8. Lee, J.C.; Arbor, A. Nuclear Reactor Physics and Engineering; John, W., Sons, Eds.; Department of Nuclear Engineering, The University of Michigan: Ann Arbor, MI, USA, 2020.
9. Duderstadt, J.J.; Hamilton, L.J. Nuclear Reactor Analysis; John Wiley & Sons: Hoboken, NJ, USA; Department of Nuclear Engineering, The University of Michigan: Ann Arbor, MI, USA, 1975.
10. Rubén, J.; Perelló, B. Development of a Coupled Neutronics/Thermal-Hydraulics/Fuel Thermo-Mechanics Multiphysics Tool for Best-Estimate PWR Core Simulations; Karlsruhe Institut für Technologie: Karlsruhe, Germany, 2020, pp. 1–172.
11. Hooper, R.; Spatz, W.; Lorber, A.; Schmidt, R. A Multi-Physics Coupling Approach for Integrated Nuclear Reactor Safety Calculations; Presented at National Nuclear Security Administration: Anaheim, CA, USA, June 2008; pp. 1–26.
12. Gaston, D.R.; Permann, C.J.; Peterson, J.W.; Andrew, E.; Slaughter, D.A.; Wang, Y.; Short, M.P.; Perez, D.M.; Tonks, M.R.; Ortensi, J.; et al. Physics-based multiscale coupling for full core nuclear reactor simulation. *Ann. Nucl. Energy* 2015, 84, 45–54. ISSN 0306-4549.
13. Romano, P.K.; Forget, B. The OpenMC Monte Carlo Particle Transport Code. *Ann. Nucl. Energy* 2013, 51, 274–281, doi:10.1016/j.anucene.2012.06.040.
14. Litskevich, D. Development of an Advanced Neutron Transport Solver for Zooming in DYN3D; Rheinisch-Westfälischen Technischen Hochschule Aachen: Aachen, Germany, 2017; pp. 1–148.
15. Detkina, A.; Peakman, A.; Litskevich, D.; Liang, J. Evaluation of BWR Burnup Calculations Using Deterministic Lattice Codes SCALE-6.2, WIMS-10A and CASMO5. *Energies* 2020, 13, 2573, doi:10.3390/en13102573.
16. Omar, M.R.; Karim, J.A.; Yoon, T.L. The development of a multigroup Monte Carlo code for TRIGA reactors. *Nucl. Eng. Des.* 2019, 342, 99–114, doi:10.1016/j.nucengdes.2018.11.039.

17. Rohde, U.; Grundmann, U.; Kliem, S. DYN3D—Advanced Reactor Simulations in 3D; Nuclear Energy Review 2007/II; Forschung Dresden Rossendorf: Dresden, Germany, 2007; pp. 1–4.
18. EDF UK PANTHER: PWR AGR Neutronics Thermal Hydraulics Evaluation Route. Available online: <https://www.answerssoftwareservice.com/panther/> (accessed on 13 August 2021).
19. Bahadir, T.; Lindahl, S-O. Studsvik’s next generation nodal code SIMULATE-5. In Proceedings of the Advances in Nuclear Fuel management IV, Hilton Head Island, SC, USA, 12–15 April 2009; pp. 1–12.
20. Davies, S.; Rohde, U.; Litskevich, D.; Merk, B.; Bryce, P.; Levers, A.; Detkina, A.; Atkinson, S.; Ravindra, V. CTF and FLOCAL Thermal Hydraulics Validations and Verifications within a Multiscale and Multiphysics Software Development. *Energies* 2021, 14, 1220, doi:10.3390/en14051220.
21. Imke, U.; Sanchez, V.H. Validation of the Subchannel Code SUBCHANFLOW Using the NUPEC PWR Tests (PSBT). *Hindawi* 2012, 12, doi:10.1155/2012/465059.
22. Bajorek, S.M.; Bernard, M.; Gingrich, C.; Hoxie, C.L.; Ireland, A.; Kelly, J.; Mahaffy, J.; Murray, C.; Spore, J.; Staudenmeier, J.; et al. Development, Validation and Assessment of the Trace Thermal Hydraulics System Code. In Proceedings of the 16th International Topical Meeting on Nuclear Reactor Thermal Hydraulics, Chicago, IL, USA, 30 August–4 September 2015; Volume 14, pp. 1–14.
23. Rossiter, G. Development of the ENIGMA fuel performance code for whole core analysis and dry storage assessments. *Nucl. Eng. Technol.* 2011, 43, 489–498.
24. Magni, A.; Nevo, A.D.; Luzzi, L.; Rozzia, D.; Adorni, M.; Schubert, A.P. Van Uffelen Chapter 8—The TRANSURANUS fuel performance code. *Woodhead Publ.* 2021, 8, 161–205, doi:10.1016/B978-0-12-818190-4.00008-5.
25. Aybar, H.Ş.; Ortego, P. A review of nuclear fuel performance codes. *Prog. Nucl. Energy* 2005, 46, doi:10.1016/j.pnucene.2005.01.004.
26. Patelli, E. COSSAN: A Multidisciplinary Software Suite for Uncertainty Quantification and Risk Management; Springer: Switzerland, 2015, doi:10.1007/978-3-319-12385-1, ISBN 9783319123851.
27. Chauliac, C.; Aragones, J.; Bestion, D.; Weiss, F.-P. NURESIM—A European simulation platform for nuclear reactor safety: Multi-scale and multi-physics calculations, sensitivity and uncertainty analysis. *Nucl. Eng. Des.* 2011, 241, 3416–3426.
28. Euratom NURESIM Nuclear Reactor Safety Simulation Platform. Available online: <https://cordis.europa.eu/project/id/323263> (accessed on 13 August 2021).
29. Szilard, R.; Zhang, H.; Kothe, B.D.; Turinsky, P. CASL The Consortium for Advanced Simulation of Light Water Reactors; INL: Idaho Falls, ID, USA, 2011; INL/CON-11-22917.
30. US Department of Energy CASL Consortium for Advanced Simulation of Light Water Reactors. Available online: <https://casl.gov/> (accessed on 13 August 2021).
31. Bergeaud, V.; Tajchman, M. Application of the SALOME Software Architecture to Nuclear Reactor Research. *Soc. Comput. Simul. Int.* 2007, 2, 383–387, doi:1565553136.
32. Sanchez, R.; Mondot, J.; Stankovski, Z.; Cossic, A. APOLLO II: A User-Oriented, Portable, Modular Code for Multigroup Transport Assembly Calculations. *Nucl. Sci. Eng.* 1988, 100, 352–362.
33. Jimenez, G.; Herrero, J.J.; Cuervo, D.; Garcia-Herranz, N.; AShnert, C. Boron dilution benchmark using COBAYA3/FLICA4 coupled codes within the NURISP European Project. In Proceedings of the 38 Annual Meeting of Spanish Nuclear Society, Caceres, Spain, 17–19 October 2012; Volume 44094049.
34. Rohde, U.; Pivovarov, V.A.; Matveev, Y.A. Studies on boiling water reactor design with reduced moderation and analysis of reactivity accidents using the code DYN3D-MG. *Kerntechnik* 2012, 77, 240–248, doi:10.3139/124.110249.
35. Höhne, T.; Bieder, U.; Prasser, H.-M.; Kliem, S. Validation of Trio_U for Transient Accident Scenarios—Numerical Simulations Of A Rocom Buoyancy Driven Test Case. In Proceedings of the 12th International Conference on Nuclear Engineering (ICONE-12), Washington DC, USA, 25–29 April 2004.

36. Karlsruhe Institute of Technology Subchannel Flow. Available online: <https://www.inr.kit.edu/english/1008.php> (accessed on 13 August 2021).
37. Toumi, I.; Bergeron, A.; Gallo, D.; Royer, E.D. Caruge FLICA-4: A three-dimensional two-phase flow computer code with advanced numerical methods for nuclear applications. *Nucl. Eng. Des.* 2000, 200, 139–155.
38. Guelfi, A.; Bestion, D.; Boucker, M.; Pascal, B.; Philippe, F.; Marc, G. NEPTUNE: A New Software Platform for Advanced Nuclear Thermal Hydraulics. *Nucl. Sci. Eng.* 2007, 156, 281–324, doi:10.13182/NSE05-98.
39. Labois, M.; Narayanan, C.; Lakehal, D. PTS Prediction Using (the) CMFD Code TransAT: The COSI Test Case. In *Computational Fluid Dynamics (CFD) for Nuclear Reactor Safety Applications—Workshop Proceedings*; NEA: France, 2012; p. 1231.
40. Geffraye, G.; Antoni, O.; Farvacque, M.; Kadri, D.; Lavialle, G.; Rameau, B.; Ruby, A. CATHARE 2 V2.5_2: A single version for various applications. *Nucl. Eng. Des.* 2011, 241, 4456–4463, ISSN 0029-5493.
41. Di Marcello, V.; Escalante, J.J.; Espinoza, V.S. Validation of the thermal-hydraulic system code ATHLET based on selected pressure drop and void fraction BFBT tests. *Nucl. Eng. Des.* 2015, 288, 183–194.
42. Georges, R.; Francois, J.; Francois, B.; Francois, L.; Jean-Marc, R. DRACCAR, a new 3D-thermal mechanical computer code to simulate LOCA transient on nuclear power plants Status of the development and the validation. In *Proceedings of the International Congress on Advances in Nuclear Power Plants*; Japan, 10-14 May 2009; p. 2572.
43. Moal, A.; Georgenthum, V.; Marchand, O. SCANAIR: A transient fuel performance code: Part One: General modelling description. *Nucl. Eng. Des.* 2014, 280, 150–171, doi:10.1016/j.nucengdes.2014.03.055.
44. Kulesza, J.A.; Franceschini, F.; Evans, T.M.; Gehin, J.C. Overview of the Consortium for the Advanced Simulation of Light Water Reactors (CASL). *EPJ Web Conf.* 2016, 106, 8, doi:10.1051/epjconf/201610603002.
45. Nuclear Energy Agency. ORIGEN-22, Isotope Generation and Depletion Code Matrix Exponential Method. Available online: <https://www.oecd-nea.org/tools/abstract/detail/ccc-0371> (accessed on 13 August 2021).
46. Rearden, B. T.; Anderson, J. M. SCALE Code System 6.2.1. *Int. At. Energy Agency* 2016, 48, 1–2712.
47. Kochunas, B.; Jabaay, D.; Downar, T.; Collins, B. S.; Stimpson, S. G.; Godfrey, A. T.. Validation and Application of the 3D Neutron Transport Code MPACT within CASL VERA-CS. In *Proceedings of the Conference: Sixteenth International Topical Meeting on Nuclear Reactor Thermal Hydraulics NURETH-16*, Chicago, IL, USA, 30 August–4 September 2015; pp. 1–14.
48. Hamilton, S.P.; Evans, M.E.; Davidson, G.G. Hot Zero Power Reactor Calculations Using the Insilico Code. Elsevier: Switzerland, 2016; Volume 314, p. 700-711, doi: 10.1016/j.jcp.2016.03.033.
49. Pandya, T.M.; Johnson, S.R.; Evans, T.M.; Gregory, G. Implementation, Capabilities, and Benchmarking of Shift, a Massively Parallel Monte Carlo Radiation Transport Code. Elsevier: Switzerland, 2015; Volume 308, p. 239-272, doi:10.1016/j.jcp.2015.12.037.
50. Zhao, X.; Wysocki, A.J.; Shirvan, K.; Salko, R.K. Assessment of the Subchannel Code CTF for Single-and Two-Phase Flows. 2019, 205, 338–351, doi:10.1080/00295450.2018.1507221.
51. Christon, M.A.; International, C.S.; Bakosi, J.; Lowrie, R.B.; Pritchett-sheats, L. Hydra-TH : A Thermal-Hydraulics Code for Nuclear Reactor Applications. In *Proceedings of the Conference: Fifteenth International Topical Meeting on Nuclear Reactor Thermal Hydraulics NURETH-15*, Pisa, Italy, 12–17 May 2013; pp. 1–33.
52. Hou, X.; Sun, Z.; Lei, W. Capability of RELAP5 code to simulate the thermal-hydraulic characteristics of open natural circulation. *Ann. Nucl. Energy* 2017, 109, 612–625, doi:10.1016/j.anucene.2017.06.010.
53. Merk, B.; Bankhead, M.; Litskevich, D.; Gregg, R.; Peakman, A.; Shearer, C. On a Roadmap for Future Industrial Nuclear Reactor Core Simulation in the U.K. to Support the Nuclear Renaissance. *Energies* 2018, 11, 3509, doi:10.3390/en1123509.

54. Labarile, A.; Olmo, N.; Miró, R.; Barrachina, T.; Verd, G. Comparison of SERPENT and SCALE methodology for LWRs transport calculations and additionally uncertainty analysis for cross-section perturbation with SAMPLER module. *EPJ Nucl. Sci. Technol.* 2016, 11, 1–14, doi:10.1051/epjn/e2016-50002-7.
55. Litskevich, D.; Atkinson, S.; Davies, S. Verification of the current coupling collision probability method with orthogonal flux expansion for the assembly calculations. *Prog. Nucl. Energy* 2020, 130, doi:10.1016/j.pnucene.2020.103562.
56. Jackson, P.; Turnbull, J.. Enigma Fuel Performance Code. *Nucl. Energy* 1990, 21, 107–114.
57. Torres, A.G.; Espinoza, V.S.; Imke, U.; Juan, R.M. Pin Level Neutronic—Thermalhydraulic Two-Way-Coupling Using DYN3D-SP3 And SUBCHANFLOW. In *Proceedings of the International Conference on Mathematics and Computational Methods Applied to Nuclear Science and Engineering*, Rio de Janeiro, 8–12 May 2011; pp. 1–20.
58. Atkinson, S.; Detkina, A.; Litskevich, D.; Merk, B. A Comparison of Advanced Boiling Water Reactor Simulations Between Serpent / CTF and Polaris / DYN3D: Steady State Operational Characteristics and Burnup Evolution. *Energies* 2021, 14, 40, doi:10.3390/en14040838 Academic.
59. Zimin, V.G.; Nikonov, S.P. Coupling of the Neutron Diffusion Code SKETCH-N and the Thermal-Hydraulics System Code ATHLET for VVER-1000 Calculations. In *Proceedings of the 28th Symposium of AER on VVER Reactor Physics and Reactor Safety Olomouc, Czechia*, 8–12 October 2018; pp. 1–20.
60. Rohde, U.; Kliem, S.; Grundmann etc. The reactor dynamics code DYN3D—Models, validation and applications. *Prog. Nucl. Energy* 2016, 89, 140, doi:10.1016/j.pnucene.2016.02.013.
61. Grundmann, U.; Rohde, U. The Code DYN3D/M2 for the Calculation of Reactivity Initiated Transients in Light Water Reactors with Hexagonal Fuel Elements—Code Manual and Input Data Description; Helmholtz-Zentrum Dresden-Rossendorf: Dresden, Germany, 2012.
62. Salko, R., Jr.; Avramova, M.; Wysocki, A.; Hu, J.; Toptan, A.; Porter, N.; Blyth, T.S. CTF 4.0 Theory Manual; ORNL: Oak Ridge, TN, USA, 2019; doi:10.2172/1550750.
63. Salko, R., Jr.; Avramova, M.; Wysocki, A.; Hu, J.; Toptan, A.; Porter, N.; Blyth, T.S. CTF 4.0 User Manual; ORNL: Oak Ridge, TN, USA, 2020; doi:10.2172/1737480.
64. Cho, N.Z. Benchmark Problem 1A: MOX Fuel-Loaded Small PWR Core (MOX Fuel with Zoning); KAIST/NurapT: Daejeon, Korea, 2000.
65. Rohde, U.; Grundmann, U. DYNAmical 3 Dimensional. Available online: <https://www.hzdr.de/db/Cms?pOid=11771&pNid=542> (accessed on 13 August 2021).
66. Avramova, M.; Toptan, A.; Porter, N. Coolant Boiling in Rod Arrays Two Fluid. Available online: <https://www.ne.ncsu.edu/rdfmg/cobra-tf/> (accessed on 13 August 2021).
67. Osmachkin, V.; Borisov, V. The hydraulic resistance of fuel rod bundles in a boiling water flow. *IAEA* 1970, 2, 24.
68. McAdams, W. Heat Transmission; Pub, K., Ed.; McGraw-Hill: New York, NY, USA, 1985; ISBN 0898748763.
69. Poljanin, L.; Ibragimov, M. Teploobmen v jadernikh reaktorakh. In *Ehnergoizdat*; USSR: Moscow, Russia, 1982; p. 296.
70. Thorn, B.J.R.S.; Walkert, W.M.; Fallon, T.A.; Reising, G.F.S. Boiling in Subcooled Water During Flow up Heated Tubes or Annuli. *Mater. Sci.* 1965, 180, 226–246, doi:10.1243/PIME_CONF_1965_180_117_02.
71. Bezrukov, Y.; Astakhov, V. Experimental investigation and static analysis of data on crisis of heat exchange in beams of rods for WWER reactors. *Teploehnergetika* 1976, 8, 80–82.
72. Tong, L.S. Prediction of Departure from Nucleate Boiling for an Axially Non-Uniform Heat Flux Distribution. *J. Nucl. Energy* 1967, 21, 221–248, doi:10.1016/S0022-3107(67)90054-8.
73. Tong, L. Boiling Crisis and Critical Heat Flux. IAEA: Pittsburgh, PA, USA, 1972; RN:4051410.
74. Rogers, J.T.; Rosehart, R.G. Mixing by Turbulent Interchange in Fuel Bundles. In *Correlations and Interfaces*; ASME: New York, NY, USA, 1972.

Chapter 5: Two Ways Coupling of a Nodal Code and a Subchannel Code

Partially improved coupled reactor physics were included in the DYN3D and CTF coupling at the fuel pin level after transferring the power distributions from the former to the latter. Improved coupled reactor physics have now been included in the DYN3D and CTF coupling at the fuel pin level after transferring the power distributions from the former to the latter and the feedback distributions from the latter to the former until achieving convergence. The coupling has been performed through modified and created modules within DYN3D and the customized coupling software environment.

The modified modules in DYN3D allow the decoupling of NK from FLOCAL and the coupling of CTF to DYN3D. The created modules within the customized coupling software environment execute a loop that runs DYN3D followed by fission power exportation, under relaxation, and importation, and then runs CTF followed by feedback exportation, under relaxation, and importation. Such loop is repeated until achieving small differences in the effective multiplication factor, fission power and feedback distributions. Hence, a verification of the outer coupling iterations and convergence in the DYN3D and CTF coupling has been performed through the modified KAIST benchmark.

The modified KAIST-1A benchmark [151] is a variation of the mentioned benchmark. It includes multi-parameter variation and full reactor start-up exercises that contain either two 17x17 fuel assemblies or two 51x51 mini cores with fuel pin cells and guide tubes, without or with burnable absorber pins and different boundary conditions. The generation of cross sections for two energy groups has been performed in SCALE-POLARIS through the ESSM and MOC methods. The simulation of the 17x17 fuel assemblies and 51x51 mini cores has been performed in DYN3D and CTF through mesh, two energy groups, NEM, partial reflection, either channel or subchannel, heat transfer, DNB, and friction pressure losses methods, without or with crossflow and turbulent mixing methods. A graphical abstract for this chapter can be seen in Figure 5.GA.

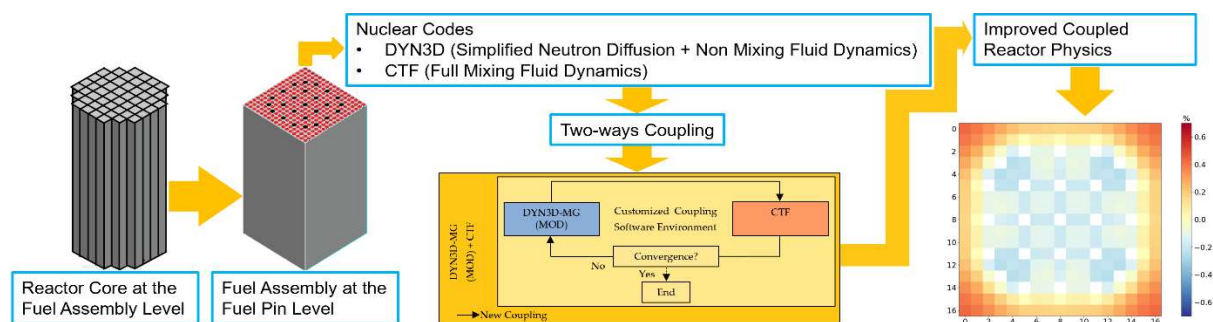


Figure 5.GA. Chapter 5 graphical abstract.

The verification of the outer coupling iterations and convergence in the DYN3D and CTF coupling when compared to DYN3D in the 17x17 fuel assemblies and 51x51 mini cores has shown some differences in the effective multiplication factor values, fission power distributions and the convergence of the absolute reactivity and maximum fission power. Effective multiplication factor, fission power, and reactivity differences, and slower convergence between fuel assembly or mini core types occurred due to the presence of burnable absorbers in one of them. Also, effective multiplication factor, fission power, and reactivity differences and variable convergence between the reference and other tests occurred due to the variation of the boundary conditions. Finally, effective multiplication factor, fission power, and reactivity differences and convergence between fuel cells occurred due to the fuel rod, heat transfer, interphase, crossflow, turbulent mixing, channel, subchannel and under-relaxation methods.

Hence, such verifications have proven that the DYN3D and CTF coupling provides improved coupled reactor physics using 1 processor within computational times of 1 to 10 hours, which further justifies its use to provide the mentioned at the fuel pin level. Also, such verifications have proven that DYN3D provides simplified coupled reactor physics using 1 processor within computational times of 2 to 20 minutes, which further justifies its use to provide the mentioned at either the fuel assembly or fuel pin level. This chapter contains the journal article DYN3D and CTF Coupling within a Multiscale and Multiphysics Software Development (Part II) [155], published in the MDPI Journal of Energies. All author contributions can be found in the list of publications section.

DYN3D and CTF Coupling within a Multiscale and Multiphysics Software Development (Part II)

Sebastian Davies ^{1,*}, Dzianis Litskevich ¹, Bruno Merk ¹, Andrew Levers ¹, Paul Bryce ² and Anna Detkina ¹

¹ School of Engineering, University of Liverpool, Liverpool L69 3GH, UK; dzianis@liverpool.ac.uk (D.L.); merk@liverpool.ac.uk (B.M.); alevvers@liverpool.ac.uk (A.L.); a.detkina@liverpool.ac.uk (A.D.)

² EDF Energy, Gloucester GL4 3R, UK; paul.bryce@edf-energy.com

* Correspondence: s.r.davies@liverpool.ac.uk; Tel.: +44-750-2270-482

Abstract: Traditionally, the complex coupled physical phenomena in nuclear reactors has resulted in them being treated separately or, at most, simplistically coupled in between within nuclear codes. Currently, coupling software environments are allowing different types of coupling, modularizing the nuclear codes or multi-physics. Several multiscale and multi-physics software developments for LWR are incorporating these to deliver improved or full coupled reactor physics at the fuel pin level. An alternative multiscale and multi-physics nuclear software development between NURESIM and CASL is being created for the UK. The coupling between DYN3D nodal code and CTF subchannel code can be used to deliver improved coupled reactor physics at the fuel pin level. In the current journal article, the second part of the DYN3D and CTF coupling was carried out to analyse a parallel two-way coupling between these codes and, hence, the outer iterations necessary for convergence to deliver verified improved coupled reactor physics at the fuel pin level. This final verification shows that the DYN3D and CTF coupling delivers improved effective multiplication factors, fission, and feedback distributions due to the presence of crossflow and turbulent mixing.

Keywords: nuclear software development; coupled reactor physics; nodal code; subchannel code; DYN3D; CTF; KAIST

5.1. Introduction

Nuclear technology development aims to both improve the existing nuclear reactors, as well as construct new nuclear reactors through innovation resulting in more efficient nuclear reactors [1]. It is usually performed by stages [2,3]. Initially, the requirements analysis is performed to understand the demands of a country. Then, the design is drafted to acknowledge all the components, such as reactor cores, pressurizers, steam generators, turbines, and condensers necessary to address the requirements analysis. Then, the improvement or construction of the nuclear reactor takes place according to the design. Then, testing is performed to guarantee the safety of the nuclear reactor improvement or construction. Then, operation takes place with the nuclear reactor operating along the safety range determined during testing. Finally, maintenance is provided to ensure the correct operation of the nuclear reactor under operation.

Nuclear software development aims to both improve the available nuclear codes, as well as deliver new nuclear codes through innovation resulting in more adequate representations of nuclear reactors. It usually occurs by stages. Initially, the requirements analysis is performed to understand the demands of the industry, the nuclear regulator, and academia [4,5]. Then, the design is drafted to acknowledge all the physical and mathematical models, as well as the possible code structure necessary to address the requirements analysis. Then, implementation and integration are conducted to create a nuclear code according to the design. Then, validation and verification are performed to proof the functionality of the nuclear code created during implementation and integration. Then, deployment takes place with the nuclear code functioning within the range of the validation and verification. Finally, maintenance is provided to ensure the correct functioning of the nuclear code within the deployment.

Coupling is present in both nuclear technology and in nuclear software development, it describes the interdependence, coordination, or information flow either between components within a nuclear reactor [6,7] or between physical and mathematical models or code structure within a nuclear code [8–10]. In nuclear technology development the components, such as reactor cores, pressurizers, steam generators, turbines, and condensers are drafted, assembled, safety proven, and operate together. In nuclear software development, the physical and mathematical models, such as the neutronics, thermal hydraulics, and thermo-mechanics, as well as the possible code structure, such as the modularity are drafted, coded, functionally proven, and function together.

Currently, the coupling within a nuclear software development is of interest. The coupling is regarded either as strong or weak [11] depending on the level of interdependence, coordination, and information flow between physical and mathematical models. The coupling is regarded either as tight or loose [12] depending on the level of interdependence, coordination, and information flow between the code structure. The complex coupling phenomena resulting from the non-linearity existing in both the physical and mathematical models, such as the neutronics, thermal hydraulics, and thermo-mechanics, has led to either fully treating them in separate nuclear codes or at most simplistically treating them in different modules within certain nuclear codes. The coupling between nuclear codes or modules can be present in several forms depending on the level of interdependence and coordination between them [13]. In serial coupling, internal libraries are used to merge a nuclear code or module with another becoming a single nuclear code, where extensive modifications are required in the former. In parallel coupling, either external coupling scripts or internal libraries are only used to exchange data between a nuclear code or module with another remaining separate nuclear codes, where mild modifications are required in the former. The coupling between nuclear codes or modules can occur in several ways depending on the information flow between them [14]. In one-way coupling, the merge or exchange of data between nuclear codes or modules takes place only from one to another. In two-way coupling the merge or exchange of data between nuclear codes or modules data takes place both from one to another and vice versa.

Coupling software environments allow to establish either serial or parallel coupling, as well as either one-way and two-way coupling between nuclear codes or modules by offering either a simplified coupling interface or a fully coupled software framework. SALOME (Simulation Numerique par Architecture Logicielle en Open Source et a Methodologie d'Evolution), is a coupling software environment [15,16] which offers a simplified coupling interface to transfer multi-physics and multiscale, modularizing the nuclear codes. It was created in the 2000s by OC (Open Cascade, Guyancourt, France), EDF (Electricite de France, Paris, France) and CEA (Commissariat à l'énergie atomique et aux énergies alternatives, Paris, France) with several versions adapted to different requirements being available. VERA (Virtual Environment for Reactor Applications) is a coupling software environment [17,18] which also offers a simplified coupling interface to transfer multi-physics and multiscale modularizing of the nuclear codes. It was created in the 2000s by ORNL (Oak Ridge National Laboratory, Oak Ridge, TN, USA) with one version created according to specific requirements being available. MOOSE (Multiphysics Object Oriented Simulation Environment) is a coupling software environment [19–21] which offers a fully coupled software framework to solve coupled multi-physics and multiscale, modularizing the coupled multi-physics rather than the nuclear codes. It was created in the 2000s by INL (Idaho National Laboratory, Idaho Falls, ID, USA) with several versions adapted to different requirements being available. All the coupling software environments execute the corresponding coupling, mapping between meshes. They allow parallelization across multiple cores within a computational cluster to reduce the simulation times. They include a graphical user interface to provide visualization. They may include additional modules for other specific tasks. Several multiscale and multi-physics software developments for LWR (Light Water Reactor) are being created which incorporate the mentioned coupling software environments to deliver either improved or full coupled reactor physics at the fuel pin level.

NURESIM (Nuclear Reactor Simulator) is a multiscale and multi-physics nuclear software development [22,23] created to deliver in LWR both improved coupled reactor physics and, hence, simplified neutron diffusion and full mixing fluid dynamics at the fuel pin level, as well as simplified coupled reactor physics and, hence, simplified neutron diffusion and non-mixing fluid dynamics at the fuel assembly level. It uses a derivative of the SALOME coupling software environment to couple the

nuclear codes. It is being created by EURATOM (European Atomic Energy Community, Brussels, Belgium). Simplified coupled reactor physics at the fuel assembly are delivered by SALOME after transferring via itself the homogenized fuel assembly cross sections from spectral codes to the nodal codes. Improved coupled reactor physics at the fuel pin level are delivered by SALOME [24–28] either after transferring via itself the homogenized fuel pin cross sections from spectral codes to the nodal codes or after performing fuel pin power reconstruction in the nodal codes. Additionally, after transferring via itself the fuel pin power distributions from the nodal codes to the subchannel codes and the fuel cells feedback distributions from the subchannel codes to the nodal codes. Finally, after transferring via itself the fuel parameters from the nodal codes to the fuel performance codes and vice versa. In NURESIM, full coupled reactor physics are not present, which does not result in the most adequate representation of an LWR.

CASL (Consortium for Advanced Simulation of LWRs) is a multiscale and multi-physics nuclear software development [29,30] created to deliver in LWR through its advanced component full coupled reactor physics and, hence, full neutron transport and full mixing fluid dynamics at the fuel pin level, as well as through its baseline component simplified coupled reactor physics at the fuel pin level and, hence, simplified neutron diffusion and non-mixing fluid dynamics at the fuel assembly level. It uses a combination between VERA and a derivative of the MOOSE coupling software environments to couple the nuclear codes. It is being created by USDE (United States Department of Energy, Washington, DC, USA). Simplified coupled reactor physics at the fuel assembly level are delivered by VERA after transferring via itself the homogenized fuel assembly cross sections from spectral codes to the nodal codes. Full coupled reactor physics at the fuel pin level are delivered by VERA [31–34] after transferring via itself the cross sections from spectral codes to transport codes. Additionally, after transferring via itself the fuel pin power distributions from the transport codes to the subchannel codes and the fuel cells feedback distributions from the subchannel codes to the transport codes. Finally, after transferring via MOOSE the fuel parameters from the transport codes to the fuel performance codes and vice versa. In CASL, full coupled reactor physics at the fuel pin level are extended to all the reactor core, which results in the most computationally expensive representation of an LWR.

An alternative for the UK (United Kingdom) is a multiscale and multi-physics nuclear software development [35] between NURESIM and CASL created to deliver in LWR both improved coupled reactor physics and hence simplified neutron diffusion and full mixing fluid dynamics at the fuel pin level and full coupled reactor physics and, hence, full neutron transport and full mixing fluid dynamics at the fuel pin level, as well as simplified coupled reactor physics and, hence, simplified neutron diffusion and non-mixing fluid dynamics at the fuel assembly level. It uses a customized coupling software environment to couple the nuclear codes. It is being created by UOL (University of Liverpool). Simplified coupled reactor physics at the fuel assembly are delivered by the customized coupling software environment after transferring via itself the homogenized fuel assembly cross sections from the spectral code SCALE [36–38] to the nodal code DYN3D [39–41]. Improved coupled reactor physics at the fuel pin level are delivered by the customized coupling software environment either after transferring via itself the homogenized fuel pin cross sections from SCALE to DYN3D or after performing fuel pin power reconstruction in DYN3D. Additionally, after transferring via itself the fuel pin power distributions from DYN3D to the subchannel code CTF [42–45] and the fuel cells feedback distributions from CTF to DYN3D. Finally, after transferring via itself the fuel parameters from DYN3D to the fuel performance code ENIGMA [46] and vice versa. Full coupled reactor physics at the fuel pin level are delivered by the customized coupling software environment after transferring via itself the cross sections from SCALE to the transport code LOTUS [47–49]. Additionally, after transferring via itself the fuel pin power distributions from LOTUS to CTF and the fuel cells feedback distributions from CTF to LOTUS. Finally, after transferring via itself the fuel parameters from LOTUS to ENIGMA and vice versa. In this multiscale and multi-physics software development between NURESIM and CASL full coupled reactor physics at the fuel pin level are present but are only extended to the hottest fuel assemblies while simplified coupled reactor physics at the fuel assembly level are extended to all the reactor core, which results in a more reliable but less computationally expensive representation of an LWR. The customized coupling software environment offers a simplified coupling interface to transfer multi-physics and multiscale, modularizing the nuclear codes. It is currently being created by UOL. It

executes the corresponding coupling mapping between meshes. It will eventually allow parallelization across multiple cores within a computational cluster. It includes additional modules for specific tasks. Both a one-way and two-way coupling between any two of the mentioned nuclear codes can be performed within the customized coupling software environment as observed in Figure 5.1.



Figure 5.1. (a) One-way coupling and (b) two-way coupling.

At present, the aim is the coupling between the nodal code DYN3D and the subchannel code CTF to deliver improved coupled reactor physics at the fuel pin level within the mentioned multiscale and multi-physics nuclear software development. Several objectives were previously carried out to achieve this aim. The first objective [42] was comprehended by CTF and FLOCAL (DYN3D thermal hydraulics module) thermal hydraulics validations and verifications which were carried to analyse the fluid dynamics in both nuclear codes and, hence, the accuracy and mixing methods available to deliver full fluid dynamics at the fuel pin level. Fluid dynamics distributions were obtained in either CTF or FLOCAL through their corresponding modules and convergence criteria. CTF was seen to be very accurate as opposed to other subchannel and system codes. CTF was also seen to include different mixing methods, as opposed to FLOCAL where no crossflow is available. The second objective [45] was comprehended by the first part of the DYN3D and CTF coupling verification which was carried out to analyse an external one-way coupling between both nuclear codes and, hence, the inner coupling iterations contained in an outer coupling iteration to deliver partially verified improved coupled reactor physics at the fuel pin level. Feedback distributions were obtained in the DYN3D and CTF coupling through external coupling scripts, the converged last iteration DYN3D fission power distributions, as well as the CTF modules and convergence criteria. This external one-way coupling analysis determined through the thermal hydraulics when should the DYN3D and CTF coupling be applied instead of DYN3D to deliver improved coupled reactor physics at the fuel pin level. The DYN3D and CTF coupling was seen to deliver more homogeneous feedback distributions as opposed to DYN3D although both were also observed to deliver similar average feedback values.

The current objective is comprehended by the second part of the DYN3D and CTF coupling which has been carried out to analyse a parallel two-way coupling between these nuclear codes and, hence, the outer coupling iterations necessary for convergence to deliver verified improved coupled reactor physics at the fuel pin level. Fission power distributions have been obtained in the DYN3D and CTF coupling through the customized coupling software environment modules, the multiple iterations CTF feedback distributions, as well as the DYN3D and CTF modules and customized coupling software environment convergence criteria. Feedback distributions have been obtained in the DYN3D and CTF coupling through the customized coupling software environment modules, the multiple iterations DYN3D fission power distributions, as well as the DYN3D and CTF modules and customized coupling software environment convergence criteria. This parallel two-way coupling analysis determines through both the neutronics and thermal hydraulics when the DYN3D and CTF coupling should be applied instead of DYN3D to deliver improved coupled reactor physics at the fuel pin level. This third article, hence, comprehends the DYN3D and CTF coupling outer iterations convergence verification to deliver verified improved coupled reactor physics at the fuel pin level, while the LOTUS and CTF coupling convergence verification to deliver verified full coupled reactor physics at the fuel pin level will be covered in a separate journal article.

This journal article is arranged into several sections which are divided into subsections. Initially, the codes used in the coupling outer iterations convergence verification consisting of DYN3D and CTF were described, including main concepts, versions, and approaches. Following, the modules modified or created for the coupling outer iterations, convergence verification within either DYN3D,

or the customized coupling software environment were explained, including the main concepts and approach. Then, the specifications used in the coupling outer iterations convergence verification conformed by the modified KAIST (Korean Advanced Institute of Science and Technology) benchmark [50] were presented including the different geometries, materials, and boundary conditions. Additionally, the models simulated in the coupling outer iterations convergence verification were described, including the meshes, methods, correlations, and property tables.

Following, the results and analysis acquired through the modified KAIST benchmark in the DYN3D and CTF coupling outer iterations convergence verification were discussed conformed by DYN3D to DYN3D and CTF coupling comparisons. The tests included provide results for the effective multiplication factor, fission power, and feedback in both 17×17 fuel assemblies containing fuel pins, as well as 3×3 mini cores containing the previously mentioned fuel assemblies. The mentioned magnitudes were selected to complete the DYN3D and CTF coupling from a coupled reactor physics perspective.

Finally, the conclusions obtained for the DYN3D and CTF coupling outer iterations convergence verification were outlined to summarize the last objective in the aim of delivering the DYN3D and CTF coupling within the multiscale and multi-physics nuclear software development, which was completed by verifying the DYN3D and CTF coupling outer iterations convergence. Additionally, future work is mentioned to present the last aim of delivering the LOTUS and CTF coupling within the multiscale and multi-physics nuclear software development.

5.2. Codes within the Verification

Previously it was discussed that the DYN3D and CTF coupling outer iterations convergence verification was carried out using both DYN3D and CTF. Hence, the codes are described in the following subsections.

5.2.1. DYN3D Nodal Code

DYN3D is a nodal code [51,52] created to deliver neutron diffusion and non-mixing fluid dynamics and hence simplified coupled reactor physics in both LWR and VVER (square and hexagonal geometries). It delivers simplified coupled reactor physics at the fuel assembly level after performing fuel assembly homogenisation. It delivers simplified coupled reactor physics at the fuel pin level either after performing fuel pin homogenization or after performing fuel pin power reconstruction. It was created in the 1990s by FZD (Forschung Zentrum Dresden, Dresden, Germany) using FORTRAN 90 (Formula Translator). DYN3D-MG is a recent version of DYN3D updated through several features. It includes multi-energy group neutron diffusion, reactivity calculation through inverse point kinetics, the Pernica DNB correlation and boron calculation through the particle in cell method to increase the fidelity. It was updated in recent years by HZDR (Helmholtz Zentrum Dresden Rossendorf, Dresden, Germany) also using FORTRAN 90. DYN3D-MG (MOD) is the present version of DYN3D-MG updated through a new feature necessary in this journal article. It allows the de-coupling within DYN3D, as well as external feedback importation to increase the fidelity. It was updated by UOL also using FORTRAN 90. DYN3D is structured into several neutronics modules which define the NK (Neutron Kinetics) code and several thermal hydraulics modules which define the FLOCAL (Thermal Hydraulics) code all of which are strongly and tightly coupled in between. A reactor core or parts of it are modelled through a set of nodes which correspond to channels.

The neutronics modules apply the multi-energy group neutron diffusion equations to the set of nodes in conjunction with cross sections tables, as well as nodal expansion methods that are used to provide a solution to the mentioned equations. The SP3 and HEXNEM1-2 nodal expansion methods can be used to integrate the mentioned equations in either square or hexagonal geometries. Albedos are applied to the neutron currents to address neutrons leakage within the reactor core. ADF (Assembly Discontinuity Factors) can be applied to the neutron fluxes to address the errors in the cross sections resulting from fuel assembly homogenization. Fuel pin power reconstruction can be applied to the neutron fluxes to increase fidelity. A control rod model can be applied to the fuel assemblies to replace at the corresponding nodes the cross sections without control rods by the cross sections with control rods.

The thermal hydraulics modules apply the two fluid non-mixing fluid dynamics equations to the set of nodes in conjunction with thermal and mechanical property tables, as well as heat and mass transfer models that are used to provide a solution to the mentioned equations. A flow regime map is used to integrate the mentioned equations over the nodes depending on the type of boiling. Constitutive relations are applied to the mentioned equations to treat the different phases within a channel according to the flow regime. The boiling model is applied to the channels to determine the evaporation and condensation rates. Heat transfer correlations are used in the channels to obtain heat transfer between phases. Several friction and form models are applied to both the subchannels and fuel rods to provide the pressure losses. A fuel rod model is applied to the fuel assemblies to determine heat transfer between the solids and fluids.

In DYN3D, the mentioned equations are formulated using finite differences and solved by using numerical methods through an implicit method. DYN3D performs iterations between the neutronics and thermal hydraulics until a convergence criterion is met in the case of the steady state which consists of small absolute and relative differences between both the fission power and feedback distributions or until a certain time is achieved in the case of the transient state.

5.2.2. CTF Subchannel Code

COBRA-TF is a subchannel code [53,54] created to deliver full mixing fluid dynamics in LWR (square geometry). It delivers full mixing fluid dynamics at the fuel pin level after providing fuel pin power distributions. It was created in the 1980s by PNL (Pacific Northwest laboratories, Richland, USA) using FORTRAN 77. CTF is the present version of COBRA-TF updated through several features. It improves the void drift, turbulent mixing, heating models, the computational efficiency, and the user friendliness to increase the fidelity. It was updated in recent years by both PSU (Pennsylvania State University, State College, PA, USA) and NCSU (North Carolina State University, Raleigh, NC, USA) using FORTRAN 90. CTF is structured into several thermal hydraulics modules which define the code all of which are strongly and tightly coupled in between. A reactor core or parts of it are modelled through a matrix of mesh cells that correspond to subchannels.

The thermal hydraulics modules apply the two fluid three-flow field full mixing fluid dynamics equations to the matrix of mesh cells in conjunction with thermal and mechanical property tables, as well as heat and mass transfer models that are used to provide a solution to the mentioned equations. A flow regime map is used to integrate the mentioned equations over the matrix of mesh cells depending on the type of boiling. Macro mesh cell closure terms are applied to the mentioned equations to treat the different phases between subchannels according to the flow regime. Several friction and form models are applied to both the subchannels and fuel rods to provide the pressure losses. Inter-cell models or crossflow is used in the subchannels to obtain heat and mass transfer between them. Turbulent mixing and void drift are used in the subchannels to improve heat and mass transfer between them. Micro-mesh cell closure terms are applied to the mentioned equations to treat the different phases within a subchannel according to the flow regime. The boiling model is applied to the subchannels to determine the evaporation and condensation rates. A droplet model is applied to the subchannels to determine the entrainment and de-entrainment rates. Inter-phase models are used in the subchannels to obtain heat and mass transfer between phases. A fuel rod model is applied to the fuel pins for heat transfer between the solids and fluids.

In CTF, the mentioned equations are formulated using finite differences and solved by using numerical methods through a semi-implicit method known as SIMPLE (Semi Implicit Method for Pressure Linked Equations). CTF performs iterations within the thermal hydraulics until a convergence criterion is met in the case of the steady state which consists of small absolute and relative differences within the feedback distributions or until a certain time is achieved in the case of the transient state.

5.3. Modules within the Verification

Previously, it was discussed that the DYN3D and CTF coupling outer iterations convergence verification was carried out modifying or creating several modules either within DYN3D or the customized coupling software environment. Hence, the modules are described in the following subsection.

DYN3D and CTF Coupling Modules

Several modules have been both modified within DYN3D via DYN3D-MG (MOD), as well as created within the customized coupling software environment to deliver the coupling between DYN3D and CTF in LWR (square geometries). They deliver improved coupled reactor physics at the fuel pin level after transferring both the fission power distributions from DYN3D-MG(MOD) to CTF, as well as the feedback distributions from CTF to DYN3D-MG(MOD). These were recently created by UOL in the case of DYN3D-MG(MOD) using FORTRAN 90 while in the case of the customized coupling software environment using PYTHON. Such modules are in the case of DYN3D-MG (MOD) strongly and tightly coupled in between while these are in the case of the customized coupling software environment strongly but loosely coupled in between. A reactor core or parts of it can be interpreted by the modules.

The modified modules in DYN3D-MG (MOD) apply the de-coupling within DYN3D between NK and FLOCAL as well as the external feedback importation from CTF into DYN3D through several changes to improve the solution in the steady state. A CTF logical parameter for control and allocatable vectors for the fuel temperature, moderator temperature, moderator density, and boron concentration are defined in the constant power/feedback parameter definitions module. The "CTF FEEDBACK CALCULATION" character flag for selection in the input is checked to enable the decoupling of NK from FLOCAL, activate the CTF logical parameter, allocate the vectors according to the number of nodes, as well as import the feedback, which is defined in the neutron diffusion constant feedback calculation module. The CTF logical parameter allows to decouple NK from FLOCAL, which is defined in the neutron diffusion steady state calculation module. It also allows to associate the allocated vectors to the internal variables, which is defined in both the thermal hydraulics feedback preparation and the neutron diffusion constant feedback calculation modules. The de-coupling within DYN3D between NK and FLOCAL, as well as the external feedback importation into DYN3D can be observed in Figure 5.2.

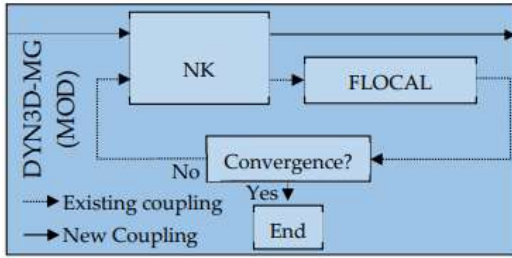


Figure 5.2. DYN3D (NK-FLOCAL) decoupling and external feedback importation.

The created modules within the customized coupling software environment apply the coupling between DYN3D and CTF through several features to improve the solution in the steady state. A loop is executed which calls DYN3D-MG (MOD), as well as several exportation, relaxation, and importation modules, and CTF, as well as several other exportation, relaxation, and importation modules until a convergence criterion is met which consists of small absolute and relative differences between the effective multiplication factor values, as well as the power and feedback distributions, which is defined in the main DYN3D and CTF coupling module. The inequalities that either the absolute or the relative differences of the mentioned magnitudes must satisfy simultaneously for a certain iteration n to achieve convergence is given by the following expressions.

$$|k_{\text{eff}}^n - k_{\text{eff}}^{n-1}| \leq \max(R_{k_{\text{eff}}} * k_{\text{eff}}^{n-1}, A_{k_{\text{eff}}}) \quad (16)$$

$$\max(|q^n - q^{n-1}|) \leq \max(R_q * q^{n-1}, A_q) \quad (17)$$

$$\max(|\rho_m^n - \rho_m^{n-1}|) \leq \max(R_{\rho_m} * \rho_m^{n-1}, A_{\rho_m}) \quad (18)$$

$$\max(|T_m^n - T_m^{n-1}|) \leq \max(R_{T_m} * T_m^{n-1}, A_{T_m}) \quad (19)$$

$$\max(|T_f^n - T_f^{n-1}|) \leq \max(R_{T_f} * T_f^{n-1}, A_{T_f}) \quad (20)$$

In the mentioned expressions, k_{eff} defines the effective multiplication factor, q defines the fission power distribution, ρ_m defines the moderator density distribution, T_m defines the moderator temperature distribution, and T_f defines the fuel temperature distribution. Finally, R defines the relative convergence tolerance for the corresponding magnitude, while A defines the absolute convergence

tolerance for the corresponding magnitude. The results exportation from DYN3D-MG (MOD) to the customized coupling software environment is performed to store both the effective multiplication factor and the fission power distributions with the latter being reshaped into a full 3D representation to improve data handling, which is defined in the DYN3D powers exportation module. Under relaxation within the customized coupling software environment is applied to the fission power distributions with the under-relaxation parameter taking values below 1 to increase the stability and above 0.1 to avoid false convergence, which is defined in the DYN3D powers under relaxation module. The traditional under relaxation method is applied to the fission power for a certain iteration n and node i and is given by the following expression.

$$q_{rel_i}^n = \theta q_{DYN3D_i}^n + (1 - \theta) q_{rel_i}^{n-1} \quad (21)$$

In the mentioned expression, q_{rel} defines the under relaxed fission power, q_{DYN3D} defines the resulting fission power from DYN3D, and θ defines the under-relaxation factor. The under-relaxed fission power distributions importation from the customized coupling software environment to CTF is performed to interpolate from node centre values to the node face values, renormalise these by their corresponding average values, reformat these according to the card groups in CTF and, finally, retrieve them into CTF, which is defined in the CTF powers importation module. The results exportation from CTF to the customized coupling software environment is performed to store the fuel temperature, the moderator temperature, the moderator density, and the boron concentration feedback distributions with these being reshaped into a full 3D representation to improve data handling, which is defined in the CTF feedback exportation module. Under relaxation within the customized coupling software environment is applied to the fuel temperature, the moderator temperature, the moderator density, and the boron concentration feedback distributions to increase the stability with the under-relaxation parameter taking values below 1 to increase the stability and above 0.1 to avoid false convergence, which is defined in the CTF feedback under relaxation module. The traditional under relaxation method is applied to the feedback distributions including moderator density and temperature, as well as fuel temperature for a certain iteration n and node I and is given by the following expressions.

$$\rho_{m_{rel_i}}^n = \theta \rho_{m_{CTF_i}}^n + (1 - \theta) \rho_{m_{rel_i}}^{n-1} \quad (22)$$

$$T_{m_{rel_i}}^n = \theta T_{m_{CTF_i}}^n + (1 - \theta) T_{m_{rel_i}}^{n-1} \quad (23)$$

$$T_{f_{rel_i}}^n = \theta T_{f_{CTF_i}}^n + (1 - \theta) T_{f_{rel_i}}^{n-1} \quad (24)$$

In the mentioned expressions, $\rho_{m_{rel}}$ defines the under relaxed moderator density, $\rho_{m_{CTF}}$ defines the resulting moderator density from CTF, $T_{m_{rel}}$ defines the under relaxed moderator temperature, $T_{m_{CTF}}$ defines the resulting moderator temperature from CTF, $T_{f_{rel}}$ defines the under relaxed fuel temperature, and $T_{f_{CTF}}$ defines the resulting fuel temperature from CTF. The under relaxed moderator density, moderator temperature, fuel temperature, and boron concentration feedback distributions importation from the customized coupling software environment to DYN3D-MG(MOD) is performed to reformat these according to the modified modules in DYN3D-MG(MOD) and, finally, retrieve them into DYN3D-MG(MOD) which is defined in the DYN3D feedback importation module. The coupling between DYN3D and CTF can be observed in Figure 5.3.

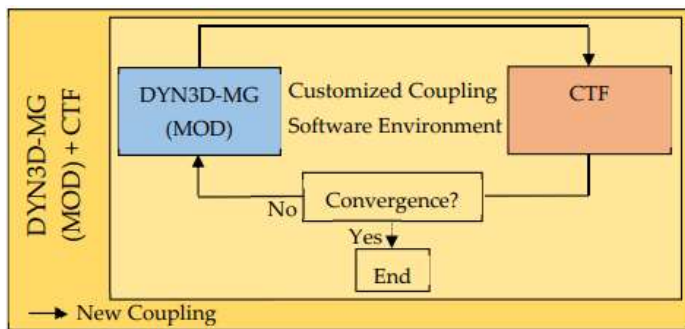


Figure 5.3. DYN3D and CTF coupling within the customized coupling software environment.

5.4 Specifications within the Verification

Previously it was discussed that the DYN3D and CTF coupling outer iterations convergence verification was carried out using the modified KAIST benchmark. Hence, the specifications are described in the following subsection.

Modified KAIST Benchmark

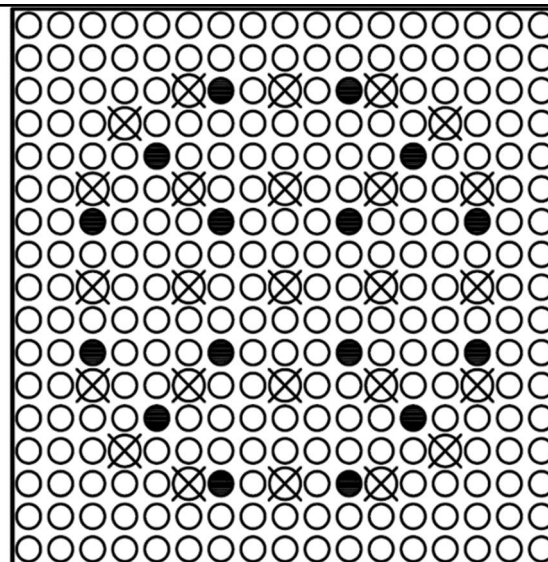
The modified KAIST benchmark is an improved version of the KAIST benchmark [151] for PWR coupled reactor physics simulations. No experimental data or other code results are available. Tests carried out in the simulations include: steady state 17×17 fuel assemblies containing fuel pins and guide tubes, as well as burnable absorber pins with different fission power and feedback distributions. Steady state 3×3 mini-cores containing the previously mentioned 17×17 fuel assemblies also with different fission power and feedback distributions.

The modified KAIST benchmark includes a multi parameter exercise for the 17×17 fuel assemblies consisting of seven coupling tests based on a full power PWR. Each of these tests includes a single parameter change applied to either the total power, the axial albedos, the inlet boron concentration, the inlet temperature, the inlet mass flux, or the outlet pressure. The modified KAIST benchmark also includes a full reactor start up exercise for the 3×3 mini cores consisting of three coupling tests based on a full power PWR. Each of these tests represents a different operation stage including the cold zero, the hot zero, and the full power. In the first part of the DYN3D and CTF coupling, high total powers were used leading to hot PWR behaviour where two phase phenomena is largely present. In the second part of the DYN3D and CTF coupling, standard total powers have been used leading to typical PWR behaviour where two phase phenomena is less present. All the data for the tests has been presented

Specifications include the geometry, materials, and initial and boundary conditions. The geometries for both the 17×17 fuel assemblies with or without burnable absorber fuel pins, as well as for the 3×3 mini-cores with or without burnable absorber fuel assembly are described as observed in Table 5.1.

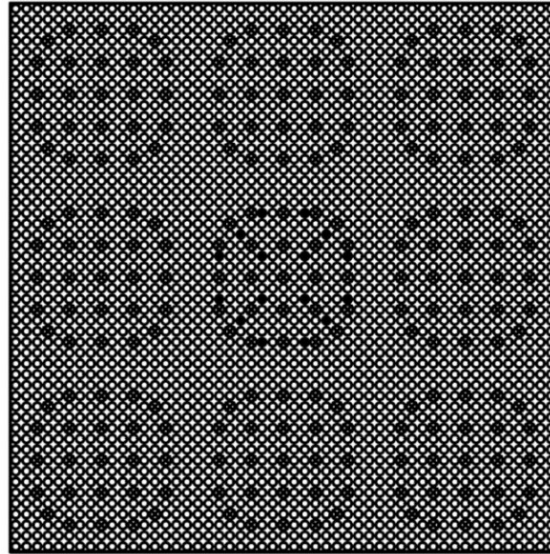
Table 5.1. The 17×17 fuel assembly and 3×3 mini-core geometries from the modified KAIST benchmark.

Type	UOX-2 (CR) 17×17 Assembly	UOX-2 (BA-16) 17×17 Assembly
Channel Width (m)	0.2142	0.2142
Cell Width (m)	0.0126	0.0126



- Fuel Pin
- Burnable Absorber/ Fuel Pin
- ⊗ Guide Tube

Axial Length (Active) (m)	3.658	3.658
Number of Fuel Pins	264	248
Number of Burnable Absorber Pins	0	16
Number of Guide Tubes	25	25



- Fuel Pin
- Burnable Absorber/Fuel Pin
- ⊗ Guide Tube

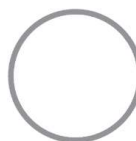
Type	Homogeneous 3 × 3 Mini-Core	Heterogeneous 3 × 3 Mini-Core
Channel Width (m)	0.6426	0.6426
Cell Width (m)	0.0126	0.0126
Axial Length (Active) (m)	3.658	3.658
Number of Fuel Pins	2376	2360
Number of Burnable Absorber Pins	0	16
Number of Guide Tubes	225	225

The geometries for the fuel pins or burnable absorber pins, as well as for the guide tubes are described as observed in Table 5.2

Table 5.2. The fuel/burnable absorber in and guide tube geometries from the modified KAIST benchmark.



Type	Fuel/Burnable Absorber Pin
Fuel Pin Diameter (m)	0.0082
Gap Thickness (m)	0.000085
Clad Thickness (m)	0.00057
Clad Diameter (m)	0.0095



Type	Guide Tube
------	------------

Clad Thickness (m)	0.000405
Guide Tube Diameter (m)	0.01224

The materials for the fuel pins or burnable absorber pins, as well as for the guide tubes, are described as observed in Table 5.3.

Table 5.3. The fuel/burnable absorber in and guide tube materials from the modified KAIST benchmark.

Neutron Energy Groups (eV)	Group 0≡ (0.62506, 2231300)
Fuel Pin Composition	Group 1≡ (0.000014, 0.62506)
Burnable Absorber Pin Composition	UO ₂ (3.3% ²³⁵ U, 96.7% ²³⁸ U)
Clad Composition	UO ₂ (0.711% ²³⁵ U, 90.289% ²³⁸ U) + Gd ₂ O ₃ (9.0%)
Fuel Density (kg/m ³)	Zircalloy (97.91% Zr, 1.59% Sn, 0.5% Fe) 10040
Fuel Specific Heat (J/kg K)	$c_{p_{fuel}} = \frac{8.5013 \cdot 10^8 e^{\frac{535.285}{T}}}{T^2 \left(e^{\frac{535.285}{T}} - 1 \right)^2} + 0.0243T + \frac{1.6587 \cdot 10^{12}}{T^2} e^{-\frac{18968}{T}}$ (25)
Fuel Thermal Conductivity (W/m K)	$k_{fuel} = \max\left(\frac{2335}{464 + T}, 1.1038\right) + 7.027 \cdot 10^{-3} \cdot 10^{-3} e^{1.867 \cdot 10^{-3} T}$ (26)
Gap Gas	He
Gap Heat Conductance (kJ/m ² K)	5678
Clad Density (kg/m ³)	6400
Clad Specific Heat (J/kg K)	$c_{p_{clad}} = 252.54 + 0.11474T$ (27)
Clad Thermal Conductivity (W/m K)	$k_{clad} = 7.51 + 2.09 \cdot 10^{-2}T - 1.45 \cdot 10^{-5}T^2 + 7.67 \cdot 10^{-9}T^3$ (28)

The initial and boundary conditions for the 17 × 17 fuel assemblies multi-parameter exercise are described as observed in Table 5.4.

Table 5.4. The 17 × 17 fuel assemblies initial and boundary conditions.

Case	Axial Albedos	Boric Acid Concentration (ppm)	Power (MW)	Inlet Temperature (C)	Mass Flux (kg/m ² s)	Outlet Pressure (Bar)
Full Power	0.5	800	17.308	293.30	2889.33	155
High Power	0.5	800	22.308	293.30	2889.33	155
High Albedo	0.75	800	17.308	293.30	2889.33	155
Zero Boron	0.5	0	17.308	293.30	2889.33	155
High Temperature	0.5	800	17.308	303.30	2889.33	155
Low Flux	0.5	800	17.308	293.30	2476.58	155
Low Pressure	0.5	800	17.308	293.30	2889.33	145

The initial and boundary conditions for the 3 × 3 mini-cores full reactor start up exercise are described as observed in Table 5.5.

Table 5.5. The 3 × 3 mini-cores initial and boundary conditions.

Case	Axial Albedos	Boric Acid Concentration (ppm)	Power (MW)	Inlet Temperature (C)	Mass Flux (kg/m ² s)	Outlet Pressure (Bar)
------	---------------	--------------------------------	------------	-----------------------	---------------------------------	-----------------------

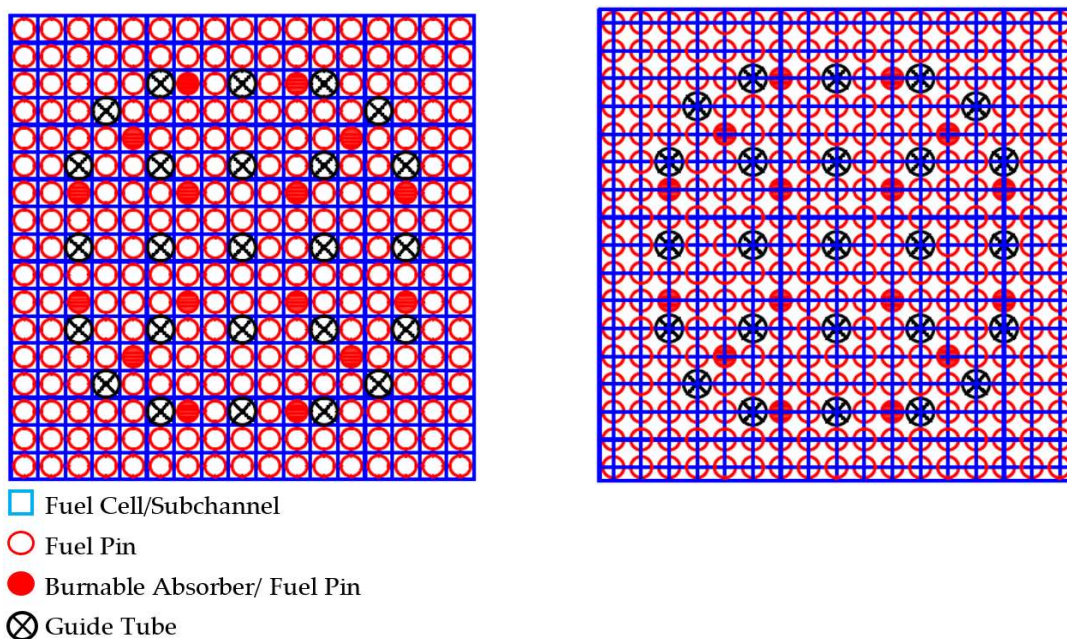
Cold Zero Power	0.5	800	0	25.30	2889.33	155
Hot Zero Power	0.5	800	0	293.30	2889.33	155
Full Power	0.5	800	155.772	293.30	2889.33	155

5.5. Models within the Verification

Previously it was discussed that the DYN3D and CTF coupling outer iterations convergence verification was carried by simulating the modified KAIST benchmark. Hence, the models are described in the following subsection.

Modified KAIST Benchmark

Different models between the 17×17 fuel assemblies and the 3×3 mini-cores in both DYN3D and CTF include the meshes. In the case of DYN3D and the UOX-2 (CR) fuel assembly, 264 fuel pins as well as 25 guide tubes are included into 289 fuel cells (fuel pin centred system) all of which are composed by 36 uniform axial node layers. In the case of CTF and the UOX-2 (CR) fuel assembly, 264 fuel pins, as well as 25 guide tubes are included in 324 subchannels (subchannel centred system) all of which are connected in between by 612 gaps and composed by 36 uniform axial node layers. In the case of DYN3D and the UOX-2 (BA-16) fuel assembly, 248 fuel pins as well as 16 burnable absorber pins, and 25 guide tubes are included into 289 fuel cells (fuel pin centred system) all of which are composed by 36 uniform axial node layers. In the case of CTF and the UOX-2 (BA-16) fuel assembly, 248 fuel pins as well as 16 burnable absorber pins and 25 guide tubes are included in 324 subchannels (subchannel centred system), all of which are connected in between by 612 gaps and composed by 36 uniform axial node layers. In the case of DYN3D and the homogeneous mini-core, 2376 fuel pins, as well 225 guide tubes, are included in 2601 fuel cells (fuel pin centred system), all of which are composed by 36 uniform axial node layers. In the case of CTF and the homogeneous mini-core, 2376 fuel pins as well as 225 guide tubes are included in 2704 subchannels (subchannel centred system) all of which are connected in between by 5304 gaps and composed by 36 uniform axial node layers. In the case of DYN3D and the heterogeneous mini-core, 2360 fuel pins as well 16 burnable absorbers and 225 guide tubes are included in 2601 fuel cells (fuel pin centred system), all of which are composed by 36 uniform axial node layers. In the case of CTF and the heterogeneous mini-core, 2360 fuel pins, as well as 16 burnable absorber pins and 225 guide tubes are included in 2704 subchannels (subchannel centred system), all of which are connected in between by 5304 gaps and composed by 36 uniform axial node layers. The fuel pin centred system mesh in DYN3D and the subchannel centred system mesh in CTF for both the fuel assemblies and mini cores can be observed in Figure 5.4.



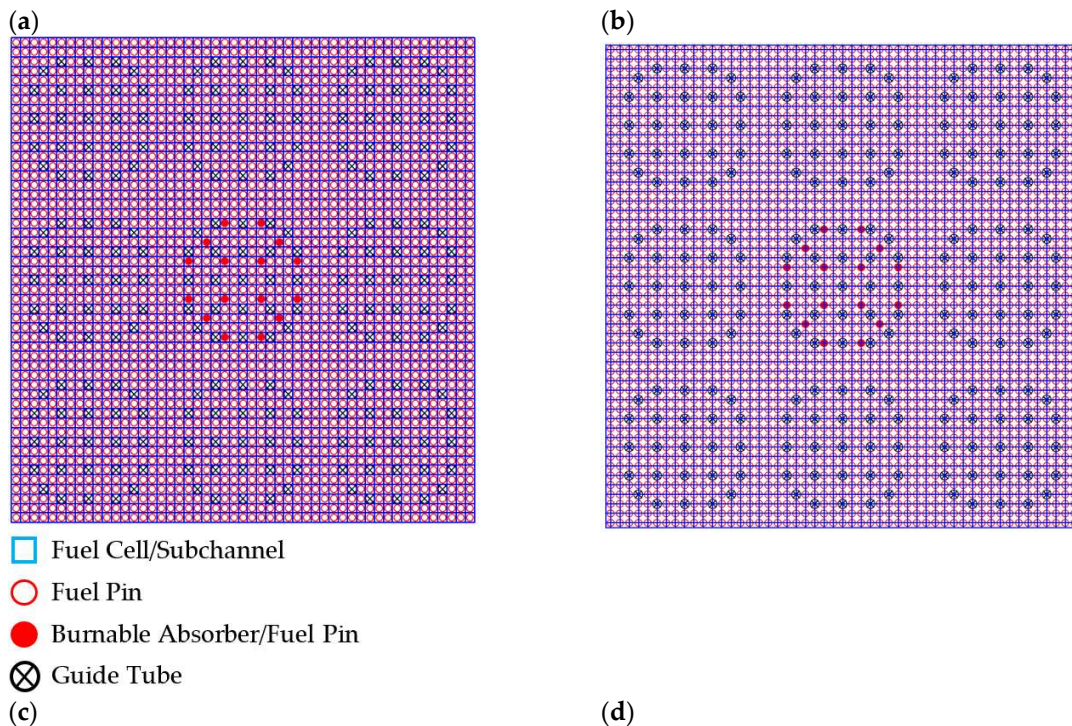


Figure 5.4. (a) DYN3D 17×17 fuel assembly mesh, (b) CTF 17×17 fuel assembly mesh, (c) DYN3D 3×3 mini-core mesh, and (d) CTF 3×3 mini-core mesh.

Common models between the 17×17 fuel assemblies and the 3×3 mini-cores in both DYN3D and CTF include the cross sections tables as well as nodal expansion methods and the thermal and mechanical property tables, as well as the heat and mass transfer models. In the case of the neutronics in DYN3D, the neutron diffusion of two energy groups has been modelled as it is available. Homogenised fuel pin cross sections for the fuel and burnable absorber pins, as well as the guide tube, have been produced using SCALE-POLARIS [55]. The SP3 nodal expansion method is modelled as it is the one available for cartesian geometries [56]. Full reflective boundary conditions are only modelled radially while different partial reflective boundary conditions are modelled axially according to the specifications to provide a more complete representation of the system. No ADF have been included for simplicity. No fuel pin power reconstruction is performed, as fuel pin discretization is used instead. No control rods are used for simplicity. In the case of the thermal hydraulics in DYN3D, no crossflow or turbulent mixing has been modelled, as it is not available. Material properties for the fuel and burnable absorber pins, as well as the guide tubes, have been used through the average of the distributions provided in the modified KAIST benchmark. Water properties for the moderator have been modelled using the IFC-67 approach out of several available [57]. Nucleate boiling has been modelled using the Rassokhin and Borishaskji correlation it being the one available [58]. Departure from nucleate boiling has been modelled using the Bezrukov and Astakhov (OKB-2) correlation, it being the most accurate out of several available [59]. No entrainment has been modelled, as it is not available. Friction pressure losses have been modelled using the Filonenko and Osmachkin one- and two-phase multiplier correlation, it being the one available [60]. No spacer grids pressure losses have been modelled for simplicity. In the case of the thermal hydraulics in CTF, crossflow and turbulent mixing have been modelled in the case of the former via the gaps and in the case of the latter using the Rogers and Rosehart correlation as it determines the two-phase mixing coefficient according to the corresponding subchannel [61]. Material properties for the fuel and burnable absorber pins have been modelled through tables of the distributions provided in the modified KAIST benchmark. Water properties have been modelled using the IAPWS approach out of several available [62]. Nucleate boiling has been modelled using the Thom correlation with it remaining valid along a wide range of pressures [63]. Departure from nucleate boiling has been modelled using the W-3 correlation it being widely used to analyse PWR. Entrainment has been modelled using the CTF method [64]. Friction

pressure losses have been modelled using the McAdam's one phase and two-phase multipliers correlation it being widely used to analyse PWR [65]. No spacer grids pressure losses have been modelled for simplicity.

In addition, another common model between the 17×17 fuel assemblies and the 3×3 mini-cores in both DYN3D and the DYN3D and CTF coupling includes the under relaxation. In both cases, it has been modelled using the traditional under relaxation method with an under-relaxation factor value of 0.5 improving the stability while avoiding false convergence.

5.6. Results and Analysis

Results for the coupled reactor physics in DYN3D and the DYN3D and CTF coupling were acquired by simulating the modified KAIST benchmark. DYN3D to DYN3D and CTF coupling comparisons within the DYN3D and CTF coupling outer iterations convergence verification in the steady state are discussed for the effective multiplication factor and the fission power in the following subsections while these are discussed for the feedback in the appendixes.

5.6.1. Fuel Assemblies

DYN3D to DYN3D and CTF coupling comparisons within the modified multi-parameter exercise for the UOX-2 (CR) and the UOX-2 (BA-16) fuel assemblies are presented for the effective multiplication factor and the fission power distributions from both physical and convergence perspectives while the fluid density feedback, fluid temperature feedback, and fuel temperature feedback are presented from both physical and convergence perspectives in Appendix A. The final iteration effective multiplication factor value for both the UOX-2 (CR) and the UOX-2 (BA-16) fuel assemblies is given for all the tests to show the similarities and differences between the DYN3D and the DYN3D and CTF coupling values. Such values are described as observed in Table 5.6.

Table 5.6. UOX-2 (CR) and UOX-2 (BA-16) fuel assemblies effective multiplication factor values.

	UOX-2 (CR) Fuel Assembly			UOX-2 (BA-16) Fuel Assembly		
	Effective Multiplication Factor		Reactivity Difference (pcm)	Effective Multiplication Factor		Reactivity Difference (pcm)
	DYN3D	DYN3D and CTF Coupling		DYN3D	DYN3D and CTF Coupling	
Full Power	1.23923	1.23733	-124	0.99991	1.00044	53
High Power	1.23387	1.23097	-191	0.99057	0.99365	313
High Albedo	1.24018	1.23855	-106	1.00069	1.00147	78
Zero Boron	1.33922	1.33532	-218	1.06322	1.06290	-28
High Temperature	1.23635	1.23445	-124	0.99570	0.99735	166
Low Flux	1.23796	1.23594	-132	0.99709	0.99875	167
Low Pressure	1.23897	1.23715	-119	0.99913	1.00022	109

DYN3D derives the effective multiplication factor from fast energy group fission and removal cross sections, as well as leakage contributions and from thermal energy group scattering and absorption cross sections, as well as leakage contributions by solving the two energy groups neutron diffusion equations where the reactivity is updated through feedback coefficients by applying cross sections interpolation.

In DYN3D, as well as in the DYN3D and CTF coupling, a decrease in the effective multiplication factor was seen in all the tests in the UOX-2 (BA-16) fuel assembly when compared to the UOX-2 (CR) fuel assembly. This decrease in the effective multiplication factor occurred due to the higher neutron absorption cross section in the burnable absorber fuel pins, which resulted in less thermal neutrons and, therefore, lower reactivities according to the two energy groups neutron diffusion equations.

In DYN3D, as well as in the DYN3D and CTF coupling, a decrease in the effective multiplication factor was seen in the high power, high temperature, low flow, and low-pressure tests when compared to the full power test in both the UOX-2 (CR) and in the UOX-2 (BA-16) fuel assemblies.

This decrease in the effective multiplication factor occurred due to several reasons: In the high-power test, this occurred due to the higher fuel and moderator temperature, as well as higher moderator density feedback coefficients in the fuel pin cells which resulted in less thermal neutrons and therefore lower reactivities according to the cross sections interpolation. In the high-temperature test, this occurred due to the higher moderator temperature feedback coefficient in the fuel pin cells which resulted in less thermal neutrons and, therefore, lower reactivities according to the cross sections interpolation. In the low flow test, this occurred due to the higher moderator density feedback coefficient in the fuel pin cells which resulted in less thermal neutrons and, therefore, lower reactivities according to the cross sections interpolation. In the low-pressure test, this occurred due to the higher moderator density feedback coefficient in the fuel pin cells which resulted in less thermal neutrons and, therefore, lower reactivities according to the cross sections interpolation. In DYN3D, as well as in the DYN3D and CTF coupling, an increase in the effective multiplication factor was seen in the high albedo, and zero boron tests when compared to the full power test in both the UOX-2 (CR) and in the UOX-2 (BA-16) fuel assemblies. This increase in the effective multiplication factor occurred due to several reasons: In the high albedo test, this occurred due to the lower neutron leakage in the fuel pins, which resulted in more neutrons and, therefore, higher reactivities according to the two energy groups neutron diffusion equations. In the zero-boron test, this occurred due to the lower boron feedback coefficient in the fuel pin cells, which resulted in more thermal neutrons and therefore higher reactivities according to the cross-sections interpolation.

Between DYN3D and the DYN3D and CTF coupling, differences in the effective multiplication factor values, as well as reactivity difference in both the UOX-2 (CR) and in the UOX-2 (BA-16) fuel assemblies are seen to be present. These differences in the effective multiplication factor as well as reactivity difference occurred due to the different fuel temperature feedback coefficients resulting from different fuel rod models, as well as the different moderator temperature and density feedback coefficients resulting from either the presence or absence of crossflow and turbulent mixing and the different boiling and inter-phase models. The achieved effective multiplication factor, as well as reactivity difference values in both the UOX-2 (CR) and UOX-2 (BA-16) fuel assemblies are compatible with each other due to either the similarity or low difference between them.

All iterations reactivity differences for both the UOX-2 (CR) and the UOX-2 (BA-16) fuel assemblies are given for all the tests to show the convergence of the DYN3D and CTF coupling values. Such differences are represented in Figure 5.5

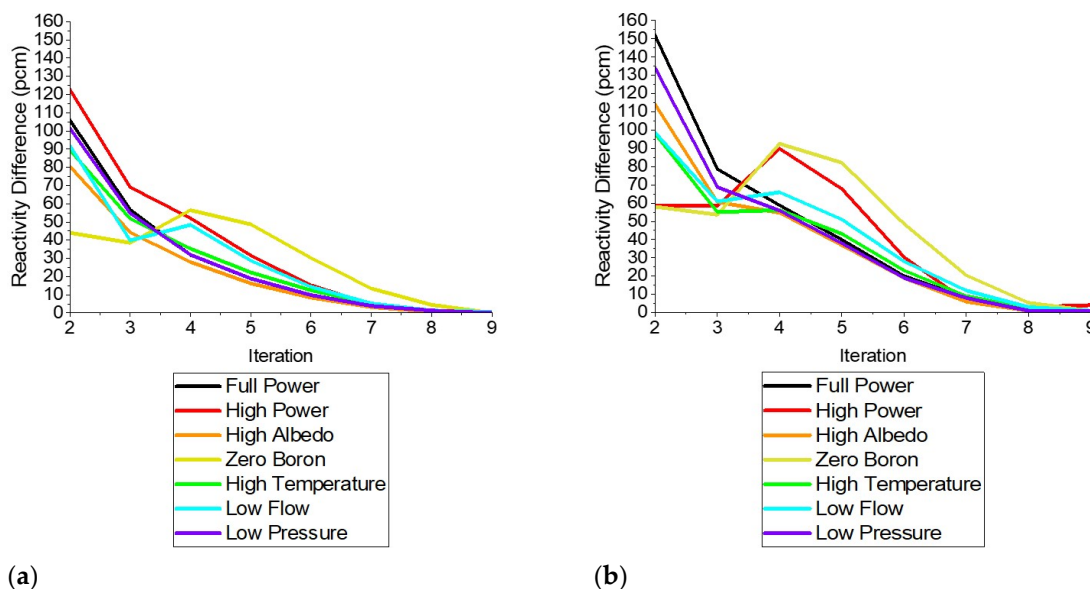


Figure 5.5. (a) DYN3D and CTF coupling UOX-2 (CR) fuel assembly reactivity difference convergence and (b) DYN3D and CTF coupling UOX-2 (BA-16) fuel assembly reactivity difference convergence.

The DYN3D and CTF coupling achieves the convergence of the reactivity via the under relaxation of both the power and feedback distributions until it achieves the steady state.

In the DYN3D and CTF coupling, the convergence of the reactivity was seen with higher iteration number in all the tests in both the UOX-2 (CR) and the UOX-2 (BA-16) fuel assemblies. The convergence of the reactivity occurred between 8 and 9 iterations due to several reasons: the presence of standard or mildly hot boundary conditions, which resulted in a faster or slower convergence rate and, therefore, less, or more required iterations according to the convergence criteria. The reasonable under relaxation factor, which results in higher stability and, therefore, in part more required iterations according to the convergence criteria. In the DYN3D and CTF coupling, a slower convergence of the reactivity was seen with higher iteration number in all the tests in the UOX-2 (BA-16) fuel assembly when compared to the UOX-2 (CR) fuel assembly. This slower convergence of the reactivity occurred due to the higher neutron absorption cross section in the burnable absorber fuel pins, which resulted in more heterogeneity and, therefore, more required iterations according to the convergence criteria.

The final iteration average axial fission power distribution peak for both the UOX-2 (CR) and the UOX-2 (BA-16) fuel assemblies are given for all the tests to show the similarities and differences between the DYN3D and the DYN3D and CTF coupling distributions. Such distributions peaks are represented in Figure 5.6.

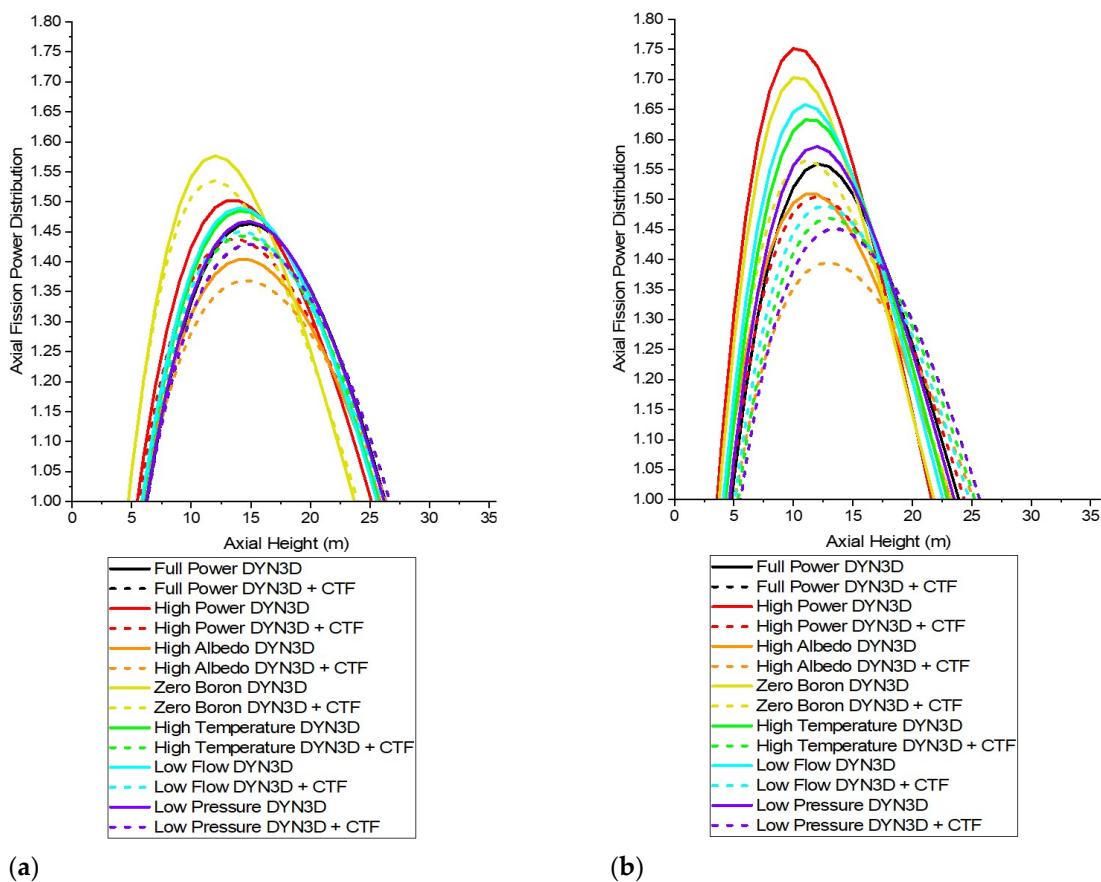


Figure 5.6. (a) UOX-2 (CR) fuel assembly average axial fission power distributions and (b) UOX-2 (BA-16) fuel assembly average axial fission power distributions.

DYN3D derives the fission power distribution from fast and thermal energy groups fission reaction rate contributions by solving the two energy groups neutron diffusion equations where the former are affected by the feedback.

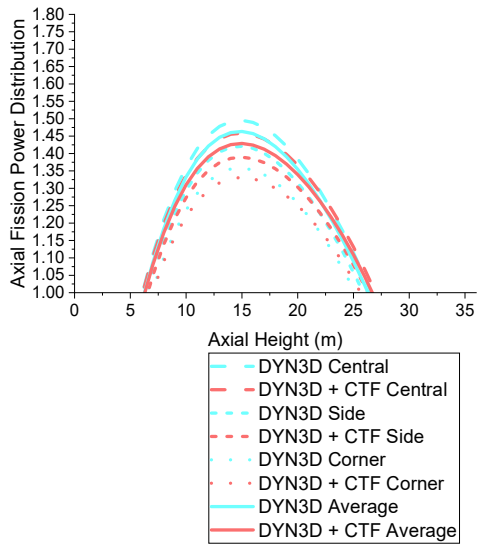
In DYN3D, as well as in the DYN3D and CTF coupling, an increase in asymmetry in the average axial fission power distributions was seen in all the tests in the UOX-2 (BA-16) fuel assembly when compared to the UOX-2 (CR) fuel assembly. This increase in asymmetry in the average axial fission power distributions occurred due to the higher neutron absorption cross section in the burnable absorber fuel pins, which resulted in less thermal neutrons and, therefore, lower fission reaction rates in the former, leading to the use of remaining neutrons in the fuel pins to preserve the same total power

as when there are only fuel pins, which resulted, therefore, in higher fission reaction rates in the latter according to the two energy groups neutron diffusion equations.

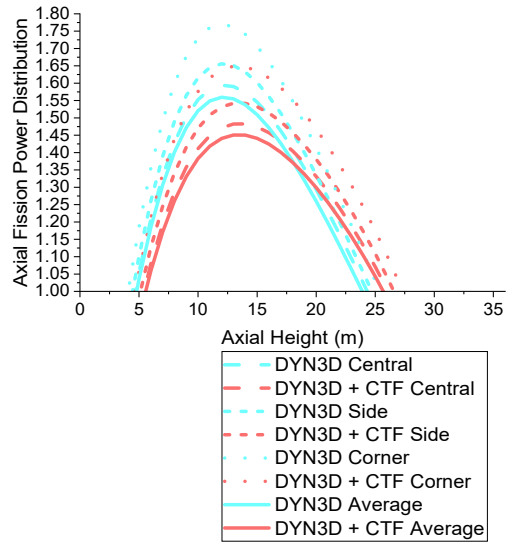
In DYN3D, as well as in the DYN3D and CTF coupling, an increase in asymmetry in the average axial fission power distributions was seen in the high-power, high-albedo, zero-boron, high-temperature, low-flow, and low-pressure tests when compared to the full power test in both the UOX-2 (CR) and in the UOX-2 (BA-16) fuel assemblies. This increase in asymmetry in the average axial fission power distributions occurred due to different reasons: In the high-power test, this occurred due to the higher fuel and moderator temperature, as well as higher moderator density feedback coefficients in the fuel pin cells, which resulted in less thermal neutrons and, therefore, lower fission reaction rates at the top layers of the fuel pin cells, leading to the use of remaining neutrons to preserve the total power, which therefore resulted in higher fission reaction rates at the bottom layers of the fuel pin cells according to the previously mentioned equations. In the high-albedo test, this occurred due to the lower neutron leakage in the fuel pin cells, which resulted in more neutrons and, therefore, higher fission reaction rates in the fuel pin cells according to the previously mentioned equations. In the zero-boron test, this occurred due to the lower boron feedback coefficient in the fuel pin cells, which resulted in more thermal neutrons and, therefore, higher fission reaction rates in the fuel pin cells according to the previously mentioned equations. In the high temperature test, this occurred due to the higher moderator temperature coefficient in the fuel pin cells, which resulted in less thermal neutrons and, therefore, lower fission reaction rates at the top layers of the fuel pins, leading to the use of remaining neutrons to preserve the total power, which, therefore, resulted in higher fission reaction rates at the bottom layers of the fuel pin cells according to the previously mentioned equations. In the low flow test, this occurred due to the higher moderator density feedback coefficient in the fuel pin cells, which resulted in less thermal neutrons and, therefore, lower fission reaction rates at the top layers of the fuel pins, leading to the use of remaining neutrons to preserve the total power, which, therefore, resulted in higher fission reaction rates at the bottom layers of the fuel pin cells according to the previously mentioned equations. In the low-pressure test, this occurred due to the higher moderator density feedback coefficient in the fuel pin cells, which resulted in less thermal neutrons and, therefore, lower fission reaction rates at the top layers of the fuel pins, leading to the use of remaining neutrons to preserve the total power, which therefore resulted in higher fission reaction rates at the bottom layers of the fuel pin cells according to the previously mentioned equations.

Between DYN3D and the DYN3D and CTF coupling, differences in the average axial fission power distributions in both the UOX-2 (CR) and in the UOX-2 (BA-16) fuel assemblies are seen to be present. These differences in the average axial fission power distributions occurred due to the different fuel temperature feedback coefficients resulting from different fuel rod models, as well as the different moderator temperature and density feedback coefficients resulting from either the presence or absence of crossflow and turbulent mixing and the different boiling and inter-phase models. The achieved average axial fission power distributions in the UOX-2 (CR) fuel assembly are compatible with each other due to the similarity between them. The achieved average axial fission power distributions in the UOX-2 (BA-16) fuel assembly are less compatible with each other due to the differences between them.

The final iteration axial fission power distribution peak for central, side, and corner fuel pins, and average between fuel pins, as well as the final iteration transversal fission power distribution for all the fuel pins at the average axial node layer are given for both the UOX-2 (CR) and UOX-2 (BA-16) fuel assemblies full power test to show the similarities and differences between the DYN3D and the DYN3D and CTF coupling distributions. Such distributions are represented in Figures 5.7 and 5.8.

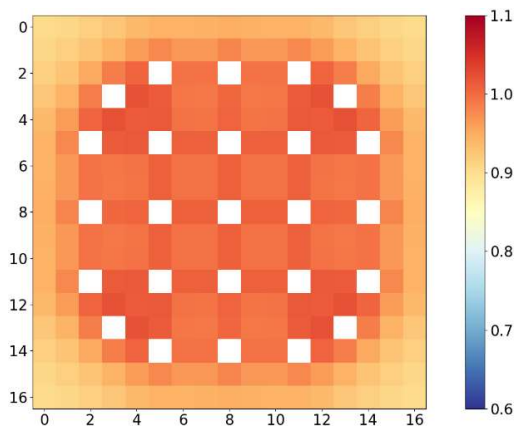


(a)

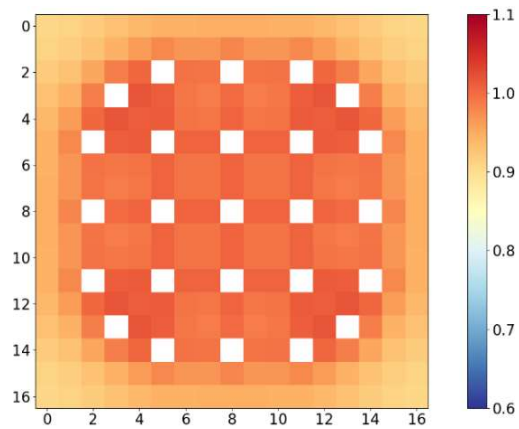


(b)

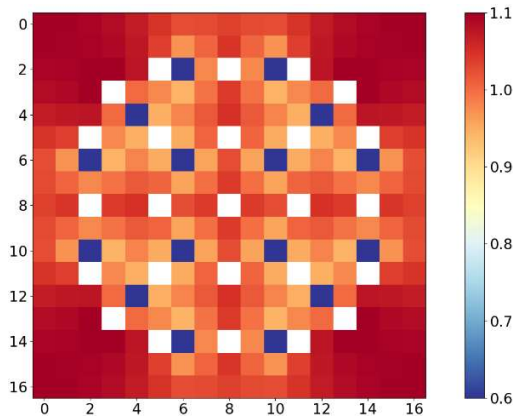
Figure 5.7. (a) UOX-2 (CR) axial fission power distributions and (b) UOX-2 (BA-16) axial fission power distributions.



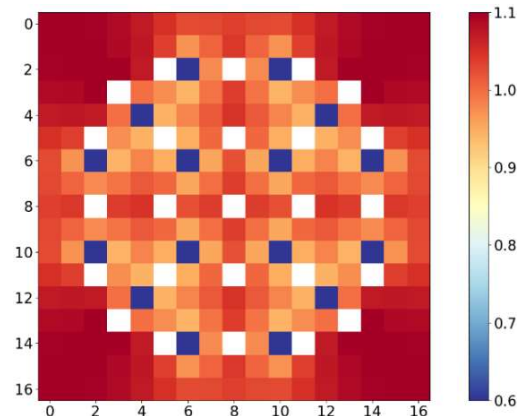
(a)



(b)



(c)



(d)

Figure 5.8. (a) DYN3D UOX-2 (CR) fuel assembly transversal fission power distribution, (b) DYN3D and CTF coupling UOX-2 (CR) fuel assembly transversal fission power distribution, (c) DYN3D UOX-2 (BA-16) fuel assembly transversal fission power distribution and (d) DYN3D and CTF coupling UOX-2 (BA-16) fuel assembly transversal fission power distribution.

In DYN3D, as well as in the DYN3D and CTF coupling, an increase in the axial fission power distribution, as well as an increase in the transversal fission power distribution at the average axial node layer was seen in the central fuel pin cells when compared to the side and corner fuel pin cells in the full power test in the UOX-2 (CR) fuel assembly. This increase in the fission power distribution occurred due to the lower neutron leakage in the central fuel pin cells, which resulted in more neutrons and, therefore, higher fission reaction rates in the former according to the two energy groups neutron diffusion equations. In DYN3D, as well as in the DYN3D and CTF coupling, a decrease in the axial fission power distribution, as well as a decrease in the transversal fission power at the average axial node layer, was seen in the central fuel pin cells when compared to the side and corner fuel pin cells in the full power test in the UOX-2 (BA-16) fuel assembly. This decrease in the fission power distribution occurred due to the higher neutron absorption cross section in the burnable absorber fuel pins, which resulted in less neutrons and, therefore, lower fission reaction rates in the central fuel pins according to the two energy groups neutron diffusion equations.

The relative difference between the former is given for both the UOX-2 (CR) and UOX-2 (BA-16) fuel assemblies full power test to show the differences between the DYN3D and the DYN3D and CTF coupling distributions. Such relative difference between distributions is represented in Figure 5.9.

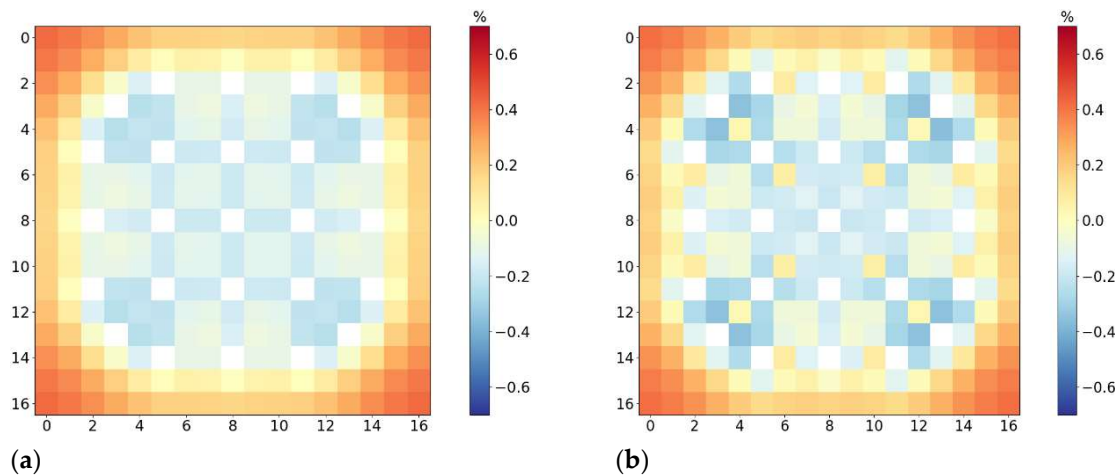


Figure 5.9. (a) Relative difference between DYN3D and CTF coupling and DYN3D UOX-2 (CR) fuel assembly transversal fission power distributions and (b) relative difference between DYN3D and CTF coupling and DYN3D UOX-2 (BA-16) fuel assembly transversal fission power distributions.

Between DYN3D and the DYN3D and CTF coupling, differences in the axial fission power distribution and in the transversal fission power distributions at the average axial node layer, as well as in the relative difference between the previously mentioned in the full power test either the UOX-2 (CR) or UOX-2 (BA-16) fuel assemblies full power test were seen to be present. These differences in the axial and transversal fission power distributions occurred due to the different fuel temperature feedback coefficients resulting from different fuel rod models, as well as the different moderator temperature and density feedback coefficients resulting from either the presence or absence of crossflow and turbulent mixing and the different boiling and inter-phase models.

All iterations maximum fission power values for both the UOX-2 (CR) and the UOX-2 (BA-16) fuel assemblies are given for all the tests to show the convergence of the DYN3D and CTF coupling distributions. Such values are represented in Figure 5.10.

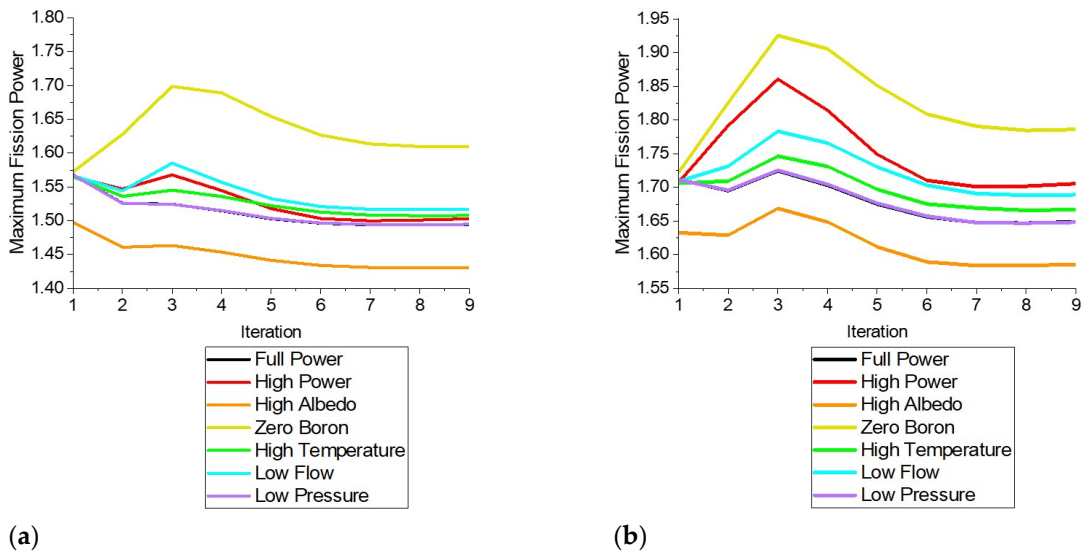


Figure 5.10. (a) DYN3D and CTF Coupling UOX-2 (CR) fuel assembly maximum fission power convergence and (b) DYN3D and CTF Coupling UOX-2 (BA-16) fuel assembly maximum fission power convergence.

The DYN3D and CTF coupling achieves the convergence of the power distributions via their own under relaxation until these achieve the steady state.

In the DYN3D and CTF coupling, the convergence of the maximum fission power values was seen with higher iteration number in all the tests in both the UOX-2 (CR) and the UOX-2 (BA-16) fuel assemblies. This convergence of the maximum fission power values occurred between 6 and 9 iterations due to several reasons: the presence of standard or mildly hot boundary conditions, which resulted on a faster or slower convergence rate and, therefore, less, or more required iterations according to the convergence criteria. The reasonable under relaxation factor, which resulted on higher stability and, therefore, more required iterations according to the convergence criteria. In the DYN3D and CTF coupling, a slower convergence of the maximum fission power values was seen with higher iteration number in all the tests in the UOX-2 (BA-16) fuel assembly when compared to the UOX-2 (CR) fuel assembly. This slower convergence of the maximum fission power values occurred due to the higher neutron absorption cross section in the burnable absorber fuel pins, which resulted in more heterogeneity and, therefore, more required iterations according to the convergence criteria.

5.6.2. Mini-Cores

DYN3D to DYN3D and CTF coupling comparisons within the full reactor start up exercise for the homogeneous and heterogeneous mini-cores are presented for the effective multiplication factor and the fission power distributions from both physical and convergence perspectives while the fluid density feedback, fluid temperature feedback and fuel temperature feedback are presented from both physical and convergence perspectives in Appendix B. The final iteration effective multiplication factor for both the homogeneous and heterogeneous mini cores is given for all the tests to show the similarities and differences between the DYN3D and the DYN3D and CTF coupling values. Such values are described as observed in Table 5.7.

Table 5.7. Homogeneous and heterogeneous mini-cores effective multiplication factor values.

	Homogeneous Mini-Core			Heterogeneous Mini-Core		
	Effective Multiplication Factor		Reactivity Difference (pcm)	Effective Multiplication Factor		Reactivity Difference (pcm)
	DYN3D	DYN3D and CTF Coupling		DYN3D	DYN3D and CTF Coupling	
Cold Zero Power	1.26175	1.26175	0	1.24026	1.24026	0

Hot Zero Power	1.25553	1.25552	-1	1.23292	1.23291	-1
Full Power	1.23924	1.23737	-122	1.21578	1.21394	-125

In DYN3D, as well as in the DYN3D and CTF coupling, a mild decrease in the effective multiplication factor was seen in all the tests in the heterogeneous mini-core when compared to the homogeneous mini-core. This mild decrease in the effective multiplication factor occurred due to the compensation between the higher neutron absorption cross-section in the central fuel assembly, which resulted in less thermal neutrons and, therefore, lower reactivity in the former with the lower neutron absorption cross section in the side and corner fuel assemblies, which resulted in more thermal neutrons and therefore higher reactivity in the latter according to the two energy groups neutron diffusion equations.

In DYN3D, as well as in the DYN3D and CTF coupling, a decrease in the effective multiplication factor was seen in the hot zero power and full power tests when compared to the cold zero power test in both the homogeneous and heterogeneous mini cores. This decrease in the effective multiplication factor occurred due to several reasons: In the hot zero power test, this occurred due to the higher moderator temperature feedback coefficient in the fuel assemblies, which resulted in less thermal neutrons and, therefore, lower reactivities according to the cross sections interpolation. In the full power test, this occurred due to the higher fuel and moderator temperature, as well as higher moderator density feedback coefficients in the fuel assemblies, which resulted in less thermal neutrons and, therefore, lower reactivities according to the cross sections interpolation.

Between DYN3D and the DYN3D and CTF coupling, differences in the effective multiplication factor values, as well as reactivity difference in both the homogeneous and heterogeneous mini cores are seen to be present. These differences in the effective multiplication factor, as well as reactivity difference occurred due to the different fuel temperature feedback coefficients resulting from different fuel rod models, as well as the different moderator temperature and density feedback coefficients resulting from either the presence or absence of crossflow and turbulent mixing and the different boiling and inter-phase models. The achieved effective multiplication factor, as well as reactivity difference values in both the homogeneous and heterogeneous mini cores are compatible with each other due to either the similarity or low difference between them.

All iterations reactivity differences for both the homogeneous and heterogeneous mini cores are given for all the tests to show the convergence of the DYN3D and CTF coupling values. Such differences are represented in Figure 5.11.

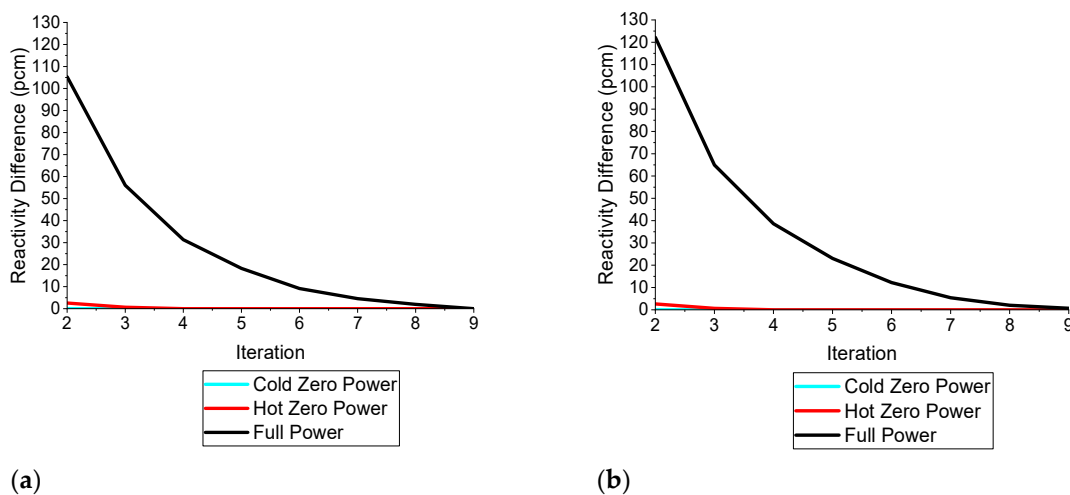


Figure 5.11. (a) DYN3D and CTF Coupling homogeneous mini-core reactivity difference convergence and (b) DYN3D and CTF Coupling heterogeneous mini-core reactivity difference convergence.

In the DYN3D and CTF coupling, the convergence of the reactivity was seen with higher iteration number in all the tests in both the homogeneous and heterogeneous mini cores. The convergence of the reactivity occurred between 3 and 9 due to several reasons: the presence of cold or

standard boundary conditions, which resulted on a very fast or fast convergence rate and therefore less required iterations according to the convergence criteria. The reasonable under relaxation factor, which resulted on higher stability and, therefore, in part more required iterations according to the convergence criteria. In the DYN3D and CTF coupling, a mildly slower convergence of the reactivity was seen with higher iteration number mainly in the full power case in the heterogeneous mini-core when compared to the homogeneous mini-core. This mildly slower convergence of the reactivity occurred due to the compensation between the higher neutron absorption cross section in the central fuel assembly with the lower neutron absorption cross section in the side and corner fuel assemblies, which resulted only in slightly more heterogeneity and therefore similar required iterations according to the convergence criteria.

The final iteration average axial fission power distribution peak for both the homogeneous and heterogeneous mini cores are given for all the tests to show the similarities and differences between the DYN3D and the DYN3D and CTF coupling distributions. Such distributions peaks are represented in Figure 5.12.

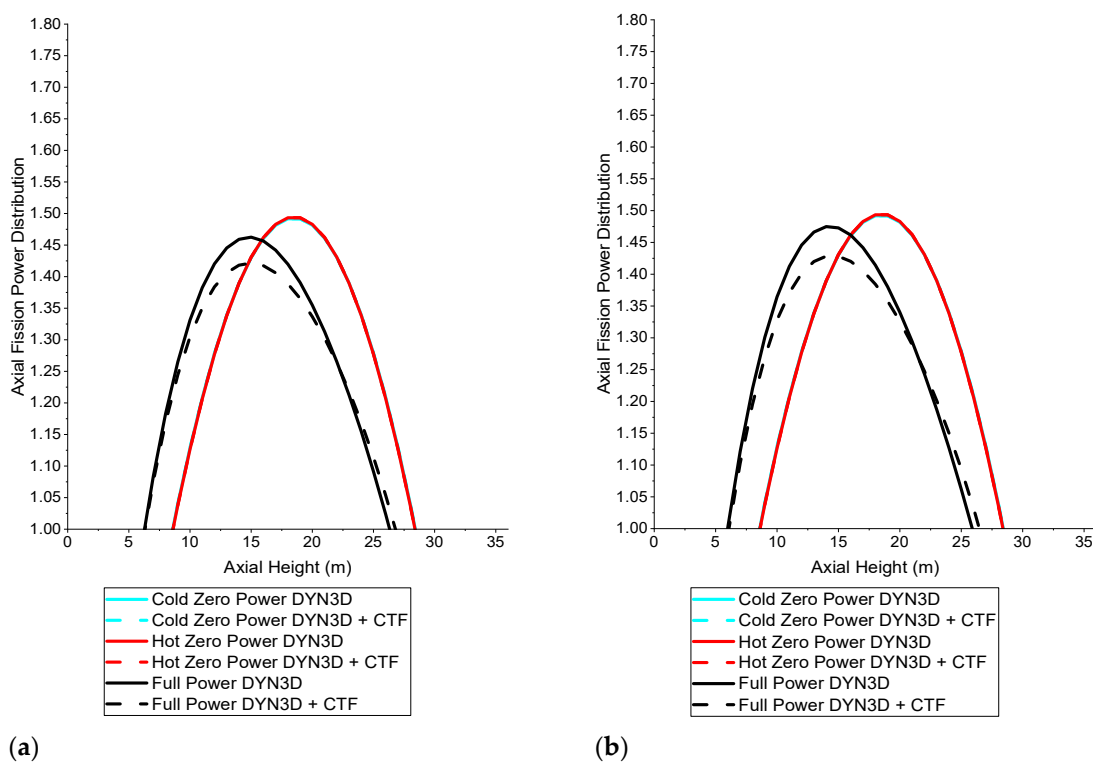


Figure 5.12. (a) Homogeneous mini-core average axial fission power distributions and (b) heterogeneous mini-core average axial fission power distributions.

In DYN3D, as well as in the DYN3D and CTF coupling, the preservation of symmetry in the average axial fission power distributions was seen in all the tests in the heterogeneous mini-core when compared to the homogeneous mini-core. This preservation of symmetry in the average axial fission power distributions occurred due to the compensation between the higher neutron absorption cross section in the central fuel assembly, which resulted in less thermal neutrons and, therefore, lower fission reaction rates in the former with the lower neutron absorption cross section in the side and corner fuel assemblies, which resulted in more thermal neutrons and, therefore, higher fission reaction rates in the latter according to the two energy groups neutron diffusion equations.

In DYN3D, as well as in the DYN3D and CTF coupling, an increase in asymmetry in the average axial fission power distributions was only in the full power test when compared to the cold zero power test in both the homogeneous and heterogeneous mini cores. This increase in asymmetry in the average axial fission power distributions occurred due to the higher fuel and moderator temperature, as well as higher moderator density feedback coefficients in the fuel assemblies, which resulted in less thermal

neutrons and, therefore, lower fission reaction rates at the top layers of the fuel assemblies, leading to the use of remaining neutrons to preserve the total power, which, therefore, resulted in higher fission reaction rates at the bottom layers of the fuel assemblies according to the previously mentioned equations.

Between DYN3D and the DYN3D and CTF coupling, differences in the average axial fission power distributions in both the homogeneous and heterogeneous mini cores are seen to be present. These differences in the average axial fission power distributions occurred due to the different fuel temperature feedback coefficients resulting from different fuel rod models, as well as the different moderator temperature and density feedback coefficients resulting from either the presence or absence of crossflow and turbulent mixing and the different boiling and inter-phase models. The achieved average axial fission power distributions in both the homogeneous and heterogeneous mini cores are compatible with each other due to the similarity between them.

The final iteration axial fission power distribution peak for central, side, and corner fuel assemblies and average between fuel assemblies, as well as the final iteration transversal fission power distribution for all the fuel assemblies at the average axial node layer are given for both the homogeneous and heterogeneous mini-cores full power test to show the similarities and differences between the DYN3D and the DYN3D and CTF coupling distributions. Such distributions are represented in Figures 5.13 and 5.14.

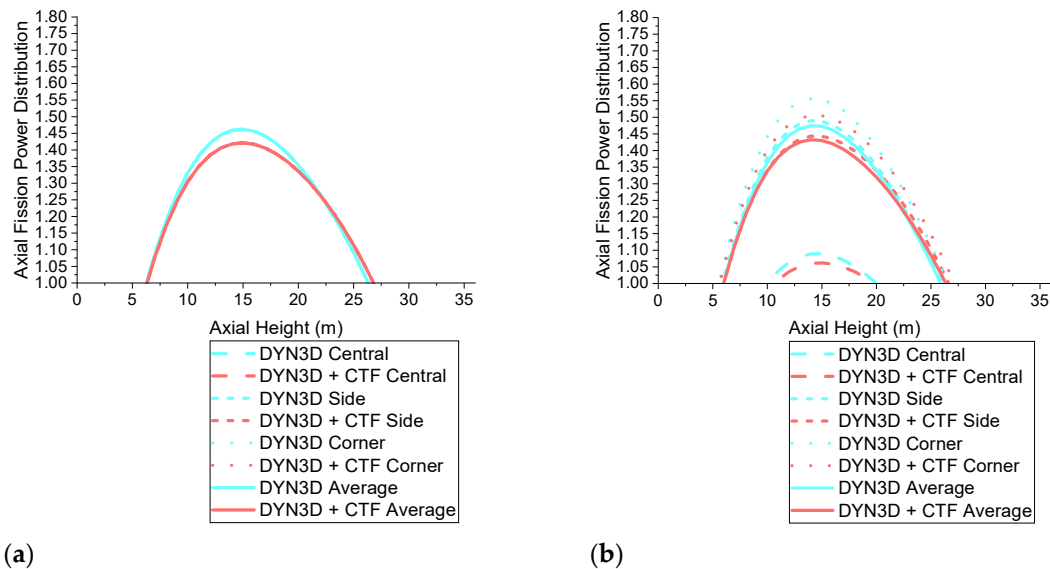
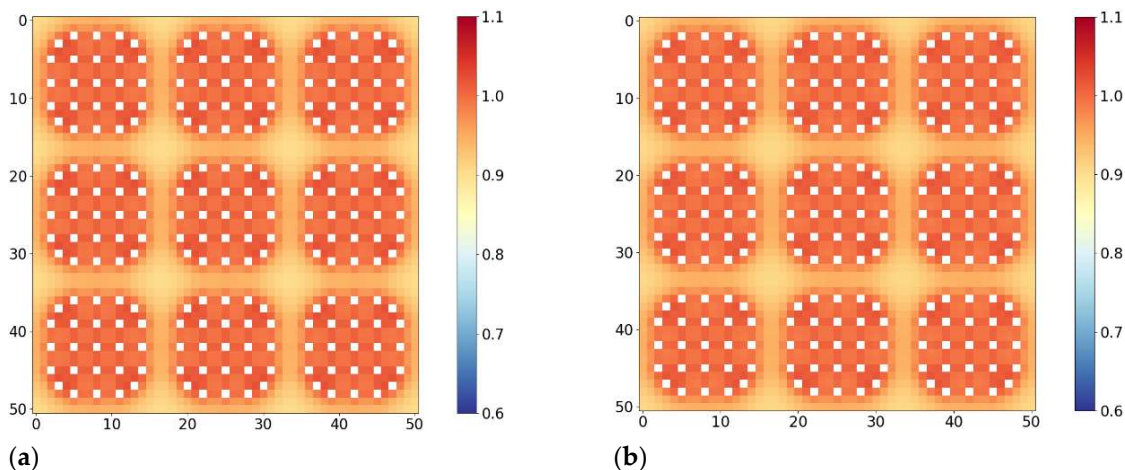


Figure 5.13. (a) Homogeneous mini-core axial fission power distributions and (b) heterogeneous mini-core axial fission power distributions.



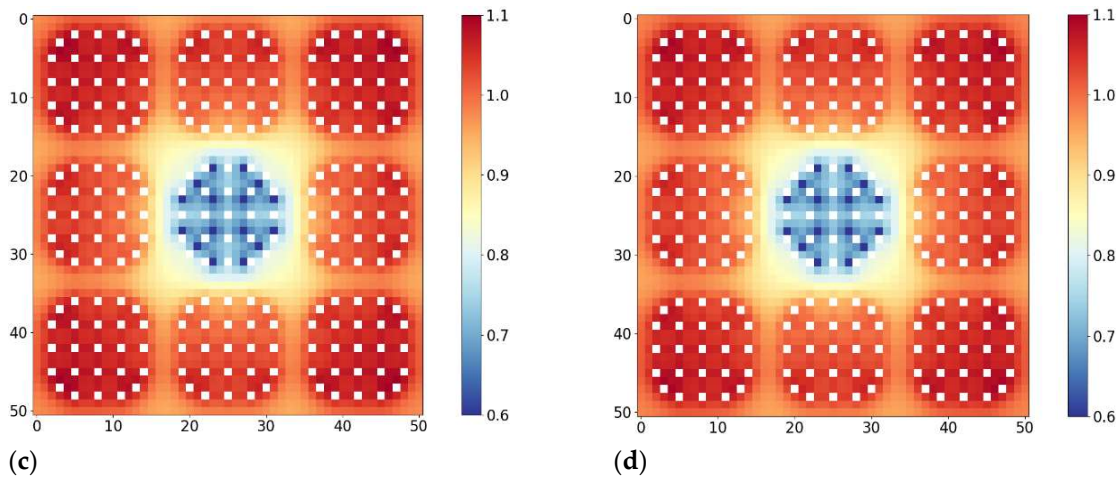


Figure 5.14. (a) DYN3D homogeneous mini-core transversal fission power distribution, (b) DYN3D and CTF coupling homogeneous mini-core transversal fission power distribution, (c) DYN3D heterogeneous mini-core transversal fission power distribution and (d) DYN3D and CTF coupling heterogeneous mini-core transversal fission power distribution.

In DYN3D, as well as in the DYN3D and CTF coupling, an equivalent axial fission power distribution, as well as an equivalent transversal fission power distribution at the average axial node layer, was seen in the central fuel assembly when compared to the side and corner fuel assemblies in full power test in the homogeneous mini core. This equivalence in the fission power distribution occurred due to the equivalent neutron absorption cross section in all the fuel assemblies, which resulted in an equivalent number of neutrons with no inter assembly power redistribution and, therefore, equivalent fission reaction rates in the central, side, and corner fuel assemblies according to the two energy groups neutron diffusion equations. In DYN3D, as well as in the DYN3D and CTF coupling, a decrease in the axial fission power distribution, as well as a decrease in the transversal fission power distribution at the average axial node layer was seen central fuel assembly when compared to the side and corner fuel assemblies in full power test in the heterogeneous mini core. This decrease in the axial fission power distribution occurred due to the higher neutron absorption cross section in the central fuel assembly which resulted in a lower number of neutrons with inter-assembly power redistribution and, therefore, lower fission reaction rates in the central fuel assembly than in the side and corner fuel assemblies according to the two energy groups neutron diffusion equations.

The relative difference between the former are given for both the homogeneous and heterogeneous mini-cores full power test to show the differences between the DYN3D and the DYN3D and CTF coupling distributions. Such relative differences between distributions are represented in Figure 5.15.

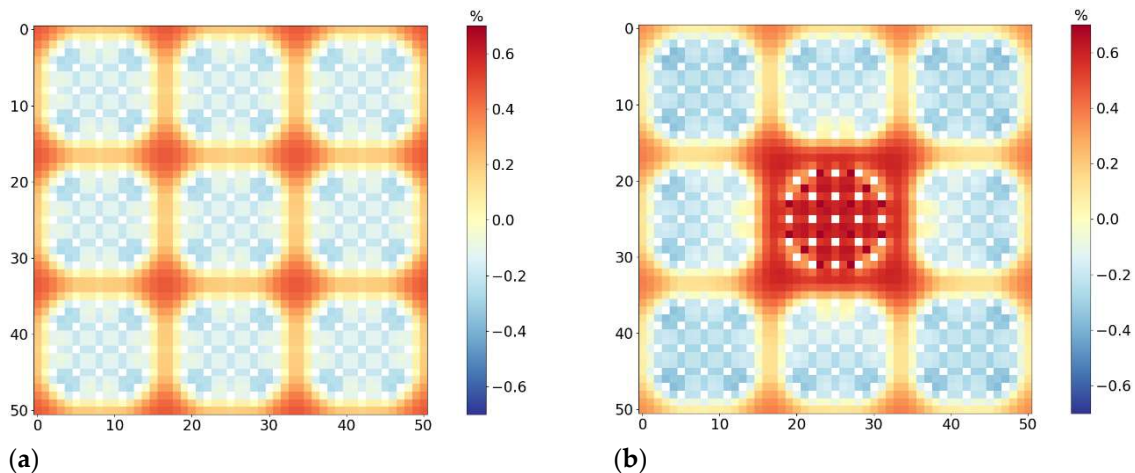


Figure 5.15. (a) Relative difference between DYN3D and CTF coupling and DYN3D homogeneous mini-core transversal fission power distributions and (b) relative difference between DYN3D and CTF coupling and DYN3D heterogeneous mini-core transversal fission power distributions.

Between DYN3D and the DYN3D and CTF coupling, differences in the axial fission power distribution and in the transversal fission power distributions at the average axial node layer, as well as in the relative difference between the previously mentioned in the full power test in either the homogeneous or heterogeneous mini core were seen to be present. These differences in the axial and transversal fission power distributions occurred due to the different fuel temperature feedback coefficients resulting from different fuel rod models, as well as the different moderator temperature and density feedback coefficients resulting from either the presence or absence of crossflow and turbulent mixing and the different boiling and inter-phase models.

All iterations maximum fission power values for both the homogeneous and the heterogeneous mini cores are given for all the tests to show the convergence of the DYN3D and CTF coupling distributions. Such values are represented in Figure 5.16.

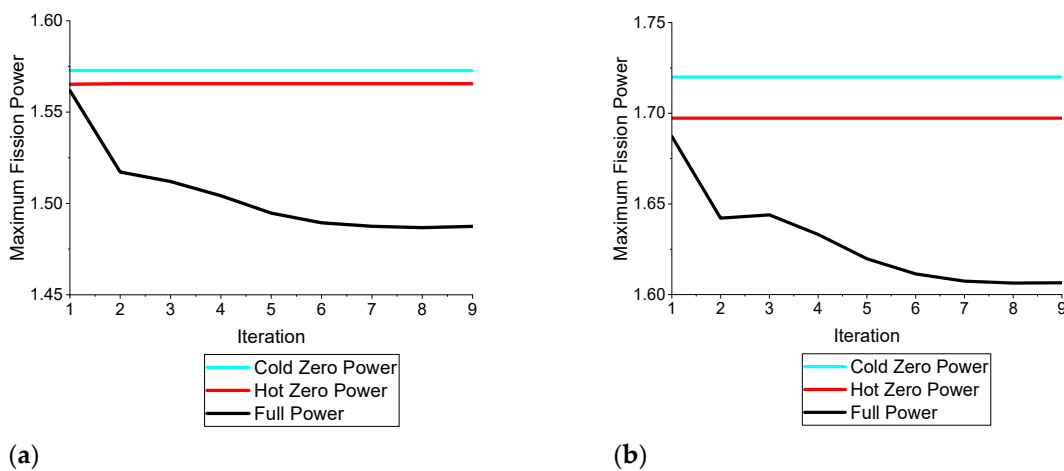


Figure 5.16. (a) DYN3D and CTF Coupling homogeneous mini-core maximum fission power convergence and (b) DYN3D and CTF Coupling heterogeneous mini-core maximum fission power convergence.

The DYN3D and CTF coupling achieves the convergence of the fission power distributions via their own under relaxation until these achieve the steady state.

In the DYN3D and CTF coupling, the convergence of the maximum fission power values was seen with higher iteration number in all the tests in both the homogeneous and heterogeneous mini cores. This convergence of the maximum fission power values occurred between 1 and 7 iterations due to several reasons: the presence of cold or standard boundary conditions, which resulted on a faster convergence rate and, therefore, less required iterations according to the convergence criteria. The reasonable under relaxation factor, which resulted on higher stability and therefore in part more required iterations according to the convergence criteria. In the DYN3D and CTF coupling, a mildly slower convergence of the maximum fission power values was seen with higher iteration number in the full power case in the heterogeneous mini-core when compared to the homogeneous mini-core. This mildly slower convergence of the maximum fission power values occurred due to the compensation between the higher neutron absorption cross section in the central fuel assembly with the lower neutron absorption cross section in the side and corner fuel assemblies, which resulted only in slightly more heterogeneity and, therefore, similar required iterations according to the convergence criteria.

5.7. Conclusions

Finally, the last objective in the aim of delivering the coupling between DYN3D and CTF within the multiscale and multi-physics nuclear software development has been completed through the

analysis of the parallel two ways coupling between them. The coupling outer iterations convergence has been verified delivering improved coupled reactor physics at the fuel pin level. In this parallel two ways coupling both converged fission power and feedback distributions were obtained through the customized coupling software environment modules, the multiple iterations CTF feedback and DYN3D fission power distributions, as well as the DYN3D and CTF modules and customized coupling software environment convergence criteria.

Comparing the improved coupled reactor physics at the fuel pin level for both the fuel assemblies and mini cores delivered by the DYN3D and CTF coupling to the simplified coupled reactor physics at the fuel pin level delivered by DYN3D. In the case of the fuel assemblies, the DYN3D and CTF coupling differs from DYN3D through the effective multiplication factor and reactivity difference values, as well as through the fission power and feedback distributions and maximum and minimum values due to the different fuel temperature feedback coefficients resulting from different fuel rod models, as well as the different moderator temperature and density feedback coefficients resulting from either the presence or absence of crossflow and turbulent mixing and the different boiling and inter-phase models. In the case of the mini cores the DYN3D and CTF coupling differs less from DYN3D through the effective multiplication factor and reactivity difference values as well as through the fission power and feedback distributions and maximum and minimum values due to the compensation between the former reasons for the fuel assemblies with power redistribution between the fuel assemblies.

In general, the DYN3D and CTF coupling provides improved coupled reactor physics over DYN3D due to the presence in the former as opposed to in the latter of crossflow and turbulent mixing. However, the DYN3D and CTF coupling is more computationally expensive compared to DYN3D which is less computationally expensive as the full simulation time in the latter ranges from around 2 min for the fuel assemblies to 20 min for the mini-cores, while the full simulation time in the former ranges from 1 h for the fuel assemblies to 10 h for the mini-cores.

5.8. Future Work

The final aim and objective is comprehended by the LOTUS and CTF coupling verification which will be carried out to analyse a parallel two-way coupling between these codes to deliver verified full coupled reactor physics at the fuel pin level. Fission power distributions will be obtained in the LOTUS and CTF coupling through the customized coupling software environment modules, the multiple iterations CTF feedback distributions, as well as the LOTUS and CTF modules and customized coupling software environment convergence criteria. Feedback distributions will be obtained in the LOTUS and CTF coupling through the customized coupling software environment modules, the multiple iterations LOTUS fission power distributions, as well as the LOTUS and CTF modules and customized coupling software environment convergence criteria. This parallel two-way coupling analysis will determine through both the neutronics and thermal hydraulics when should the LOTUS and CTF coupling be used instead of the DYN3D and CTF coupling to deliver full coupled reactor physics at the fuel pin level.

Author Contributions: S.D., as the main author, wrote this article including the introduction, codes used in the verification, modules used in the verification, specifications used in the verification, models used in the verification, results and analysis, conclusions, and future work. D.L., as the next author, provided LOTUS because of being the developer and introduced the multiscale and multi-physics Nuclear Software Development. B.M. and A.L., as the next authors and academic supervisors, provided help from a theoretical perspective. P.B., as the next author and industrial supervisor, provided help from a theoretical perspective. A.D., as the last author, provided the fuel pin cross sections using SCALE-POLARIS. All authors have read and agreed to the published version of the manuscript.

Funding: This research was funded by the EPSRC, EDF, and the UOL through the funding of the EPSRC grant “Innovative LWR Simulation Tool for the Nuclear Renaissance in the UK”, EPSRC grant number EP/R005850/1.

Institutional Review Board Statement: Not applicable.

Informed Consent Statement: Not applicable

Data Availability Statement: See the references.

Conflicts of Interest: The authors declare no conflicts of interest. The funders had no role in the design of the study; in the collection, analyses, or interpretation of data; in the writing of the manuscript, or in the decision to publish the results.

5.9. Nomenclature

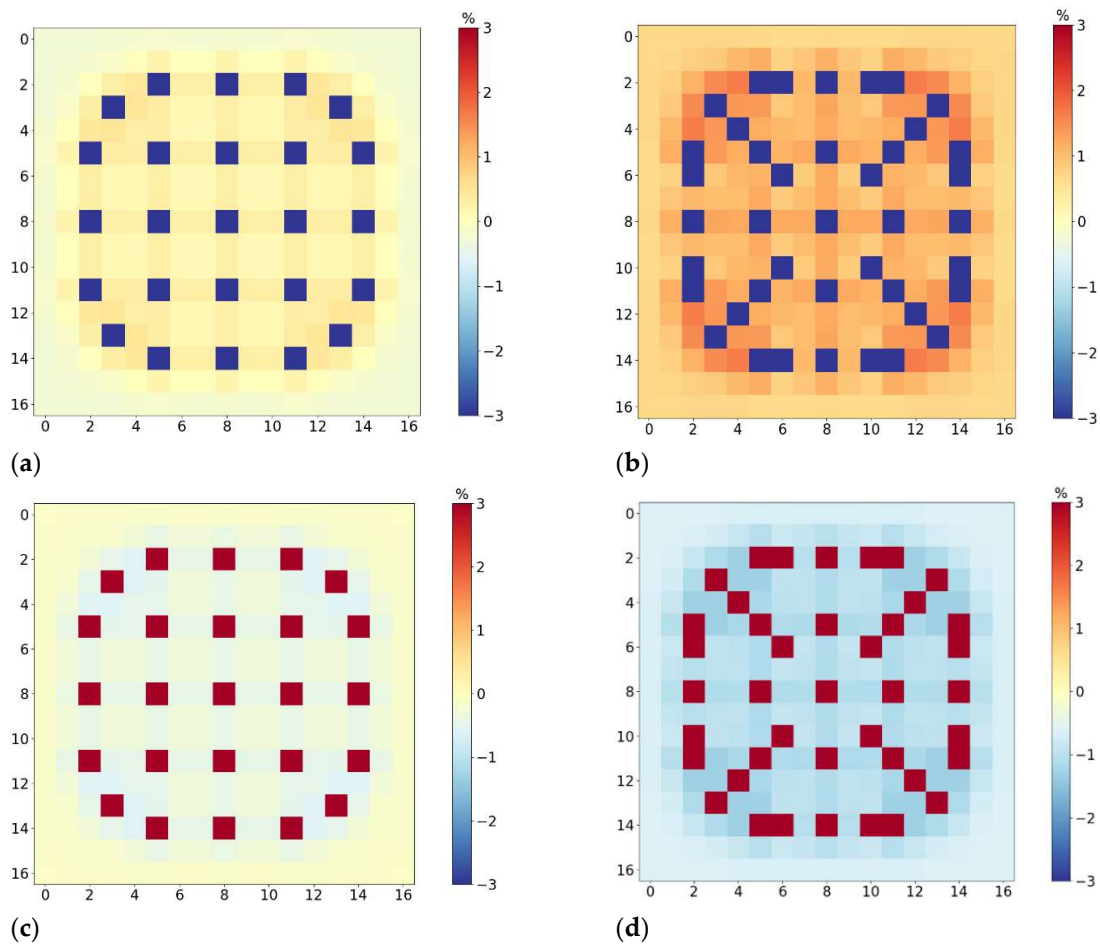
ADF	Assembly Discontinuity Factor
CASL	Consortium for Advanced Simulation of LWRs
CEA	Commissariat à l'énergie atomique et aux énergies alternatives
CFD	Computational Fluid Dynamics
CTF/COBRA-TF	Coolant Boiling in Rod Arrays Two Fluid
$c_{p,clad}$	Clad Specific Heat
$c_{p,fuel}$	Fuel Specific Heat
DNB/DNBR	Departure from Nucleate Boiling
DYN3D/FLOCAL	Dynamical 3 Dimensional
EDF	Electricite De France
EURATOM	European Atomic Energy Community
FDR/HZDR	Forschung Zentrum Dresden/Helmholtz Zentrum Dresden Rossendorf
Fe	Iron
FORTRAN	Formula Translator
Gd_2O_3	Gadolinium Trioxide
He	Helium
HEXNEM	Nodal Expansion Method in Hexagonal Geometries
INL	Idaho National Laboratory
KAIST	Korean Advanced Institute of Science and Technology
k_{eff}	Effective Multiplication Factor
k_{clad}	Clad Thermal Conductivity
k_{fuel}	Fuel Thermal Conductivity
LOTUS	Liverpool Transport Solver
LWR	Light Water Reactor
MOOSE	Multiphysics Object Oriented Simulation Environment
NCSU	North Carolina State University
NURESIM	Nuclear Reactor Simulator
OC	Open Cascade
ORNL	Oak Ridge National Laboratory
PNL	Pacific Northwest Laboratories
PSU	Pennsylvania State University
PWR	Pressurised Water Reactor
q, q_{DYN3D}, q_{rel}	Fission Power Distribution
$\rho_m, \rho_{m,CTF}, \rho_{m,rel}$	Moderator Density Distribution
SALOME	Simulation Numerique par Architecture Logicielle en Open Source et a Methodologie d'Evolution
SP3	Nodal Expansion Method in Square Geometries
θ	Under Relaxation Factor
$T_m, T_{m,CTF}, T_{m,rel}$	Moderator Temperature Distribution
$T_f, T_{f,CTF}, T_{f,rel}$	Fuel Temperature Distribution
$^{235}U, ^{238}U$	Uranium Isotopes
Sn	Tin
UK	United Kingdom
USA	United States of America
USDE	United States Department of Energy

UO₂
 UOL
 UOX-2 (CR/BA-
 16)
 VERA
 Zr

Uranium Dioxide
 University of Liverpool
 Uranium Oxide Fuel Assembly Without or With 16 Burnable Absorbers
 Virtual Environment for Reactor Applications
 Zirconium

5.10. Appendix A. Fuel Assemblies

DYN3D to DYN3D and CTF coupling comparisons within the modified multi parameter exercise for the UOX-2 (CR) and the UOX-2 (BA-16) fuel assemblies are briefly presented from both physical and convergence perspectives for the fluid density feedback, fluid temperature feedback, and fuel temperature feedback, as these were fully presented from a physical perspective in previous work. The relative difference between the final iteration transversal feedback distributions including moderator density and temperature, as well as fuel temperature for all the fuel pins at the average axial node layer are given for both the UOX-2 (CR) and UOX-2 (BA-16) fuel assemblies full power test to show the similarities and differences between the DYN3D and the DYN3D and CTF coupling distributions. Such relative difference between distributions is represented in Figure 5.A1.



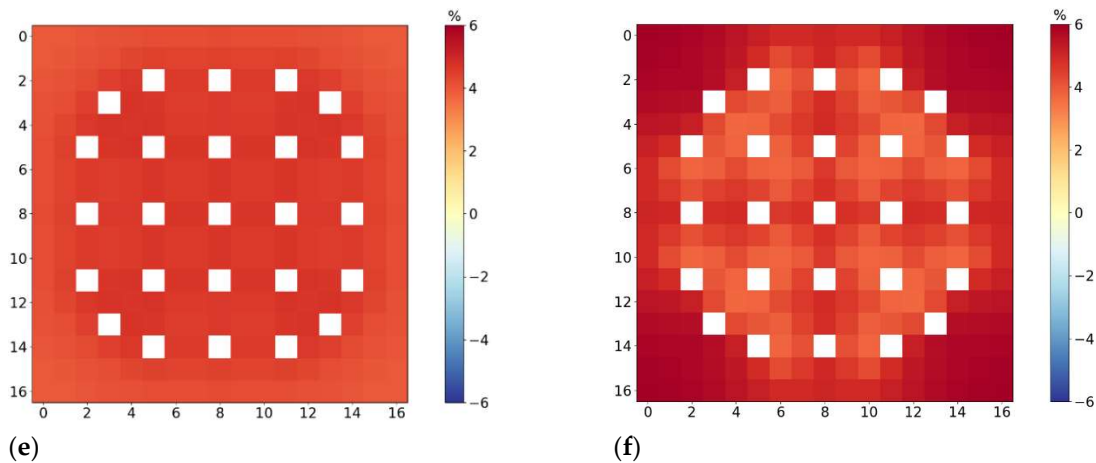
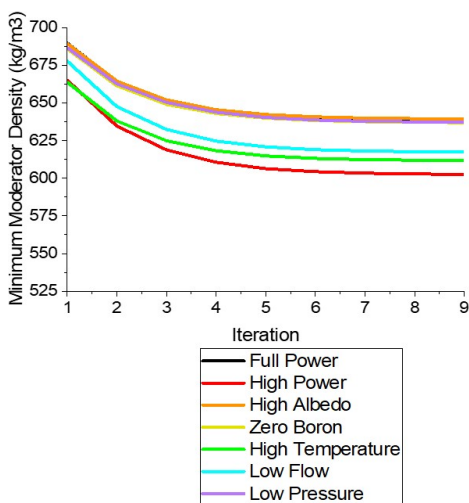


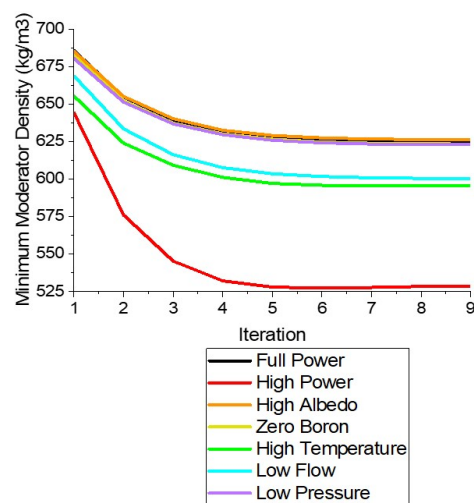
Figure 5.A1. (a) Relative difference between DYN3D and CTF coupling and DYN3D UOX-2 (CR) fuel assembly transversal moderator density distributions, (b) relative difference between DYN3D and CTF coupling and DYN3D UOX-2 (BA-16) fuel assembly moderator density distributions, (c) relative difference between DYN3D and CTF coupling and DYN3D UOX-2 (CR) fuel assembly transversal moderator temperature distributions, (d) relative difference between DYN3D and CTF coupling and DYN3D UOX-2 (BA-16) fuel assembly moderator temperature distributions, (e) relative difference between DYN3D and CTF coupling and DYN3D UOX-2 (CR) fuel assembly transversal fuel temperature distributions and (f) relative difference between DYN3D and CTF coupling and DYN3D UOX-2 (BA-16) fuel assembly fuel temperature distributions.

Between DYN3D and the DYN3D and CTF coupling, differences in the relative difference between transversal feedback distributions including moderator density and temperature, as well as fuel temperature at the average axial node layer in the full power test either the UOX-2 (CR) or UOX-2 (BA-16) fuel assemblies full power test were seen to be present. These differences in the transversal moderator density and temperature, as well as fuel temperature distributions occurred due to the different moderator density and temperature, as well as fuel temperature feedback coefficients resulting from either the presence or absence of crossflow and turbulent mixing and the different boiling and inter-phase models, as well as the different fuel rod models.

All iterations feedback values, including minimum moderator density and maximum moderator temperature, as well as the maximum fuel temperature for both the UOX-2 (CR) and the UOX-2 (BA-16) fuel assemblies, are given for all the tests to show the convergence of the DYN3D and CTF coupling distributions. Such values are represented in Figure 5.A2.



(a)



(b)

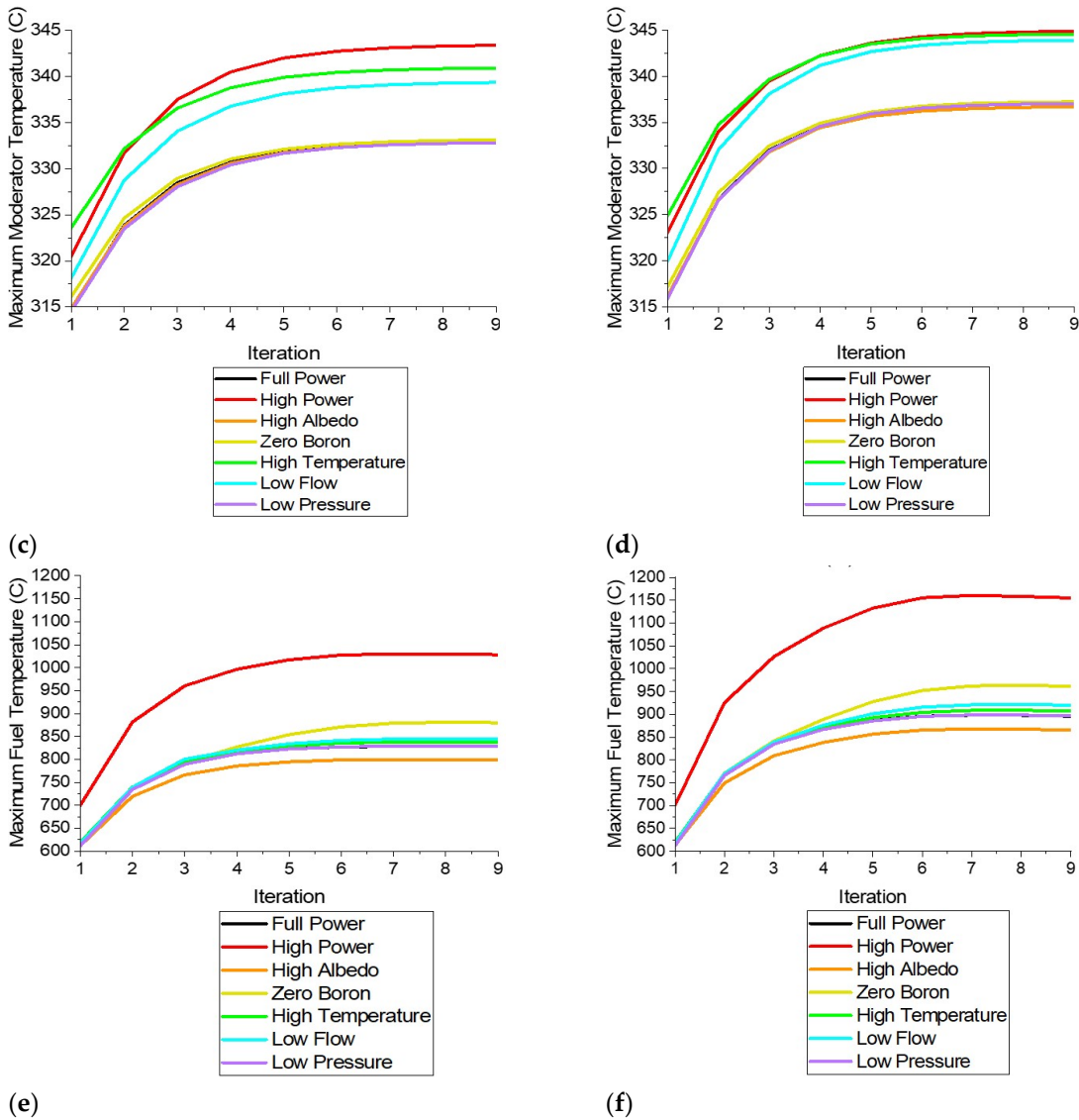


Figure 5.A2. (a) DYN3D and CTF coupling UOX-2 (CR) fuel assembly minimum moderator density convergence, (b) DYN3D and CTF coupling UOX-2 (BA-16) fuel assembly minimum moderator density convergence, (c) DYN3D and CTF coupling UOX-2 (CR) fuel assembly maximum moderator temperature convergence, (d) DYN3D and CTF coupling UOX-2 (BA-16) fuel assembly maximum moderator temperature convergence, (e) DYN3D and CTF coupling UOX-2 (CR) fuel assembly maximum fuel temperature convergence and (f) DYN3D and CTF coupling UOX-2 (BA-16) fuel assembly maximum fuel temperature convergence.

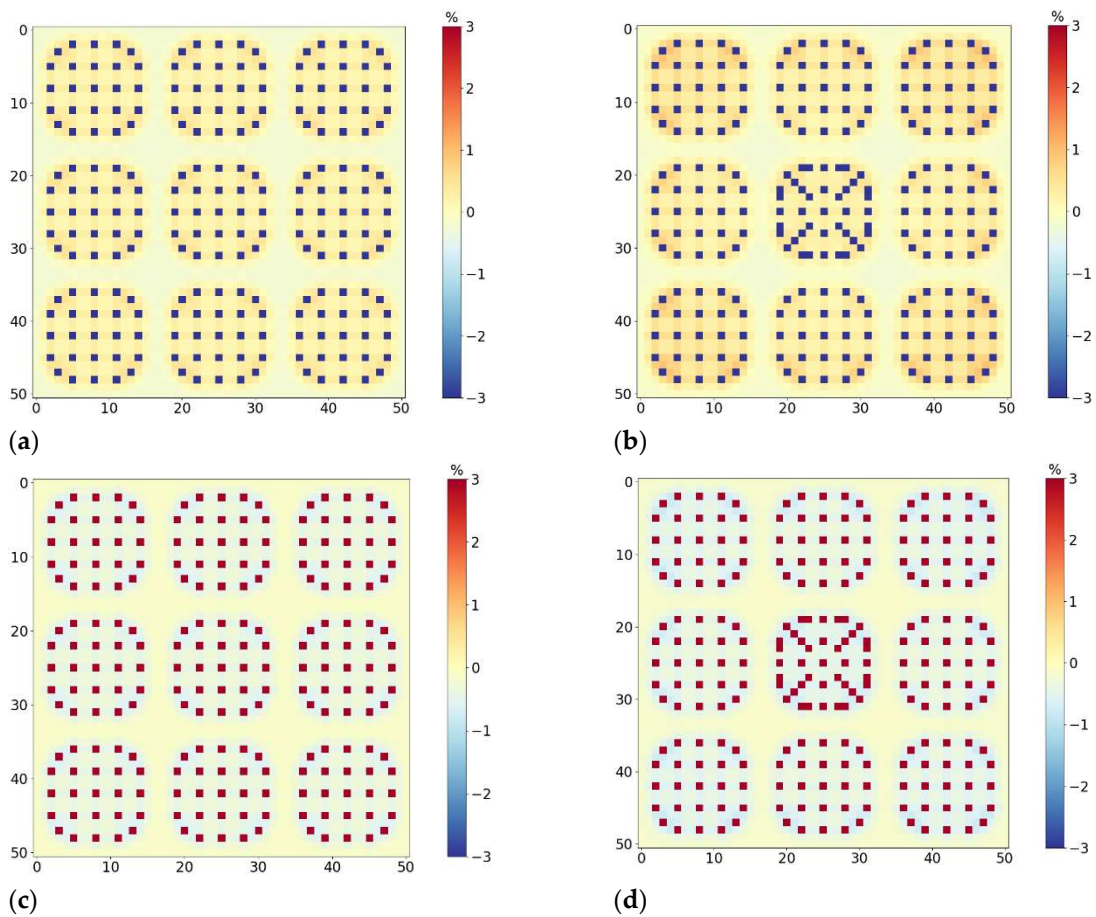
The DYN3D and CTF coupling achieves the convergence of the feedback distributions, including the moderator density and temperature, as well as the fuel temperature distributions, via their own under relaxation until these achieve the steady state.

In the DYN3D and CTF coupling, the convergence of the minimum moderator density and the maximum moderator temperature, as well as the maximum fuel temperature values was seen with higher iteration number in all the tests in both the UOX-2 (CR) and the UOX-2 (BA-16) fuel assemblies. The convergence of the minimum moderator density and maximum moderator temperature, as well as maximum fuel temperature values occurred between 6 and 9 iterations due to several reasons: the presence of standard or mildly hot boundary conditions, which resulted on a faster or slower convergence rate and, therefore, less, or more required iterations according to the convergence criteria. The reasonable under relaxation factor, which resulted in higher stability and, therefore, required more iterations according to the convergence criteria. In the DYN3D and CTF coupling, the slower convergence of the minimum moderator density and the maximum moderator temperature, as well as

the maximum fuel temperature values was seen with higher iteration number in the full power test case in the UOX-2 (BA-16) fuel assembly when compared to the UOX-2 (CR) fuel assembly. This slower convergence of the minimum moderator density and maximum moderator temperature, as well as maximum fuel temperature values occurred due to the higher neutron absorption cross section in the burnable absorber fuel pins, which resulted in more heterogeneity and, therefore, more required iterations according to the convergence criteria.

5.11. Appendix B. Mini-Cores

DYN3D to DYN3D and CTF coupling comparisons within the full reactor start up exercise for the homogeneous and the heterogeneous mini cores are briefly presented from both physical and convergence perspectives for the fluid density feedback, fluid temperature feedback and fuel temperature feedback as these were fully presented from a physical perspective in previous work. The relative difference between the final iteration transversal moderator temperature distributions for all the fuel assemblies at the average axial node layer are given for both the homogeneous and heterogeneous mini-cores full power test to show the similarities and differences between the DYN3D and the DYN3D and CTF coupling distributions. Such relative difference between distributions is represented in Figure 5.A3.



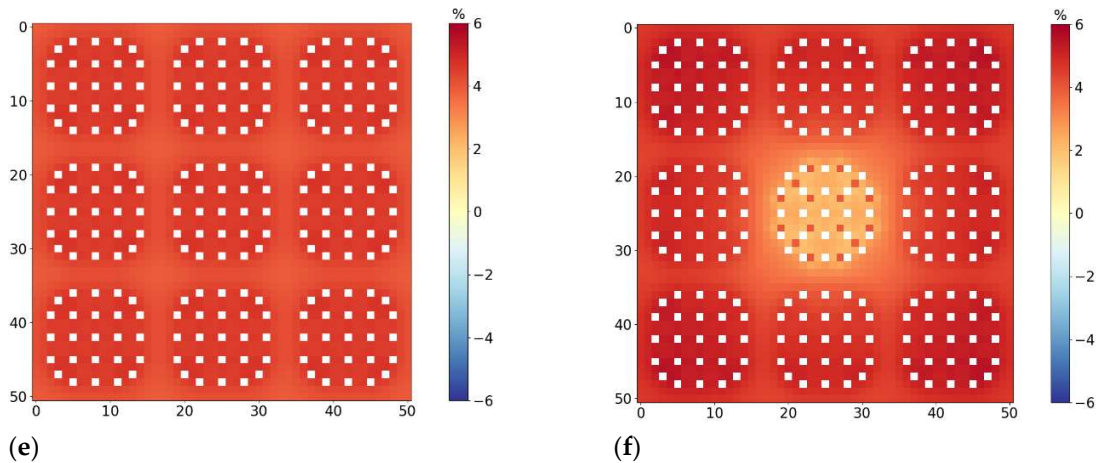
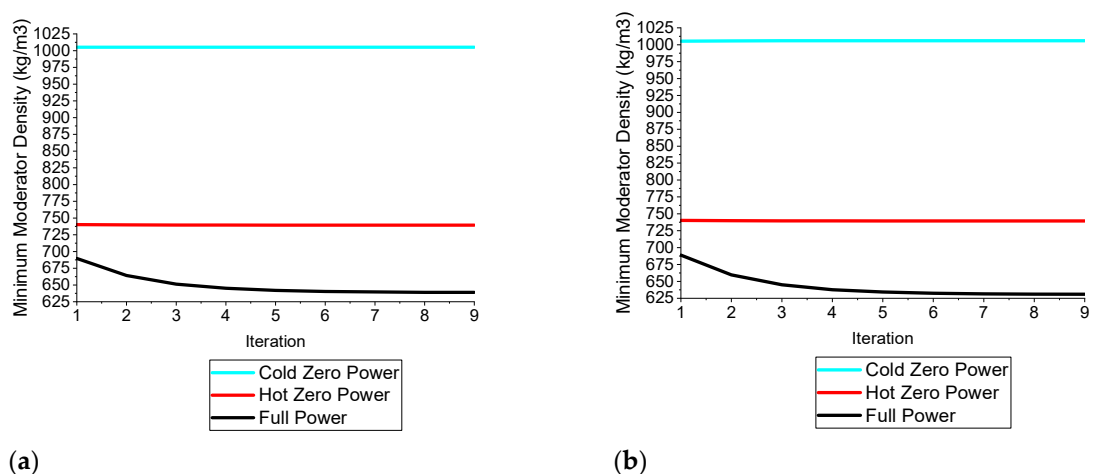


Figure 5.A3. (a) Relative difference between DYN3D and CTF coupling and DYN3D homogeneous mini-core transversal moderator density distributions, (b) relative difference between DYN3D and CTF coupling and DYN3D heterogeneous mini-core transversal moderator density distributions, (c) relative difference between DYN3D and CTF coupling and DYN3D homogeneous mini-core transversal moderator temperature distributions, (d) relative difference between DYN3D and CTF coupling and DYN3D heterogeneous mini-core transversal moderator temperature distributions, (e) relative difference between DYN3D and CTF coupling and DYN3D homogeneous mini-core transversal fuel temperature distributions and (f) relative difference between DYN3D and CTF coupling and DYN3D heterogeneous mini-core transversal fuel temperature distributions.

Between DYN3D and the DYN3D and CTF coupling, differences in the relative difference between transversal feedback distributions, including moderator density and temperature, as well as fuel temperature for all the fuel assemblies at the average axial node layer in the full power test in either the homogeneous or heterogeneous mini cores were seen to be different. These differences in the transversal moderator density and temperature, as well as fuel temperature distribution, occurred due to the different moderator density and temperature, as well as fuel temperature feedback coefficients resulting from either the presence or absence of crossflow and turbulent mixing and the different boiling and inter-phase models, as well as the different fuel rod models.

All iterations feedback values including minimum moderator density and maximum moderator temperature as well as the maximum fuel temperature for both the homogeneous and heterogeneous mini cores for all the tests to show the convergence of the DYN3D and the DYN3D and CTF coupling distributions. Such values are represented in Figures 5.A4.



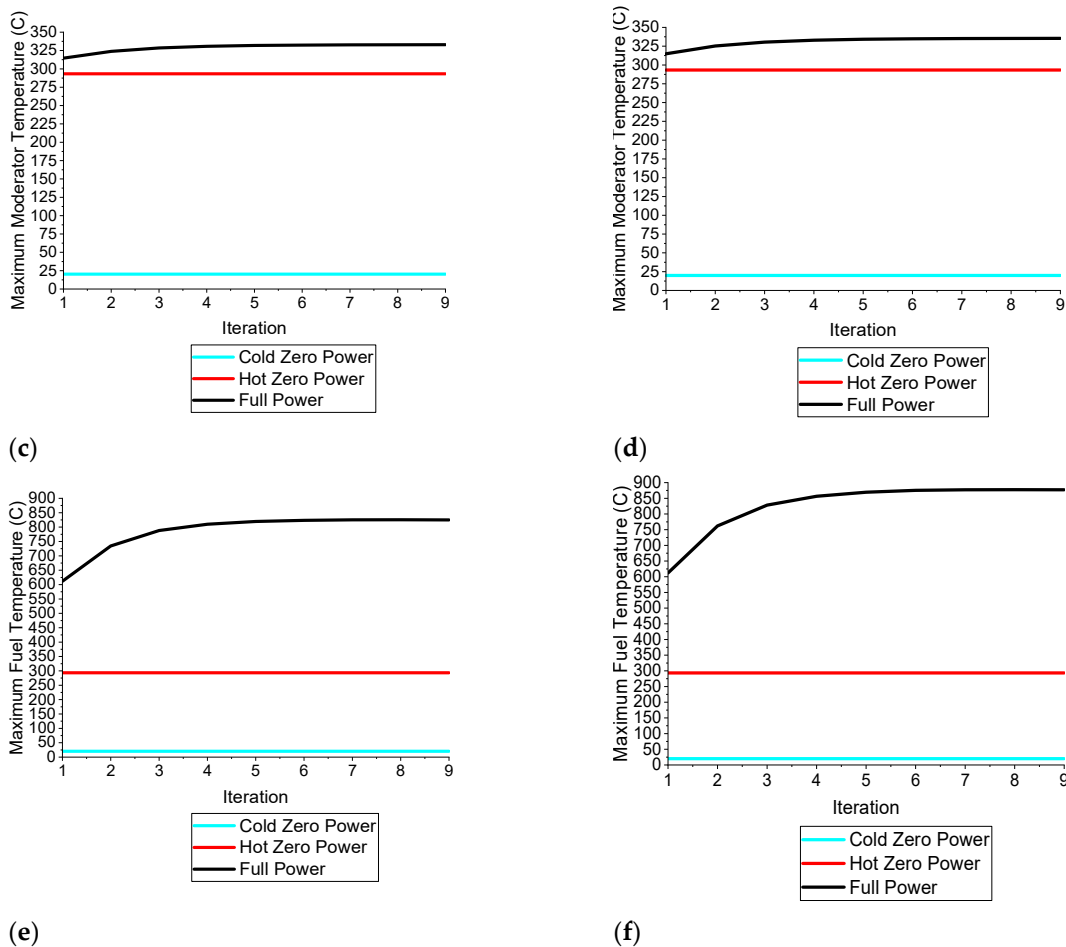


Figure 5.A4. (a) DYN3D and CTF coupling homogeneous mini-core minimum moderator density convergence, (b) DYN3D and CTF coupling heterogeneous mini-core minimum moderator density convergence, (c) DYN3D and CTF coupling homogeneous mini-core maximum moderator temperature convergence, (d) DYN3D and CTF coupling heterogeneous mini-core maximum moderator temperature convergence, (e) DYN3D and CTF coupling homogeneous mini-core maximum fuel temperature convergence and (f) DYN3D and CTF coupling heterogeneous mini-core maximum fuel temperature convergence.

In the DYN3D and CTF coupling, the convergence of the minimum moderator density and the maximum moderator temperature, as well as the maximum fuel temperature values was seen with higher iteration number in the full power case in both the homogeneous and heterogeneous mini cores. This convergence of the minimum moderator density and maximum moderator temperature, as well as maximum fuel temperature values occurred between 1 and 7 iterations due to several reasons: the presence of cold or standard boundary conditions, which resulted on a faster convergence rate and, therefore, less required iterations according to the convergence criteria. The reasonable under relaxation factor, which resulted on higher stability and, therefore, in part more required iterations according to the convergence criteria In the DYN3D and CTF coupling, a mildly slower convergence of the minimum moderator density and the maximum moderator temperature, as well as the maximum fuel temperature values was seen with higher iteration number in the full power case in the heterogeneous mini-core when compared to the homogeneous mini-core. This mildly slower convergence of the minimum moderator density and maximum moderator temperature, as well as the maximum fuel temperature values occurred due to the compensation between the higher neutron absorption cross section in the central fuel assembly with the lower neutron absorption cross section in the side and corner fuel assemblies, which resulted only in slightly more heterogeneity and, therefore, similar required iterations according to the convergence criteria.

5.12. References

1. Merk, B.; Litskevich, D.; Whittle, K.R.; Bankhead, M.; Taylor, R.J.; Mathers, D.; Mathers, D. On a Long Term Strategy for the Success of Nuclear Power. *Energies* 2017, 10, 867. <https://doi.org/10.3390/en10070867>.
2. IAEA. IAEA Nuclear Energy Series Nuclear Reactor Technology Assessment for Near Term Deployment; IAEA: Vienna, Austria, 2013; ISBN 978-92-0-140310-0.
3. Merk, B.; Litskevich, D.; Peakman, A.; Bankhead, M. IMAGINE-A Disruptive Change to Nuclear or How Can We Make More out of the Existing Spent Nuclear Fuel and What Has to Be Done to Make It Possible in the UK? *Atw-Int. Z. Fuer Kernenerg.* 2019, 64, 353–359.
4. Kececi, N.; Modarres, M. Software Development Life Cycle Model to Ensure Software Quality. In *Proceedings of the International PSAM IV Conference*; University of Maryland: College Park, MD, USA, 1998; pp. 1–7.
5. Park, J.; Suh, Y. A Development Framework for Software Security in Nuclear Safety Systems: Integrating Secure Development And System Security Activities. *Nucl. Eng. Technol.* 2014, 46, 47–54. <https://doi.org/10.5516/net.04.2012.061>.
6. IAEA. Optimization of the Coupling of Nuclear Reactors and Desalination Systems; IAEA: Vienna, Austria, 2005; ISBN 920102505X.
7. Forsberg, C.; Brick, S.; Haratyk, G. Coupling heat storage to nuclear reactors for variable electricity output with baseload reactor operation. *Electr. J.* 2018, 31, 23–31. <https://doi.org/10.1016/j.tej.2018.03.008>.
8. Vazquez, M.; Tsigé-Tamirat, H.; Ammirabile, L.; Martin-Fuertes, F. Coupled neutronics thermal-hydraulics analysis using Monte Carlo and sub-channel codes. *Nucl. Eng. Des.* 2012, 250, 403–411. <https://doi.org/10.1016/j.nucengdes.2012.06.007>.
9. Basualdo, J.R.; Sánchez-Espinoza, V.; Stieglitz, R.; Macián-Juan, R. Integration of the subchannel thermal-hydraulic code SubChanFlow into the reactor dynamics code PARCS: Development and testing based on a computational benchmark. *Prog. Nucl. Energy* 2020, 119, 103138. <https://doi.org/10.1016/j.pnucene.2019.103138>.
10. Atkinson, S.; Detkina, A.; Litskevich, D.; Merk, B. A Comparison of Advanced Boiling Water Reactor Simulations between Serpent/CTF and Polaris/DYN3D: Steady State Operational Characteristics and Burnup Evolution. *Energies* 2021, 14, 838. <https://doi.org/10.3390/en14040838>.
11. Zhang, Q.; Cen, S. *Multiphysics Modeling: Numerical Methods and Engineering Applications*; Tsinghua University Press Computational Mechanical Series: Beijing, China, 2015; ISBN 9780124077379.
12. Skillen, A. *Code Coupling*; UKRI STFC: Warrington, UK, 2020; pp. 1-20.
13. NEA. *OECD Neutronics/Thermal-Hydraulics Coupling in LWR Technology*; NEA: Pisa, Italy, 2004; Volume 1; ISBN 9264020837.
14. Benra, F.-K.; Dohmen, H.J.; Pei, J.; Schuster, S.; Wan, B. A Comparison of One-Way and Two-Way Coupling Methods for Numerical Analysis of Fluid-Structure Interactions. *J. Appl. Math.* 2011, 2011, 853560. <https://doi.org/10.1155/2011/853560>.
15. Ribes, A.; Caremoli, C.; Salomé Platform Component Model for Numerical Simulation. In *Proceedings of the 31st Annual International Computer Software and Applications Conference*, Beijing, China, 24–27 July 2007; pp. 1–6. <https://doi.org/10.1109/COMPSAC.2007.185>.
16. Bergeaud, V.; Tajchman, M. Application of the SALOME Software Architecture to Nuclear Reactor Research. *SpringSim '07*: In *Proceedings of the 2007 Spring Simulation Multiconference*, Norfolk, VA, USA 25-29 March 2007; Volume 2, pp. 383–387. <https://doi.org/10.1145/1404680.1404740>.
17. Kochunas, B.; Collins, B.; Stimpson, S.; Salko, R.; Jabaay, D.; Graham, A.; Liu, Y.; Kim, K.S.; Wieselquist, W.; Godfrey, A.; et al. VERA Core Simulator Methodology for Pressurized Water Reactor Cycle Depletion. *Nucl. Sci. Eng.* 2017, 185, 217–231. <https://doi.org/10.13182/nse16-39>.
18. Turner, J.A.; Clarno, K.; Sieger, M.; Bartlett, R.; Collins, B.; Pawlowski, R.; Schmidt, R.; Summers, R. The Virtual Environment for Reactor Applications (VERA): Design and architecture. *J. Comput. Phys.* 2016, 326, 544–568. <https://doi.org/10.1016/j.jcp.2016.09.003>.

19. Gaston, D.; Newman, C.; Hansen, G.; Lebrun-Grandié, D. MOOSE: A parallel computational framework for coupled systems of nonlinear equations. *Nucl. Eng. Des.* 2009, 239, 1768–1778. <https://doi.org/10.1016/j.nucengdes.2009.05.021>.
20. Permann, C.J.; Gaston, D.R.; Andrš, D.; Carlsen, R.W.; Kong, F.; Lindsay, A.D.; Miller, J.M.; Peterson, J.W.; Slaughter, A.E.; Stogner, R.H.; et al. MOOSE: Enabling massively parallel multiphysics simulation. *SoftwareX* 2020, 11, 100430. <https://doi.org/10.1016/j.softx.2020.100430>.
21. Martineau, R.C. The MOOSE Multiphysics Computational Framework for Nuclear Power Applications: A Special Issue of Nuclear Technology. *Nucl. Technol.* 2021, 207. <https://doi.org/10.1080/00295450.2021.1915487>.
22. Chanaron, B.; Ahnert, C.; Crouzet, N.; Sanchez, V.; Kolev, N.; Marchand, O.; Kliem, S.; Papukchiev, A. Advanced multi-physics simulation for reactor safety in the framework of the NURESAFE project. *Ann. Nucl. Energy* 2015, 84, 166–177. <https://doi.org/10.1016/j.anucene.2014.12.013>.
23. Chauliac, C.; Aragonés, J.-M.; Bestion, D.; Cacuci, D.G.; Crouzet, N.; Weiss, F.-P.; Zimmermann, M.A. NURESIM—A European simulation platform for nuclear reactor safety: Multi-scale and multi-physics calculations, sensitivity and uncertainty analysis. *Nucl. Eng. Des.* 2011, 241, 3416–3426. <https://doi.org/10.1016/j.nucengdes.2010.09.040>.
24. Calleja, M.; Sanchez, V.; Jimenez, J.; Imke, U.; Stieglitz, R.; Macián, R. Coupling of COBAYA3/SUBCHANFLOW inside the NURESIM platform and validation using selected benchmarks. *Ann. Nucl. Energy* 2014, 71, 145–158. <https://doi.org/10.1016/j.anucene.2014.03.036>.
25. Grahn, A.; Gommlich, A.; Kliem, S.; Bilodid, Y.; Kozmenkov, Y. Simulation of an MSLB scenario using the 3D neutron kinetic core model DYN3D coupled with the CFD software Trio_U. *Nucl. Eng. Des.* 2017, 315, 117–127. <https://doi.org/10.1016/j.nucengdes.2017.02.002>.
26. Jimenez, G.; Herrero, J.J.; Cuervo, D.; Garcia-Herranz, N.; Ashnert, C. Boron Dilution Benchmark Using CO-BAYA3/FLICA4 Coupled Codes within the NURISP European Project. In Proceedings of the Annual Meeting of Spanish Nuclear Society, Caceres, Spain, 17-19 October 2012.
27. Kozmenkov, Y.; Kliem, S.; Rohde, U. Validation and verification of the coupled neutron kinetic/thermal hydraulic system code DYN3D/ATHLET. *Ann. Nucl. Energy* 2015, 84, 153–165. <https://doi.org/10.1016/j.anucene.2014.12.012>.
28. Mignot, G.; Royer, E.; Rameau, B.; Todorova, N. Computation of a BWR Turbine Trip with CATHARE-CRONOS2-FLICA4 Coupled Codes. *Nucl. Sci. Eng.* 2004, 1184, 235–246. <https://doi.org/10.13182/nse04-a2454>.
29. Turinsky, P.J.; Kothe, D.B. Modeling and simulation challenges pursued by the Consortium for Advanced Simulation of Light Water Reactors (CASL). *J. Comput. Phys.* 2016, 313, 367–376. <https://doi.org/10.1016/j.jcp.2016.02.043>.
30. Szilard, R.; Zhang, H.; Brian Kothe, D.; Turinsky, P. CASL The Consortium for Advanced Simulation of Light Water Reactors; INL: Idaho Falls, ID, USA, 2011.
31. Liu, Y.; Salko, R.; Kim, K.S.; Wang, X.; Kabelitz, M.; Choi, S.; Kochunas, B.; Collins, B.; Martin, W. Improved MPACT energy deposition and explicit heat generation coupling with CTF. *Ann. Nucl. Energy* 2020, 152, 107999. <https://doi.org/10.1016/j.anucene.2020.107999>.
32. Kelly, D.J.; Kelly, A.E.; Aviles, B.N.; Godfrey, A.T.; Salko, R.K.; Collins, B.S. MC21/CTF and VERA multiphysics solutions to VERA core physics benchmark progression problems 6 and 7. *Nucl. Eng. Technol.* 2017, 49, 1326–1338. <https://doi.org/10.1016/j.net.2017.07.016>.
33. Schmidt, R.; Belcourt, K.; Hooper, R.; Pawlowski, R.; Clarno, K.; Simunovic, S.; Slattery, S.; Turner, J.; Palmtag, S. An approach for coupled-code multiphysics core simulations from a common input. *Ann. Nucl. Energy* 2015, 84, 140–152. <https://doi.org/10.1016/j.anucene.2014.11.015>.
34. Stimpson, S.; Clarno, K.; Pawlowski, R.; Gardner, R.; Powers, J.; Collins, B.; Toth, A.; Novascone, S.; Pitts, S.; Hales, J.; et al. Coupled fuel performance calculations in VERA and demonstration on Watts Bar unit 1, cycle 1. *Ann. Nucl. Energy* 2020, 145, 107554. <https://doi.org/10.1016/j.anucene.2020.107554>.

35. Merk, B.; Bankhead, M.; Litskevich, D.; Gregg, R.; Peakman, A.; Shearer, C. On a Roadmap for Future Industrial Nuclear Reactor Core Simulation in the U.K. to Support the Nuclear Renaissance. *Energies* 2018, 11, 3509. <https://doi.org/10.3390/en1123509>.
36. Kim, K.S.; Williams, M.L.; Holcomb, A.M.; Wiarda, D.; Jeon, B.K.; Yang, W.S. The SCALE/AMPX multigroup cross section processing for fast reactor analysis. *Ann. Nucl. Energy* 2019, 132, 161–171. <https://doi.org/10.1016/j.anucene.2019.04.034>.
37. Jessee, M.A.; Wieselquist, W.A.; Mertyurek, U.; Kim, K.S.; Evans, T.M.; Hamilton, S.P.; Gentry, C. Lattice physics calculations using the embedded self-shielding method in Polaris, Part I: Methods and implementation. *Ann. Nucl. Energy* 2020, 150, 107830. <https://doi.org/10.1016/j.anucene.2020.107830>.
38. Mertyurek, U.; Jessee, M.A.; Betzler, B.R. Lattice physics calculations using the embedded self-shielding method in polaris, Part II: Benchmark assessment. *Ann. Nucl. Energy* 2020, 150, 107829. <https://doi.org/10.1016/j.anucene.2020.107829>.
39. Kliem, S.; Gommlich, A.; Grahn, A.; Rohde, U.; Schütze, J.; Frank, T.; Gomez, A.; Sanchez, V. Development of multi-physics code systems based on the reactor dynamics code DYN3D. *Kerntechnik* 2011, 76, 160–165. <https://doi.org/10.3139/124.110146>.
40. Viebach, M.; Lange, C.; Kliem, S.; Demazière, C.; Rohde, U.; Hennig, D.; Hurtado, A. Verification of the code DYN3D for calculations of neutron flux fluctuations. *Ann. Nucl. Energy* 2022, 166, 108735. <https://doi.org/10.1016/j.anucene.2021.108735>.
41. Gomez-Torres, A.M.; Sanchez-Espinoza, V.H.; Kliem, S.; Gommlich, A. Implementation of a fast running full core pin power reconstruction method in DYN3D. *Nucl. Eng. Des.* 2014, 274, 44–55. <https://doi.org/10.1016/j.nucengdes.2014.04.028>.
42. Davies, S.; Rohde, U.; Litskevich, D.; Merk, B.; Bryce, P.; Levers, A.; Detkina, A.; Atkinson, S.; Ravindra, V. CTF and FLOCAL Thermal Hydraulics Validations and Verifications within a Multiscale and Multiphysics Software Development. *Energies* 2021, 14, 1220. <https://doi.org/10.3390/en14051220>.
43. Salko, R.K.; Lange, T.; Kucukboyaci, V.; Palmtag, S.; Sung, Y.; Gehin, J.; Avramova, M. Development of Cobra-Tf for Modeling Full-Core, Reactor Operating CycleS. In *Proceedings of the Advances in Nuclear Fuel Management, Hilton Head Island, SC, USA, 29 March–1 April, 2015*; American Nuclear Society: La Grange Park, IL, USA, 2015; pp. 1–18.
44. Kucukboyaci, V.; Sung, Y.; Salko, R. Cobra-Tf Parallelization and Application to Pwr Reactor Core Subchannel Dnb Analysis. In *Proceedings of the Joint International Conference on Mathematics and Computation, Supercomputing in Nuclear Applications and the Monte Carlo Method, Nashville, TN, USA, 19-23 April 2015*. <https://doi.org/10.13140/rg.2.1.1247.6962>.
45. Davies, S.; Litskevich, D.; Rohde, U.; Detkina, A.; Merk, B.; Bryce, P.; Levers, A.; Ravindra, V. DYN3D and CTF Coupling within a Multiscale and Multiphysics Software Development (Part I). *Energies* 2021, 14, 5060. <https://doi.org/10.3390/en14165060>.
46. Rossiter, G. Development of The Enigma Fuel Performance Code for Whole Core Analysis and Dry Storage Assessments. *Nucl. Eng. Technol.* 2011, 43, 489–498. <https://doi.org/10.5516/net.2011.43.6.489>.
47. Litskevich, D.; Merk, B. SP3Solution versus Diffusion Solution in Pin-by-Pin Calculations and Conclusions Concerning Advanced Methods. *J. Comput. Theor. Transp.* 2014, 43, 214–239. <https://doi.org/10.1080/00411450.2014.913184>.
48. Litskevich, D.; Atkinson, S.; Davies, S. Verification of the current coupling collision probability method with orthogonal flux expansion for the assembly calculations. *Prog. Nucl. Energy* 2020, 130, 103562. <https://doi.org/10.1016/j.pnucene.2020.103562>.
49. Litskevich, D. Development of an Advanced Neutron Transport Solver for Zooming in DYN3D.; Rheinisch-Westfälischen Technischen Hochschule Aachen: Aachen, Germany, 2017.
50. Cho, N.Z.; Nurapt, K. Benchmark Problem 1A Benchmark Problem 1A: MOX Fuel-Loaded Small PWR Core (MOX Fuel with Zoning); KAIST: Daejeon, South Korea, 2000.
51. Grundmann, U.; Rohde, U.; Mittag, S.; Kliem, S. DYN3D Version 3.2 Code for Calculation of Transients in Light Water Reactors (LWR) with Hexagonal or Quadratic Fuel Elements-Description of Models and Methods; HZDR: Dresden, Germany, 2005.

52. Grundmann, U.; Mittag, S.; Rohde, U. DYN3D Version 3.2—Code for Calculation of Transients in Light Water Reactors (LWR) with Hexagonal or Quadratic Fuel Elements—Code Manual and Input Data Description for Release; HZDR: Dresden, Germany, 2007.
53. Salko, R.; Avramova, M.; Wysoski, A.; Hu, J.; Toptan, A.; Porter, N. CTF 4.0 Theory Manual; Oak Ridge National Lab: Oak Ridge, TN, USA, 2019. <https://doi.org/10.2172/1550750>.
54. Salko, R.; Avramova, M.; Wysoski, A.; Hu, J.; Toptan, A.; Porter, N. CTF 4.0 User Manual; Oak Ridge National Lab: Oak Ridge, TN, USA, 2020. <https://doi.org/10.2172/1550748>.
55. Petkov, P.T.; Christoskov, I.D.; Kamenov, K.; Antov, A. Generation of a Two-Group Diffusion and Kinetics Parameters for DYN3D. In Proceedings of the 12th Symposium of AER, Sunny Beach, Bulgaria, 22-28 September 2002.
56. Rajic, H.L.; Ougouag, A. ILLICO: A Nodal Neutron Diffusion Method for Modern Computer Architectures. Nucl. Sci. Eng. 1989, 103, 392–408. <https://doi.org/10.13182/nse89-a23691>.
57. Grigull, U. Properties of Water and Steam in SI Units; Springer: Berlin/Heidelberg, Germany; New York, NY, USA, 1990.
58. Poljanin, L.; Ibragimov, M. Teploobmen v Jadernikh Reaktorakh; Ehnergoizdat: Moscow, USSR, 1982; p. 296.
59. Bezrukov, Y.; Astakhov, V. Experimental Investigation and Static Analysis of Data on Crisis of Heat Exchange in Beams of Rods for WWER Reactors. Teploehnergetika 1976, 8, 80–82.
60. Osmachkin, V.; Borisov, V. The Hydraulic Resistance of Fuel Rod Bundles in a Boiling Water Flow; IAEA: Vienna, Austria, 1970; Volume 2.
61. Rogers, J.T.; Rosehart, R.G. Mixing by Turbulent Interchange in Fuel Bundles in Correlations and Interfaces. In Proceedings of the ASME, New York, NY, USA, 1972.
62. Cooper, J.R.; Dooley, R.B. The International Association for the Properties of Water and Steam; IAPWS: Lucerne, Switzerland, 2007.
63. Thorn, J.R.S.; Walker, W.M.; Fallon, T.A.; Reising, G.F.S. Paper 6: Boiling in Sub-Cooled Water during Flow up Heated Tubes or Annuli. Proc. Inst. Mech. Eng. Conf. Proc. 1965, 180, 226–246. https://doi.org/10.1243/pime_conf_1965_180_117_02.
64. Ha, K.-S.; Jeoung, J.-J.; Sim, S.K. Improvement of Liquid Droplet Entrainment Model in the COBRA-TF Code. J. Korean Nucl. Soc. 1998, 3, 181–193.
65. Mc Adams, W. Heat Transmission; McGraw-Hill: New York, NY, USA, 1985; ISBN 0898748763.

Chapter 6: Multi Ways Coupling of a Transport Code a Subchannel Code and a Nodal Code

Full coupled reactor physics simulation of a reactor core at either the fuel pin or materials level involves 3D neutron transport, mixing fluid and solid dynamics, leading to long computational times. However, full coupled reactor physics simulation of fuel assemblies at either the fuel pin or materials level would involve the former and additional boundary conditions, leading to lower computational times. Only 2D neutron transport is available in LOTUS at either the fuel pin or materials levels, while 3D neutron diffusion is available in DYN3D at either the fuel assembly or fuel pin levels. A combination of 2D transversal neutron transport and 1D axial neutron diffusion can become available through fission power 2D to 3D conversion in a coupling between LOTUS and CTF at either the fuel pin or materials level with DYN3D at the fuel assembly level. Also, 3D mixing fluid dynamics and solid dynamics are available in CTF at the fuel pin level. The 3D mixing fluid dynamics and solid dynamics can be used for cross sections interpolation and 3D to 2D conversion in a coupling between LOTUS and CTF at either the fuel pin or materials level with DYN3D at the fuel assembly level. Boundary conditions are available from DYN3D at the fuel assembly level. Such boundary conditions can be included for certain parts of a reactor core, such as fuel assemblies in a coupling between LOTUS and CTF at either the fuel pin or materials level with DYN3D at the fuel assembly level.

Currently, the aim is the coupling of the transport code LOTUS, the subchannel code CTF and the nodal code DYN3D to deliver within the multi-scale and multi-physics software development full coupled reactor physics at either the fuel pin or materials levels. An initial objective within this aim that was covered was the accuracy and performance evaluation of LOTUS at the materials level [124], where high accuracy and low computational times were demonstrated through the full neutron transport with uniform feedback distributions. This was compared to Open MC at the materials level, which showed similar accuracy but higher computational times through the corresponding full neutron transport.

The present objective within this aim that is being covered is a multi ways coupling between LOTUS and CTF at either the fuel pin or materials levels with DYN3D at the fuel assembly level. In this coupling, full coupled reactor physics will be demonstrated through full neutron transport, mixing fluid dynamics and solid dynamics with feedback and fission power distributions converged via the customized coupling software environment, and boundary conditions converged via DYN3D at the fuel assembly level. This is compared to a multi ways coupling between DYN3D and CTF at the fuel pin level with DYN3D at the fuel assembly level. In this other coupling, improved coupled reactor physics will be demonstrated through simplified neutron diffusion, full mixing fluid dynamics and solid dynamics with feedback and fission power distributions converged via the customized coupling software environment, and boundary conditions converged via DYN3D at the fuel assembly level. Thus, this sixth chapter includes the coupling between LOTUS and CTF at either the fuel pin or materials level with DYN3D at the fuel assembly level verification of the full coupled reactor physics at either the fuel pin or materials level. It also includes the coupling between DYN3D and CTF at the fuel pin level with DYN3D at the fuel assembly level verification of the improved coupled reactor physics at the fuel pin level.

The chapter structure is composed of several sections, each composed of several subsections. Initially, the description of the customized coupling software environment used within the verifications is presented, consisting of the couplings between LOTUS or DYN3D and CTF at either the fuel pin or materials levels with DYN3D at the fuel assembly level, which includes main features and modules. Then, the tabulation of the specifications used within the verifications is stated, comprising the customized benchmark, which contains the geometries, materials, and boundary conditions. Then, the description of the models used in the verifications is mentioned for either the fuel assembly, fuel pin or materials levels comprising the meshes, parameters, correlations, and property tables. Then, results and analysis acquired in the verifications are discussed composed of comparisons. The tests included provide boundary conditions from a 3×3 quarter with reflectors at the fuel assembly level, including the total fission power and mass flow, and the average axial fission power distribution. Also, the tests included provide results for 17×17 fuel assemblies and 34×34 quarter core without reflectors at either the fuel assembly, fuel pin, or materials levels, including the effective multiplication factor, and the fission power and feedback distributions.

6.1. Coupling Software Environment Used within the Verifications

At the beginning, it was indicated that the verifications were performed by using a customized coupling software environment. Therefore, the couplings are presented in the following subsection.

Customized Coupling Software Environment

The customized coupling software environment is comprehended by the coupling between LOTUS and CTF at either the fuel pin or materials levels with DYN3D at the fuel assembly level, and the coupling between DYN3D and CTF at the fuel pin level with DYN3D at the fuel assembly level. Each of these is composed of multiple modules coupled in between. Such modules allow to obtain either full or improved coupled reactor physics in LWR in the steady state. All these modules have been created at the UOL quite recently using PYTHON. The couplings at different scale levels can be seen simplified in Figure 6.1.

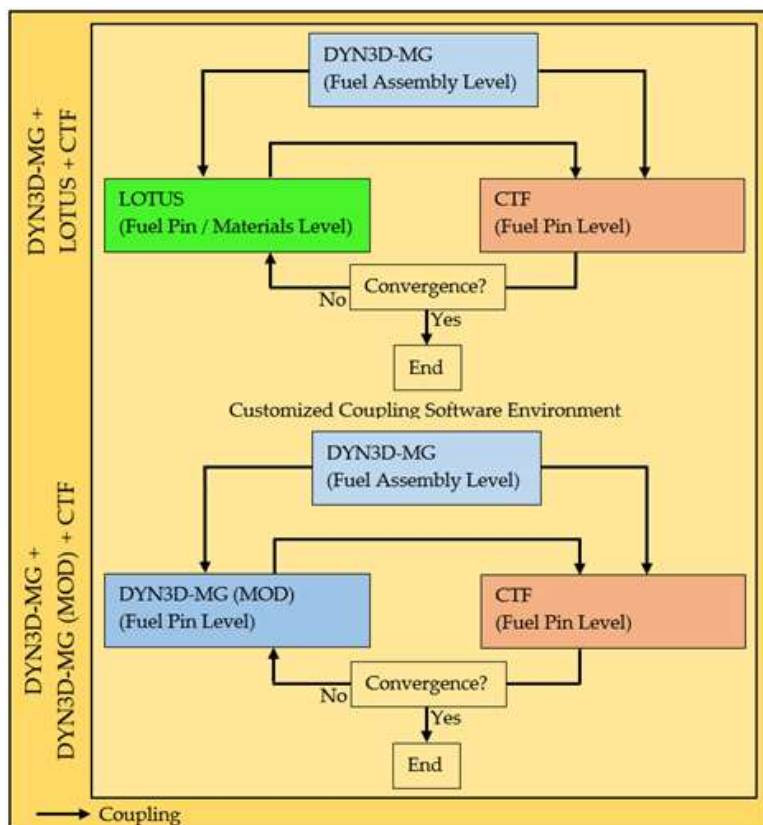


Figure 6.1. Coupling between LOTUS and CTF at the fuel pin/materials level with DYN3D at the fuel assembly level vs coupling between DYN3D and CTF at the fuel pin level with DYN3D at the fuel assembly level (Simplified).

These modules allow to couple DYN3D at the fuel assembly level to either LOTUS at either the fuel pin or materials levels or DYN3D at the fuel pin level via the customized coupling software environment through the albedo distributions. Also, these modules allow to couple DYN3D at the fuel assembly level to CTF at the fuel pin level via the customized coupling software environment through the total fission power and mass flow values. Finally, these modules allow to couple either LOTUS at either the fuel pin or materials levels or DYN3D at the fuel pin level to CTF at the fuel pin level through the fission power distributions and vice versa through the feedback distributions. The couplings at different scale levels can be seen in detail in Figure 6.2.

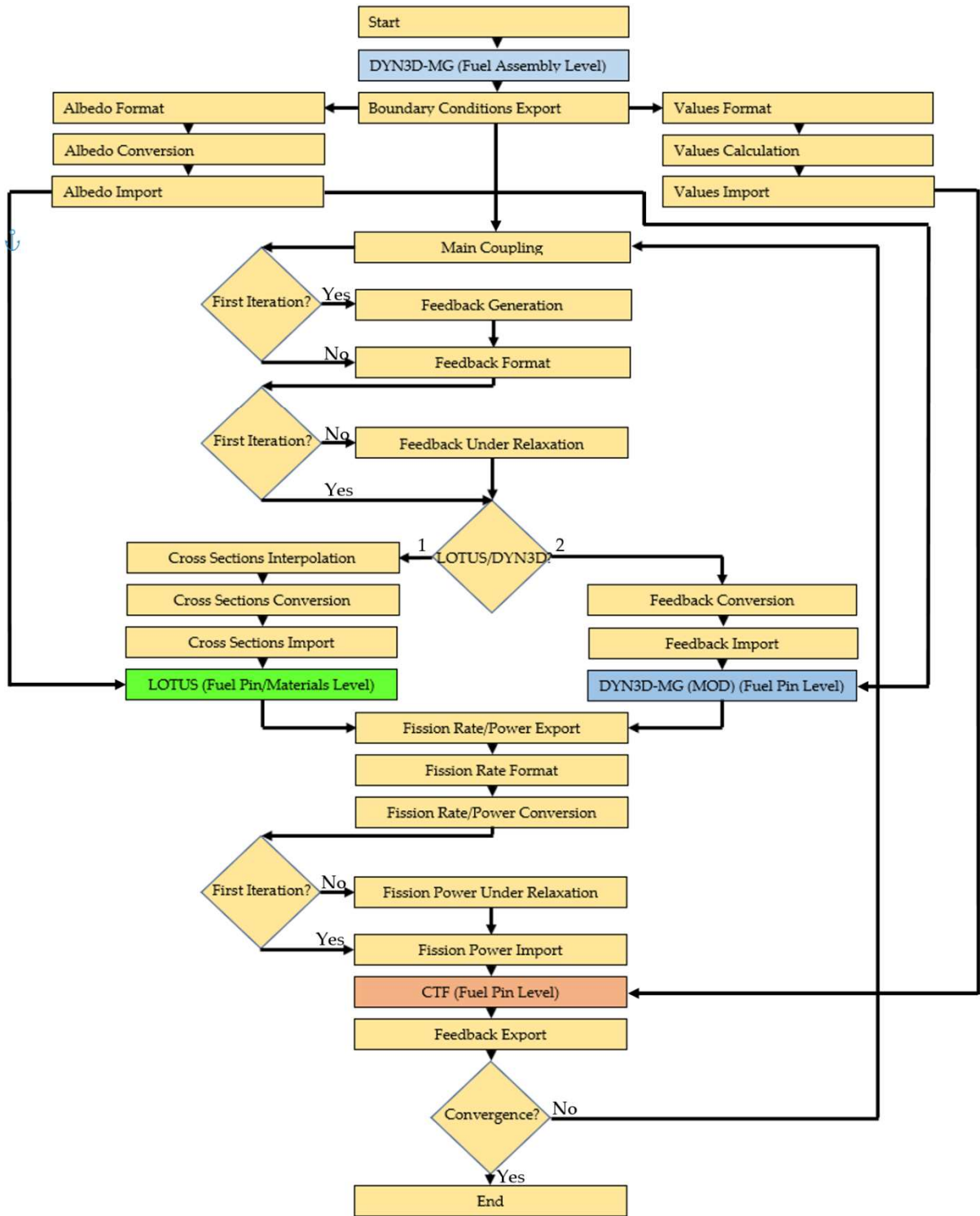


Figure 6.2. Coupling between LOTUS and CTF at the fuel pin level with DYN3D at the fuel assembly level vs coupling between DYN3D and CTF at the fuel pin level with DYN3D at the fuel assembly level (Detailed).

An instance is executed, and a full or part of a reactor core is simulated in DYN3D at the fuel assembly level through the start module.

Boundary conditions, such as the albedo, average axial and transversal fission power and mass flow distributions for the full or part of a reactor core, are exported from DYN3D at the fuel assembly level into the customized coupling software environment through the DYN3D boundary conditions export module.

The albedo distributions for the fuel assemblies or reactor core region are reformatted into east, north, west, south, top, and bottom side arrays within the customized coupling software environment through the LOTUS/DYN3D albedo format module. Then, the albedo distributions for each fuel assembly or reactor core region are converted from arrays to values for each side by splitting them within the customized coupling software environment through the 3D to 2D LOTUS/DYN3D albedo conversion module. Finally, the albedo values for each fuel assembly or reactor core region side are imported from the customized coupling software environment into either LOTUS at either the fuel pin or materials levels, or DYN3D at the fuel pin level through the LOTUS/DYN3D albedo import module.

The average transversal fission power and mass flow distributions for the fuel assemblies or reactor core region are reformatted into arrays within the customized coupling software environment through the CTF values format module. Then, the average transversal fission power and the mass flow distributions for each fuel assembly or reactor core region are used to obtain total fission power and mass flow values within the customized coupling software environment through the CTF values calculation module. Finally, the total fission power and mass flow values for each fuel assembly or reactor core region are imported from the customized coupling software environment into CTF at the fuel pin level through the CTF values import module.

A closed loop is executed, and the fuel assemblies or reactor core region are simulated in either the coupling between LOTUS and CTF at either the fuel pin or materials levels or the coupling between DYN3D and CTF at the fuel pin level through the main coupling module.

In the first iteration, in both couplings, uniform feedback distributions for each fuel assembly or reactor core region are generated based on initial values within the customized coupling software environment through the LOTUS/DYN3D feedback generation module. In all the iterations, in both couplings, the feedback distributions for each fuel assembly or reactor core region are reformatted into 3D arrays within the customized coupling software environment through the LOTUS/DYN3D feedback format module. In later iterations, in both couplings, the feedback distributions for each fuel assembly or reactor core region are under relaxed using the previous iteration and the traditional method within the customized coupling software environment through the LOTUS/DYN3D feedback under-relaxation module. For the closed loop, the under-relaxation equations are given by:

$$\rho_{m,rel}^i = \theta \rho_{m,CTF}^i + (1 - \theta_{feed}) \rho_{m,rel}^{i-1} \quad (29)$$

$$T_{m,rel}^i = \theta T_{m,CTF}^i + (1 - \theta_{feed}) T_{m,rel}^{i-1} \quad (30)$$

$$T_{f,rel}^i = \theta T_{f,CTF}^i + (1 - \theta_{feed}) T_{f,rel}^{i-1} \quad (31)$$

In these equations $\rho_{m,rel}^i$, $T_{m,rel}^i$, $T_{f,rel}^i$ and $\rho_{m,rel}^{i-1}$, $T_{m,rel}^{i-1}$, $T_{f,rel}^{i-1}$ represent the current and previous iteration underrelaxed moderator density and temperature, and fuel temperature distributions while $\rho_{m,CTF}^i$, $T_{m,CTF}^i$, $T_{f,CTF}^i$ represent the current iteration CTF at the fuel pin level moderator density and temperature, and fuel temperature distributions, θ_{feed} represents the feedback under-relaxation factor, and i the iteration.

In all the iterations, in the first coupling, the fuel pin or materials cross sections for each fuel assembly or reactor core region are interpolated according to the feedback distributions and multi-material and multi-group 3D interpolation method within the customized coupling software environment through the LOTUS cross sections interpolation module. In all the iterations, in the first coupling, the fuel pin or materials cross sections for each fuel assembly or reactor core region are converted from 3D arrays to 2D slices by splitting them within the customized coupling software environment through the 3D to 2D LOTUS cross sections conversion module. In all the iterations, in the first coupling, the fuel pin or materials cross sections for each fuel assembly or reactor core region are imported from the customized coupling software environment into LOTUS at either the fuel pin or materials level through the LOTUS cross sections import module. For each iteration, transversal fission reaction rate distributions for each fuel assembly or reactor core region and slice are obtained by running LOTUS at either the fuel pin or materials levels in parallel within the customized coupling software environment.

In all the iterations, in the second coupling, the feedback distributions for each fuel assembly or reactor core region are converted from 3D arrays to 2D slices by splitting them within the customized coupling software environment through the 3D to 2D DYN3D feedback conversion module. In all the

iterations, in the second coupling, the feedback distributions for each fuel assembly or reactor core region are imported from the customized coupling software environment into DYN3D at the fuel pin level through the DYN3D feedback import module. For each iteration, transversal fission reaction rate distributions for each fuel assembly or reactor core region and slice are obtained by running DYN3D at the fuel pin level in parallel within the customized coupling software environment.

In all the iterations, in both couplings, either the fission reaction rate or the fission power distributions for each fuel assembly or reactor core region are exported from either LOTUS at either the fuel pin or materials levels, or DYN3D at the fuel pin level into the customized coupling software environment through the LOTUS/DYN3D fission rate or fission power export module. In all the iterations, in both couplings, either the transversal fission reaction rate or fission power distributions for each fuel assembly or reactor core region are reformatted into 2D slices within the customized coupling software environment through the CTF fission rate format module. In all the iterations, in all couplings, either the transversal fission reaction rate or fission power distributions for each fuel assembly or reactor core region are converted from 2D slices to a 3D array by normalizing them by the average and multiplying these by the average axial fission power distribution within the customized coupling software environment through the 2D to 3D CTF fission rate to power synthesis module. In later iterations, in both the first and second couplings, the fission power distributions for each fuel assembly or reactor core region are under relaxed using the previous iteration within the customized coupling software environment through the CTF power under-relaxation module. For the closed loop, the under-relaxation equation is given by:

$$q_{fis,rel}^i = \theta q_{fis,LOTUS/DYN3D}^i + (1 - \theta_{fis}) q_{fis,rel}^{i-1} \quad (32)$$

In these equations $q_{fis,rel}^i$ and $q_{fis,rel}^{i-1}$ represent the current and previous iteration underrelaxed fission power distribution while $q_{fis,LOTUS/DYN3D}^i$ represents the current iteration LOTUS at either the fuel pin or materials levels or DYN3D at the fuel pin level fission power distribution, and θ_{fis} represents the fission power under-relaxation factor.

In all the iterations, in both couplings, the fission power distributions for each fuel assembly or reactor core region are imported from the customized coupling software environment into CTF at the fuel pin level through the CTF power import module. For each iteration, the feedback distributions for each fuel assembly or reactor core region are obtained by running CTF at the fuel pin level within the customized coupling software environment. In all the iterations, in both couplings, the feedback distributions for each fuel assembly or reactor core region are exported from CTF at the fuel pin level into the customized coupling software environment through the CTF feedback export module.

Finally, the closed loop continues in later iterations until achieving a convergence criterion in either the coupling between LOTUS and CTF at either the fuel pin or materials levels or coupling between DYN3D and CTF at the fuel pin level defined by small reactivity, fission power, and feedback differences. For the closed loop, the convergence criteria are given by:

$$\max(\rho_{m,rel}^i - \rho_{m,rel}^{i-1}) \leq \max(R_{\rho_{m,rel}} \rho_{m,rel}^{i-1}, A_{\rho_{m,rel}}) \quad (33)$$

$$\max(T_{m,rel}^i - T_{m,rel}^{i-1}) \leq \max(R_{T_{m,rel}} T_{m,rel}^{i-1}, A_{T_{m,rel}}) \quad (34)$$

$$\max(T_{f,rel}^i - T_{f,rel}^{i-1}) \leq \max(R_{T_{f,rel}} T_{f,rel}^{i-1}, A_{T_{f,rel}}) \quad (35)$$

$$\max(q_{fis,rel}^i - q_{fis,rel}^{i-1}) \leq \max(R_{q_{fis,rel}} q_{fis,rel}^{i-1}, A_{q_{fis,rel}}) \quad (36)$$

$$|k_{eff}^i - k_{eff}^{i-1}| \leq \max(R_{k_{eff}} k_{eff}^{i-1}, A_{k_{eff}}) \quad (37)$$

In these convergence criteria $R_{\rho_{m,rel}}$, $R_{T_{m,rel}}$, $R_{T_{f,rel}}$, $R_{q_{fis,rel}}$, $R_{k_{eff}}$ and $A_{\rho_{m,rel}}$, $A_{T_{m,rel}}$, $A_{T_{f,rel}}$, $A_{q_{fis,rel}}$, $A_{k_{eff}}$ represent the relative and absolute convergence tolerances for each magnitude while k_{eff}^i and k_{eff}^{i-1} represent the current and previous iteration effective multiplication factor.

6.2. Specifications Used within the Verifications

At the beginning, it was indicated that the verifications were performed through the simulation of the customized benchmark. Therefore, the specifications are indicated in the current subsection.

Customized Benchmark

A customized benchmark is proposed to simulate PWR neutronics and thermal hydraulics. Initial tests are comprehended by steady-state 3x3 quarter core with reflectors composed of fuel assemblies from which boundary conditions are obtained and used in later tests. Main tests are comprehended by steady-state 17x17 fuel assemblies and 34x34 quarter core without reflectors containing fuel pins, guide tubes, and burnable absorber pins and previous boundary conditions.

The customized benchmark includes a multiscale, multi-physics, and multigroup PWR evaluation exercise for the quarter core with reflectors consisting of several coupling tests based on a small PWR. These tests range in total fission power from hot zero to full power. In previous work on the coupling between DYN3D and CTF at the fuel pin level, the boundary conditions for the 17x17 fuel assemblies and other parts of a reactor core were symmetric. This led to a less realistic representation of a PWR. In current work on the couplings between LOTUS or DYN3D and CTF at either the fuel pin or materials levels with DYN3D at the fuel assembly level, the boundary conditions for the 17x17 fuel assemblies and 34x34 quarter core without reflectors are asymmetric. This leads to a more realistic representation of a small PWR. The data for the tests is described.

The specifications are composed of the geometry and boundary conditions for the 3x3 quarter core with reflectors, the geometries for the 17x17 fuel assemblies and the 34x34 quarter core without reflectors, the guide tube and burnable absorber/fuel pin geometry, and materials that are common to all of them. The geometry and boundary conditions for the quarter core with reflectors are given in Tables 6.1 and 6.2.

Table 6.1. Quarter core with reflectors geometry.

Type	Quarter Core with Reflectors Transversal Geometry
Channel Width (m)	0.2142
Type	Quarter Core with Reflectors Axial Geometry
Axial Length (Active) (m)	3.658

Table 6.2. Quarter core with reflectors boundary conditions.

Boundary Conditions	Total Fission Power (MW)	Total Mass Flow (kg/s)	Inlet Temperature (C)	Outlet Pressure (bar)	Boric Acid Concentration (ppm)	Albedo
Hot Zero Power	1.000E-06	756.800	287	153.750	900	reflective/vacuum
Full Power	67.133	756.800	287	153.750	900	reflective/vacuum

The geometries for the 17x17 fuel assemblies and the 34x34 quarter core without reflectors are given in Table 6.3.

Table 6.3. 17x17 fuel assemblies and 34x34 quarter core without reflectors geometry.

Type	17x17 Fuel Assemblies Transversal Geometry
Cell Width (m)	0.0126
Number of Guide Tubes	25
Number of Burnable Absorber Pins	0 / 16
Number of Fuel Pins	264 / 248
Type	34x34 Quarter Core without Reflectors Transversal Geometry

Cell Width (m)	0.0126
Number of Guide Tubes	100
Number of Burnable Absorber Pins	32
Number of Fuel Pins	1024

The geometry for the guide tube and burnable absorber / fuel pin common to all of them are given in Table 6.4.

Table 6.4. Guide tube and burnable absorber / fuel pin geometry.

Type	Guide Tube	Fuel/Burnable Absorber Pin (Clad/Fuel)	
External Diameter (m)	0.01224	0.00950	0.00819
Internal Diameter (m)	0.01143	0.00836	-

The materials common to all of them are given in Table 6.5.

Table 6.5. Materials.

Reflector Composition	H ₂ O		
Clad Composition	Zircalloy (97.91% Zr, 1.59% Sn, 0.5% Fe)		
Clad Density (kg/m ³)	6400		
Clad Thermal Conductivity (W/m K)	$k_{clad} = 7.51 + 2.09 \cdot 10^{-2}T - 1.45 \cdot 10^{-5}T^2 + 7.67 \cdot 10^{-9}T^3$	(38)	
Clad Specific Heat (J/kg K)	$c_{p_{clad}} = 252.54 + 0.11474T$	(39)	
Gap Composition	He		
Gap Heat Conductance (kJ/m ² K)	5678		
Burnable Absorber Pin Composition	UO ₂ (0.711% ²³⁵ U, 90.289% ²³⁸ U) + Gd ₂ O ₃ (9.0%)		
Fuel Pin Composition	UO ₂ (3.3% ²³⁵ U, 96.7% ²³⁸ U)		
Fuel Density (kg/m ³)	10040		
Fuel Thermal Conductivity (W/m K)	$k_{fuel} = \max\left(\frac{2335}{464 + T}, 1.1038\right) + 7.027 \cdot 10^{-3} \cdot 10^{-3} e^{1.867 \cdot 10^{-3} T}$	(40)	
Fuel Specific Heat (J/kg K)	$c_{p_{fuel}} = \frac{8.5013 \cdot 10^8 e^{\frac{535.285}{T}}}{T^2 \left(e^{\frac{535.285}{T}} - 1\right)^2} + 0.0243T + \frac{1.6587 \cdot 10^{12}}{T^2} e^{-\frac{18968}{T}}$	(41)	
Neutron energy groups limits (eV)	Group 0≡ (0.625, 20000000) Group 1≡ (0.00001, 0.625)		

6.3. Models Used within the Verifications

At the beginning, it was indicated that the verifications were performed through the simulation of the customized benchmark. Therefore, the models are indicated in the current subsections.

6.3.1. Fuel Assembly Level

In DYN3D at the fuel assembly level, models for the quarter core with reflectors include the mesh. In total, 9 transversal nodes and 36 axial node layers have been used to represent it, which may contain an average fuel pin obtained from either 25 guide tubes, 16 burnable absorber pins and 248 fuel pins, or 25 guide tubes and 264 fuel pins. The quarter core with reflectors model of the mesh can be seen in Figure 6.3.

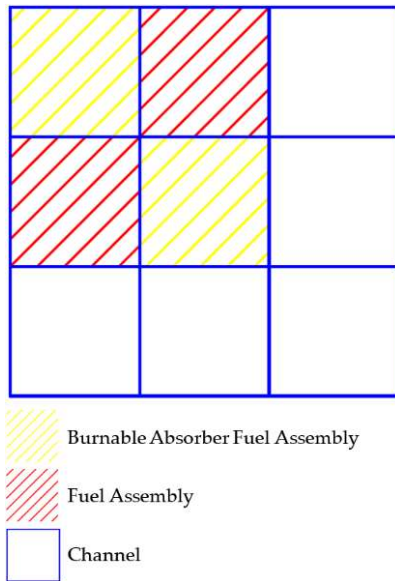


Figure 6.3. DYN3D at the fuel assembly level quarter core with reflectors.

In NK within DYN3D at the fuel assembly level, other models include the cross sections, the MG and NEM methods, and the boundary conditions. Homogenized cross sections at the fuel assembly level have been used, which depend on the feedback, and were generated through the ESSM (Embedded Self Shielded Method) and homogenization methods within SCALE-POLARIS. Interpolation within DYN3D has been used according to the feedback distributions obtained within FLOCAL at the fuel assembly level. Only two neutron energy groups have been considered to preserve low computational times. Second-order polynomials have been used to solve the neutrons motion. The albedo distributions have been set according to the specifications to achieve heterogeneity.

In FLOCAL within DYN3D at the fuel assembly level, other models include the water thermophysical properties, the channel method, the constitutive relations, the fuel and clad thermophysical properties and the fuel rods method. IAPWS tables have been used, which are commonly used in PWR. The Filonenko and Osmachkin multi-phase friction pressure losses correlation has been considered, out of several available. No form pressure losses have been considered to reduce the complexity. The Rassokhin and Borishaskji nucleate boiling correlation has been used, being the only one available [156]. The Bezrukov and Astakhov DNB correlation has been considered, out of several available [157]. The total mass flow, outlet pressure, inlet moderator temperature, and boric acid concentration have been set according to the specifications. Average thermophysical properties have been considered and included according to the specifications. Conversion within DYN3D has been used according to the fission reaction rates obtained within NK at the fuel assembly level. The total fission power has been set according to the specifications.

6.3.2. Fuel Pin or Materials Level

Either in LOTUS at either fuel pin or materials level or in DYN3D at the fuel pin level, different models between the fuel assemblies and quarter core without reflectors include the meshes. Up to 289 transversal cells or nodes in a fuel cell approach or 1131 transversal cells in a smaller cell approach and 36 split axial node layers have been used to represent the former, which contain either 25 guide tubes, 16 burnable absorber pins, and 248 fuel pins, or 25 guide tubes and 264 fuel pins. Up to 1156 transversal cells or nodes in a fuel cell approach or 4524 transversal cells in a smaller cell approach and 36 split axial node layers have been used to represent the latter, which contains 100 guide tubes, 32 burnable absorber pins and 1024 fuel pins. Both the fuel assemblies and quarter core without reflectors model of the meshes in a fuel cell approach can be seen in Figure 6.4.

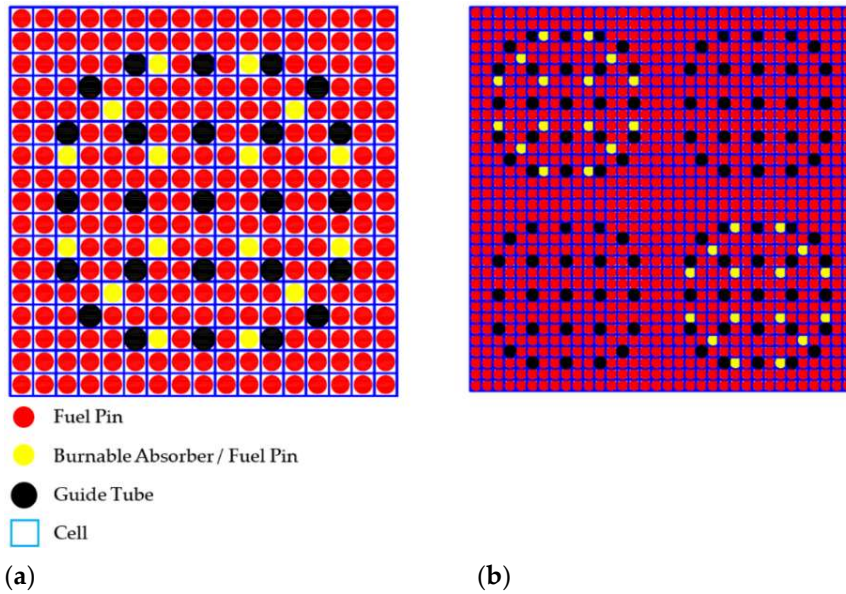


Figure 6.4. (a) DYN3D at the fuel pin level or LOTUS at either the fuel pin or materials level fuel assembly; (b) DYN3D at the fuel pin level or LOTUS at either the fuel pin or materials level quarter core without reflectors.

Either in LOTUS at either fuel pin or materials level or in DYN3D at the fuel pin level, common models between the fuel assemblies and quarter core without reflectors include the cross sections, the MG and either the CCCP or NEM methods, and the boundary conditions. Either homogenized cross sections at the fuel pin level or fuel, gap, clad, and moderator cross sections at the materials level have been used, which depend on the feedback, and were generated through the ESSM and homogenization methods within SCALE-POLARIS. Interpolation within the customized coupling software environment has been used in LOTUS at either fuel pin or materials level, while interpolation within DYN3D has been used in DYN3D at the fuel pin level, according to the feedback distributions obtained within CTF at the fuel pin level. Only two neutron energy groups have been considered to preserve low computational times. Zero-order orthonormal polynomials and discretization parameters including a segment size of 0.9 cm, a number of azimuthal angles of 12 and a number of polar angles of 3 have been used to solve the neutrons motion in LOTUS at either fuel pin or materials level. Second-order polynomials have been used to solve the neutrons motion in DYN3D at the fuel pin level. The albedo distributions have been set to the corresponding obtained in DYN3D at the fuel assembly level to reconstruct the heterogeneity.

In CTF at the fuel pin level, different models between the fuel assemblies and quarter core without reflectors include the meshes. In sum, 324 transversal mesh cells in a subchannel approach connected by 612 gaps and 36 axial layers have been used to represent the former, which contain either 16 burnable absorber pins, 248 fuel pins, and 25 guide tubes or 264 fuel pins and 25 guide tubes. In sum, 1225 transversal mesh cells and 36 axial layers have been used to represent the latter, which contains 32 burnable absorber pins, 1024 fuel pins, and 25 guide tubes. Both the fuel assemblies and quarter core without reflectors model of the meshes in a subchannel approach can be seen in Figure 6.5.

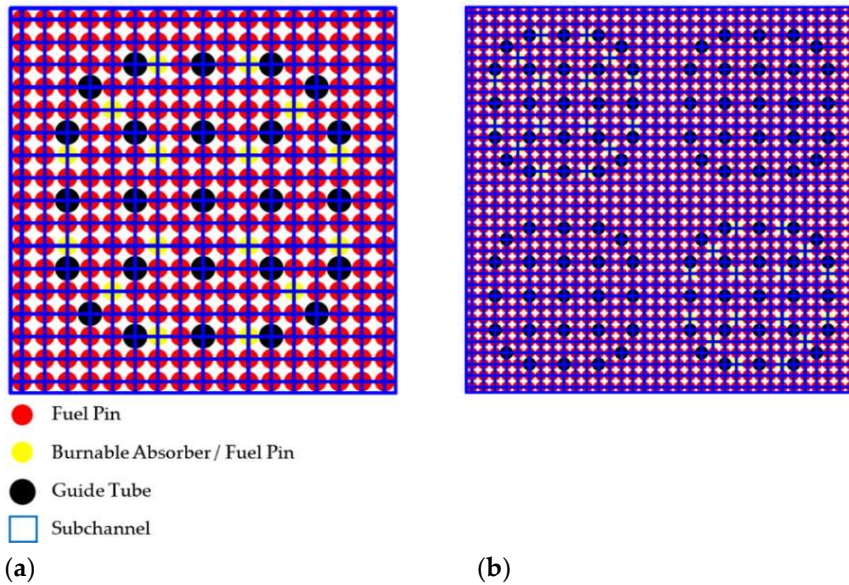


Figure 6.5. (a) CTF at the fuel pin level fuel assembly; **(b)** CTF at the fuel pin level quarter core without reflectors.

In CTF at the fuel pin level, common models between the fuel assemblies and quarter core without reflectors include the water thermophysical properties, the subchannel method, the closure terms, the fuel and clad thermophysical properties and the fuel rods method. IAPWS tables have been used, which are commonly used in PWR. The Mc Adams multi-phase friction pressure losses correlation has been considered, out of several available. No form pressure losses have been considered to reduce the complexity. The Rogers and Rosehart turbulent mixing has been used, which determines the mixing coefficients according to the corresponding mesh cell [158]. The Thorn nucleate boiling correlation has been considered, which is needed for high pressure [159]. Groeneveld DNB look-up tables have been considered, which are the most robust available [160]. Thermophysical properties tables interpolation has been considered and included according to the specifications. The total mass flow, outlet pressure, inlet moderator temperature, and boric acid concentration have been set to the corresponding obtained in DYN3D at the fuel assembly level. Average thermophysical properties have been considered and included according to the specifications. Conversion within the customized coupling software environment has been used according to the fission reaction rates obtained within either LOTUS at either the fuel pin or materials levels, or DYN3D at the fuel pin level. The total fission power has been set to the corresponding obtained in DYN3D at the fuel assembly level.

6.4. Results and Analysis

Considering the results for the coupled reactor physics in the couplings between LOTUS or DYN3D and CTF at either the fuel pin or materials levels with DYN3D at the fuel assembly level, these are presented at the corresponding level. These are included for DYN3D at the fuel assembly level, and the coupling between DYN3D and CTF at the fuel pin level. Also, these are included for the coupling between LOTUS and CTF at the fuel pin level, and the coupling between LOTUS and CTF at the materials level. Such results were achieved through the simulation of the customized benchmark. Initially, DYN3D at the fuel assembly level boundary conditions from the quarter core with reflectors within the coupling verifications are presented for the individual fuel assemblies and quarter core without reflectors, including the total fission powers and mass flows, and the average axial fission power distributions in the first subsection. Finally, coupling at different scale level comparisons within the coupling verifications are presented for the individual fuel assemblies and quarter core without reflectors, including the effective multiplication factor, fission power, fuel temperature, and DNBR in the second subsection and local Appendix.

6.4.1. Quarter Core with Reflectors

The DYN3D at the fuel assembly level boundary conditions from the quarter core with reflectors within the multiscale, multi-physics, and multigroup PWR evaluation exercise for the individual fuel assemblies and the quarter core without reflectors consist of several magnitudes and distributions. These include the total fission power, mass flow, and the average axial fission power distributions but do not include the albedo distributions for practical reasons. The total fission powers and mass flows for the individual fuel assemblies and quarter core without reflectors are given for all the tests, which allow the simulation in the couplings at different scale levels. All these values can be seen in Figure 6.6 and Table 6.6.

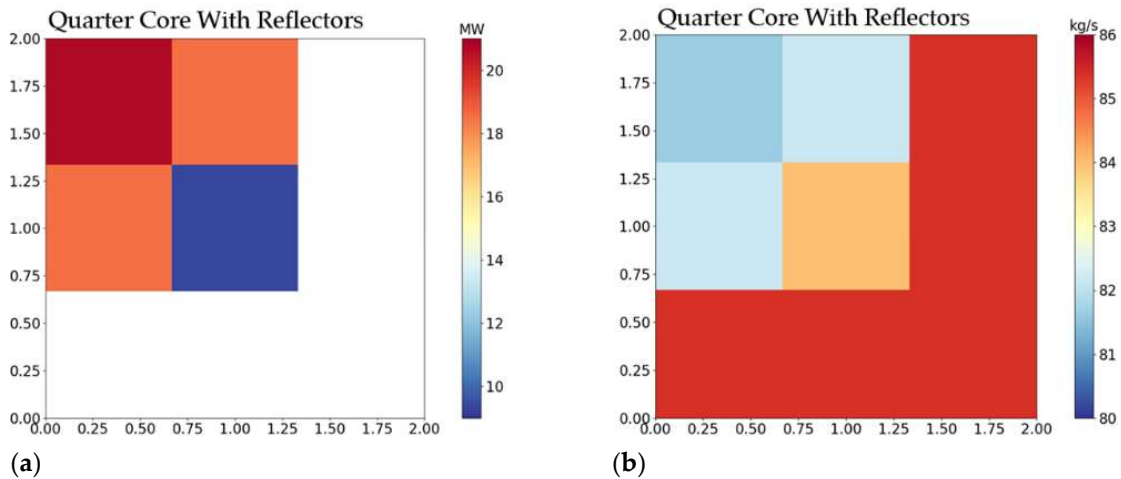


Figure 6.6. (a) DYN3D at the fuel assembly level quarter core with reflectors total fission power distribution; (b) DYN3D at the fuel assembly level quarter core with reflectors total mass flow distribution.

Table 6.6. Boundary conditions for the individual fuel assemblies and quarter core without reflectors.

Boundary Conditions	Total Fission Power (MW)				Total Mass Flow (kg/s)			
	Central Fuel Assembly	Side Fuel Assembly	Corner Fuel Assembly	Quarter Core	Central Fuel Assembly	Side Fuel Assembly	Corner Fuel Assembly	Quarter Core
Hot Zero Power	3.140E-07	2.760E-07	1.340E-07	1.000E-06	84.089	84.089	84.089	336.356
Full Power	20.707	18.534	9.357	67.133	81.660	82.169	83.962	329.960

An increase in the total fission power and a decrease in the total mass flow were noticed in the tests in the central fuel assembly in contrast to the side fuel assembly and in contrast to the corner fuel assembly in the quarter core with reflectors. This increase in the total fission power and decrease in the total mass flow were caused by the reflection of neutrons in the north and west outer boundaries of the quarter core with reflectors in contrast to the east and south outer boundaries of the quarter core with reflectors. This results in higher fission reaction rates and lower moderator densities in the central and side fuel assemblies as opposed to in the corner fuel assembly as per the neutron diffusion and fluid mass and momentum equations.

The composition of the total fission power and total mass flow was noticed in the tests in the quarter core without reflectors in contrast to the individual fuel assemblies in the quarter core with reflectors. This composition in the total fission power and mass flow was caused by the conservation of neutrons in the quarter core without reflectors in contrast to the individual fuel assemblies. This results in the combination of fission reaction rates and moderator densities in the quarter core without reflectors as opposed to in the individual fuel assemblies as per the preceding equations.

An increase in the total fission power and a decrease in the total mass flow was noticed in the full power tests in contrast to the hot zero power tests in the quarter core with reflectors. This increase in the total fission power and decrease in the total mass flow was caused by the additional neutrons in the full power tests in contrast to the hot zero power tests. This results in higher fission reaction rates

and lower moderator densities in the full power tests as opposed to in the hot zero power tests as per the cross sections interpolation and fission powers conversion.

The average axial fission power distributions for the individual fuel assemblies and quarter core without reflectors are given for all the tests, which allow the simulation in the couplings at different scale levels. These distributions can be seen in Figure 6.7.

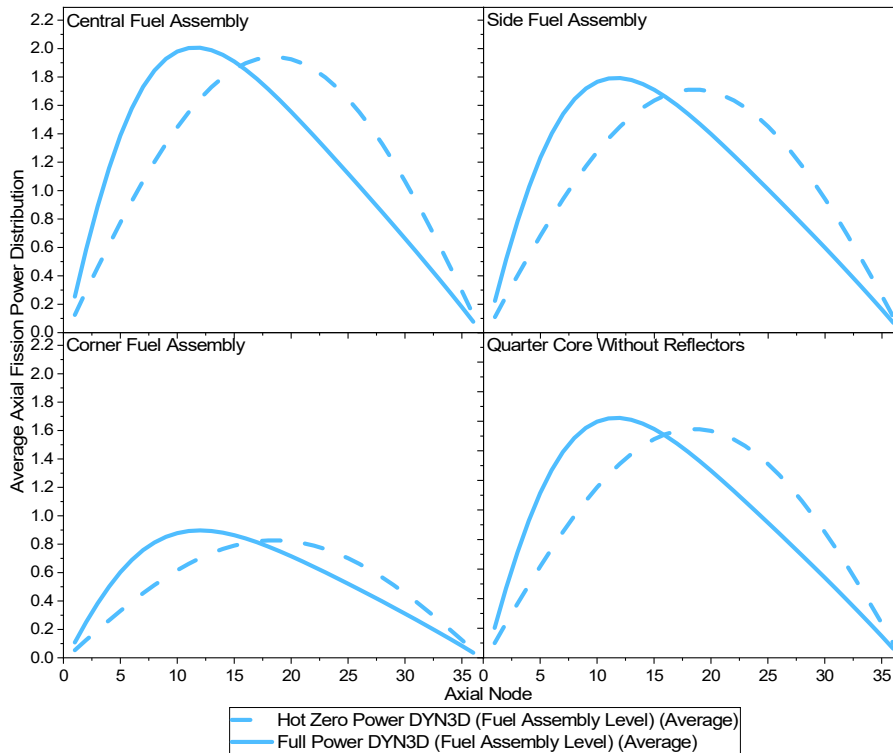


Figure 6.7. Average axial fission power distribution for the individual fuel assemblies and quarter core without reflectors.

A variation of the symmetry of the average axial fission power distribution was noticed in the tests in the central fuel assembly in contrast to the side fuel assembly and in contrast to the corner fuel assembly in the quarter core with reflectors. This variation of the symmetry of the average axial fission power distribution was caused by the different axial streaming of neutrons between layers in the central and side fuel assemblies in contrast to the corner fuel assembly, which depend on the albedo distributions. This results in additional thermal neutrons and, hence, higher fission reaction rates at the intermediate layers of the central and side fuel assemblies as opposed to in the corner fuel assembly as per the neutron diffusion equation.

An average symmetry of the average axial fission power distribution was noticed in the tests in the quarter core without reflectors in contrast to the individual fuel assemblies in the quarter core with reflectors. This average symmetry of the average axial fission power distribution was caused by the composition of the axial streaming of neutrons between layers in the quarter core without reflectors in contrast to the individual fuel assemblies, which depends on the previously mentioned distributions. This results in the combination of thermal neutrons and, hence, fission reaction rates at the layers of the quarter core without reflectors as opposed to in the individual fuel assemblies as per the preceding equation.

A variation of the symmetry of the average axial fission power distribution was noticed in the full power tests in contrast to the hot zero power tests in the quarter core with reflectors. This variation of the symmetry of the average axial fission power distribution was caused by the higher moderator and fuel temperature and lower moderator density in the full power tests in contrast to the hot zero power tests. This results in fewer thermal neutrons and, hence, lower fission reaction rates at the top layers in the full power tests as opposed to in the hot zero power tests as per the cross sections interpolation and fission powers conversion.

6.4.2. Fuel Assemblies & Quarter Core without Reflectors

The DYN3D at the fuel assembly level, coupling between DYN3D and CTF at the fuel pin level, coupling between LOTUS and CTF at the fuel pin level, and coupling between LOTUS and CTF at the materials level comparisons within the previously mentioned exercise for the individual fuel assemblies and the quarter core without reflectors, consist of several magnitudes. These include the effective multiplication factor, fission power distribution, and fuel temperature distribution. However, the DNBR distribution is included in the appendix. The last iteration effective multiplication factor value for the individual fuel assemblies and quarter core without reflectors are given for all the tests, to show the physics of the couplings at different scale levels. These values can be seen in Figure 6.8.

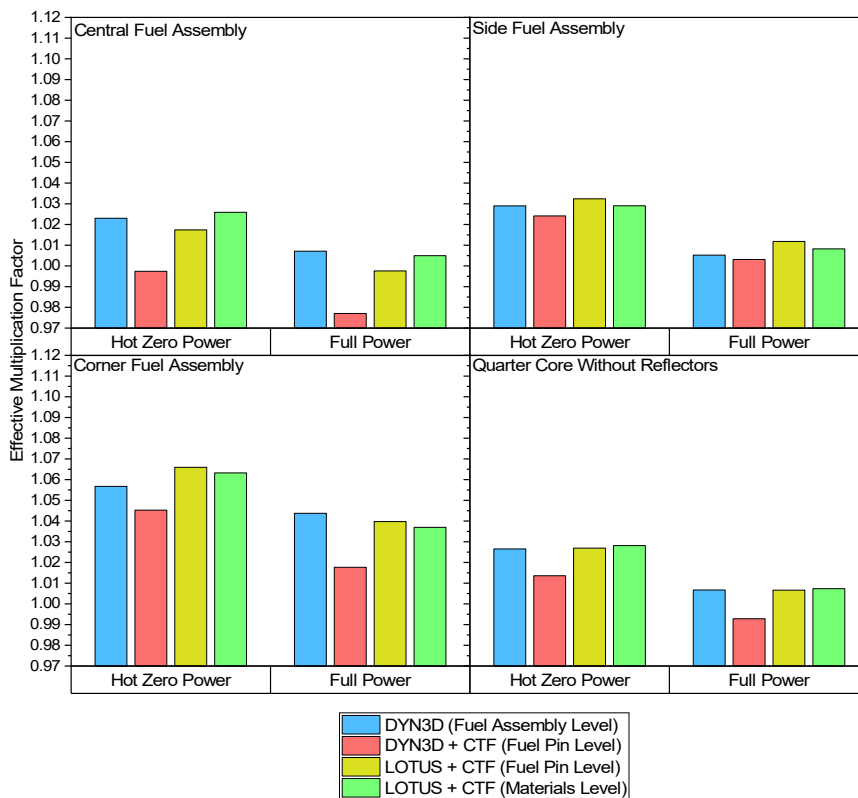


Figure 6.8. Effective multiplication factor values for the individual fuel assemblies and quarter core without reflectors.

A decrease in the effective multiplication factor was noticed in the tests in the central fuel assembly in contrast to the side fuel assembly and in contrast to the corner fuel assembly. This decrease in the effective multiplication factor was caused by the different neutron leakage at the outer boundaries of the central and side fuel assemblies in contrast to the corner fuel assembly, which depend on the albedo distributions. This results in fewer fast neutrons and, hence, lower reactivity in the central and side fuel assemblies as opposed to in the corner fuel assembly as per the neutron diffusion or transport equation.

An average effective multiplication factor was noticed in the tests in the quarter core without reflectors in contrast to the individual fuel assemblies. This average effective multiplication factor was caused by the redistribution of neutron leakage within the outer boundaries of the quarter core without reflectors in contrast to the individual fuel assemblies, which depend on the previously mentioned distributions. This results in the combination of fast neutrons and, hence, reactivities in the quarter core without reflectors as opposed to in the individual fuel assemblies as per the preceding equations.

A decrease in the effective multiplication factor was noticed in the full power test in contrast to the hot zero power test in the individual fuel assemblies and quarter core without reflectors. This decrease in the effective multiplication factor was caused by the higher neutron capture and lower neutron scattering cross sections in the full power test in contrast to the hot zero power test, which

depend on the feedback distributions. This results in fewer thermal neutrons and, therefore, lower reactivities in the full power tests as opposed to in the hot zero power tests as per the cross sections interpolation.

Comparing the coupling between DYN3D and CTF at the fuel pin level and DYN3D at the fuel assembly level, differences in the effective multiplication factor were noticed in the tests in the individual fuel assemblies and quarter core without reflectors. These differences in the effective multiplication factor were caused by several reasons. The application of simplified neutron diffusion through the NEM method in the coupling between DYN3D and CTF at the fuel pin level in contrast to DYN3D at the fuel assembly level. Also, the cross sections homogenization in the coupling between DYN3D and CTF at the fuel pin level in contrast to in DYN3D at the fuel assembly level. Finally, the application of full mixing fluid dynamics and solid dynamics through the subchannel method in the coupling between DYN3D and CTF at the fuel pin level in contrast to DYN3D at the fuel assembly level.

Comparing the coupling between LOTUS and CTF at the fuel pin level and the coupling between DYN3D and CTF at the fuel pin level, differences in the effective multiplication factor were noticed in the tests in the individual fuel assemblies and quarter core without reflectors. These differences in the effective multiplication factor were caused by the application of full neutron transport through the CCCP method in the coupling between LOTUS and CTF at the fuel pin level in contrast to the coupling between DYN3D and CTF at the fuel pin level.

Comparing the coupling between LOTUS and CTF at the materials level and the coupling between LOTUS and CTF at the fuel pin level, differences in the effective multiplication factor were noticed in the tests in the individual fuel assemblies and quarter core without reflectors. These differences in the effective multiplication factor were caused by the cross sections in the coupling between LOTUS and CTF at the materials level in contrast to the coupling between LOTUS and CTF at the fuel pin level.

The multiple iteration absolute reactivity differences for the individual fuel assemblies and for the quarter core without reflectors are given for all the tests to show the convergence of the couplings at different scale levels. All these differences can be seen in Figure 6.9.

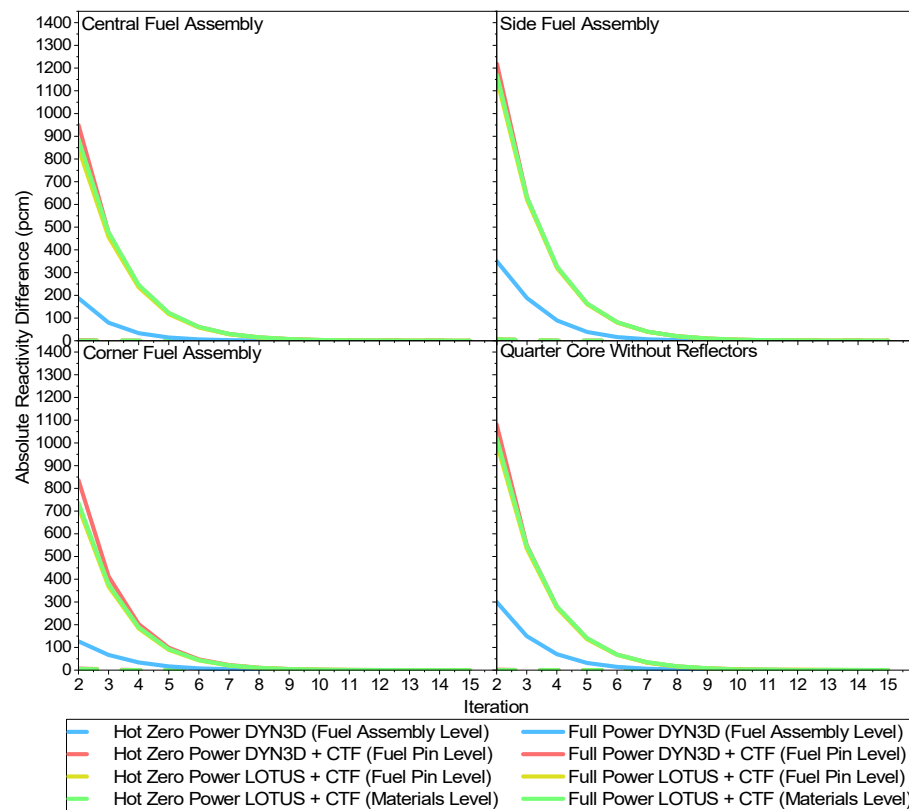


Figure 6.9. Absolute reactivity difference convergence for the individual fuel assemblies and quarter core without reflectors.

A slower convergence of the absolute reactivity was noticed in the tests in the side fuel assembly in contrast to the central fuel assembly and in contrast to the corner fuel assembly. This slower convergence of the absolute reactivity was caused by the asymmetry of the neutron leakage in the side fuel assembly in contrast to the central and corner fuel assemblies as per either the neutron diffusion or transport equation.

An average convergence of the absolute reactivity was noticed in the tests in the quarter core without reflectors in contrast to the individual fuel assemblies. This average convergence of the absolute reactivity was caused by the redistribution of the neutron leakage in the quarter core without reflectors in contrast to the individual fuel assemblies as per the preceding equations.

A slower convergence of the absolute reactivity was noticed in the full power tests in contrast to the hot zero power tests in the individual fuel assemblies and quarter core without reflectors. This slower convergence of the absolute reactivity was caused by the non-uniform neutron cross sections in the full power tests in contrast to the hot zero power tests as per the cross sections interpolation.

Comparing any of the couplings at different scale levels and DYN3D at the fuel assembly level, a slower convergence of the absolute reactivity was noticed in the tests in the individual fuel assemblies and quarter core without reflectors. These differences in the convergence of the absolute reactivity were caused by the more heterogeneous cross sections in any of the couplings at different scale levels in contrast to DYN3D at the fuel assembly level as per the preceding interpolation.

The average transversal fission power distribution for the individual fuel assemblies and the quarter core without reflectors is given only for the full power test to show the similarities and differences between them. These distributions can be seen in Figure 6.10.

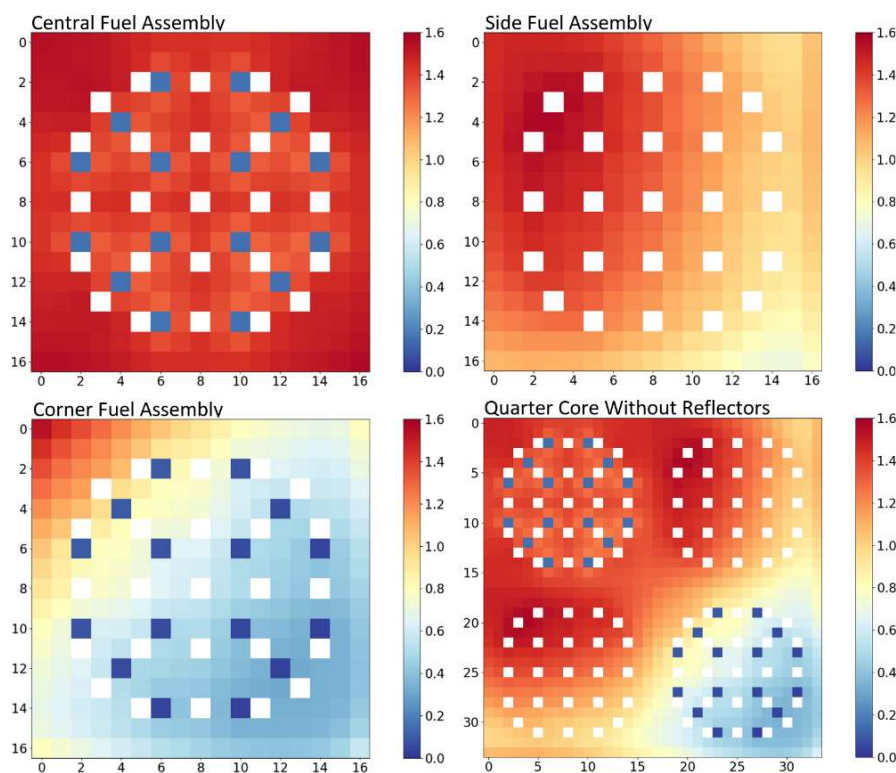


Figure 6.10. Average transversal fission power distribution for the individual fuel assemblies and quarter core without reflectors.

A variation of the symmetry of the average transversal fission power distribution was noticed in the full power tests in the central fuel assembly in contrast to the side fuel assembly and in contrast to the corner fuel assembly. This variation of the symmetry of the average transversal fission power distribution was caused by the different transversal streaming of neutrons between fuel cells in the central and side fuel assemblies in contrast to the corner fuel assembly, which depend on the albedo distributions. This results in additional thermal neutrons and, hence, higher fission reaction rates in the

fuel pins of the central and side fuel assemblies as opposed to in the corner fuel assembly as per either the neutron diffusion or transport equation.

A mild variation of the symmetry of the average transversal fission power distribution was noticed in the full power tests in the quarter core without reflectors in contrast to the individual fuel assemblies. This mild variation of the symmetry of the average transversal fission power distribution was caused by the redistribution in the transversal streaming of neutrons between fuel cells in the quarter core without reflectors in contrast to the individual fuel assemblies, which depend on the previously mentioned distributions. This results in the combination of thermal neutrons and, hence, fission reaction rates in the fuel pins of the quarter core without reflectors as opposed to in the individual fuel assemblies as per the preceding equations.

The relative average transversal fission power distribution differences for the individual fuel assemblies and the quarter core without reflectors are given only for the full power test to show the physics of the couplings at different scale levels. These distribution differences can be seen in Figure 6.11.

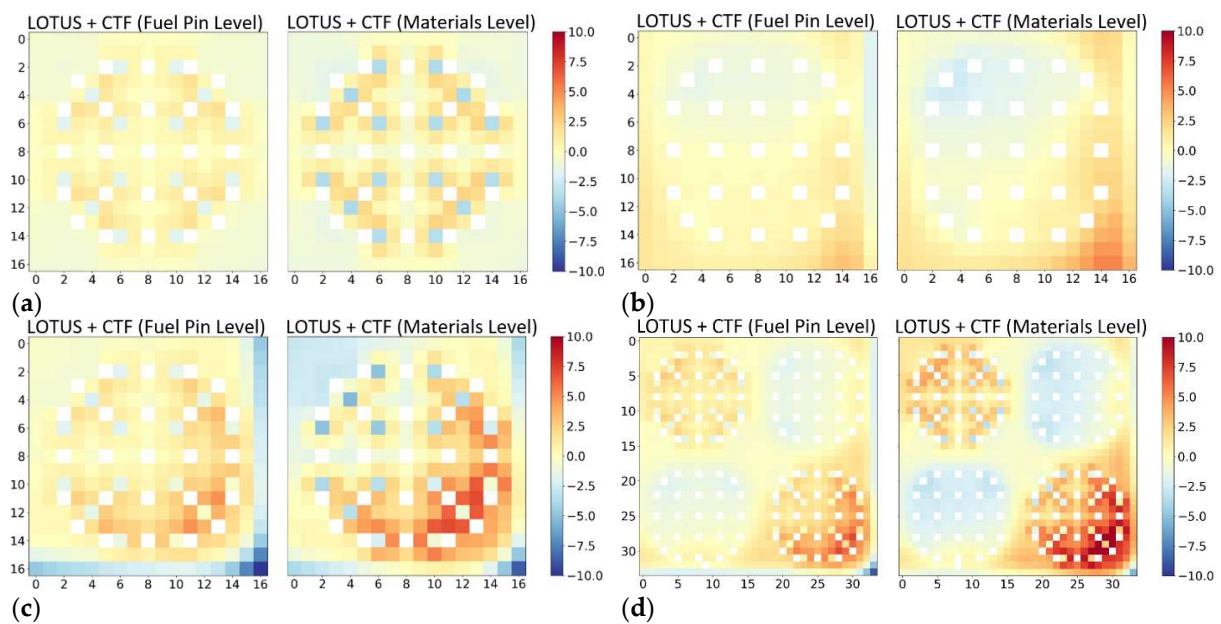


Figure 6.11. (a) LOTUS + CTF (Fuel Pin/Materials Level) and DYN3D + CTF (Fuel Pin Level) relative average transversal fission power distribution differences for the central fuel assembly; (b) LOTUS + CTF (Fuel Pin/Materials Level) and DYN3D + CTF (Fuel Pin Level) relative average transversal fission power distribution differences for the side fuel assembly; (c) LOTUS + CTF (Fuel Pin/Materials Level) and DYN3D + CTF (Fuel Pin Level) relative average transversal fission power distribution differences for the corner fuel assembly; (d) LOTUS + CTF (Fuel Pin/Materials Level) and DYN3D + CTF (Fuel Pin Level) relative average transversal fission power distribution differences for the quarter core without reflectors.

Comparing the coupling between LOTUS and CTF at the fuel pin level and the coupling between DYN3D and CTF at the fuel pin level, relative average transversal fission power distribution differences were noticed in the full power tests in the individual fuel assemblies and quarter core without reflectors. These relative average transversal fission power distribution differences were caused by the application of full neutron transport through the CCCP method in the coupling between LOTUS and CTF at the fuel pin level in contrast to the coupling between DYN3D and CTF at the fuel pin level.

Comparing the coupling between LOTUS and CTF at the materials level and the coupling between DYN3D and CTF at the fuel pin level, relative average transversal fission power distribution differences were noticed in the full power tests in the individual fuel assemblies and quarter core without reflectors. These relative average transversal fission power distribution differences were

caused by the previously mentioned reason and the cross sections in the coupling between LOTUS and CTF at the materials level in contrast to the coupling between DYN3D and CTF at the fuel pin level

The multiple iteration maximum fission power difference for the central, side, and corner fuel assemblies and the quarter core without reflectors is given only for the full power tests to show the convergence of the couplings at different scale levels. All these differences can be seen in Figure 6.12.

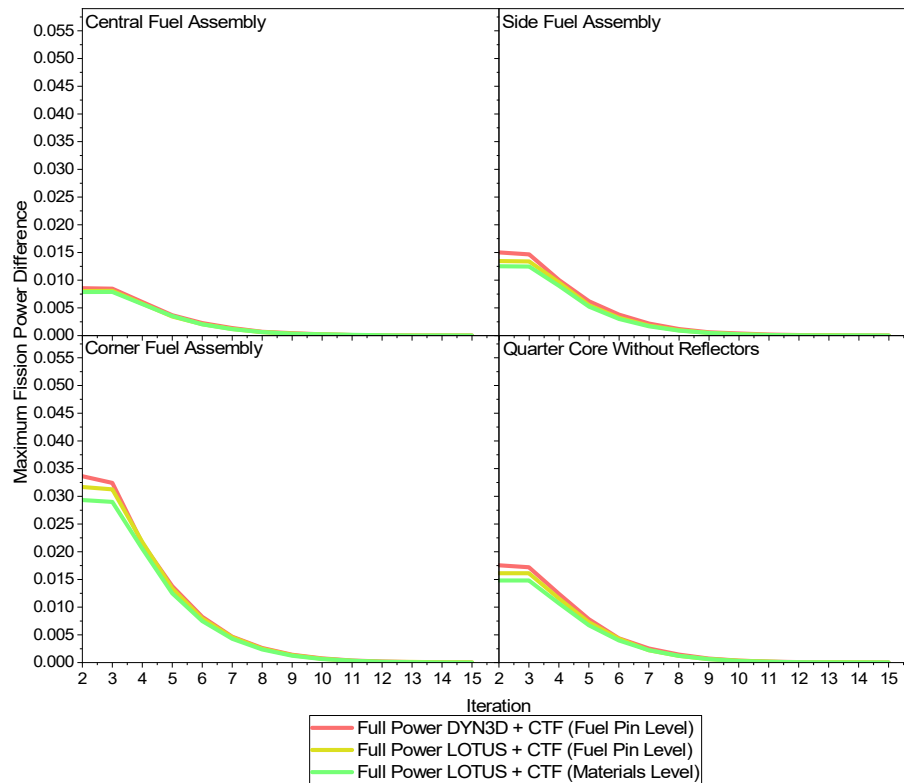


Figure 6.12. Maximum fission power differences for the individual fuel assemblies and quarter core without reflectors.

A slower convergence of the maximum fission power difference was noticed in the full power tests in the corner fuel assembly in contrast to the side fuel assembly and in contrast to the central fuel assembly. This slower convergence of the maximum fission power difference was caused by the variation in the transversal streaming of neutrons in the corner fuel assembly in contrast to the central and side fuel assemblies as per either the neutron diffusion or transport equation.

A mildly different convergence of the maximum fission power difference was noticed in the full power tests in the quarter core without reflectors in contrast to the individual fuel assemblies. This mildly different convergence of the maximum fission power was caused by the redistribution in the transversal streaming of neutrons in the quarter core without reflectors in contrast to the individual fuel assemblies as per the preceding equations.

Comparing any of the couplings at different scale levels, a similar convergence of the maximum fission power difference was noticed in the full power tests in the individual fuel assemblies and quarter core without reflectors. These similarities in the convergence of the maximum fission power difference were caused by the common under-relaxation in any of the couplings at different scale levels as per the fission power under relaxation.

The maximum and average axial fuel temperature distributions for the individual fuel assemblies and the quarter core without reflectors are given only for the full power test to show the physics of the couplings at different scale levels. These distributions can be seen in Figure 6.13.

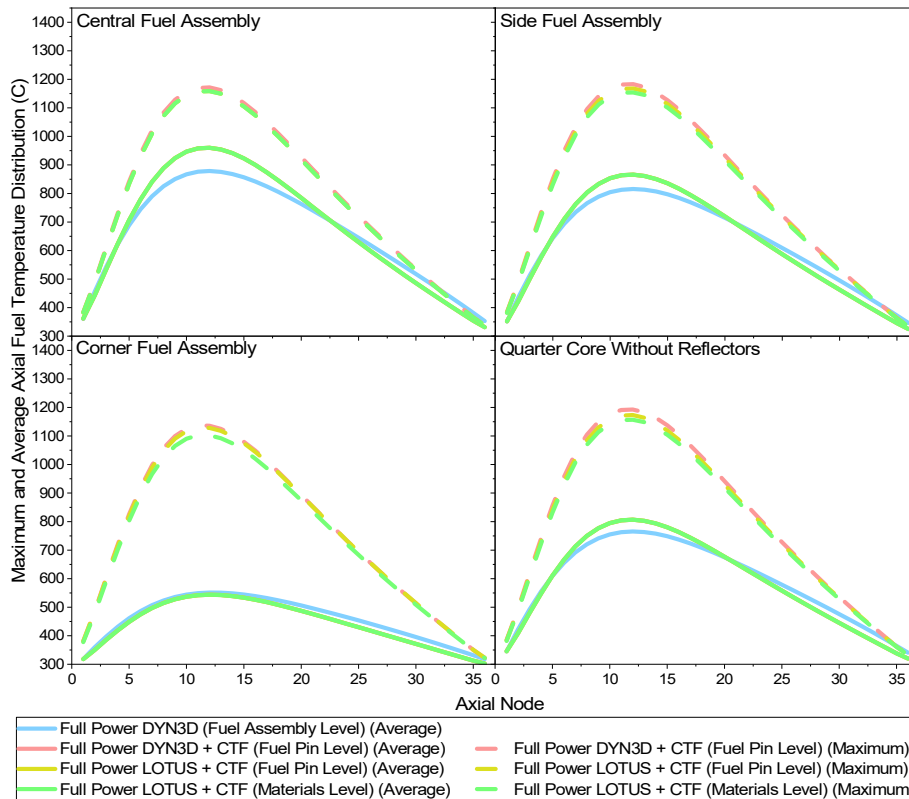


Figure 6.13. Maximum and average axial fuel temperature distributions for the individual fuel assemblies and quarter core without reflectors.

A similar increase in the maximum axial fuel temperature distribution and a different increase in the average axial fuel temperature distribution were noticed in the full power tests in the central fuel assembly in contrast to the side fuel assembly and in contrast to the corner fuel assembly. This similar increase of the maximum axial fuel temperature distribution and different increase in the average axial fuel temperature distribution was caused by the higher total fission power and the variation in the symmetry in the transversal and axial fission power distributions in the central and side fuel assemblies in contrast to in the corner fuel assembly. This results in higher solid enthalpies at the intermediate layers in the hottest fuel pin of the individual fuel assemblies as per the solid energy equation.

A similar increase in the maximum axial fuel temperature distribution and an average increase of the average axial fuel temperature distribution were noticed in the full power tests in the quarter core without reflectors in contrast to the individual fuel assemblies. This similar increase of the maximum axial fuel temperature distribution and average increase of the average axial fuel temperature distribution was caused by the composition of total fission power and the mild variation in the symmetry in the transversal and axial fission power distributions in the quarter core without reflectors in contrast to in the individual fuel assemblies. This results in similar solid enthalpies at the intermediate layers in the hottest fuel pin of the quarter core without reflectors as per the preceding equation.

Comparing any of the couplings at different scale levels and DYN3D at the fuel assembly level, a different increase in the average axial fuel temperature distribution was noticed in the full power tests at the different layers of the individual fuel assemblies and quarter core without reflectors. These differences in the axial fuel temperature distributions were caused by several reasons. The application of full mixing fluid dynamics and solid dynamics through the subchannel method in any coupling with CTF at the corresponding scale level in contrast to in DYN3D at the fuel assembly level. Also, the fuel rods method in any coupling with CTF at the corresponding scale level in contrast to in DYN3D at the fuel assembly level.

The relative maximum transversal fuel temperature distribution differences for the individual fuel assemblies and the quarter core without reflectors are given only for the full power test to show

the physics of the couplings at different scale levels. These distribution differences can be seen in Figure 6.14.

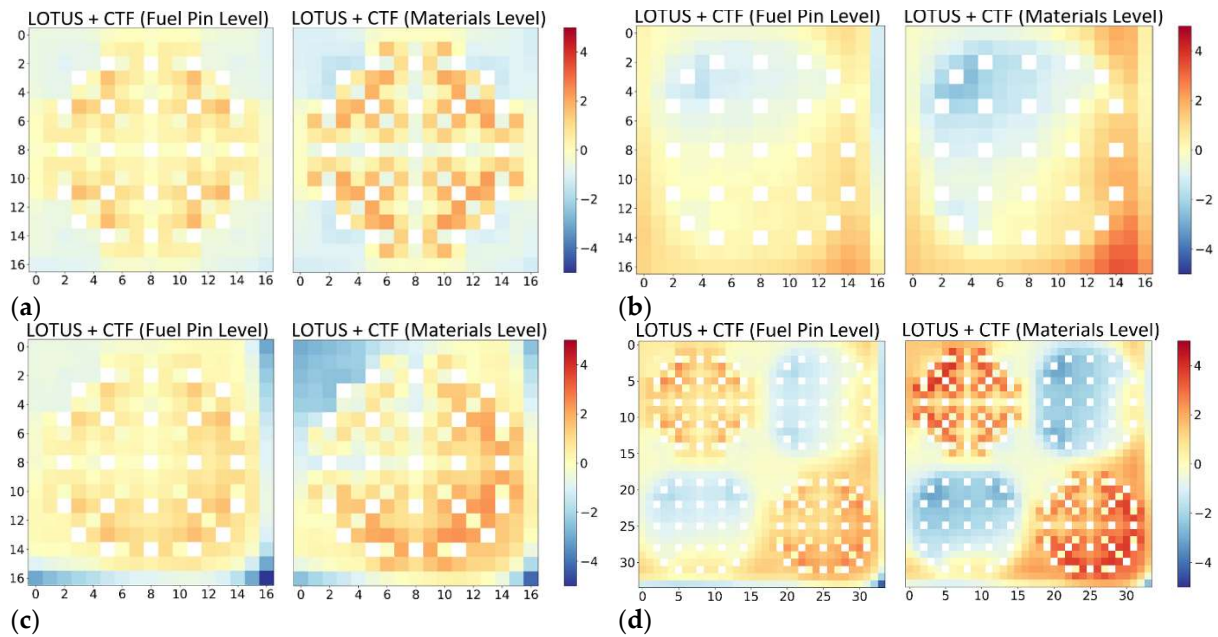


Figure 6.14. (a) LOTUS + CTF (Fuel Pin/Materials Level) and DYN3D + CTF (Fuel Pin Level) relative maximum transversal fuel temperature distribution differences for the central fuel assembly; (b) LOTUS + CTF (Fuel Pin/Materials Level) and DYN3D + CTF (Fuel Pin Level) relative maximum transversal fuel temperature distribution differences for the side fuel assembly; (c) LOTUS + CTF (Fuel Pin/Materials Level) and DYN3D + CTF (Fuel Pin Level) relative maximum transversal fuel temperature distribution differences for the corner fuel assembly; (d) LOTUS + CTF (Fuel Pin/Materials Level) and DYN3D + CTF (Fuel Pin Level) relative maximum transversal fuel temperature distribution differences for the quarter core without reflectors.

Comparing the coupling between LOTUS and CTF at the fuel pin level and the coupling between DYN3D and CTF at the fuel pin level, relative maximum transversal fuel temperature distribution differences were noticed in the full power tests in the individual fuel assemblies and quarter core without reflectors. These relative maximum transversal fuel temperature distribution differences were caused by the application of full neutron transport through the CCCP method in the coupling between LOTUS and CTF at the fuel pin level in contrast to the coupling between DYN3D and CTF at the fuel pin level.

Comparing the coupling between LOTUS and CTF at the materials level and the coupling between DYN3D and CTF at the fuel pin level, relative maximum transversal fuel temperature distribution differences were noticed in the full power tests in the individual fuel assemblies and quarter core without reflectors. These relative maximum transversal fuel temperature distribution differences were caused by the previously mentioned reason and the cross sections in the coupling between LOTUS and CTF at the materials level in contrast to the coupling between DYN3D and CTF at the fuel pin level.

The multiple iteration maximum fuel temperature difference for the individual fuel assemblies and the quarter core without reflectors is given only for the full power tests to show the convergence of the couplings at different scale levels. All these differences can be seen in Figure 6.15.

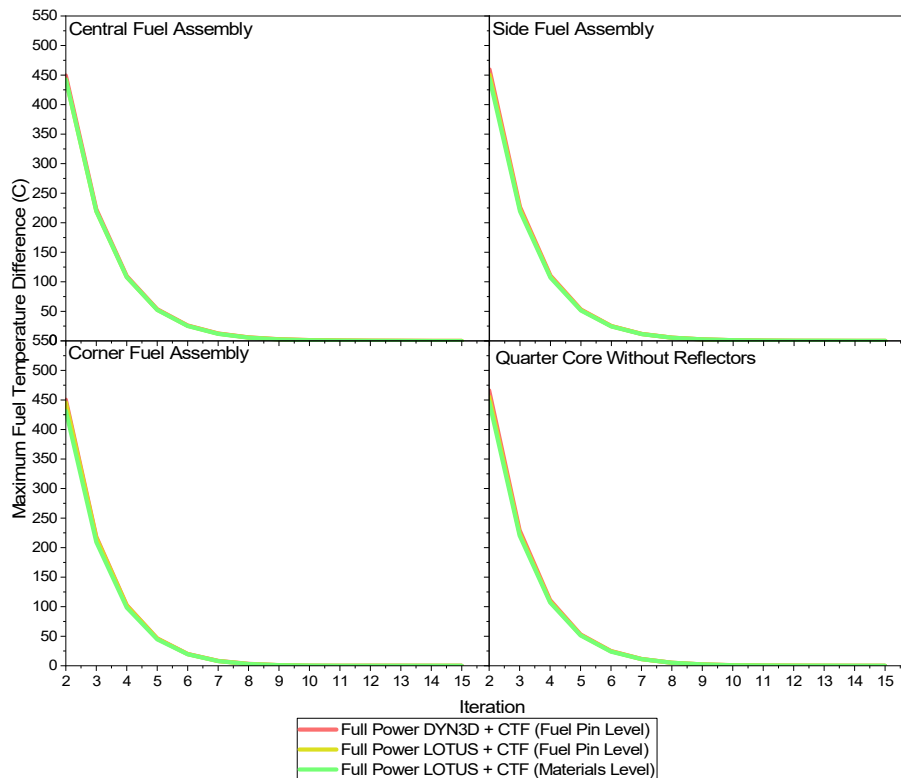


Figure 6.15. Maximum fuel temperature difference convergence for the individual fuel assemblies and quarter core without reflectors.

A mildly different convergence of the maximum fuel temperature difference was noticed in the corner fuel assembly in contrast to the side fuel assembly and in contrast to the central fuel assembly. This mildly different convergence of the maximum fuel temperature difference was caused by the variation in the fission power in the individual fuel assemblies as per the solid energy equation.

A mildly different convergence of the maximum fuel temperature difference was noticed in the quarter core without reflectors in contrast to the individual fuel assemblies. This mildly different convergence of the maximum fuel temperature was caused by the redistribution of fission power in the quarter core without reflectors in contrast to the individual fuel assemblies as per the preceding equation.

Comparing any of the couplings at different scale levels, a similar convergence of the maximum fuel temperature difference was noticed in the full power tests in the individual fuel assemblies and quarter core without reflectors. These similarities in the convergence of the maximum fuel temperature difference were caused by the common under-relaxation in any of the couplings at different scale levels as per the feedback under relaxation.

6.5. Appendix. Fuel Assemblies & Quarter Core without Reflectors

The minimum and average axial DNBR distribution for the central, side, and corner fuel assemblies and the quarter core without reflectors are given only for the full power test are given only for the full power test to show the physics of the couplings at different scale levels. These distributions can be seen in Figure 6.A1.

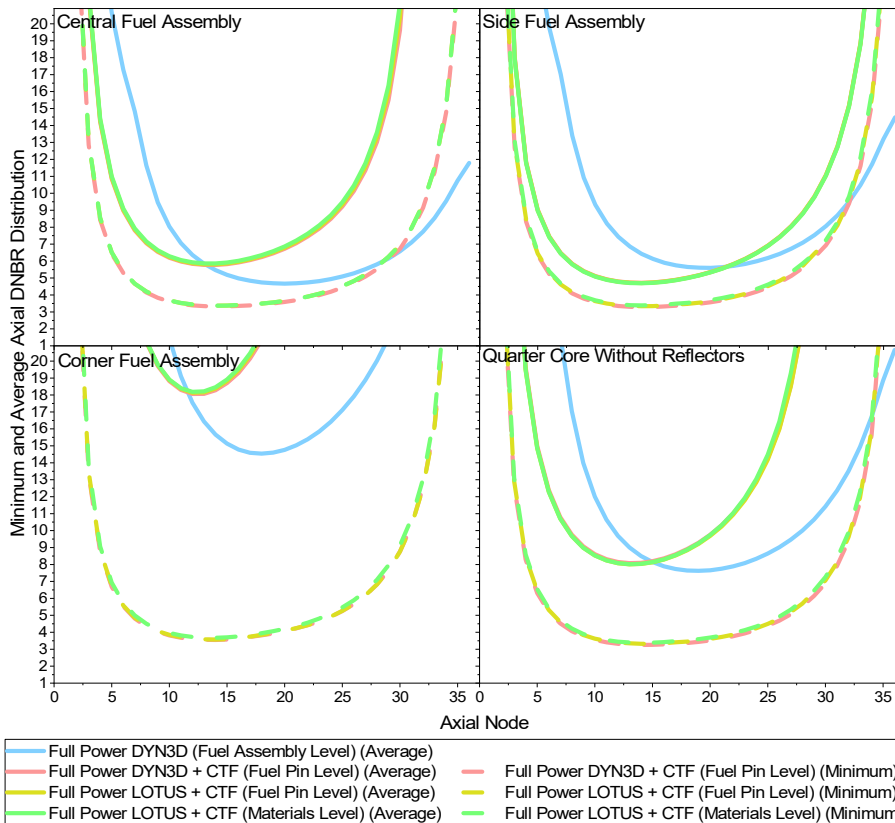


Figure 6.A1. Minimum and average axial DNBR distributions for the individual fuel assemblies and quarter core without reflectors.

A similar decrease in the minimum axial DNBR distribution and a different decrease in the average axial DNBR distribution was noticed in the full power test in the central fuel assembly in contrast to the side fuel assembly and in contrast to the corner fuel assembly. This similar decrease of the minimum axial DNBR distribution and different decrease of the average axial DNBR distribution was caused by the higher total fission power and lower mass flow, and the variation in the symmetry in the transversal and axial fission power distributions in the central and side fuel assemblies in contrast to the corner fuel assembly. This results in lower critical heat fluxes at the intermediate layers in the hottest fuel pin of the individual fuel assemblies as per the critical heat flux correlation.

A similar decrease of the minimum axial DNBR distribution and an average decrease of the average axial DNBR distribution was noticed in the full power test in the quarter core without reflectors in contrast to the individual fuel assemblies. This similar decrease of the minimum axial DNBR distribution and average decrease of the average axial DNBR distribution was caused by the composition of the total fission power and mass flow, and the mild variation in the symmetry in the transversal and axial fission power distributions in the quarter core without reflectors in contrast to the individual fuel assemblies. This results in similar critical heat fluxes at the intermediate layers in the hottest fuel pin of the quarter core without reflectors as per the preceding correlation.

Comparing any of the couplings at different scale levels and DYN3D at the fuel assembly level, a different decrease in the average axial DNBR distributions was noticed in the full power tests at the different layers of the individual fuel assemblies and quarter core without reflectors. These differences in the axial DNBR distributions were caused by several reasons. The application of full mixing fluid dynamics and solid dynamics through the subchannel method in any coupling with CTF at the fuel pin level in contrast to in DYN3D at the fuel assembly level. Also, the DNB correlation in any coupling with CTF at the corresponding scale level in contrast to in DYN3D at the fuel assembly level.

The relative minimum transversal DNBR distribution differences for the central, side, and corner fuel assemblies and the quarter core without reflectors are given only for the full power test to show the physics of the couplings at different scale levels. These distribution differences can be seen in Figure 6.A2.

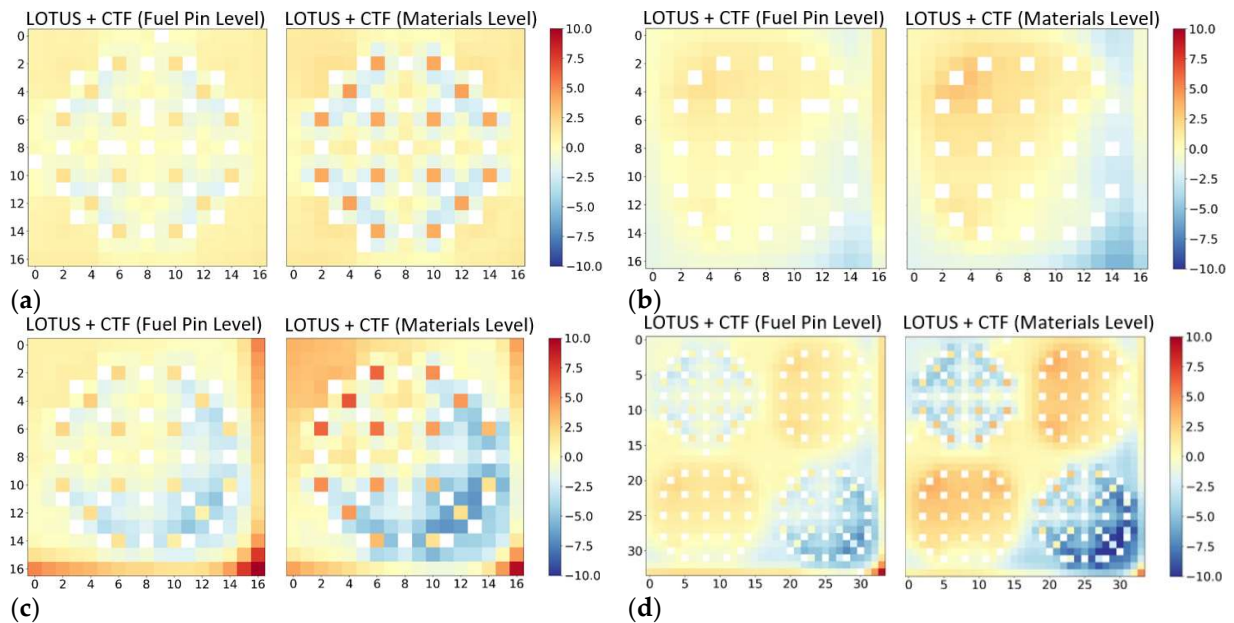


Figure 6.A2. (a) LOTUS + CTF (Fuel Pin/Materials Level) and DYN3D + CTF (Fuel Pin Level) relative minimum transversal DNBR distribution differences for the central fuel assembly; (b) LOTUS + CTF (Fuel Pin/Materials Level) and DYN3D + CTF (Fuel Pin Level) relative minimum transversal DNBR distribution differences for the side fuel assembly; (c) LOTUS + CTF (Fuel Pin/Materials Level) and DYN3D + CTF (Fuel Pin Level) relative minimum transversal DNBR distribution differences for the corner fuel assembly; (d) LOTUS + CTF (Fuel Pin/Materials Level) and DYN3D + CTF (Fuel Pin Level) minimum transversal DNBR distribution differences for the quarter core without reflectors.

Comparing the coupling between LOTUS and CTF at the fuel pin level and the coupling between DYN3D and CTF at the fuel pin level, relative minimum transversal DNBR distribution differences were noticed in the full power tests in the individual fuel assemblies and quarter core without reflectors. These relative minimum transversal DNBR distribution differences were caused by the application of full neutron transport through the CCCP method in the coupling between LOTUS and CTF at the fuel pin level in contrast to in the coupling between DYN3D and CTF at the fuel pin level.

Comparing the coupling between LOTUS and CTF at the materials level and the coupling between DYN3D and CTF at the fuel pin level, relative minimum transversal DNBR distribution differences were noticed in the full power tests in the individual fuel assemblies and quarter core without reflectors. These relative minimum transversal DNBR distribution differences were caused by the previously mentioned reason and the cross sections in the coupling between LOTUS and CTF at the materials level in contrast to in the coupling between DYN3D and CTF at the fuel pin level.

Chapter 7: Conclusions

Overall, the aim of a multiscale and multi-physics software development between NURESIM and CASL, along with its associated validations and verifications, has been answered through the different sub-aims and objectives. This multiscale and multi-physics software development is similar to NURESIM and CASL due to several reasons. It is similar to NURESIM and CASL as it uses a customised coupling software environment to couple the nuclear codes with a simplified coupling interface, parallelisation within a computational cluster, and visualisation through several modules. Also, it is similar to NURESIM as it uses a nodal code and a subchannel code to provide simplified and improved coupled reactor physics at the fuel assembly and fuel pin levels. Finally, it is similar to CASL as it uses a transport code and a subchannel code to provide full coupled reactor physics at the fuel pin and materials levels. However, this multiscale and multi-physics software development is different from NURESIM and CASL due to several reasons. It is different from NURESIM as it includes full neutron transport at the fuel pin and materials levels through the transport code LOTUS. Also, it is different from CASL as it requires either one or few processors to deliver a solution within less than a day through the Barkla HPC or a personal workstation. Finally, it is different from NURESIM and CASL as it applies the CCCP, subchannel and other methods through the transport code LOTUS and subchannel code CTF only in the hottest fuel assemblies with boundary conditions obtained applying the NEM, channel, and other methods through the nodal code DYN3D in all the reactor core.

Initially, the acknowledgement of the neutronics, thermal hydraulics and coupled reactor physics and of SCALE-POLARIS, LOTUS, Open MC, DYN3D, and CTF was performed as part of this multiscale and multi-physics software development. Such acknowledgement was performed through their descriptions.

- In the cases of neutronics, thermal hydraulics, and coupled reactor physics, these included the neutron transport, fluid and solid dynamics, and the power equations, cross sections feedback and common approximations to them.
- In the cases of SCALE-POLARIS, LOTUS, Open MC, DYN3D, or CTF, these included their general overview, methods such as the ESSM and MOC, CCCP, MC, NEM, and channel, or subchannel, and solution scheme.
- These acknowledgements have allowed the comprehension of the neutronics, thermal hydraulics and coupled reactor physics used in the mentioned nuclear codes and of SCALE-POLARIS, LOTUS, Open MC, DYN3D and CTF, used in later work.

Then, validations and verifications of the accuracy and methodology available in CTF and FLOCAL to provide thermal hydraulics at the heater rod level were performed as part of this multiscale and multi-physics software development. The validations and verifications were performed through the PSBT and FLOCAL developer benchmarks and methods in CTF and FLOCAL.

- CTF provided high accuracy in 1x1 and 5x5 bundles through the void fraction and DNB values, void fraction mean errors, standard deviations, and DNB first occurrence heights when compared to experimental data and other thermal hydraulics codes. Differences occurred due to the γ ray transmission, nucleate boiling, crossflow and turbulent mixing, thermo-couples, and critical heat flux methods, as well as the different nature of the codes.
- CTF provided a wide methodology in 2x1 bundles through the void fraction and DNBR distributions when compared to FLOCAL. Differences in the mentioned magnitudes occurred due to the variation in boundary conditions, range of fluid mass, momentum, energy transfer, turbulent mixing, and void drift, subchannel or channel, and other methods.
- These validations and verifications further justified the selection of CTF to provide thermal hydraulics at the heater rod level in the most heterogeneous cases and of FLOCAL to provide thermal hydraulics at the heater rod level in the most homogeneous cases.

Moreover, a one-way DYN3D and CTF coupling to partially provide improved coupled reactor physics at the fuel pin level and the verification of the inner coupling iterations were performed as part of this multiscale and multi-physics software development. The coupling included the transfer of fission power distributions from DYN3D to CTF. Such verification was performed through the KAIST benchmark, coupling scripts, cross sections from SCALE-POLARIS, and methods in DYN3D and CTF.

- The DYN3D and CTF coupling provided improved fluid density and temperature, fuel temperature and pressure drop values and distributions in 17x17 fuel assemblies when compared to DYN3D. Differences in the mentioned magnitudes occurred due to the presence or absence of burnable absorber pins, variation of boundary conditions, different methods such as the channel or subchannel, evaporation, nucleate boiling, fuel rod, friction and form pressure losses and the absence or presence of crossflow and turbulent mixing.
- This verification justified the use of the DYN3D and CTF coupling to partially provide improved coupled reactor physics at the fuel pin level and of DYN3D to provide simplified coupled reactor physics at the fuel assembly or fuel pin levels. The former required computational times of 20 or more minutes, while the latter required computational times of 1 to 2 minutes, to simulate the 17x17 fuel assemblies using 1 processor.

Furthermore, a two-ways DYN3D and CTF coupling to provide improved coupled reactor physics at the fuel pin level and the verification of the outer coupling iterations and convergence were performed as part of this multiscale and multi-physics software development. The coupling included the transfer of fission power and feedback distributions between DYN3D and CTF until achieving convergence. Such verification was performed through several modified and created modules within DYN3D and the customized coupling software environment, the modified KAIST benchmark, cross sections from SCALE-POLARIS, and methods in DYN3D and CTF.

- The DYN3D and CTF coupling provided improved effective multiplication factor values, fission power distributions and convergence in 17x17 fuel assemblies and 51x51 mini cores when compared to DYN3D. Differences, variations, and convergence in the mentioned magnitudes occurred due to the presence or absence of burnable absorber pins, variation of boundary conditions, different fuel rod, heat transfer, interphase, crossflow, turbulent mixing, channel, and subchannel methods, redistribution, and under-relaxation methods.
- This verification justified the use of the DYN3D and CTF coupling to provide improved coupled reactor physics at the fuel pin level and of DYN3D to provide simplified coupled reactor physics at the fuel assembly or fuel pin levels. The former required computational times ranging from 1 to 10 hours, while the latter required computational times ranging from 2 to 20 minutes, to simulate the 17x17 fuel assemblies and 51x51 mini cores using 1 processor.

Finally, a multi-ways coupling between LOTUS and CTF with DYN3D to provide full coupled reactor physics at either the fuel pin or materials levels and its verification were performed as part of this multiscale and multi-physics software development. The coupling included the transfer of albedo distributions from DYN3D to LOTUS, fission power and mass flow values from DYN3D to CTF, and fission power and feedback distributions between LOTUS and CTF until achieving convergence. This verification was performed through the customised coupling software environment, customised benchmark, cross sections from SCALE-POLARIS, and methods in LOTUS, DYN3D, and CTF.

- The coupling between LOTUS and CTF with DYN3D provided improved effective multiplication factor values, fission power, fuel temperature, and DNBR distributions and convergence in a 3x3 quarter core with reflectors composed of either 17x17 fuel assemblies, or a 34x34 quarter core without reflectors, when compared to a coupling between DYN3D and CTF with DYN3D. Differences, variations, and convergence in the mentioned magnitudes occurred due to the different albedo distributions at the outer boundaries, redistribution, variation of boundary conditions, and methods such as the CCCP or NEM, cross section homogenisation, feedback under-relaxation, the subchannel or channel, fuel rod, DNB, and fission power under-relaxation.
- This verification justified the selection of the coupling between LOTUS and CTF with DYN3D to provide full coupled reactor physics at the fuel pin or materials level in the hottest and most heterogeneous fuel assemblies and of the coupling between DYN3D and CTF with DYN3D to provide improved coupled reactor physics at the fuel pin level in homogeneous fuel assemblies. The former required computational times ranging from 3 to 24 hours, while the latter required computational times ranging from 1 to 8 hours, to simulate the 17x17 fuel assemblies and 34x34 quarter core without reflectors with parallelization across 36 processors.

Chapter 8: Future Work

This multiscale and multi-physics software development could be improved by including axial streaming in LOTUS, further albedo distribution discretization, analysis, and expansion of the specific approximations in DYN3D. Neutron leakage occurs in 3D and affects the full neutron transport at the fuel pin and materials levels. Axial streaming could be implemented in LOTUS by modifying its modules, including the CCCP and albedo methods, to avoid synthesis, providing 3D neutron transport. The albedo distribution discretization affects the improved and full coupled reactor physics at the fuel pin and materials levels. Further albedo distribution discretization could be achieved through DYN3D at the fuel pin level instead of at the fuel assembly level, applied to all the reactor core, providing albedo distributions for each fuel pin at the boundaries of the fuel assemblies. The specific approximations in DYN3D could affect the simplified coupled reactor physics at the fuel assembly level. Further analysis of the specific approximations in DYN3D could be carried out through software such as MAPLE and Mathematica, including the NEM method, allowing to decide the required expansion.

Also, this multiscale and multi-physics software development could be improved by including direct cross sections generation in SCALE-POLARIS and full neutron transport through Open MC into the customized coupling software environment. The lack of direct cross section generation affects user-friendliness. Direct cross section generation could be achieved within the customized coupling software environment through the corresponding coupling between SCALE-POLARIS, LOTUS, and DYN3D, providing cross-sections at the fuel assembly, fuel pin, and materials levels. The full neutron transport in LOTUS requires further verification. Other full neutron transport could be included in the customized coupling software environment through the corresponding coupling between Open MC, CTF and DYN3D, providing further full coupled reactor physics at the materials level.

Additionally, this multiscale and multi-physics software development could be improved by including the burnup in LOTUS and improved solid dynamics through ENIGMA into the customized coupling software environment. The burnup affects the full neutron transport at the materials level. The burnup could be included in LOTUS and the customized coupling software environment by modifying their modules, including the CCCP and cross section interpolation methods, to account for different burnup stages. The burnup affects the solid dynamics at the materials level. Improved solid dynamics could be included in the customized coupling software environment through the corresponding coupling between ENIGMA, LOTUS, CTF and DYN3D, providing further full coupled reactor physics at the materials level.

Also, this multiscale and multi-physics software could be improved by including the transient state in LOTUS and other boundary conditions through RELAP-5 in the customized coupling software environment. The transient state occurs under general nuclear reactor behaviour. The transient state could be included in LOTUS and the customized coupling software environment by creating new modules, including time step methods to account for delayed neutron precursors. The transient state depends on other boundary conditions under accident scenarios. These boundary conditions could be included in the customized coupling software environment through the corresponding coupling with RELAP-5.

Finally, this multiscale and multi-physics software could be improved by including a unified input for all the nuclear codes, a GUI, and uncertainty quantification through COSSAN-X into the customized coupling software environment. Several inputs and the lack of a GUI affect user-friendliness. A unified input for all the nuclear codes and a GUI could be included in the customized coupling software environment by creating new modules. The uncertainty in the data affects the simplified, improved, and full coupled reactor physics. Uncertainty quantification could be included in the customized coupling software environment through the corresponding coupling with COSSAN-X.

In general, further validation and verification of this multiscale and multi-physics software development are fundamental for it to become state-of-the-art software. Validation and verification could be performed from the perspective of academia and the industry, where after a certain time, the prototype delivered by academia could be reprogrammed and used by the industry. This multiscale and multi-physics software development could eventually become state-of-the-art software and answer the demands of academia, industry, and nuclear regulator.

Appendix

The development of LOTUS to provide neutronics at the fuel pin and materials levels with high accuracy, flexible treatment of the boundary conditions and low computational times is needed in this research. Such high accuracy and low computational times can be achieved through the CCCPO method. This flexible treatment of the boundary conditions can be achieved through the albedo and other methods. Hence, a verification of the CCCPO method within LOTUS is performed through one group fixed source, the C5G7 hexagonal MOX and the KAIST MOX benchmarks.

The one-group fixed source benchmark is a benchmark proposed by the authors. It includes calibration, accuracy, visualization, and performance exercises that contain 3x3 square and 1x1 hexagonal bundles with fuel pins and a burnable absorber pin with one group cross sections excluding fission for the fuel, clad moderator, and a fixed source. The C5G7 hexagonal MOX benchmark is an extension of the C5G7 benchmark previously tested using other neutronics codes. It includes an accuracy exercise that contains a 9x9 hexagonal fuel assembly with different fuel pins and guide tubes with seven groups cross sections for different MOX fuel, helium, clad, and cold state boundary conditions. The KAIST MOX benchmark is a verified benchmark for LWR neutronics previously tested using other neutronics codes. It includes an accuracy exercise that contains a 17x17 square fuel assembly with different fuel pins and guide tubes, with two or eight groups cross sections for different MOX fuel, helium, clad, and cold state boundary conditions. In Open MC, the cross sections are generated, including methods such as ACE and MC. In LOTUS, the mentioned benchmarks are simulated, including methods for the 3x3 square and 1x1 hexagonal bundles or the 9x9 hexagonal and 17x17 square fuel assemblies such as the meshes, multigroup, CCCP, full reflection and variable order of the polynomials expansion including zero, first and second order.

The calibration of LOTUS according to discretization parameters such as the size of the segments and the number of azimuthal and polar sectors has shown a variation of the effective multiplication factor in the 3x3 square and 1x1 hexagonal bundles. Such effective multiplication factor variation with the discretization parameters decreased with a small size of the segments and a large number of azimuthal and polar sectors.

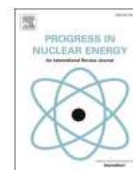
The verification of the CCCP method within LOTUS, when compared to the MC method in Open MC, has shown small fission reaction rate absolute error value and distribution differences in the 3x3 square and 1x1 hexagonal bundles. Additionally, it has shown small effective multiplication factor and fission reaction rate absolute error value and distribution differences in the 9x9 hexagonal fuel assembly. Also, it has shown variable infinite multiplication factor, fission reaction rate absolute error value, and distribution differences in the 17x17 square fuel assembly. Finally, it has shown the visualization of the neutron flux and the performance in the 3x3 square fuel assembly. Magnitude differences between zero, first, and second order polynomials occurred due to the improved expansion in the 3x3 square and 1x1 hexagonal bundles, 9x9 hexagonal and 17x17 square fuel assemblies. Also, magnitude differences between LOTUS and Open MC occurred due to the second order polynomials not being able to reproduce the neutron flux completely and the partially converged Monte Carlo solution in the 9x9 hexagonal fuel assembly. Additionally, magnitude differences between two and eight energy groups occurred due to the improved discretization in the 17x17 square fuel assembly. Also, magnitude differences between LOTUS and either Open MC with the MG approximation or Open MC with the CE approximation occurred due to error cancellation in the multigroup discretization in the 17x17 square fuel assembly.

Therefore, such verification has proven that LOTUS offers high accuracy and low computational times, which further justifies its selection to provide neutronics at the fuel pin and materials levels in the most heterogeneous cases. This chapter is composed of the journal article Verification of the current coupling collision probability method with orthogonal flux expansion for the assembly calculations [124], published in the ELSEVIER journal of Progress in Nuclear Energy. All author contributions can be found in the list of publications section.



Contents lists available at ScienceDirect

Progress in Nuclear Energy

journal homepage: <http://www.elsevier.com/locate/pnucene>

Verification of the current coupling collision probability method with orthogonal flux expansion for the assembly calculations

Dzianis Litskevich^{*}, Seddon Atkinson, Sebastian Davies

University of Liverpool, School of Engineering, Department of Mech, Materials and Aerospace Engineering, Liverpool, Merseyside L69 3BX, United Kingdom

ARTICLE INFO

Keywords:

Neutron transport
Current coupling collision probabilities
Orthogonal polynomials

ABSTRACT

The operation of nuclear reactors requires detailed knowledge of important safety parameters, such as the spatial power distribution, control rod worth, margin to departure from nucleate boiling (DNB), fuel pin burnup etc. To obtain a detailed analysis of all of the safety parameters requires a full core pin-by-pin coupled neutronics and thermal-hydraulics simulations which are too computationally expensive even for modern high-performance computer clusters. Therefore, the industrial standard approach in design and safety calculations are coupled neutronics and thermal-hydraulics codes for the steady state and transient simulations. In these codes, the neutronics calculations are typically performed at a nodal level using the diffusion approximation and assembly-homogenised sets of cross-sections while the thermal hydraulics relies on a channel model with fuel assembly sized channels. However, for determining safety limits, which are based on local pin-based parameters, the knowledge of the power and temperature distribution on a nodal level is not sufficient. Therefore, novel new approaches are required to resolve this multiscale and multiphysics problem to resolve the power distribution within the zones of interest. Pin-wise calculations, in this case, are performed by applying a transport solver using the heterogeneous fuel assembly geometry on an unstructured mesh with boundary conditions extracted from the 3D full core nodal diffusion solution. This combined nodal-transport approach will provide the detailed power distribution on the pin-level and perform coupled multiphysics simulations within reasonable simulation time limits, which is important for industry.

To follow this strategy, a transport solver is required which can be used for the flux reconstruction on the pin level. Current coupling collision probability (CCCP) method seems to be a good choice for the development of such a solver.

In this study, the developed transport solver utilising CCCP method with orthogonal flux expansion is tested and verified on the set of the benchmark problems. The results of simulations are compared with the results of Monte Carlo and deterministic code. The expansion of the flux by orthogonal polynomials allows us to avoid discretisation of the calculation regions while keeping the accuracy of the calculations to an acceptable level. The results of the calculations demonstrate good agreement with the results of Monte Carlo calculations. The comparison of the new method with the flat flux (today's industry standard approach) approximation demonstrates either an improved quality of the result for identical cell discretisation or reduced computational time to achieve the identical solution.

References

1. Department for Business Energy and Industrial Strategy *Energy Consumption in the UK*; 2016;
2. Department for Business Energy and Industrial Strategy *Energy Consumption in the UK (ECUK) 1970 to 2021*; 2021;
3. Yin, L.; Liao, Y.; Zhou, L.; Wang, Z.; Ma, X. Life Cycle Assessment of Coal-Fired Power Plants and Sensitivity Analysis of CO₂ Emissions from Power Generation Side. *IOP Conf Ser Mater Sci Eng* **2017**, *199*, 012055, doi:10.1088/1757-899X/199/1/012055.
4. Hu, Y.; Shi, Y. Estimating CO₂ Emissions from Large Scale Coal-Fired Power Plants Using OCO-2 Observations and Emission Inventories. *Atmosphere (Basel)* **2021**, *12*, 811, doi:10.3390/atmos12070811.
5. Garrido-Perez, J.M.; Ordóñez, C.; Barriopedro, D.; García-Herrera, R.; Paredes, D. Impact of Weather Regimes on Wind Power Variability in Western Europe. *Appl Energy* **2020**, *264*, 114731, doi:10.1016/j.apenergy.2020.114731.
6. Hasanah, P.; Wiradinata, S.A.; Azka, M. Forecasting Approach for Solar Power Based on Weather Parameters (Case Study: East Kalimantan). *J Phys Conf Ser* **2021**, *2106*, 012022, doi:10.1088/1742-6596/2106/1/012022.
7. Hadri, M.; Trovato, V.; Bialecki, A.; Merk, B.; Peakman, A. Assessment of High-Electrification UK Scenarios with Varying Levels of Nuclear Power and Associated Post-Fault Behaviour. *Energies (Basel)* **2021**, *14*, 1780, doi:10.3390/en14061780.
8. World Nuclear Association Nuclear Development in the United Kingdom Available online: <https://world-nuclear.org/information-library/country-profiles/countries-t-z/appendices/nuclear-development-in-the-united-kingdom.aspx> (accessed on 22 March 2023).
9. House of Commons *The Future of the Advanced Gas-Cooled Reactors Third Report of Session 2022-23*; London, 2022;
10. HM Government *The Ten Point Plan for a Green Industrial Revolution*; 2020;
11. HM Government *Net Zero Strategy: Build Back Greener*; 2021;
12. HM Government *British Energy Security Strategy*; 2022;
13. Matthew, C.; Walker, A. *Nuclear Energy in the UK*; 2022;
14. Framatome *EPR Design Description*; 2005;
15. Nuclear Innovation and Research Office *Advanced Modular Reactors Technical Assessment*; 2021;
16. HM Government *Nuclear Energy Research and Development Roadmap: Future Pathways*; 2013;
17. Nuclear Innovation and Research Advisory Board *UK Nuclear Innovation and Research Programme Recommendations*; 2016;
18. Office for Nuclear Regulation *A Guide to the Regulatory Process*; 2013;
19. Patterson, E.A.; Taylor, R.J.; Bankhead, M. A Framework for an Integrated Nuclear Digital Environment. *Progress in Nuclear Energy* **2016**, *87*, 97–103, doi:10.1016/j.pnucene.2015.11.009.
20. Merk, B.; Allen, D.; Bankhead, M.; Bowen, A.; Bowman, D.; De Haas, S.; Draup, J. The UK National Program R&D on Digital Nuclear Reactor Design. In Proceedings of the Proceedings of the 2018 International Congress on Advances in Nuclear Power Plants, ICAPP 2018; American Nuclear Society: Charlotte, April 8 2018; pp. 1–6.
21. Lindley, B.; Allen, D.; Lillington, J.; Smethurst, A.; Smith, P.; Bowman, D.; Dwyer, L.; Lai, K.; Levers, A.; Vikhorev, K.; et al. Modelling and Simulation Activities in Support of the UK Nuclear R&D Programme on Digital Reactor Design. In Proceedings of the Volume 3: Nuclear Fuel and Material, Reactor Physics, and Transport Theory; American Society of Mechanical Engineers: London, UK, July 22 2018; pp. 1–8.
22. Merk, B.; Bankhead, M.; Litskevich, D.; Gregg, R.; Peakman, A.; Shearer, C. On a Roadmap for Future Industrial Nuclear Reactor Core Simulation in the U.K. To Support the Nuclear Renaissance. *Energies (Basel)* **2018**, *11*, doi:10.3390/en11123509.
23. Duderstadt, J.J.; Hamilton, L.J. *Nuclear Reactor Analysis*; JOHN WILEY and SONS, Ed.; The University of Michigan, United States of America, 1975;
24. Lamarsh, J.R.; Baratta, A.J.; Prentice, H.----- *Introduction to Nuclear Engineering Third Edition Late Professor with the New York Polytechnic Institute*; Horton, M.J., Ed.; 3rd ed.; Prentice Hall: New Jersey, 2001; ISBN ISBN 0-201-82498-1.

25. Bahadir, T.; Lindahl, St.O.; Palmtag, S.P. SIMULATE-4 Multigroup Nodal Code with Microscopic Depletion Model. In Proceedings of the M and C 2005: international topical meeting on mathematics and computation, supercomputing, reactor physics and nuclear and biological applications; SFEN: France, 2005.
26. Pirouzmand, A.; Mohammadhasani, F. PARCS Code Multi-Group Neutron Diffusion Constants Generation Using Monte Carlo Method. *Progress in Nuclear Energy* **2016**, *86*, 71–79, doi:10.1016/j.pnucene.2015.10.005.
27. Électricité de France PWR AGR Neutronics Thermal Hydraulics Evaluation Route Available online: <https://www.answerssoftwareservice.com/panther/>.
28. Evans, T.M.; Stafford, A.S.; Slaybaugh, R.N.; Clarno, K.T. Denovo: A New Three-Dimensional Parallel Discrete Ordinates Code in SCALE. *Nucl Technol* **2010**, *171*, 171–200, doi:10.13182/NT171-171.
29. Choi, S.; Kim, W.; Choe, J.; Lee, W.; Kim, H.; Ebiwonjumi, B.; Jeong, E.; Kim, K.; Yun, D.; Lee, H.; et al. Development of High-Fidelity Neutron Transport Code STREAM. *Comput Phys Commun* **2021**, *264*, 107915, doi:10.1016/j.cpc.2021.107915.
30. Leppänen, J.; Pusa, M.; Viitanen, T.; Valtavirta, V.; Kaltiaisenaho, T. The Serpent Monte Carlo Code: Status, Development and Applications in 2013. *Ann Nucl Energy* **2015**, *82*, 142–150, doi:10.1016/j.anucene.2014.08.024.
31. Gonnet, M.; Haulbert, A.; Canac, M. Nuclear Plant Simulation Using Three-Dimensional Core Modeling. In Proceedings of the International conference on supercomputing in nuclear applications SNA'2003; France, 2003.
32. Bajorek, S.; Bernard, M.; Gingrich, C.; Hoxie, C.L.; Ireland, A.; Kelly; Murray, J. *Development, Validation and Assessment of the Trace Thermal-Hydraulics Systems Code*;
33. CD-adapco STAR-CD V4.04: The Power of Integration. *Aircraft Engineering and Aerospace Technology* **2008**, *80*, doi:10.1108/aeat.2008.12780bad.010.
34. Papukchiev, A. Experimental Validation of ANSYS CFX for Transient Flows With Heat Transfer in a Tubular Heat Exchanger. *Journal of Nuclear Engineering and Radiation Science* **2020**, *6*, doi:10.1115/1.4045074.
35. Kim, W.-S.; Kim, Y.-G. *Development of Subchannel Analysis Code MATRA-LMR for KALIMER Subassembly Thermal-Hydraulics*; International Atomic Energy Agency (IAEA), 2000;
36. Srikantiah, G.S. VIPRE—A Reactor Core Thermal-Hydraulics Analysis Code for Utility Applications. *Nucl Technol* **1992**, *100*, 216–227, doi:10.13182/NT92-A34744.
37. Magni, A.; Del Nevo, A.; Luzzi, L.; Rozzia, D.; Adorni, M.; Schubert, A.; Van Uffelen, P. The TRANSURANUS Fuel Performance Code. In *Nuclear Power Plant Design and Analysis Codes*; Elsevier, 2021; Vol. 8, pp. 161–205.
38. Koebke, K. A New Approach to Homogenization and Group Condensation. *Specialists' Meeting on Homogenization Methods in Reactor Physics* **1980**, *12*, 303–322.
39. Smith, K.S. Assembly Homogenization Techniques for Light Water Reactor Analysis. *Progress in Nuclear Energy* **1986**, *17*, 303–335, doi:10.1016/0149-1970(86)90035-1.
40. Singh, K.; Kumar, V. Reconstruction of Pin Power in Fuel Assemblies from Nodal Calculations in Hexagonal Geometry. *Ann Nucl Energy* **1995**, *22*, 629–647, doi:10.1016/0306-4549(95)00001-9.
41. Koebke, K.; Hetzelt, L. On the Reconstruction of Local Homogeneous Neutron Flux and Current Distributions of Light Water Reactors from Nodal Schemes. *Nuclear Science and Engineering* **1985**, *91*, 123–131, doi:10.13182/NSE85-A27435.
42. Gómez Torres, A.; Sánchez Espinoza, V.; Imke, U.; Macián Juan, R. Pin Level Neutronic – Thermohydraulic Two-Way-Coupling Using DYN3D-SP3 and SUBCHANFLOW. In Proceedings of the In Proceedings of the International Conference on Mathematics and Computational Methods Applied to Nuclear Science and Engineering; May 8 2011; pp. 1–20.
43. Basualdo, J.R.; Sánchez-Espinoza, V.; Stieglitz, R.; Macián-Juan, R. Integration of the Subchannel Thermal-Hydraulic Code SubChanFlow into the Reactor Dynamics Code PARCS: Development and Testing Based on a Computational Benchmark. *Progress in Nuclear Energy* **2020**, *119*, 103138, doi:10.1016/j.pnucene.2019.103138.
44. Peakman, A.; Gregg, R.; Bennett, T.; Casamor, M.; Martínez-Quiroga, V.; Freixa, J.; Pericas, R.; Rossiter, G. Multi-Physics Framework for Whole-Core Analysis of Transient Fuel Performance

- after Load Following in a Pressurised Water Reactor. *Ann Nucl Energy* **2022**, *173*, 109086, doi:10.1016/j.anucene.2022.109086.
45. Krecicki, M.; Kotlyar, D. Full-Core Coupled Neutronic, Thermal-Hydraulic, and Thermo-Mechanical Analysis of Low-Enriched Uranium Nuclear Thermal Propulsion Reactors. *Energies (Basel)* **2022**, *15*, 7007, doi:10.3390/en15197007.
 46. Atkinson, S.; Detkina, A.; Litskevich, D.; Merk, B. A Comparison of Advanced Boiling Water Reactor Simulations between Serpent/CTF and Polaris/DYN3D: Steady State Operational Characteristics and Burnup Evolution. *Energies (Basel)* **2021**, *14*, 838, doi:10.3390/en14040838.
 47. Ribes, A.; Caremoli, C. Salome Platform Component Model for Numerical Simulation. In Proceedings of the 31st Annual International Computer Software and Applications Conference - Vol. 2 - (COMPSAC 2007); IEEE, July 2007; pp. 553–564.
 48. Bergeaud, V.; Tajchman, M. Application of the SALOME Software Architecture to Nuclear Reactor Research. *SpringSim '07: Proceedings of the 2007 spring simulation multiconference* **2007**, *2*, 383–387, doi:10.1145/1404680.1404740.
 49. Turner, J.A.; Clarno, K.; Sieger, M.; Bartlett, R.; Collins, B.; Pawlowski, R.; Schmidt, R.; Summers, R. The Virtual Environment for Reactor Applications (VERA): Design and Architecture. *J Comput Phys* **2016**, *326*, 544–568, doi:10.1016/j.jcp.2016.09.003.
 50. Kochunas, B.; Collins, B.; Stimpson, S.; Salko, R.; Jabaay, D.; Graham, A.; Liu, Y.; Kim, K.S.; Wieselquist, W. VERA Core Simulator Methodology for Pressurized Water Reactor Cycle Depletion. *Nuclear Science and Engineering* **2017**, *185*, 217–231, doi:10.13182/NSE16-39.
 51. Permann, C.J.; Gaston, D.R.; Andrš, D.; Carlsen, R.W.; Kong, F.; Lindsay, A.D.; Miller, J.M.; Peterson, J.W.; Slaughter, A.E.; Stogner, R.H.; et al. MOOSE: Enabling Massively Parallel Multiphysics Simulation. *SoftwareX* **2020**, *11*, 100430, doi:10.1016/j.softx.2020.100430.
 52. Martineau, R.C. The MOOSE Multiphysics Computational Framework for Nuclear Power Applications: A Special Issue of *Nuclear Technology*. *Nucl Technol* **2021**, *207*, iii–viii, doi:10.1080/00295450.2021.1915487.
 53. Zerkak, O.; Coddington, P.; Crouzet, N.; Royer, E.; Jimenez, J.; Cuervo, D. *LWR Multi-Physics Developments and Applications within the Framework of the NURESIM Project*; American Nuclear Society - ANS: United States, 2007; ISBN 0-89448-059-6.
 54. Chanaron, B.; Ahnert, C.; Crouzet, N.; Sanchez, V.; Kolev, N.; Marchand, O.; Kliem, S.; Papukchiev, A. Advanced Multi-Physics Simulation for Reactor Safety in the Framework of the NURESIM Project. *Ann Nucl Energy* **2015**, *84*, 166–177, doi:10.1016/j.anucene.2014.12.013.
 55. Turinsky, P.J.; Kothe, D.B. Modeling and Simulation Challenges Pursued by the Consortium for Advanced Simulation of Light Water Reactors (CASL). *J Comput Phys* **2016**, *313*, 367–376, doi:10.1016/j.jcp.2016.02.043.
 56. Kulesza, J.A.; Franceschini, F.; Evans, T.M.; Gehin, J.C. Overview of the Consortium for the Advanced Simulation of Light Water Reactors (CASL). *EPJ Web Conf* **2016**, *106*, 03002, doi:10.1051/epjconf/201610603002.
 57. Lautard, J.J.; Loubiere, S.; Fedon-Magnaud, C. *CRONOS: A Modular Computational System for Neutronic Core Calculations*; International Atomic Energy Agency (IAEA), 1992;
 58. Grundmann, U.; Rohde, U. *DYN3D - a 3-Dimensional Core Model for Steady State and Transient Analysis in Thermal Reactors*; Japan, 1996;
 59. Jiménez, J.; Herrero, J.; Lozano, J.; Cuervo, D.; Herranz, N.; Ahnert, C.; Beltrán, J. Descomposición Espacial En Subdominios Para Reactores de Agua Ligera a La Escala de La Barra de Combustible. **2009**.
 60. Mañes, J.P.; Sánchez Espinoza, V.H.; Chiva Vicent, S.; Böttcher, M.; Stieglitz, R. Validation of NEPTUNE-CFD Two-Phase Flow Models Using Experimental Data. *Science and Technology of Nuclear Installations* **2014**, *2014*, 1–19, doi:10.1155/2014/185950.
 61. Angeli, P.-E.; Bieder, U.; Fauchet Cea-saclay, G. Overview of the TRIO CFD Code: Main Feature, V&V Procedures and Typical Applications to Nuclear Engineering. In Proceedings of the NURETH-16; American Nuclear Society, August 30 2015.
 62. Imke, U.; Sanchez, V.H. Validation of the Subchannel Code SUBCHANFLOW Using the NUPEC PWR Tests (PSBT). *Science and Technology of Nuclear Installations* **2012**, *2012*, 1–12, doi:10.1155/2012/465059.

63. Bergeron, A.; Caruge, D.; Royer, E. *FLICA-IV: An Advanced Code for Advanced Water Cooled Reactor*; International Atomic Energy Agency (IAEA), 2000;
64. Emonot, P.; Souyri, A.; Gandrille, J.L.; Barré, F. CATHARE-3: A New System Code for Thermal-Hydraulics in the Context of the NEPTUNE Project. In *Proceedings of the Nuclear Engineering and Design*; November 2011; Vol. 241, pp. 4476–4481.
65. Teschendorff, V.; Miro, J.; Lerchl, G. *ATHLET - an Advanced System Code for the Analysis of Thermohydraulic Processes*; ATHLET - ein fortschrittlicher Systemcode zur Analyse thermohydraulischer Prozesse; Germany, 1989;
66. Bascou, S.; De Luze, O.; Ederli, S.; Guillard, G. Development and Validation of the Multi-Physics DRACCAR Code. *Ann Nucl Energy* **2015**, *84*, 1–18, doi:10.1016/j.anucene.2014.09.040.
67. Georghentum, V.; Moal, A.; Marchand, O. SCANAIR a Transient Fuel Performance Code Part Two: Assessment of Modelling Capabilities. *Nuclear Engineering and Design* **2014**, *280*, 172–180, doi:10.1016/j.nucengdes.2014.04.030.
68. Calleja, M.; Sanchez, V.; Jimenez, J.; Imke, U.; Stieglitz, R.; Macián, R. Coupling of COBAYA3/SUBCHANFLOW inside the NURESIM Platform and Validation Using Selected Benchmarks. *Ann Nucl Energy* **2014**, *71*, 145–158, doi:10.1016/j.anucene.2014.03.036.
69. Grahn, A.; Gommlich, A.; Kliem, S.; Bilodid, Y.; Kozmenkov, Y. Simulation of an MSLB Scenario Using the 3D Neutron Kinetic Core Model DYN3D Coupled with the CFD Software Trio_U. *Nuclear Engineering and Design* **2017**, *315*, 117–127, doi:10.1016/j.nucengdes.2017.02.002.
70. Kozmenkov, Y.; Kliem, S.; Rohde, U. Validation and Verification of the Coupled Neutron Kinetic/Thermal Hydraulic System Code DYN3D/ATHLET. *Ann Nucl Energy* **2015**, *84*, 153–165, doi:10.1016/j.anucene.2014.12.012.
71. Mignot, G.; Royer, E.; Rameau, B.; Todorova, N. Computation of a BWR Turbine Trip with CATHARE-CRONOS2-FLICA4 Coupled Codes. *Nuclear Science and Engineering* **2004**, *148*, 235–246, doi:10.13182/NSE04-A2454.
72. Sanchez, R.; Mondot, J.; Stankovski, Ž.; Cossic, A.; Zmijarevic, I. APOLLO II: A User-Oriented, Portable, Modular Code for Multigroup Transport Assembly Calculations. *Nuclear Science and Engineering* **1988**, *100*, 352–362, doi:10.13182/NSE88-3.
73. Lee, Y.-K.; Hugot, F.-X. Current Status of TRIPOLI-4® Monte Carlo Radiation Transport Code on Adult and Pediatric Computational Phantoms for Radiation Dosimetry Study. *Nuclear Science and Engineering* **2024**, *198*, 274–286, doi:10.1080/00295639.2023.2197856.
74. Kochunas, B.; Collins, B.; Jabaay, D.; Downar, T.J.; Martin, W.R. *Overview of Development and Design of MPACT: Michigan Parallel Characteristics Transport*; American Nuclear Society - ANS: United States, 2013; ISBN 978-0-89448-700-2.
75. Stagg, A.K.; Yoon, S.-J. *Hydra-TH Extensions for Multispecies and Thermosolutal Convection*; Oak Ridge, TN (United States), 2015;
76. Salko, R.; Wysocki, A.; Blyth, T.; Toptan, A.; Hu, J.; Kumar, V.; Dances, C.; Dawn, W.; Sung, Y.; Kucukboyaci, V.; et al. CTF: A Modernized, Production-Level, Thermal Hydraulic Solver for the Solution of Industry-Relevant Challenge Problems in Pressurized Water Reactors. *Nuclear Engineering and Design* **2022**, *397*, 111927, doi:10.1016/j.nucengdes.2022.111927.
77. Williamson, R.L.; Gamble, K.A.; Perez, D.M.; Novascone, S.R.; Pastore, G.; Gardner, R.J.; Hales, J.D.; Liu, W.; Mai, A. Validating the BISON Fuel Performance Code to Integral LWR Experiments. *Nuclear Engineering and Design* **2016**, *301*, 232–244, doi:10.1016/j.nucengdes.2016.02.020.
78. Petrov, V.; Kendrick, B.K.; Walter, D.; Manera, A.; Secker, J. Prediction of CRUD Deposition on PWR Fuel Using a State-of-the-Art CFD-Based Multi-Physics Computational Tool. *Nuclear Engineering and Design* **2016**, *299*, 95–104, doi:10.1016/j.nucengdes.2015.10.010.
79. Zou, L.; Berry, R.A.; Martineau, R.C.; Andrs, D.; Zhang, H.; Hansel, J.E.; Sharpe, J.P.; Johns, R.C. *RELAP-7 Closure Correlations*; Idaho Falls, ID (United States), 2017;
80. Liu, Y.; Salko, R.; Kim, K.S.; Wang, X.; Kabelitz, M.; Choi, S.; Kochunas, B.; Collins, B.; Martin, W. Improved MPACT Energy Deposition and Explicit Heat Generation Coupling with CTF. *Ann Nucl Energy* **2021**, *152*, 107999, doi:10.1016/j.anucene.2020.107999.

81. Suk, P.; Chvála, O.; Maldonado, G.I.; Frýbort, J. Simulation of a NuScale Core Design with the CASL VERA Code. *Nuclear Engineering and Design* **2021**, *371*, 110956, doi:10.1016/j.nucengdes.2020.110956.
82. Stimpson, S.; Clarno, K.; Pawlowski, R.; Gardner, R.; Powers, J.; Collins, B.; Toth, A.; Novascone, S.; Pitts, S.; Hales, J.; et al. Coupled Fuel Performance Calculations in VERA and Demonstration on Watts Bar Unit 1, Cycle 1. *Ann Nucl Energy* **2020**, *145*, 107554, doi:10.1016/j.anucene.2020.107554.
83. Rose, M.; Downar, T.; Gleicher, F.N. *Redwing: A MOOSE Application for Coupling MPACT and BISON American Nuclear Society Winter Meeting 2014*; 2014;
84. Hamilton, S.P.; Evans, T.M.; Davidson, G.G.; Johnson, S.R.; Pandya, T.M.; Godfrey, A.T. Hot Zero Power Reactor Calculations Using the Insilico Code. *J Comput Phys* **2016**, *314*, 700–711, doi:10.1016/j.jcp.2016.03.033.
85. Pandya, T.M.; Bostelmann, F.; Jessee, M.; Ortensi, J. Two-Step Neutronics Calculations with Shift and Griffin for Advanced Reactor Systems. *Ann Nucl Energy* **2022**, *173*, 109131, doi:10.1016/j.anucene.2022.109131.
86. Litskevich, D.; Davies, S.; Detkina, A.; Merk, B. Verification of the LOTUS Code with C5G7 Benchmark. In Proceedings of the International Conference on Physics of Reactors 2022 (PHYSOR 2022); American Nuclear Society: Illinois, 2022; pp. 1784–1791.
87. Kliem, S.; Bilodid, Y.; Fridman, E.; Baier, S.; Grahn, A.; Gommlich, A.; Nikitin, E.; Rohde, U. The Reactor Dynamics Code DYN3D. *Kerntechnik* **2016**, *81*, 170–172, doi:10.3139/124.110692.
88. Salko, R.K.; Lange, T.; Kucukboyaci, V.; Palmtag, S.; Sung, Y.; Avramova, M. Development of Cobra-TF for Modelling Full-Core, Reactor Operating Cycles. In Proceedings of the Advances in Nuclear Fuel Management; American Nuclear Society, April 2015; pp. 1–18.
89. Jessee, M.A.; Wieselquist, W.A.; Evans, T.M.; Hamilton, S.P.; Jarrell, J.J.; Kim, K.S.; Lefebvre, J.P.; Lefebvre, R.A.; Mertuyrek, U.; Thompson, A.B.; et al. POLARIS: A New Two-Dimensional Lattice Physics Analysis Capability for the SCALE Code System.; United States, 2014.
90. Romano, P.K.; Horelik, N.E.; Herman, B.R.; Nelson, A.G.; Forget, B.; Smith, K. OpenMC: A State-of-the-Art Monte Carlo Code for Research and Development. *Ann Nucl Energy* **2015**, *82*, 90–97, doi:10.1016/j.anucene.2014.07.048.
91. Rossiter, G.; Peakman, A. Development and Validation of Loss of Coolant Accident (LOCA) Simulation Capability in the ENIGMA Fuel Performance Code for Zirconium-Based Cladding Materials. *Nuclear Engineering and Design* **2024**, *416*, 112767, doi:10.1016/j.nucengdes.2023.112767.
92. Zhang, H.; Zhao, H.; Gleicher, F.N.; DeHart, M.D.; Zou, L.; Andrs, D.; Martineau, R.C. *RELAP-7 Development Updates*; Idaho Falls, ID (United States), 2015;
93. Cao, L. Neutron Transport Equation. In *Deterministic Numerical Methods for Unstructured-Mesh Neutron Transport Calculation*; Elsevier, 2021; pp. 1–34 ISBN 9780128182215.
94. Zheng, Y. The Discrete Ordinate Method. In *Deterministic Numerical Methods for Unstructured-Mesh Neutron Transport Calculation*; Elsevier, 2021; pp. 167–213 ISBN 9780128182215.
95. Cao, L.; Fang, C. P -FEM Method. In *Deterministic Numerical Methods for Unstructured-Mesh Neutron Transport Calculation*; Elsevier, 2021; pp. 109–165.
96. Li, Y. Collision Probability Method. In *Deterministic Numerical Methods for Unstructured-Mesh Neutron Transport Calculation*; Elsevier, 2021; pp. 35–42 ISBN 9780128182215.
97. He, Q.; Cao, L. Current-Coupled Collision Probability Method. In *Deterministic Numerical Methods for Unstructured-Mesh Neutron Transport Calculation*; Elsevier, 2021; pp. 61–71 ISBN 9780128182215.
98. Liu, Z. The Method of Characteristics. In *Deterministic Numerical Methods for Unstructured-Mesh Neutron Transport Calculation*; Elsevier, 2021; pp. 73–108 ISBN 9780128182215.
99. Zheng, Y.; Li, Y.; Cao, L. Other Methods. In *Deterministic Numerical Methods for Unstructured-Mesh Neutron Transport Calculation*; Elsevier, 2020; pp. 243–270 ISBN 9780128182215.
100. Bogado Leite, S.Q.; Palma, D.A.P.; de Vilhena, M.T.; Bodmann, B.E.J. Analytical Representation of the Solution of the Point Reactor Kinetics Equations with Adaptive Time Step. *Progress in Nuclear Energy* **2014**, *70*, 112–118, doi:10.1016/j.pnucene.2013.07.008.

101. Srivastava, A.; Singh, K.P.; Degweker, S.B. Monte Carlo Methods for Reactor Kinetic Simulations. *Nuclear Science and Engineering* **2018**, *189*, 152–170, doi:10.1080/00295639.2017.1388091.
102. Bestion, D.; Morel, C. Balance Equations. In *Thermal-Hydraulics of Water Cooled Nuclear Reactors*; Elsevier, 2017; pp. 167–244 ISBN 9780081006627.
103. Yang, B.-W.; Han, B.; Liu, A.; Wang, S. Recent Challenges in Subchannel Thermal-Hydraulics-CFD Modeling, Subchannel Analysis, CHF Experiments, and CHF Prediction. *Nuclear Engineering and Design* **2019**, *354*, 110236, doi:10.1016/j.nucengdes.2019.110236.
104. Jeong, J.J. Constitutive Equations. NUREG/CR-1230, ANL-79-105. In *Thermal-Hydraulics of Water Cooled Nuclear Reactors*; Elsevier, 2017; pp. 549–594 ISBN 9780081006627.
105. Umminger, K.; D’Auria, F. Pressure Drops in Nuclear Thermal-Hydraulics: Principles, Experiments, and Modeling. Principles, Experiments, and Modeling. In *Thermal-Hydraulics of Water Cooled Nuclear Reactors*; Elsevier, 2017; pp. 493–547 ISBN 9780081006627.
106. Aksan, N. Target Phenomena in Nuclear Thermal-Hydraulics. In *Thermal-Hydraulics of Water Cooled Nuclear Reactors*; Elsevier, 2017; pp. 245–356 ISBN 9780081006627.
107. Shen, D.; Liu, X.; Cheng, X. A New Turbulent Mixing Modeling Approach for Sub-Channel Analysis Code. *Ann Nucl Energy* **2018**, *121*, 194–202, doi:10.1016/j.anucene.2018.07.023.
108. Kirillov, P.L.; Ninokata, H. Heat Transfer in Nuclear Thermal Hydraulics. Report EUR 12402 EN, Commission of the European Communities, Nuclear Science and Technology. In *Thermal-Hydraulics of Water Cooled Nuclear Reactors*; Elsevier, 2017; pp. 357–492 ISBN 9780081006627.
109. Gandhir, A.; Hassan, Y. RANS Modeling for Flow in Nuclear Fuel Bundle in Pressurized Water Reactors (PWR). *Nuclear Engineering and Design* **2011**, *241*, 4404–4408, doi:10.1016/j.nucengdes.2011.08.084.
110. Merzari, E.; Obabko, A.; Fischer, P.; Halford, N.; Walker, J.; Siegel, A.; Yu, Y. Large-Scale Large Eddy Simulation of Nuclear Reactor Flows: Issues and Perspectives. *Nuclear Engineering and Design* **2017**, *312*, 86–98, doi:10.1016/j.nucengdes.2016.09.028.
111. Fang, J.; Cambareri, J.J.; Brown, C.S.; Feng, J.; Gouws, A.; Li, M.; Bolotnov, I.A. Direct Numerical Simulation of Reactor Two-Phase Flows Enabled by High-Performance Computing. *Nuclear Engineering and Design* **2018**, *330*, 409–419, doi:10.1016/j.nucengdes.2018.02.024.
112. Watson, J.K.; Ivanov, K.N. Improved Cross-Section Modeling Methodology for Coupled Three-Dimensional Transient Simulations. *Ann Nucl Energy* **2002**, *29*, 937–966, doi:10.1016/S0306-4549(01)00085-8.
113. Zhang, H.; Guo, J.; Lu, J.; Li, F.; Xu, Y.; Downar, T.J. An Assessment of Coupling Algorithms in HTR Simulator TINTE. *Nuclear Science and Engineering* **2018**, *190*, 287–309, doi:10.1080/00295639.2018.1442061.
114. Wang, J.; Wang, Q.; Ding, M. Review on Neutronic/Thermal-Hydraulic Coupling Simulation Methods for Nuclear Reactor Analysis. *Ann Nucl Energy* **2020**, *137*, 107165, doi:10.1016/j.anucene.2019.107165.
115. Zhou, X. Operator Split, Picard Iteration and JFNK Methods Based on Nonlinear CMFD for Transient Full Core Models in the Coupling Multiphysics Environment. *Ann Nucl Energy* **2023**, *183*, 109669, doi:10.1016/j.anucene.2022.109669.
116. Wieselquist, W.; Lefebvre, R. *SCALE 6.3.1 User Manual*; Oak Ridge, TN (United States), 2023;
117. Jessee, M.A.; Wieselquist, W.A.; Gentry, C.A.; Mertyurek, U. BWR Geometry Enhancements for the Polaris Lattice Physics Code 1. In Proceedings of the Transactions of the American Nuclear Society; ORNL, November 2017; pp. 1301–1305.
118. Gentry, C.; Jessee, M.; Kim, K.S. Improvements in the Polaris Implementation of the Embedded Self-Shielding Method.; United States, 2018.
119. Jessee, M.A.; Wieselquist, W.A.; Mertyurek, U.; Kim, K.S.; Evans, T.M.; Hamilton, S.P.; Gentry, C. Lattice Physics Calculations Using the Embedded Self-Shielding Method in Polaris, Part I: Methods and Implementation. *Ann Nucl Energy* **2021**, *150*, 107830, doi:10.1016/j.anucene.2020.107830.
120. Mertyurek, U.; Jessee, M.A.; Betzler, B.R. Lattice Physics Calculations Using the Embedded Self-Shielding Method in Polaris, Part II: Benchmark Assessment. *Ann Nucl Energy* **2021**, *150*, 107829, doi:10.1016/j.anucene.2020.107829.

121. Kim, K.S.; Wiarda, D.; Chapman, C.; McDonnell, J.; Wieselquist, W. Improvement of the SCALE-6.3/XSProc Pointwise Slowing-Down Capability with the Bound Thermal Scattering Data Including High Forward Peaks.; United States, 2023.
122. Litskevich, D. *Development of an Advanced Neutron Transport Solver for Zooming in DYN3D*; Rheinisch-Westfälischen Technischen Hochschule Aachen: Aachen, 2017;
123. Litskevich, D.; Merk, B.; Atkinson, S. Verification of the Current Coupling Collision Probability Method with Orthogonal Flux Expansion for the Case of Single Cell. *Progress in Nuclear Energy* **2020**, *120*, 103219, doi:10.1016/j.pnucene.2019.103219.
124. Litskevich, D.; Atkinson, S.; Davies, S. Verification of the Current Coupling Collision Probability Method with Orthogonal Flux Expansion for the Assembly Calculations. *Progress in Nuclear Energy* **2020**, *130*, 103562, doi:10.1016/j.pnucene.2020.103562.
125. Massachusetts Institute of Technology (MIT); UChicago Argonne The Open MC Monte Carlo Code Available online: <https://docs.openmc.org/en/stable/usersguide/index.html> (accessed on 18 February 2024).
126. Romano, P.K.; Forget, B. The OpenMC Monte Carlo Particle Transport Code. *Ann Nucl Energy* **2013**, *51*, 274–281, doi:10.1016/j.anucene.2012.06.040.
127. Walsh, J.; Forget, B.; Smith, K. *Validation of OpenMC Reactor Physics Simulations with the B&W 1810 Series Benchmarks*; 2013; Vol. 109;.
128. Herman, B.R.; Forget, B.; Smith, K.; Romano, P.K.; Sutton, T.M.; Kelly, D.J.; Aviles, B.N. *Analysis of Tally Correlation in Large Light Water Reactors*; Japan, 2015;
129. Kelly, D.J.; Aviles, B.N.; Romano, P.K.; Herman, B.R.; Horelik, N.E.; Forget, B. *Analysis of Select BEAVRS PWR Benchmark Cycle 1 Results Using MC21 and OpenMC*; Japan, 2015;
130. Qayyum, F.; Ali, M.R.; Zahur, A.; Khan, R. Improvements in Methodology to Determine Feedback Reactivity Coefficients. *Nuclear Science and Techniques* **2019**, *30*, 63, doi:10.1007/s41365-019-0588-0.
131. Grundmann, U.; Rohde, U.; Mittag, S.; Kliem, S. *DYN3D Version 3.2 Code for Calculation of Transients in Light Water Reactors (LWR) with Hexagonal or Quadratic Fuel Elements-Description of Models and Methods*; HZDR: Dresden, Germany, 2005;
132. Grundmann, U.; Mittag, S.; Rohde, U. *DYN3D Version 3.2 - Code for Calculation of Transients in Light Water Reactors (LWR) with Hexagonal or Quadratic Fuel Elements - Code Manual and Input Data Description for Release*; HZDR: Dresden, Germany, 2007;
133. Rohde, U. The Modeling of Fuel Rod Behaviour under RIA Conditions in the Code DYN3D. *Ann Nucl Energy* **2001**, *28*, 1343–1363, doi:10.1016/S0306-4549(00)00128-6.
134. Gomez Torres, A.; Sanchez-Espinoza, V.H.; Kliem, S.; Gommlich Andre Implementation of a Fast Running Full Core Pin Power Reconstruction Method in DYN3D. *Nuclear Engineering and Design* **2014**, *274*, 44–55, doi:10.1016/j.nucengdes.2014.04.028.
135. Bilodid, Y.; Fridman, E.; Kotlyar, D.; Shwageraus, E. Explicit Decay Heat Calculation in the Nodal Diffusion Code DYN3D. *Ann Nucl Energy* **2018**, *121*, 374–381, doi:10.1016/j.anucene.2018.07.045.
136. Viebach, M.; Lange, C.; Kliem, S.; Demazière, C.; Rohde, U.; Hennig, D.; Hurtado, A. Verification of the Code DYN3D for Calculations of Neutron Flux Fluctuations. *Ann Nucl Energy* **2022**, *166*, 108735, doi:10.1016/j.anucene.2021.108735.
137. Duerigen, S.; Fridman, E. The Simplified P3 Approach on a Trigonal Geometry of the Nodal Reactor Code DYN3D. *Kerntechnik* **2012**, *77*, 226–229, doi:10.3139/124.110247.
138. Salko Jr, R.; Avramova, M.; Wysocki, A.; Toptan, A.; Hu, J.; Porter, N.; Blyth, T.S.; Dances, C.A.; Gomez, A.; Jernigan, C.; et al. *CTF 4.0 Theory Manual*; ORNL: Oak Ridge, TN (United States), 2019;
139. Salko Jr, R.; Avramova, M.; Wysocki, A.; Hu, J.; Toptan, A.; Porter, N.; Blyth, T.S.; Dances, C.A.; Gomez, A.; Jernigan, C.; et al. *CTF 4.0 User's Manual*; ORNL: Oak Ridge, TN (United States), 2019;
140. Ha, K.S.; Jeong, J.J.; Sim, S.K. Improvement of Liquid Droplet Entrainment Model in the COBRA-TF Code. *Journal of the Korean Nuclear Society* **1998**, *30*, 181–193.
141. Liping, C.; Sung, Y.; Kucukboyaci, V. Implementation and Validation of COBRA-TF Subcooled Nucleate Boiling Model. *Proceedings of ICAPP* **2014**, *1*, 01513–01516.

142. Porter, N.W.; Salko, R.K.; Pilch, M. Development and Implementation of a CTF Code Verification Suite. *Nuclear Engineering and Design* **2020**, *370*, 110879, doi:10.1016/j.nucengdes.2020.110879.
143. Nguyen, N.H.; Kim, J.; Hong, S.-H.; Moon, S.-K.; Song, Ch.-H. Improvements of COBRA-TF on the Effect of Flow Blockage during a LB LOCA with Consideration of Fuel Relocation Phenomenon. *Nuclear Engineering and Design* **2017**, *325*, 218–231, doi:10.1016/j.nucengdes.2017.08.015.
144. Salko Jr, R.; Pilch, M.; Kumar, V. *Code and Solution Verification Assessment of the CTF Thermal Hydraulic Subchannel Code*; United States, 2021;
145. Rubin, A.; Schoedel, A.; Avramova, M.; Utsuno, H.; Bajorek, S.; Velazquez-Lozada, A. *OECD/NRC Benchmark Based on NUPEC PWR Sub-Channel and Bundle Tests (PSBT) Volume I: Experimental Database and Final Problem Specifications* NUCLEAR ENERGY AGENCY Organisation for Economic Co-Operation and Development; 2012;
146. Nuclear Energy Agency *International Benchmark on Pressurised Water Reactor Sub-Channel and Bundle Tests: Benchmark Results of Phase I - Void Distribution*; 2016;
147. Nuclear Energy Agency *International Benchmark on Pressurised Water Reactor Sub-Channel and Bundle Tests Volume III: Departure from Nucleate Boiling*; 2016;
148. Avramova, M.; Cuervo, D. Assessment of CTF Boiling Transition and Critical Heat Flux Modeling Capabilities Using the OECD/NRC BFBT and PSBT Benchmark Databases. *Science and Technology of Nuclear Installations* **2013**, *2013*, 1–12, doi:10.1155/2013/508485.
149. Zhao, X.; Wysocki, A.; Salko, R.; Shirvan, K. *Validation and Benchmarking of CTF for Single- and Two-Phase Flow*; 2017;
150. Davies, S.; Rohde, U.; Litskevich, D.; Merk, B.; Bryce, P.; Levers, A.; Detkina, A.; Atkinson, S.; Ravindra, V. CTF and Flocal Thermal Hydraulics Validations and Verifications within a Multiscale and Multiphysics Software Development. *Energies (Basel)* **2021**, *14*, doi:10.3390/en14051220.
151. Cho, N.Z.; Nurapt, K./ *Benchmark Problem 1A Benchmark Problem 1A: MOX Fuel-Loaded Small PWR Core (MOX Fuel with Zoning)*;
152. Calloo, A.; Leroyer, H.; Fliscounakis, M.; Couyras, D. *Core Neutronics Methodologies Applied to the MOX-Loaded KAIST 1A Benchmark: Reference to Industrial Calculations*; 2014;
153. Yuan, Y.; Xing, J.; Huo, X.; Wang, K. Research on the On-the-Fly Homogenization Method Based on RMC Code for Criticality Calculations. *Ann Nucl Energy* **2020**, *135*, 106985, doi:10.1016/j.anucene.2019.106985.
154. Davies, S.; Litskevich, D.; Rohde, U.; Detkina, A.; Merk, B.; Bryce, P.; Levers, A.; Ravindra, V. Dyn3d and CTF Coupling within a Multiscale and Multiphysics Software Development (Part I). *Energies (Basel)* **2021**, *14*, doi:10.3390/en14165060.
155. Davies, S.; Litskevich, D.; Merk, B.; Levers, A.; Bryce, P.; Detkina, A. DYN3D and CTF Coupling within a Multiscale and Multiphysics Software Development (Part II). *Energies (Basel)* **2022**, *15*, doi:10.3390/en15134843.
156. Poljanin, L.; Ibragimov, M. Teploobmen v Jadernikh Reaktorakh. In *Proceedings of the Ehnergoizdat*; Moscow, USSR, 1982; p. 296.
157. Bezrukov, Y.; Astakhov, V. Experimental Investigation and Static Analysis of Data on Crisis of Heat Exchange in Beams of Rods for WWER Reactors. *Teploehnergetika* **1976**, *8*, 80–82.
158. Rogers, J.T.; Rosehart, R.G. Mixing by Turbulent Interchange in Fuel Bundles in Correlations and Interfaces. In *Proceedings of the ASME*; New York, USA, 1972; pp. 1–12.
159. Thorn, J.R.S.; Walker, W.M.; Fallon, T.A.; Reising, G.F.S. Paper 6: Boiling in Sub-Cooled Water during Flow up Heated Tubes or Annuli. *Proceedings of the Institution of Mechanical Engineers, Conference Proceedings* **1965**, *180*, 226–246, doi:10.1243/PIME_CONF_1965_180_117_02.
160. Groeneveld, D.C.; Shan, J.Q.; Vasić, A.Z.; Leung, L.K.H.; Durmayaz, A.; Yang, J.; Cheng, S.C.; Tanase, A. The 2006 CHF Look-up Table. *Nuclear Engineering and Design* **2007**, *237*, 1909–1922, doi:10.1016/j.nucengdes.2007.02.014.